

AD-A116 777

AIR FORCE INST OF TECH WRIGHT-PATTERSON AFB OH F/G 7/4  
PHOTOACOUSTIC SPECTROSCOPY OF CHEMICALLY MODIFIED SURFACES. (U)  
AUG 81 L W BURGGRAB

**UNCLASSIFIED**

AFIT-81-16D

NL

1 of 3

UNCLASS

SECURITY CLASSIFICATION OF THIS PAGE (When Data Entered)

REPORT DOCUMENTATION PAGE		READ INSTRUCTIONS BEFORE COMPLETING FORM
1. REPORT NUMBER 81-16D	2. GOVT ACCESSION NO. AD-A116777	3. RECIPIENT'S CATALOG NUMBER
4. TITLE (and Subtitle) Photoacoustic Spectroscopy of Chemically Modified Surfaces		5. TYPE OF REPORT & PERIOD COVERED THESIS/DISSERTATION
7. AUTHOR(s) Larry Wilson Burggraf		6. PERFORMING ORG. REPORT NUMBER
9. PERFORMING ORGANIZATION NAME AND ADDRESS AFIT STUDENT AT: University of Denver		8. CONTRACT OR GRANT NUMBER(s)
11. CONTROLLING OFFICE NAME AND ADDRESS AFIT/NR WPAFB OH 45433		10. PROGRAM ELEMENT, PROJECT, TASK AREA & WORK UNIT NUMBERS
14. MONITORING AGENCY NAME & ADDRESS (if different from Controlling Office)		12. REPORT DATE August 1981
		13. NUMBER OF PAGES 257
		15. SECURITY CLASS. (of this report) UNCLASS
16. DISTRIBUTION STATEMENT (of this Report) APPROVED FOR PUBLIC RELEASE; DISTRIBUTION UNLIMITED		15a. DECLASSIFICATION/DOWNGRADING SCHEDULE
17. DISTRIBUTION STATEMENT (of the abstract entered in Block 20, if different from Report)		
18. SUPPLEMENTARY NOTES APPROVED FOR PUBLIC RELEASE: IAW AFR 190-17 LYNN E. WOLAVER Dean for Research and Professional Development APPROVED FOR PUBLIC RELEASE: IAW AFR 190-17		
19. KEY WORDS (Continue on reverse side if necessary and identify by block number) AIR FORCE-INITIATIVE OF TECHNOLOGY (ATC) WRIGHT-PATTERSON AFB, OH 45433 2 July 82		
20. ABSTRACT (Continue on reverse side if necessary and identify by block number) ATTACHED 82 07 07 062		

DTIC  
SELECTED  
JUL 9 1982

FILE COPY

DD FORM 1 JAN 73 1473

EDITION OF 1 NOV 65 IS OBSOLETE

UNCLASS

SECURITY CLASSIFICATION OF THIS PAGE (When Data Entered)

ABSTRACT

The ultimate goal of this research was to apply photoacoustic spectroscopy to the study of surface species on chemically modified surfaces. The study begins with a review of the theory of photoacoustic spectroscopy developed by Rosencwaig and Gersho. The theory for thermally thick samples is cast into a form more suitable for quantification. The photoacoustic magnitude and phase information are combined in a response function which is linear with optical absorption. The theory is extended to account for scattered-light effects in intensely light-scattering materials. Also, a method to correct for the effects of stray light in photoacoustic spectroscopy is presented. The potential of this spectroscopic technique for obtaining ultraviolet absorption spectra of organic functional groups immobilized on silica surfaces by silylation is demonstrated. The complexation of copper (II) by an ethylenediammine analog immobilized on silica gel by silylation was characterized by photoacoustic spectroscopy and heterogeneous binding studies. Independent mono and bis binding sites are formed on the silica surface. Photoacoustic spectroscopy was used to study  $\text{Ni}/\gamma\text{-Al}_2\text{O}_3$ ,  $\text{Co}/\gamma\text{-Al}_2\text{O}_3$  and  $\text{Co-Mo}/\gamma\text{-Al}_2\text{O}_3$  catalysts. Visible spectral features are identified with octahedrally and tetrahedrally coordinated metal ions and metal oxides. A model is advanced to account for the dependence of speciation on metal loading and calcination temperature.



Accession For	
NTIS GRA&I	✓
DTIC TAB	
Unannounced	
Justification	
By	
Distribution/	
Availability Codes	
Avail and/or	
Dist	Special
A	

## ABSTRACT

The ultimate goal of this research was to apply photoacoustic spectroscopy to the study of surface species on chemically modified surfaces. The study begins with a review of the theory of photoacoustic spectroscopy developed by Rosencwaig and Gersho. The theory for thermally thick samples is cast into a form more suitable for quantification. The photoacoustic magnitude and phase information are combined in a response function which is linear with optical absorption. The theory is extended to account for scattered-light effects in intensely light-scattering materials. Also, a method to correct for the effects of stray light in photoacoustic spectroscopy is presented. The potential of this spectroscopic technique for obtaining ultraviolet absorption spectra of organic functional groups immobilized on silica surfaces by silylation is demonstrated. The complexation of copper (II) by an ethylenediamine analog immobilized on silica gel by silylation was characterized by photoacoustic spectroscopy and heterogeneous binding studies. Independent mono and bis binding sites are formed on the silica surface. Photoacoustic spectroscopy was used to study  $\text{Ni}/\gamma\text{-Al}_2\text{O}_3$ ,  $\text{Co}/\gamma\text{-Al}_2\text{O}_3$  and  $\text{Co-Mo}/\gamma\text{-Al}_2\text{O}_3$  catalysts. Visible spectral features are identified with octahedrally and tetrahedrally coordinated metal ions and metal oxides. A model is advanced to account for the dependence of speciation on metal loading and calcination temperature.

## AFIT RESEARCH ASSESSMENT

81-16D

The purpose of this questionnaire is to ascertain the value and/or contribution of research accomplished by students or faculty of the Air Force Institute of Technology (ATC). It would be greatly appreciated if you would complete the following questionnaire and return it to:

AFIT/NR  
Wright-Patterson AFB OH 45433

RESEARCH TITLE: Photoacoustic Spectroscopy of Chemically Modified Surfaces

AUTHOR: Larry Wilson Burggraf

## RESEARCH ASSESSMENT QUESTIONS:

1. Did this research contribute to a current Air Force project?

☐ a. YES

☐ b. NO

2. Do you believe this research topic is significant enough that it would have been researched (or contracted) by your organization or another agency if AFIT had not?

☐ a. YES

☐ b. NO

3. The benefits of AFIT research can often be expressed by the equivalent value that your agency achieved/received by virtue of AFIT performing the research. Can you estimate what this research would have cost if it had been accomplished under contract or if it had been done in-house in terms of manpower and/or dollars?

☐ a. MAN-YEARS \_\_\_\_\_

☐ b. \$ \_\_\_\_\_

4. Often it is not possible to attach equivalent dollar values to research, although the results of the research may, in fact, be important. Whether or not you were able to establish an equivalent value for this research (3. above), what is your estimate of its significance?

☐ a. HIGHLY  
SIGNIFICANT

☐ b. SIGNIFICANT

☐ c. SLIGHTLY  
SIGNIFICANT

☐ d. OF NO  
SIGNIFICANCE

5. AFIT welcomes any further comments you may have on the above questions, or any additional details concerning the current application, future potential, or other value of this research. Please use the bottom part of this questionnaire for your statement(s).

NAME

GRADE

POSITION

ORGANIZATION

LOCATION

STATEMENT(s):

PHOTOACOUSTIC SPECTROSCOPY OF CHEMICALLY  
MODIFIED SURFACES

---

A Dissertation

Presented to  
the Faculty of the Graduate School of Arts and Sciences  
University of Denver

---

In Partial Fulfillment  
of the Requirements for the Degree  
Doctor of Philosophy

---

by  
Larry Wilson Burggraf

August 1981

THE GRADUATE SCHOOL OF ARTS AND SCIENCES  
OF  
THE UNIVERSITY OF DENVER

Upon the recommendation of the chairman of  
the Department of Chemistry this dissertation  
is hereby accepted in partial fulfillment of  
the requirements for the degree of

Doctor of Philosophy

Donald E. Lyden  
Professor in charge of dissertation

James R. Davis  
Associate Dean for Graduate Studies

July 13, 1981  
Date

"Experiments never deceive. It is our judgement that sometimes  
deceives itself, because it expects results that experiment refuses."

Leonardo da Vinci



## TABLE OF CONTENTS

	Page
LIST OF TABLES . . . . .	v
LIST OF FIGURES . . . . .	vi
 Chapter	
1. INTRODUCTION . . . . .	1
The Optoacoustic Effect . . . . .	1
Revival of Optoacoustics . . . . .	3
Photoacoustic Spectroscopy . . . . .	4
Research Direction . . . . .	5
References . . . . .	7
2. INSTRUMENTATION AND DATA PROCESSING . . . . .	11
PAS Instrumentation . . . . .	11
PAS Data Processing . . . . .	22
Other Instrumentation . . . . .	27
References . . . . .	28
3. PHOTOACOUSTIC SPECTROSCOPY THEORY . . . . .	29
Introduction . . . . .	29
Rosencwaig-Gersho Theory . . . . .	31
Correction for Saturation Effects . . . . .	37
Intensely Light-Scattering Samples . . . . .	46
Experimental Confirmation . . . . .	54
Stray Light Correction in Photoacoustic Spectroscopy . . . . .	92
References . . . . .	101

Chapter	Page
4. COPPER (II) COMPLEXATION WITH A SURFACE-IMMOBILIZED LIGAND . . . . .	103
Introduction . . . . .	103
Experimental . . . . .	104
Silylation . . . . .	104
Photoacoustic Spectroscopy (PAS) Study . . . . .	106
Binding Studies . . . . .	106
Results and Discussion . . . . .	107
Solution-Phase Equilibrium . . . . .	107
Photoacoustic Spectroscopy Results . . . . .	110
Conclusions . . . . .	132
References . . . . .	133
5. ULTRAVIOLET PHOTOACOUSTIC SPECTROSCOPY OF IMMOBILIZED ORGANIC FUNCTIONAL GROUPS ON SILICA SURFACES . . . . .	135
Introduction . . . . .	135
Experimental . . . . .	138
Measurements . . . . .	138
Synthesis . . . . .	140
Dithiocarbamate Derivatives . . . . .	140
Immobilized Benzylacetylacetone Derivative . . . . .	141
Benzylacetylacetone Model Compounds . . . . .	142
Results and Discussion . . . . .	143
Dithiocarbamate Derivatives of Immobilized Amines . . . . .	143

Chapter	Page
Immobilized 3-Benzylacetylacetone Derivative . . . . .	147
Conclusion . . . . .	154
References . . . . .	155
Appendix . . . . .	156
6. PHOTOACOUSTIC SPECTROSCOPY OF $\gamma$ -ALUMINA SUPPORTED METAL OXIDE CATALYSTS . . . . .	165
Introduction . . . . .	165
Experimental . . . . .	166
Results and Discussion . . . . .	169
Considerations for Quantitative PAS . . . . .	169
Nickel/ $\gamma$ -Alumina Catalysts . . . . .	178
Qualitative PAS Results . . . . .	180
Quantitative PAS Results . . . . .	196
Conclusions . . . . .	207
Cobalt/ $\gamma$ -Alumina Catalysts . . . . .	210
Qualitative PAS Results . . . . .	211
Quantitative PAS Results . . . . .	227
Conclusions . . . . .	233
Cobalt-Molybdenum/ $\gamma$ -Alumina Catalysts . . . . .	236
Qualitative PAS Results . . . . .	238
Conclusions . . . . .	244
Model for Metal-Support Interactions . . . . .	244
References . . . . .	257

## LIST OF TABLES

Table		Page
	<u>Chapter 3</u>	
1.	Thermal diffusion properties of substrate materials . . . . .	67
2.	Comparison of opaque reference materials made by depositing suspended carbon black on substrates . . . . .	70
3.	Results of least-squares fit of phase data for chromate- loaded substrates to Equation 49 . . . . .	74
	<u>Chapter 5</u>	
1.	Chelating agents immobilized on silica surfaces . . . . .	139
	<u>Chapter 6</u>	
1.	Statistics, at 95% confidence limit, for least-squares fit of $C\beta\mu_s$ versus percent of NiO in $\gamma\text{-Al}_2\text{O}_3$ up to 11% NiO . . . . .	177
2.	Approximate wavelengths of spin-orbit maxima for Co materials . . . . .	243
3.	Assignments for application of interaction model to catalyst systems . . . . .	251

## LIST OF FIGURES

Figure	Page
<u>Chapter 2</u>	
1. Schematic diagram of photoacoustic spectrometer . . . . .	12
2. Photoacoustic magnitude spectrum for $\text{Ho}_2\text{O}_3$ . . . . .	15
3. Acoustic cell diagram . . . . .	17
4. Oscilloscope trace of microphone preamplifier output . . . . .	20
5. Visible magnitude spectrum and phase spectrum for carbon powder reference material . . . . .	24
<u>Chapter 3</u>	
1. Idealized photoacoustic cell . . . . .	32
2. Rosencwaig-Gersho special cases for thermally thick samples . . . . .	38
3. Representation of variation of photoacoustic response vector in phase space as $\beta\mu_s$ increases . . . . .	42
4. Calculated dependence of phase angle on absorbance for increasing values of $S\mu_s$ . . . . .	50
5. Calculated dependence of phase function on absorbance for increasing values of $S\mu_s$ . . . . .	52
6. Photoacoustic spectrum of chromate on alumina substrate for various loadings . . . . .	56
7. Dependence of photoacoustic magnitude on chromate loading for alumina . . . . .	58

Figure	Page
8. Dependence of photoacoustic magnitude on chromate loading for silica materials . . . . .	60
9. Dependence of phase function on chromate loading for alumina . . . . .	62
10. Dependence of phase function on chromate loading for silica materials . . . . .	64
11. Plot of logarithm of photoacoustic magnitude versus logarithm of chromate loading for silica materials . . . . .	68
12. Least-squares fit of quadratic dependence of $f^2(\psi)$ on chromate loading for alumina substrate . . . . .	72
13. Dependence of corrected response function on chromate loading for alumina substrate with and without reflectance correction . . . . .	77
14. Logarithmic plot of corrected response function versus loading with least-squares linear fit . . . . .	79
15. Dependence of corrected response function on chromate loading for silica materials . . . . .	81
16. Comparison of photoacoustic magnitude spectrum (A) and corrected photoacoustic spectrum (B) of chromate-loaded fumed silica with solution phase chromate spectrum (C) . . . . .	83
17. Photoacoustic magnitude spectrum of undiluted chemically modified fumed silica . . . . .	86
18. Dependence of photoacoustic magnitude on mass fraction of chemically modified fumed silica . . . . .	88

Figure	viii Page
19. Corrected photoacoustic response function versus mass fraction of chemically modified fumed silica . . . . .	90
20. Reference ultraviolet photoacoustic magnitude spectrum with air-only light filter (A) and color glass light filter (B) . . . . .	96
21. Ultraviolet photoacoustic magnitude spectrum of salicylaldehyde derivative of N-2-aminoethyl-3-aminopropyltri- methoxysilane immobilized on silica gel with (A) and without (B) stray light correction . . . . .	99

#### Chapter 4

1. Corrected absorbance versus AEAPS mole fraction at 556 nm and 656 nm . . . . .	108
2. Visible spectra of bis copper (II) - AEAPS (A) and mono copper (II) - AEAPS (B) with nitrate counterion in aqueous solution . . . . .	111
3. Copper loading and wavelength of absorption maximum for AEAPS- modified silica gel versus initial copper (II) concentration in 0.10 mol L <sup>-1</sup> acetate buffer . . . . .	113
4. Scaled PAS absorption spectra for AEAPS- modified silica gel loaded with copper (II) at 1X10 <sup>-3</sup> mol L <sup>-1</sup> (A) and 1X10 <sup>-1</sup> mol L <sup>-1</sup> (B) initial copper (II) concentration in 0.10 mol L <sup>-1</sup> acetate buffer. Spectrum of mono species (C) found by difference . . . . .	116
5. Absorbance of AEAPS-modified silica gel at 535 nm versus total copper loading as determined by XRF measurement . . . . .	119

## Figure

## Page

6. Photoacoustic magnitude spectra for copper (II) - SAEAPS chelates on silica gel formed at  $1.0 \times 10^{-1}$  mol L<sup>-1</sup> copper (II) concentration (A), copper (II) - SAEAPS chelates on silica gel formed at  $1.0 \times 10^{-3}$  mol L<sup>-1</sup> copper (II) concentration (B) and unloaded SAEAPS - modified silica gel (C) . . . . . 123
7. Corrected photoacoustic response function at 620 nm versus copper loading of SAEAPS - modified silica gel as determined by XRF . . . . . 126
8. Reciprocal of amount of bound copper versus reciprocal of solution-phase copper (II) concentration. Solid curve results from iterative fit of two-site model . . . . . 130

Chapter 5

1. Silylation scheme . . . . . 136
2. Ultraviolet photoacoustic magnitude spectra of dithiocarbamate derivatives of AEAPS immobilized on fumed silica using mono (A) and bis (B) synthesis procedures and dithiocarbamate derivatives of APS immobilized on fumed silica using mono (C) and bis (D) synthesis procedures . . . . . 145
3. Ultraviolet spectra of (I) 3-benzylacetylacetone in cyclohexane and (II) 3,3-dibenzylacetylacetone in cyclohexane . . . . . 149
4. Ultraviolet photoacoustic magnitude spectra of 3-benzylacetylacetone analog immobilized on silica gel (A) and 3-benzylacetylacetone adsorbed on silica gel (B) . . . . . 151



## Figure

## Page

Appendix to Chapter 5

A-1.	Ultraviolet photoacoustic spectrum of AEAPS immobilized on silica gel . . . . .	157
A-2.	Ultraviolet photoacoustic spectra of DTC-AEAPS and BDTC-AEAPS immobilized on controlled pore glass . . . . .	159
A-3.	Ultraviolet photoacoustic spectra of DK-APS (A) and DK-AEAPS (B) immobilized on fumed silica . . . . .	161
A-4.	Ultraviolet photoacoustic spectra of AA-AEAPS (A) and HFA-AEAPS (B) immobilized on silica gel . . . . .	163

Chapter 6

1.	Photoacoustic magnitude versus percent NiO in $\gamma\text{-Al}_2\text{O}_3$ for wavelengths 420 nm, 500 nm and 578 nm . . . . .	171
2.	Photoacoustic phase function versus percent NiO in $\gamma\text{-Al}_2\text{O}_3$ for wavelengths 420 nm, 500 nm and 578 nm . . . . .	173
3.	Photoacoustic response function versus percent NiO in $\gamma\text{-Al}_2\text{O}_3$ for wavelengths 420 nm, 500 nm and 578 nm . . . . .	175
4.	Photoacoustic spectrum of largely normal $\text{NiAl}_2\text{O}_4$ spinel (A) and a disordered $\text{NiAl}_2\text{O}_4$ spinel (B) . . . . .	181
5.	Photoacoustic spectrum of 20% $\text{Ni}(\text{NO}_3)_2 \cdot 6\text{H}_2\text{O}$ ground in $\gamma\text{-Al}_2\text{O}_3$ . . . . .	183
6.	Photoacoustic spectrum of NiO . . . . .	185

Figure	Page
7. Photoacoustic spectra of Ni/ $\gamma$ -Al <sub>2</sub> O <sub>3</sub> catalysts calcined at 600°C . . . . .	187
8. Photoacoustic spectrum of Ni/ $\gamma$ -Al <sub>2</sub> O <sub>3</sub> catalyst loaded with 2.5% Ni calcined at 600°C . . . . .	189
9. Photoacoustic spectra of Ni/ $\gamma$ -Al <sub>2</sub> O <sub>3</sub> catalysts calcined at 500°C . . . . .	192
10. Photoacoustic spectra of selected Ni/ $\gamma$ -Al <sub>2</sub> O <sub>3</sub> catalysts calcined at 400°C . . . . .	194
11. Photoacoustic spectrum of Ni/ $\gamma$ -Al <sub>2</sub> O <sub>3</sub> catalyst loaded with 7% nickel prepared by calcining at 400°C. Spectra recorded before (I) and after (II) re-calcining at 600°C for 5 hours . . . . .	197
12. Photoacoustic response function at 504 nm divided by the percent of nickel in the catalyst plotted versus the percent of nickel for catalysts calcined at 600°C (A) and 400°C (B) . . . . .	199
13. Net photoacoustic response function at 590 nm, A <sub>590</sub> , and A <sub>590</sub> / % Ni plotted versus percent of nickel in catalysts calcined at 600°C . . . . .	203
14. Net photoacoustic response function at 450 nm, A <sub>450</sub> , and A <sub>450</sub> / % Ni plotted versus percent of nickel in catalysts calcined at 600°C . . . . .	205
15. Sum of weighted photoacoustic response functions for Ni(T) and Ni(O) divided by percent of nickel plotted versus percent of nickel in catalysts calcined at 600°C . . . . .	208

Figure	Page
16. Photoacoustic spectrum of 1% CoAl <sub>2</sub> O <sub>4</sub> ground in $\gamma$ -Al <sub>2</sub> O <sub>3</sub> . . . . .	212
17. Photoacoustic spectrum of (I) Co <sub>3</sub> O <sub>4</sub> ground with $\gamma$ -alumina and (II) CoO-enhanced cobalt oxide ground with $\gamma$ -alumina . . . . .	214
18. Photoacoustic spectrum of 20% Co(NO <sub>3</sub> ) <sub>2</sub> · 6 H <sub>2</sub> O ground with $\gamma$ -alumina with background subtracted . . . . .	217
19. Photoacoustic spectrum of 5% Co(CH <sub>3</sub> COCHCOCH <sub>3</sub> ) <sub>3</sub> ground with $\gamma$ -alumina . . . . .	219
20. Photoacoustic spectra of Co/ $\gamma$ -Al <sub>2</sub> O <sub>3</sub> catalysts calcined at 600°C . . . . .	221
21. Photoacoustic spectra of Co/ $\gamma$ -Al <sub>2</sub> O <sub>3</sub> catalysts calcined at 400°C . . . . .	223
22. Difference spectrum for 0.50% Co/ $\gamma$ -Al <sub>2</sub> O <sub>3</sub> catalysts in which the spectrum of the catalyst calcined at 400°C is subtracted from that of the catalyst calcined at 600°C . . . . .	225
23. Net photoacoustic response function at 578 nm, A <sub>578</sub> , and A <sub>578</sub> / % Co plotted versus percent of cobalt in catalysts calcined at 400°C and 600°C . . . . .	229
24. Net photoacoustic response function at 420 nm, A <sub>420</sub> , and A <sub>420</sub> / % Co plotted versus percent of cobalt in catalysts calcined at 400°C and 600°C . . . . .	231

Figure	Page
25. Sum of weighted photoacoustic response functions for Co(T) and Co(O) divided by percent of cobalt plotted versus percent of cobalt in catalysts calcined at 400°C and 600°C . . . . .	234
26. Photoacoustic spectrum of 6% CoMoO <sub>4</sub> in $\gamma$ -Al <sub>2</sub> O <sub>3</sub> . . . . .	239
27. Photoacoustic spectra of Co-Mo/ $\gamma$ -Al <sub>2</sub> O <sub>3</sub> catalysts calcined at 550°C . . . . .	241
28. Comparison of photoacoustic spectra of Co-Mo/ $\gamma$ -Al <sub>2</sub> O <sub>3</sub> catalysts loaded with 7% Co (A) with CoMoO <sub>4</sub> spectrum (B) . . . . .	245
29. Prediction by model of relative amounts of M(T) and M(O) versus metal loading, represented by $mk_i\pi/DA$ . . . . .	254

## ACKNOWLEDGMENTS

The author acknowledges those who encouraged, those who helped,  
and those (giants) on whose shoulders he stood:

Joyce E. Burggraf

Dr. Donald E. Leyden

Dr. J. Keith Grime

Dr. Bruce B. Jablonski

Dr. Douglas S. Kendall

Dr. Roland L. Chin

Fu-Jann Pern

Steven E. Northcott

## Chapter 1

### INTRODUCTION

#### Purpose

Chemical modification of existing materials to produce more useful materials is the ultimate reason for doing chemistry. The reason for this study is to contribute to the understanding of chemically modified surfaces. High surface area supports have been chemically modified with numerous inorganics, organics and biologically active species to adapt these surfaces to various purposes. By better understanding the nature of the active species on the surface of these materials, more useful chemically modified surfaces might be made.

Early in the development of solid state photoacoustic spectroscopy, Rosencwaig pointed out the potential of this technique for obtaining qualitative optical absorption information about catalyst surfaces and chemisorbed species.<sup>1</sup> The successful application of photoacoustic spectroscopy to the qualitative study of molybdate species on chemically modified glass by Leyden et al.<sup>2</sup> motivated its application to other chemically modified materials.<sup>3</sup> As a natural extension of this earlier work, this study applies photoacoustic spectroscopy as a quantitative tool to the study of chemically modified surfaces.

#### The Photoacoustic Effect

In 1880 Alexander Graham Bell presented his work on the photophone to the American Association for the Advancement of Science.<sup>4</sup> In that

paper he told of the accidental discovery of the optoacoustic effect in solids. He observed that a rapidly modulated beam of sunlight focused on solids caused the emission of sound. The following year Bell detailed investigations of the optoacoustic effect in solids, liquids, and gases.<sup>5</sup> Strong acoustic signals were obtained for dark porous solids and light-absorbing gases, while weak acoustic signals were produced for light-absorbing liquids. He was able to demonstrate that the optoacoustic effect depends on the absorptivity of the material used. In that same year, John Tyndall<sup>6</sup> and Wilhelm Roentgen<sup>7</sup> reported the optoacoustic effect for various gases. Tyndall tried to make an instrument for methane detection but failed only because sufficiently sensitive acoustic detectors were not available. Practical applications of the optoacoustic effect were to await development of the electrostatic microphone (Wente, 1917) and signal processing electronics. In his book, Rosencwaig<sup>8</sup> wrote that Mercadier<sup>9</sup> and Preece<sup>10</sup> were first to offer a mechanism for the optoacoustic effect in solids which is essentially the same as that accepted today. Preece<sup>10</sup> wrote that the optoacoustic effect "...is purely an effect of radiant heat, and it is essentially one due to the changes of volume in vapors or gases produced by the degradation and absorption of heat in a confined space..." He further concluded that "...any absorbent surfaces placed inside a closed transparent vessel will, by first absorbing and then radiating heat rays to the confined gas, emit sonorous vibrations."

### Revival of Optoacoustics

The revival of interest in optoacoustics began with gas-phase work. Viengerov<sup>11</sup> in 1938 first applied an electrostatic microphone to gas detection using a periodically modulated thermal radiation source and an acoustically resonant sample cell. Later, Viengerov<sup>12</sup> recorded the first optoacoustic absorption spectrum using radiation from a carbon light and a prism monochromator. Luft<sup>13</sup> improved on the design of Viengerov by incorporating differential detection. He achieved CO<sub>2</sub> detection limits of parts per million. This early work was the basis for development of commercial non-dispersive infrared spectrophone analyzers. This application has been reviewed by Hill and Powell.<sup>14</sup> Gorelik<sup>15</sup> suggested in 1946 that an optoacoustic phase measurement would give information on the rate of energy transfer between vibrational and translational degrees of freedom in gases. Slobodskaya<sup>16</sup> first demonstrated this method. The use of the optoacoustic effect to study vibrational relaxation has been treated by Read<sup>17</sup> and Bauer.<sup>18</sup> Recently, applications of the optoacoustic effect in gases have mushroomed. DeGroot et al.<sup>19</sup> applied this technique to the study of aldehyde photochemical reactions in the gas phase. Harshbarger and Robin<sup>[20,21]</sup> briefly studied photochemical processes in NO<sub>2</sub> and iodine vapor. Robin and coworkers have studied radiationless decay in biacetyl,<sup>22</sup> aromatic ketones,<sup>23</sup> and azabenzenes.<sup>24</sup> Kreuzer, Patel, and coworkers applied laser technology to optoacoustic spectroscopy for analysis of parts per billion concentration of gas.<sup>[25,26,27,28,29]</sup>



These studies are only the ground breakers in the expanding field of gas phase optoacoustic (photoacoustic) spectroscopy.

### Photoacoustic Spectroscopy

Appropriately, Bell Laboratories at Murray Hill, New Jersey was the site of the revival of interest in the optoacoustic effect in condensed phase. Three workers there: Rosencwaig,<sup>[30,31,32]</sup> Harshbarger, and Robin<sup>20</sup> demonstrated that qualitative absorption spectra of various solids can be obtained using the optoacoustic effect. Rosencwaig has been the most active advocate of optoacoustic spectroscopy in solids.<sup>[1,8,33,34,35,36,37]</sup> Rosencwaig has also been a vocal proponent for changing the name of the technique from optoacoustic spectroscopy to photoacoustic spectroscopy primarily to avoid confusion with the acousto-optic phenomenon. After promoting and popularizing the name "photoacoustic", Rosencwaig proposed at the August 1979 Topical Meeting on Photoacoustic Spectroscopy in Ames, Iowa that the name change be accepted by the scientific community. C. K. N. Patel argued against the new name on the basis of the historical precedent. A majority of the conferees agreed with Rosencwaig's proposal. At this time the new name is in widespread use.

Condensed-phase photoacoustic spectroscopy applications have also rapidly increased. Various quantitative applications for liquids<sup>[38,39,40]</sup> and solids<sup>[41,42,43]</sup> have been made. Radiationless relaxation processes of ions in solid state, especially laser materials, have been studied.<sup>[44,45,46,47,48]</sup> Several investigators have employed the technique as a calorimetric tool to determine fluorescence yields

in liquids and solids.<sup>[49,50,51,52,53,54]</sup> Others have attempted to measure thermal diffusivity and thickness in layered systems.<sup>[55,56]</sup> New spectroscopy variations based on photoacoustic spectroscopy have been developed, for example Fourier-transform photoacoustic spectroscopy,<sup>[57,58]</sup> photoacoustic Raman spectroscopy,<sup>59</sup> and photoacoustic microscopy.<sup>[60,61,62,63,64]</sup> Photoacoustic spectroscopy has also been used as a detector coupled to other analytical instruments, for example electrochromic detection<sup>65</sup> and liquid chromatography detection.<sup>66</sup> This list of applications is by no means exhaustive.

#### Research Direction

The ultimate goal of this research was to apply photoacoustic spectroscopy to the study of surface species on chemically modified surfaces. Initial studies of chemically modified silica illustrated the usefulness of photoacoustic spectroscopy for obtaining qualitative electronic and vibrational spectra of surface-immobilized species.<sup>[2,3,67,68,69,70,71]</sup> However, it was obvious that the usefulness of the technique would be greatly enhanced if it were made a quantitative absorption spectroscopy tool for particulate solids. Toward that end, the study began with a review of the now-classic theory of photoacoustic spectroscopy developed by Rosencwaig and Gersho.<sup>72</sup> First, it was determined that the useful dynamic range of photoacoustic spectroscopy could be increased by approximately an order of magnitude by using combined photoacoustic magnitude and phase information. Second, the theory was extended to account for the effect of intense

light-scattering in particulate solids. The predictions of the extended theory were experimentally tested. Armed with this information, several problems involving chemically modified surfaces were attacked using photoacoustic spectroscopy (PAS) as a primary tool.

### References

1. A. Rosencwaig in Y. H. Pao (ed.), "Optoacoustic Spectroscopy and Detection," Academic Press, New York, 1977.
2. D. E. Leyden, M. L. Steele, B. B. Jablonski and R. B. Somoano, Anal. Chim. Acta **100**, 545 (1978).
3. B. B. Jablonski, Doctoral Dissertation, University of Denver, Denver, Colorado, 1979.
4. A. G. Bell, Am. J. Sci. **20**, 305 (1880).
5. A. G. Bell, Philos. Mag. **11**, (5) 510 (1881).
6. J. Tyndall, Proc. Roy. Soc. (London) **31**, 307 (1881).
7. W. C. Roentgen, Philos. Mag. **11**, (5) 308 (1881).
8. A. Rosencwaig, "Photoacoustics and Photoacoustic Spectroscopy," John Wiley and Sons, New York, 1980, p.11.
9. M. E. Mercadier, C. R. Hebd. Serv. Acad. Sci. **92**, 409 (1881).
10. W. H. Preece, Proc. Roy. Soc. (London) **31**, 506 (1881).
11. M. L. Viengerov, Dokl. Akad. Nauk. SSSR **19**, 687 (1938).
12. M. L. Viengerov, Izv. Akad. Nauk. SSSR Fiz. **4**, 94 (1940).
13. K. F. Luft, Z. Tech. Phys. **24**, 97 (1943).
14. D. W. Hill and T. Powell, "Non-dispersive Infrared Gas Analysis in Science, Medicine, and Industry," Hilger, London, 1968.
15. G. Gorelik, Dokl. Akad. Nauk. SSSR **54**, 779 (1946).
16. P. V. Slobodskya, Izv. Akad. Nauk. SSSR Fiz. **12**, 656 (1948).
17. A. W. Read, Adv. Mol. Relaxation Processes **1**, 257 (1967-1968).
18. H. J. Bauer, J. Chem. Phys. **57**, 3130 (1972).
19. M. S. DeGroot, C. A. Emeis, I. A. M. Hesselman, E. Drent and E. Farenhorst, Chem. Phys. Lett. **17**, 332 (1972).
20. W. R. Harshbarger and M. B. Robin, Acc. Chem. Res. **6**, 329 (1973).

21. W. R. Harshbarger and M. B. Robin, Chem. Phys. Lett. 21, 462 (1973).
22. K. Kaya, W. R. Harshbarger and M. B. Robin, J. Phys. Chem. 60, 4231 (1974).
23. M. B. Robin and N. A. Kuebler, J. Am. Chem. Soc. 97, 4822 (1975).
24. K. Kaya, C. L. Chatelain, M. B. Robin and N. A. Kuebler, J. Am. Chem. Soc. 97, 2153 (1975).
25. L. B. Kreuzer, J. Appl. Phys. 42, 2934 (1971).
26. L. B. Kreuzer and C. K. N. Patel, Science 173, 45 (1971).
27. L. B. Kreuzer, N. D. Kenyon and C. K. N. Patel, Science 177, 347 (1972).
28. L. B. Kreuzer, Anal. Chem. 46, 239A (1974).
29. C. K. N. Patel, Science 202, 157 (1978).
30. A. Rosencwaig, Science 181, 657 (1973).
31. A. Rosencwaig, Bull. Amer. Phys. Soc. 18, 357 (1973).
32. A. Rosencwaig, Opt. Commun. 7, 305 (1973).
33. A. Rosencwaig, Physics Today 28, (9) 23 (1975).
34. A. Rosencwaig, Anal. Chem. 47, 592A (1975).
35. A. Rosencwaig and S. S. Hall, Anal. Chem. 47, 548 (1975).
36. A. Rosencwaig, A. P. Ginnsberg and J. W. Kopeke, Inorganic Chem. 15, 2540 (1976).
37. A. Rosencwaig, Rev. Sci. Instrum. 48, 1133 (1977).
38. S. Oda, T. Sawada and H. Kamada, Anal. Chem. 50, 865 (1978).
39. S. Oda, T. Sawada, M. Nomura and H. Kamada, Anal. Chem. 51, 686 (1979).
40. C. K. N. Patel and A. C. Tam, Appl. Phys. Lett. 34, 467 (1979).
41. H. E. Eaton, D. R. Anton and J. D. Stuart, Spect. Lett. 10, 847 (1977).

42. S. L. Castleden, C. M. Elliott, G. F. Kirkbright and D. E. M. Spillane, Anal. Chem. **51**, 2152 (1979).
43. D. Hursh and T. Kuwana, Anal. Chem. **52**, 646 (1980).
44. J. C. Murphy and L. C. Aamodt, J. Appl. Phys. **48**, 3502 (1977).
45. L. D. Merkle and R. C. Powell, Chem. Phys. Lett. **46**, 303 (1977).
46. R. S. Quimby and W. M. Yen, Opt. Lett. **3**, 181 (1978).
47. J. M. Flaherty and R. C. Powell, Phys. Rev. B **19**, 32 (1979).
48. R. C. Powell, D. P. Neikirk and D. Sardar, J. Opt. Soc. Am. **70**, 486 (1980).
49. W. Lahmann and H. J. Ludewig, Chem. Phys. Lett. **45**, 177 (1977).
50. I. O. Starobogatov, Opt. Spectrosc. **42**, 172 (1977).
51. T. K. Razumova and I. O. Starobogatov, Opt. Spectrosc. **42**, 274 (1977).
52. M. J. Adams, J. G. Highfield and G. F. Kirkbright, Anal. Chem. **49**, 1850 (1977).
53. M. G. Rockley and K. M. Waugh, Chem. Phys. Lett. **54**, 597 (1978).
54. D. Cahen, H. Garty and R. S. Becker, J. Phys. Chem. **84**, 3384 (1980).
55. M. J. Adams and G. F. Kirkbright, Analyst **102**, 678 (1977).
56. D. Betteridge and P. J. Meyler, Fresenius Z. Anal. Chem. **300**, 337 (1980).
57. M. M. Farrow, R. K. Burnham and E. M. Eyring, Appl. Phys. Lett. **33**, 735 (1978).
58. M. G. Rockley, Appl. Spect. **34**, 405 (1980).
59. J. J. Barrett and M. J. Berry, Appl. Phys. Lett. **34**, 144 (1979).
60. M. J. Brienza and A. J. DeMaria, Appl. Phys. Lett. **11**, 44 (1967).
61. R. J. von Gutfeld and R. L. Melcher, Appl. Phys. Lett. **30**, 257 (1977).

62. Y. H. Wong, R. L. Thomas and G. F. Hawkins, Appl. Phys. Lett. 32, 538 (1978).
63. H. K. Wickramasinghe, R. C. Bray, V. Jipson, C. F. Quate and J. R. Salcedo, Appl Phys. Lett. 33, 923 (1978).
64. A. Rosencwaig, Am. Lab. 11, (4) 39 (1979).
65. R. E. Malpas and A. J. Bard, Anal. Chem. 52, 109 (1980).
66. S. Oda and T. Sawada, Anal. Chem. 53, 471 (1981).
67. A. B. Fischer, J. B. Kinney, R. H. Staley and M. S. Wrighton, J. Am. Chem. Soc. 101, 6501 (1979).
68. C. H. Lochmuller and D. R. Wilder, Anal. Chim. Acta 116, 19 (1980).
69. C. H. Lochmuller and D. R. Wilder, Anal. Chim. Acta 118, 101 (1980).
70. C. H. Lochmuller, S. F. Marshall and D. R. Wilder, Anal. Chem. 52, 19 (1980).
71. M. J. D. Low and G. A. Parodi, Appl. Spect. 34, 76 (1980).
72. A. Rosencwaig and A. Gersho, J. Appl. Phys. 47, 64 (1976).

## Chapter 2

### INSTRUMENTATION AND DATA PROCESSING

#### PAS Instrumentation

The physical basis of photoacoustic spectroscopy, the optoacoustic effect, has been known for more than 100 years. Alexander Graham Bell predicted that the optoacoustic effect had potential application for absorption spectroscopy measurements of condensed-phase materials complementing conventional absorption spectroscopy.<sup>1</sup> However, fulfillment of that prediction awaited development of sophisticated signal processing instrumentation.

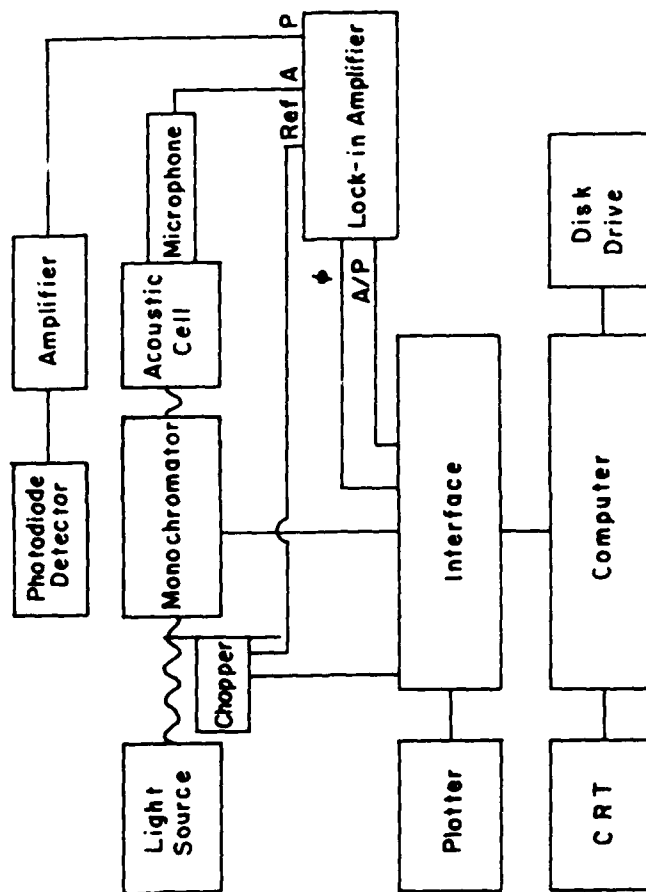
The photoacoustic spectrometer used in these studies is a modification of that constructed by B. B. Jablonski.<sup>2</sup> Modifications were made to enhance the signal-to-noise ratio and to incorporate a phase measurement capability. The photoacoustic spectrometer is shown schematically in Figure 1. Each of the major elements of the spectrometer will be discussed.

The light source used is a 1000-watt xenon arc lamp (Oriel model 6269) for ultraviolet spectroscopy or a 300-watt high-pressure xenon arc lamp (Varian/Eimac model PS-300) for visible spectroscopy. The advantage of the high-pressure xenon arc lamp for visible measurements is the pressure broadening of the xenon lines at 468 nm and 764 nm which can produce spectral artifacts for low resolution spectral band width.

For wavelength selection, a 0.25 meter f/3.5 computer-controlled Ebert monochromator (Jarrell-Ash model 82-410) is used in combination



Figure 1. Schematic diagram of photoacoustic spectrometer.



with appropriate absorption filters to eliminate order effects. The monochromator is equipped with two replica gratings, one blazed at 300 nm (2360 grooves/mm) for ultraviolet measurements and one blazed at 500 nm (1180 grooves/mm) for visible measurements. The monochromator is used with 2 mm slits for general applications and 1 mm slits for higher resolution applications. The spectral band width is 6.6 nm and 3.3 nm for the visible grating and the ultraviolet grating, respectively, using the 2 mm slits. The calibration of the monochromator was checked by recording a photoacoustic spectrum of  $\text{Ho}_2\text{O}_3$  which exhibits narrow f-f electronic transitions. The visible photoacoustic spectrum of  $\text{Ho}_2\text{O}_3$  is shown in Figure 2.

The light beam is modulated by a variable-speed chopper (Princeton Applied Research model 192). The typical modulation frequency used was 45 Hz. Calibration of the modulation frequency was checked using an electronic counter (Hewlett Packard model 521DR). The modulation frequency was monitored by the computer before and after each spectrum was recorded. The light beam is focused and directed using ultraviolet quality lenses and first-surface mirrors. The light sources, chopper, and monochromator are positioned on a different platform from that on which the acoustic cell is mounted. This precaution minimizes the transfer of acoustic noise from the chopper to the acoustic cell.

The acoustic cell, shown schematically in Figure 3, is machined out of a block of aluminum. The total void volume of the acoustic chamber is less than 1 mL. The microphone chamber is connected to the acoustic chamber by a "listening tube". The design of the sample tray takes

Figure 2. Photoacoustic magnitude spectrum for  $\text{Ho}_2\text{O}_3$ .

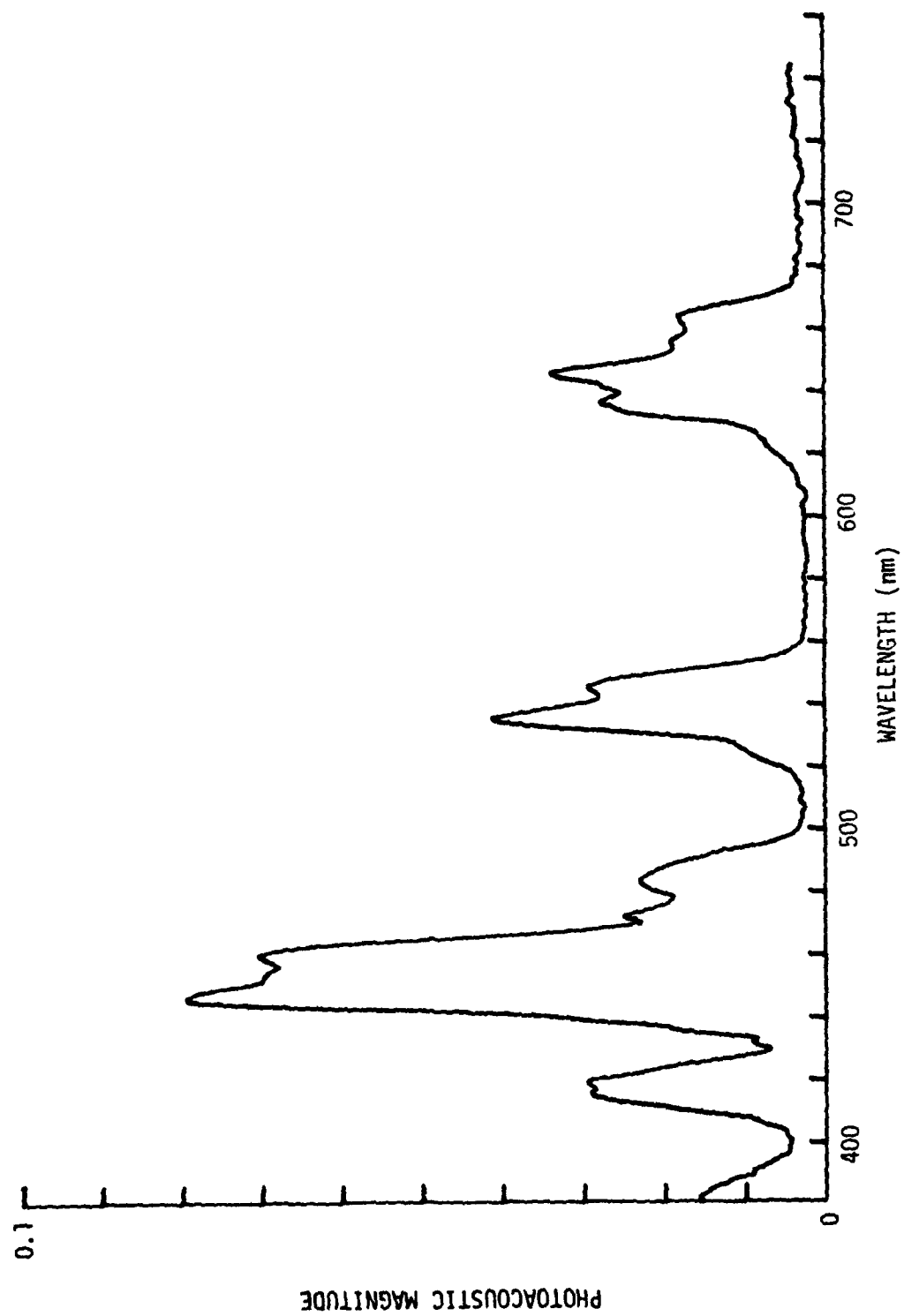
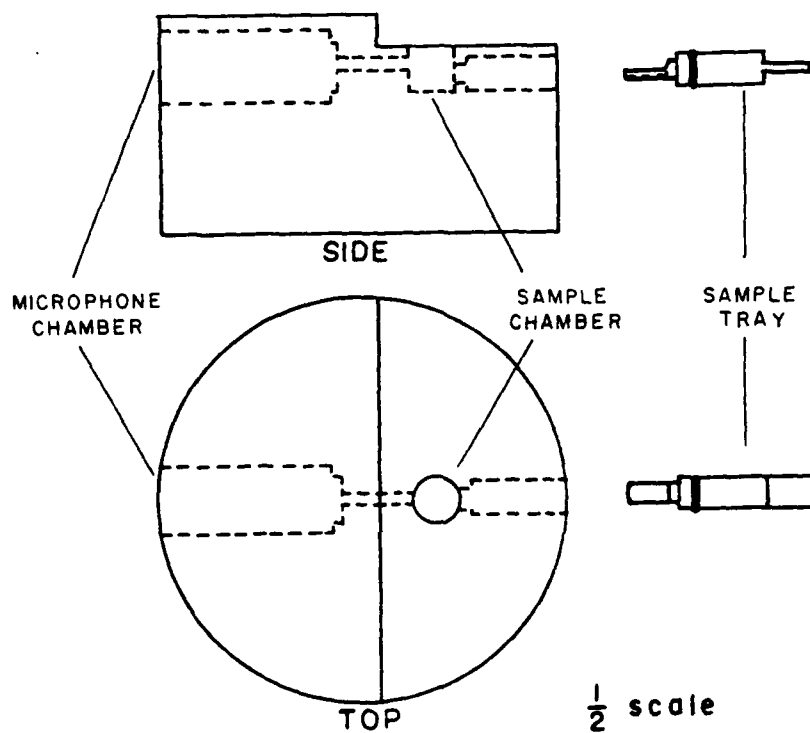


Figure 3. Acoustic cell diagram.



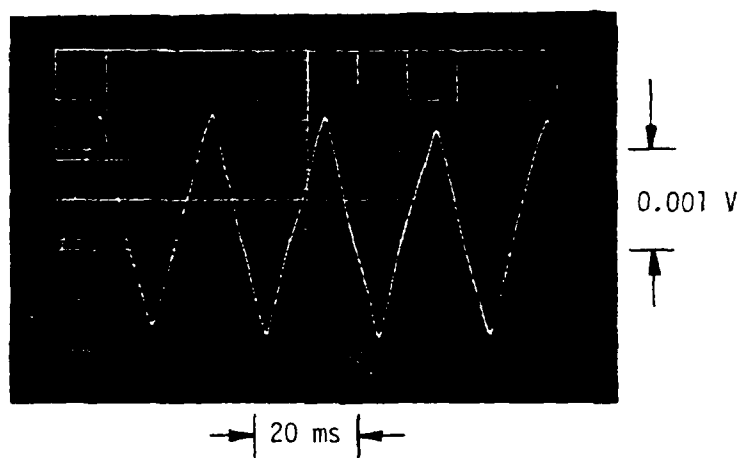
advantage of the entire available length of the focused slit image. The sample volume required is approximately 0.025 mL. Microphone and sample tray are sealed in the cell using o-rings. Light enters the cell through a sapphire window which is directly above the sample. This window is sealed to the cell body using silicone grease. The entire acoustic cell assembly is placed in a foam-rubber box which is mounted on an optical bench.

Detection is achieved using a 1/2-inch diameter condenser microphone (Bruel and Kjaer model 4165). The microphone preamplifier output is a sawtooth signal with frequency equal to the modulation frequency of the light beam. Typical output of the microphone preamplifier for modulation frequency of 45 Hz is shown in Figure 4. This signal is input to a dual-phase lock-in amplifier (Princeton Applied Research model 5204). This device measures the acoustic amplitude at a particular phase angle and at a quadrature phase angle relative to a reference frequency. The reference signal is provided by the mechanical chopper so that the acoustic signal with frequency equal to the modulation frequency is preferentially detected. The lock-in amplifier used in these studies is equipped with a vector/noise option which first calculates the acoustic magnitude and phase relative to the modulation frequency and then outputs d. c. signals proportional to the acoustic magnitude and phase. The acoustic magnitude signal is normalized to the lamp intensity as monitored by a photodiode detector (Oriel model 7072) to correct for long term variation in lamp intensity.

Spectrum acquisition is totally automated. Data acquisition and monochromator control are performed through an instrument interface



Figure 4. Oscilloscope trace of microphone preamplifier output.



(On line Instrument Systems model 3620) to a 32k computer (Data General Corporation Nova 1220) equipped with a dual drive floppy disk system. The outputs of the lock-in amplifier are read by a 12 bit successive approximation analog-to-digital converter. The monochromator is driven by a computer-generated pulse train applied to a stepping motor which is mechanically coupled to the monochromator drive. The computer interface permits CRT display and plotter hardcopy of spectra. BASIC language programs were written for the Nova 1220 computer which call the assembly level subroutines and perform data manipulations.

#### PAS Data Processing

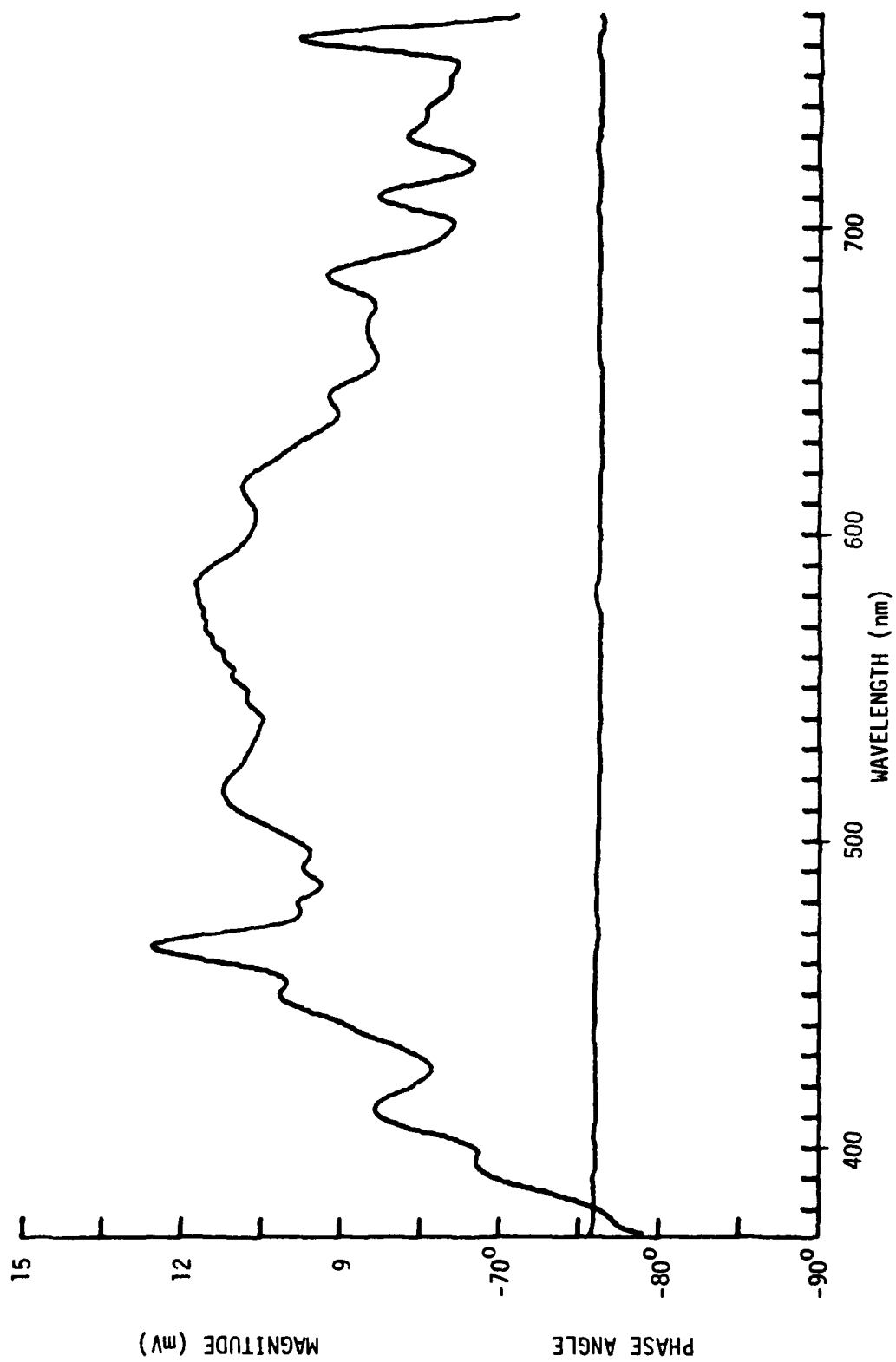
Three basic data processing steps are performed for spectrum acquisition: data collection, normalization, and spectral smoothing. Each of these will be discussed in turn.

The data collection program acquires a magnitude spectrum and/or a phase spectrum. The first function of this program is to call an analog-to-digital conversion subroutine. This subroutine activates the analog-to-digital converter at a specified data acquisition rate for a predetermined number of data points. Typically 100 to 500 points are collected at a rate of one point every 20 ms to 50 ms. These data points are stored in an array. The BASIC program calculates the average for this data array which is stored as a spectrum point. Signal averaging is performed in this manner. Before the next spectral point is acquired, the monochromator is stepped to the next measurement wavelength. The program calls a pulse-output subroutine which causes a pulse train of specified frequency and duration to be applied to the

monochromator stepping motor. The data acquisition and monochromator stepping processes are repeated alternately until the entire spectrum has been acquired. The spectrum and spectrum parameters are stored under a spectrum identifier on a floppy disk. The spectrum is displayed on the CRT display. Before and after each spectral acquisition the program calls a counter subroutine which monitors the modulation frequency of the light beam.

The dependence of the magnitude spectrum on the light intensity is removed by normalizing the raw magnitude spectrum to the spectrum of an opaque reference material. For most of this work carbon powder was used as the reference material (activated charcoal powder, Merck and Company, Rahway, New Jersey). A visible spectrum of the carbon powder is shown in Figure 5. This spectrum reflects the source intensity variation with wavelength. Generally, reference spectra were acquired at the beginning and end of each series of spectra. The normalization program performs a point-by-point division of the sample magnitude spectrum by the reference magnitude spectrum. The normalization program also permits subtraction of stray light contribution, if necessary. The resulting normalized magnitude spectrum and spectrum parameters are stored on a floppy disk under a spectrum identifier. The phase spectrum is nearly independent of source intensity. Figure 5 also shows a visible phase spectrum for carbon powder. Sample phase spectra were referenced to the carbon powder phase spectrum by performing a point-by-point subtraction of the reference phase spectrum from the sample phase spectra.

Figure 5. Visible magnitude spectrum and phase spectrum for carbon powder reference material.



The smoothing program is based on the smoothing procedure described by Savitzky and Golay.<sup>3</sup> This method is a convolution scheme which is equivalent to a least-squares fit. A window is centered on a given point in a set of evenly-spaced spectral points. All the error is assumed to be in the ordinate. A set of convolution integers,  $C_i$ , are used to calculate a weighting function for the point at the center of the window:

$$Y'_j = \frac{\sum_{i=-m}^{i=m} C_i Y_{j+i}}{2m + 1} \quad (1)$$

where  $Y_j$  are the original ordinate values,  $Y'_j$  are the smoothed ordinate values and  $(2m + 1)$  is the number of points within the window width. This convolution method, using the Savitzky-Golay coefficient arrays, is equivalent to a least-squares fit of the spectral data to a polynomial. In the case of this smoothing program the polynomial is of order 3. In a study of Lorentzian- and Gaussian-shaped lines, Enke and Nieman<sup>4</sup> found that the best signal-to-noise enhancement from a single-pass quadratic-cubic smoothing is obtained for a smoothing window that is twice as wide as the full width at half maximum of the peak being smoothed. Hence, the choice of the width of the smoothing window depends on the spectral feature of importance. In general, the width of the smoothing window used was one to three times the spectral band width.

After these three basic procedures were performed on the spectra, various other spectral manipulations were carried out depending on the

application. These included spectral subtraction, vector background correction, and saturation/scattering correction.

#### Other Instrumentation

The other instruments used in conjunction with this work were the Cary 219 (Varian) double-beam spectrophotometer, the Perkin-Elmer 2380 atomic absorption spectrophotometer, and the United Scientific Spectrace 440 energy dispersive x-ray fluorescence spectrometer equipped with a Tracor Northern 880 spectrum analyzer.



References

1. A. G. Bell, Philos. Mag. 11, (5) 510 (1881).
2. B. B. Jablonski, Doctoral Dissertation, University of Denver, 1979.
3. A. Savitzky and M. J. E. Golay, Anal. Chem. 36, 1627 (1964).
4. C. G. Enke and T. A. Nieman, Anal. Chem. 48, 705A (1976).

## Chapter 3

### PHOTOACOUSTIC SPECTROSCOPY THEORY

#### Introduction

Photoacoustic spectroscopy (PAS) is rapidly achieving importance as a technique for obtaining ultraviolet, visible, and infrared absorption spectra of particulate solids. The theory of Rosencwaig and Gersho<sup>1</sup> successfully accounts for the dependence of photoacoustic response on the optical and thermal properties of nonscattering samples. However, the implications of this theory for quantitative PAS have not been fully exploited partly because of the awkward functional form of their complex PAS response function. Two other factors, saturation and scattering, complicate quantitative application of PAS to particulate solids. Although quantitative PAS of condensed-phase materials has been reported,<sup>[2,3,4]</sup> the use of PAS as a quantitative tool has been limited to materials with low absorptivity because of the nonlinear dependence of photoacoustic amplitude upon concentration of chromophore in more highly absorptive materials. It has also been recognized that light scattering in particulate solids can have a pronounced effect on the photoacoustic response because both absorption and scattering influence the photon distribution in the sample.<sup>[5,6]</sup> Freeman, et al.<sup>7</sup> applied the Kubelka-Munk analysis of diffused reflectance to correct their photoacoustic spectra for light-scattering effects using diffuse reflectance spectroscopy. They did

not, however, consider the implications of the Kubelka-Munk analysis for the PAS theory.

The first objective is to cast the result of Rosencwaig and Gersho<sup>1</sup> for thermally thick solids into a form more suitable for quantification. Only the thermally thick case will be considered because of its more general analytical applicability. The photoacoustic magnitude and phase are combined in a response function which is linear with sample absorption. An extension of the Rosencwaig-Gersho theory which accounts for scattered-light effects is developed based on the Kubelka analysis of the optics of intensely light-scattering materials.<sup>8</sup> Experimental substantiation of this result is presented for a chemically modified substrate.

A second problem which is addressed is the effect of stray light on ultraviolet photoacoustic spectra. The problem of stray light is common to all optical spectroscopies which use broad band sources. The contribution of stray light is especially severe for the ultraviolet region below 250 nm because of the reduced intensity of sources and the reduced efficiency of optical elements. In conventional absorption spectroscopy a common solution is to use multiple monochromators. With each monochromator stage the stray light is reduced by a multiplicative factor. Unfortunately, this technique reduces the monochromator throughput thereby decreasing the signal to noise ratio. For photoacoustic spectroscopy a simple method is presented to account for the effect of stray light without reducing the monochromator throughput.

### Rosencwaig-Gersho Theory

The Rosencwaig-Gersho (RG) theory<sup>1</sup> is based on the generally accepted mechanism for the photoacoustic effect in condensed phase. A modulated monochromatic beam of light is incident on the sample surface. The light is absorbed by the sample to a degree dependent upon the optical absorption coefficient of the sample. As a result the sample is periodically heated and cooled at the modulation frequency. The periodic temperature change is transmitted to a boundary layer of gas at the sample surface. The boundary layer of gas expands and contracts with the temperature variation, acting as a small acoustic piston analogous to a vibrating plate. The acoustic signal which is produced in the confined gas is detected by a microphone.

An outline of the RG derivation is given making reference to Figure 1. A monochromatic beam of light with intensity  $I_0$  is modulated at frequency  $\omega/2\pi$ . The incident modulated beam has intensity  $I$ :

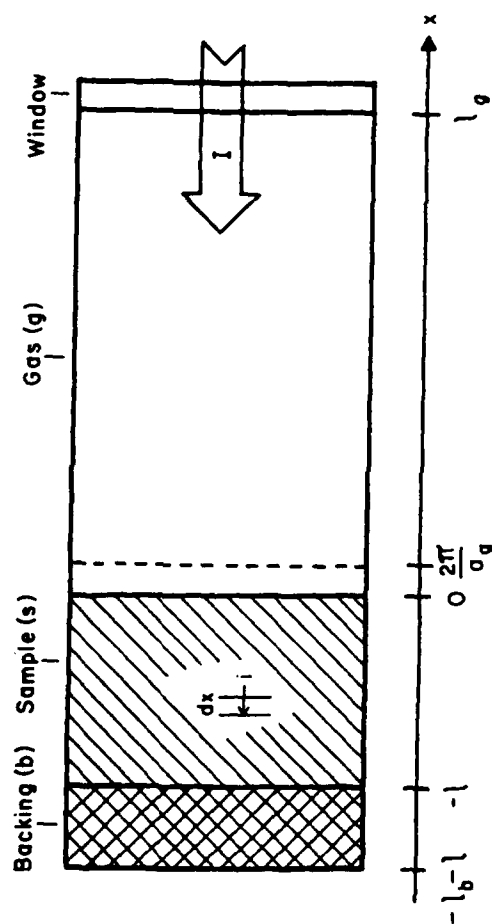
$$I = 1/2 I_0 (1 + \cos \omega t) \quad (1)$$

As the light beam is transmitted into the sample, energy is deposited in the sample in a Lambert's law manner:

$$di = i\beta dx \quad (2)$$

where  $i$  is the transmitted intensity and  $\beta$  is the absorption coefficient. Assuming that the absorbed energy is degraded to heat in time,  $t$ , shorter than  $2\pi/\omega$  and assuming that the absorbed energy is completely degraded to heat, the heat density at depth  $x$  in the sample is:

Figure 1. Idealized photoacoustic cell.



$$I\beta e^{\beta x} = 1/2 I_0 \beta e^{\beta x} (1 + \cos \omega t) \quad (3)$$

Thus, for a nonscattering sample the heat density which drives the periodic heating of the sample depends on the optical absorption coefficient and the modulation frequency.

The temperature fluctuation produced at the sample surface ( $x=0$ ) depends not only on the heat density but also on the thermal diffusivity of the sample,  $\alpha_s$ . The temperature change produced in the acoustic cell is described by the thermal diffusion equations shown below.

$$\frac{\partial^2 \phi}{\partial x^2} = \frac{1}{\alpha_s} \frac{\partial \phi}{\partial t} - \frac{\beta I_0}{2k_s} e^{\beta x} (1 + e^{i\omega t}), \quad -l \leq x \leq 0 \quad (4)$$

$$\frac{\partial^2 \phi}{\partial x^2} = \frac{1}{\alpha_b} \frac{\partial \phi}{\partial t}, \quad -l-l_b \leq x \leq -l \quad (5)$$

$$\frac{\partial^2 \phi}{\partial x^2} = \frac{1}{\alpha_g} \frac{\partial \phi}{\partial t}, \quad 0 \leq x \leq l_g \quad (6)$$

The terms used to describe thermal properties are defined as follows:

$\phi$ , temperature

$\alpha_j$ , thermal diffusivity of material  $j$

$a_j$ , thermal diffusion coefficient of material  $j$

$k_j$ , thermal conductivity of material  $j$

$\rho_j$ , density of material  $j$

$c_j$ , specific heat of material  $j$

where

$$\alpha_j = \frac{k_j}{\rho_j c_j} \quad (7)$$

and

$$a_j = \left[ \frac{\omega}{2\alpha_j} \right]^{1/2} \quad (8)$$

The subscript,  $j$ , denotes backing (b), gas (g), sample (s), or reference sample (r).

Rosencwaig and Gersho derive a solution to these equations for the time-dependent temperature at the sample surface using appropriate boundary conditions and reasonable simplifying assumptions. The time-dependent temperature at the gas-solid boundary is integrated over the thickness of the gas boundary layer,  $2\pi\mu_g$ , giving the spatially averaged temperature of the boundary layer.

$$\bar{\phi}(t) = \int_0^{2\pi\mu_g} \phi(x,t) dx \approx \frac{1}{2\sqrt{2}\pi} \phi_0 e^{i(\omega t - \eta)} \quad (9)$$

Assuming that the gas boundary layer acts as an adiabatic acoustic piston, Rosencwaig and Gersho solve for the pressure change as a function of time. The general RG solution for the acoustic response function,  $\Delta P(t)$ , is:

$$\Delta P(t) = Q e^{i(\omega t - \eta)} \quad (10)$$

where



$$Q = \frac{\beta I_0 \gamma P_0}{2\sqrt{2} k_s \ell_g a_g T_0 (\beta^2 - \sigma_s^2)} \left[ \frac{(r+1)(b+1)e^{\sigma_s \ell} - (r+1)(b-1)e^{-\sigma_s \ell} + 2(b-r)e^{\beta \ell}}{(g+1)(b+1)e^{\sigma_s \ell} - (g-1)(b-1)e^{-\sigma_s \ell}} \right] \quad (11)$$

The terms used are defined as follows:

$P_0$ , ambient pressure

$T_0$ , ambient temperature

$\gamma$ , ratio of specific heats for gas

$\eta$ , phase delay for production of acoustic signal ( $\sqrt{\frac{\pi}{4}}$ )

where

$$b = \frac{k_b a_b}{k_s a_s} \quad (12)$$

$$g = \frac{k_g a_g}{k_s a_s} \quad (13)$$

$$r = \frac{(1-i)\beta}{2a_s} \quad (14)$$

$$\sigma_s = (1+i)a_s \quad (15)$$

Because this complex function is not easily interpreted, Rosencwaig and Gersho develop six special cases depending on the limiting relative magnitudes of sample thickness ( $\ell$ ), thermal diffusion length ( $\mu_s = a_s^{-1}$ ), and optical absorption length ( $\mu_\beta = \beta^{-1}$ ). Three of these special cases deal with thermally thick samples. Either the thermally thick assumption ( $\mu_s \ll \ell$ ) or the thermally thin assumption ( $\mu_s \gg \ell$ ) permit simplification of the general RG result. The thermally thin limiting condition has much less general analytical applicability because it is

difficult to achieve experimentally for many materials. Only the thermally thick limiting case will be considered. The three RG special cases for thermally thick samples are summarized in Figure 2. For optically transparent samples the signal amplitude is predominantly due to light absorbed within the first thermal diffusion length and that the magnitude of the complex response function,  $Q$ , is proportional to the optical absorption coefficient times this length. Rosencwaig and Gersho suggest that this relationship is also approximately true for optically opaque samples as long as  $\mu_B > \mu_S$ , but that when  $\mu_B < \mu_S$  the signal originates predominately from the first optical absorption length and  $Q$  becomes independent of the optical absorption coefficient. At this point the signal is saturated.

The Rosencwaig-Gersho special cases are useful for understanding the dependence of the photoacoustic response on the optical absorption coefficient; however, for quantitative applications they are as much an oversimplification as the general solution is overcomplex. An alternative presentation of their result is useful in quantitative applications.

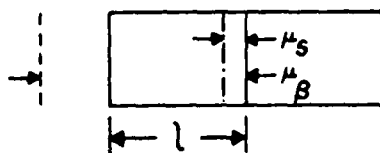
#### Correction For Saturation Effects

From the general result of the RG theory a PAS response function which is linear with absorption coefficient is now developed. The photoacoustic response function may be viewed as a vector rotating in the complex plane with angular frequency,  $\omega$ , corresponding to the modulation frequency of the light beam. A lock-in amplifier is

Figure 2. Rosencwaig-Gersho special cases for thermally thick samples ( $\mu_s \ll l$ ).

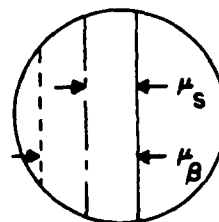
RG SPECIAL CASES

Optically  
Transparent  
( $\mu_s \ll l < \mu_\beta$ )



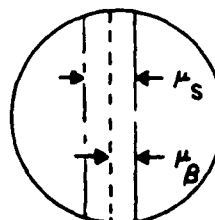
$$Q\alpha - i\beta\mu_s$$

Optically  
Opaque  
( $\mu_s < \mu_\beta < l$ )



$$Q\tilde{\alpha} - i\beta\mu_s$$

Photoacoustically  
Opaque  
( $\mu_\beta < \mu_s \ll l$ )



$$Q\tilde{\alpha}(1+i)$$

capable of measuring the projection of this vector, an acoustic amplitude, at a prescribed phase angle relative to  $\omega$ . Measurement of the acoustic amplitude at two different phase angles serves to completely characterize the photoacoustic response. The measured response,  $\Delta P_m$ , is:

$$\Delta P_m = Qe^{-i(\eta+\theta)} = qe^{-i\chi} \quad (16)$$

where

$$Q = qe^{-i\psi} \quad (17)$$

Here,  $q$  is the magnitude of the response function and  $\psi$  is the phase of  $Q$ . The measured response is represented as a vector in the complex plane with magnitude  $q$  and phase angle  $\chi$ . The phase angle is made up of the phase lag due to the thermal propagation in the sample ( $\psi$ ), the phase lag due to production of the acoustic signal ( $\eta$ ), and the instrumental phase lag ( $\theta$ ). Hence, the photoacoustic response is completely determined by  $q$  and  $\psi$  once the constant sum,  $\eta+\theta$ , is known.

The RG general result is now simplified to give equations for the magnitude and phase of the acoustic response for the thermally thick case. The thermally thick assumption ( $\mu_s \ll l$ ) permits the approximation  $e^{-\sigma_s l} \sim 0$ , which simplifies the RG response function:

$$Q = C_s \beta \mu_s \frac{(\beta \mu_s - 2) - i \beta \mu_s}{\beta^2 \mu_s^2 - 2i} \quad (18)$$

where:

$$C_s = \frac{I_o \gamma P_o}{4\sqrt{2} \ell_g a_g T_o (k_g a_g + k_s a_s)} \quad (19)$$

Casting this function into the form of Equation 17 gives:

$$q = C_s \beta \mu_s \left[ \frac{2}{(\beta \mu_s + 1)^2 + 1} \right]^{1/2} \quad (20)$$

and

$$\psi = \arctan \left( 1 + \frac{2}{\beta \mu_s} \right) \quad (21)$$

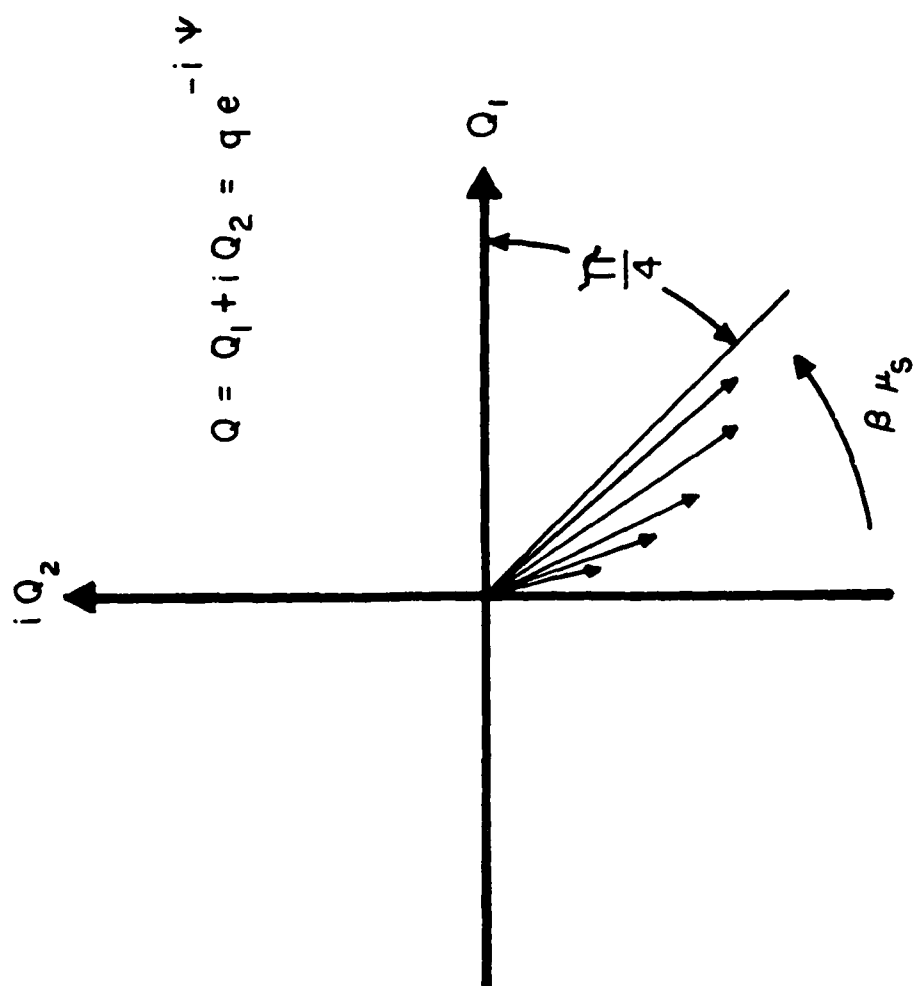
Equation 21 was first used by Teng and Royce.<sup>8</sup>

Both the magnitude and phase of the photoacoustic response vary with  $\beta \mu_s = \frac{\beta}{a_s}$ , the magnitude of the optical absorption coefficient relative to the thermal diffusion coefficient. This ratio can be thought of as a photoacoustic opacity. The variation of the photoacoustic response with the photoacoustic opacity is illustrated in Figure 3. Note that the optically transparent and optically opaque RG special cases correspond approximately to the projection of the acoustic response vector onto the imaginary axis and the photoacoustically opaque case corresponds to the projection of the vector onto the line at  $-\frac{\pi}{4}$ . In the limit of photoacoustically transparent samples ( $\beta \mu_s \ll 1$ ) the magnitude of the photoacoustic response is:

$$q = C_s \beta \mu_s \left( \frac{1}{1 + \beta \mu_s} \right)^{1/2} \rightarrow C_s \beta \mu_s \quad (22)$$

and the phase is:

Figure 3. Representation of variation of photoacoustic response vector in phase space as  $\beta\mu_s$  increases.





$$\psi = \arctan \left( \frac{2}{\beta\mu_s} \right) + \frac{\pi}{2} \quad (23)$$

In the limit of photoacoustically opaque samples ( $\beta\mu_s \ll 1$ ) the magnitude of the photoacoustic response is:

$$q = C_s \sqrt{2} \left( 1 - \frac{2}{\beta\mu_s} \right)^{1/2} \rightarrow \sqrt{2} C_s \quad (24)$$

and the phase is:

$$\psi \approx \arctan(1) = \frac{\pi}{4} \quad (25)$$

In this extreme the photoacoustic response is saturated.

The photoacoustic magnitude for a sample may be normalized by dividing by the magnitude of a perfectly opaque reference material to cancel the dependence on the source intensity,  $I_0$ . The normalized magnitude is  $q_n$ :

$$q_n = C\beta\mu_s \left[ \frac{2}{(\beta\mu_s + 1)^2 + 1} \right]^{1/2} \quad (26)$$

where:

$$C = \frac{C_s}{C_r} = \frac{1}{\sqrt{2}} \left( \frac{k_g a_g + k_r a_r}{k_g a_g + k_s a_s} \right) \quad (27)$$

In order to use the phase information, the sum,  $\eta + \theta$ , must be determined. The most general method is to measure the phase lag for a perfectly opaque reference material. The phase lag for a perfect absorber is:

$$\chi_r = \frac{\pi}{4} + \eta + \theta \quad (28)$$

So,  $\psi$  for the sample is calculated from:

$$\psi = \chi_s - \chi_r + \frac{\pi}{4} \quad (29)$$

Once the phase lag associated with the measurement has been removed, then the product  $\beta\mu_s$  is calculated from:

$$\beta\mu_s = f(\psi) = \frac{2}{\tan \psi - 1} \quad (30)$$

These results from the theory of Rosencwaig and Gersho suggest that either the photoacoustic magnitude or the phase may be used to quantitatively characterize the sample absorption. Both approaches have been employed; however, each has practical drawbacks. The greatest problem with using only the photoacoustic magnitude is the small linear range. The photoacoustic magnitude becomes severely nonlinear at moderate values of  $\beta\mu_s$  as is apparent from Equation 24. Roark et al.<sup>10</sup> have observed that this is less of a problem in phase angle PAS. They found that the practical upper limit of absorptivity in phase angle PAS is an order of magnitude larger than that for magnitude PAS. On the other hand, the photoacoustic phase measurement suffers from large errors for small sample absorptivity due to contributions from acoustic background and from extraneous absorption in the cell. These problems can be minimized by combining magnitude and phase information. In this alternative approach the magnitude and phase for the sample are corrected for the effect of extraneous cell

absorption and acoustic background. The phase measurement is then used to linearize the magnitude thereby taking advantage of the greater sensitivity of the phase measurement at large sample absorptivity. By combining Equations 26 and 30 it is found that:

$$C\beta\mu_s = q_n \left[ \frac{(f+1)^2 + 1}{2} \right]^{1/2} = \frac{2q_n}{\sin(\psi - \frac{\pi}{4})} \quad (31)$$

In samples for which Beer's law obtains,  $C\beta\mu_s$  is proportional to the concentration of the chromophore. Note, however, that as the saturation limit is approached  $\psi \rightarrow \frac{\pi}{4}$  and small errors in  $\psi$  produced large errors in the denominator of Equation 31.

#### Intensely Light-Scattering Samples

In intensely light-scattering samples the photon density near the illuminated surface is greater than predicted by the Lambert's law distribution assumed in the Rosencwaig-Gersho theory. As a result, the acoustic magnitude is larger and the phase lag is smaller for a scattering sample than for a nonscattering sample having the same absorption coefficient and thermal properties. Using Kubelka's theory for the optics of intensely light-scattering materials,<sup>8</sup> an energy distribution which describes this effect is obtained. By combining this energy distribution with the Rosencwaig-Gersho formalism, the implications of light-scattering for quantitative PAS are examined.

In Kubelka's analysis, as in the RG theory, edge effects are neglected and incoherent scattering is ignored. For an intensely light-scattering sample it is assumed that the light is perfectly

diffused throughout the sample; i.e. it is assumed that the angular distribution of light in the sample is everywhere the same so the average path length of the transmitted beam traversing an elemental thickness is equal to the average path length of the reflected beam traversing the elemental thickness. The number of scattering orders required to achieve an isotropic distribution increases with the ratio of particle diameter to wavelength.<sup>11</sup> It is important to realize that this assumption is strictly valid for this analysis only if the particle diameter is much less than the thermal diffusion length.

Referring again to Figure 1, imagine a reflected beam,  $j$ , moving toward the illuminated surface as well as a transmitted beam,  $i$ , moving toward the backing. Both the transmitted and reflected beams are subject to scattering and absorption in each element of thickness. The differential changes in intensity of the transmitted and reflected beams are given in Equations 32 and 33 respectively.

$$di = (\tau + \beta)v dx - \tau v j dx \quad (32)$$

$$dj = -(\tau + \beta)v j dx + \tau v i dx \quad (33)$$

Here,  $\tau$  is the scattering coefficient and  $v$  is the average path length multiplier. Following Kubelka,<sup>7</sup> the scattering coefficient and absorption coefficient are defined in terms of the average path length:

$$S = v\tau \quad (34)$$

$$K = v\beta \quad (35)$$

To solve for  $i$  and  $j$ , the procedure of Kubelka and the RG convention for the origin of the  $x$ -axis are used:

$$i = I \left[ \sinh Sbx \left( \frac{a \operatorname{ctgh} Sb1 + b}{a + b \operatorname{ctgh} Sb1} \right) + \cosh Sbx \right] \quad (36)$$

$$j = RI \left[ \cosh Sbx + \sinh Sbx (\operatorname{ctgh} Sb1) \right] \quad (37)$$

where:

$$a = \frac{S + K}{S} \quad (38)$$

and

$$b = (a^2 - 1)^{1/2} \quad (39)$$

The reflectance, R, is given by:

$$R = \frac{1}{a + b \operatorname{ctgh} Sb1} \quad (40)$$

Now, it is assumed that the sample is not only thermally thick but optically thick as well; i.e. it is assumed that the combined scattering power,  $S\ell$ , and absorbing power,  $K\ell$ , of the sample is large. For intensely scattering samples this condition is easily achieved even for small values of K. Under this assumption  $\operatorname{ctgh}(Sb1) \rightarrow 1$  giving the following formulas for i and j:

$$i = I e^{Sbx} \quad (41)$$

$$j = I \frac{e^{Sbx}}{a + b} \quad (42)$$

Under the assumptions of the RG theory the heat distribution in a thick, intensely light-scattering sample is:

$$I b e^{Sbx} (1 + R) \quad (43)$$

The difference between this function and the Lambert's law distribution in Equation 3 is apparent. In this case the heat density near the surface is greater and it falls off more rapidly with depth.

Using this heat distribution the Rosencwaig-Gersho formalism<sup>1</sup> yields the following formulas for the normalized photoacoustic magnitude and phase of thick, light-scattering samples:

$$q_n = C\beta\mu_s(1+R) \left[ \frac{2}{(S\mu_s b + 1)^2 + 1} \right]^{1/2} \quad (44)$$

$$\psi = \arctan \left( 1 + \frac{2}{S\mu_s b} \right) \quad (45)$$

Figure 4 demonstrates the effect of scattering on the phase angle. The phase angle is closer to the saturation value for the scattering sample as compared to the nonscattering sample for the same value of  $K\mu_s$ . In Figure 5 the phase dependence is presented in the form of Equation 30 showing the expected effect of scattering on the phase function.

The magnitude and phase are combined as before:

$$C\beta\mu_s = \frac{q_n}{(1+R)} \left[ \frac{(f+1)^2 + 1}{2} \right]^{1/2} = \frac{\sqrt{2}q_n}{(1+R) \sin(\psi - \frac{\pi}{4})} \quad (46)$$

The reflectance can also be written in terms of the phase:

$$R = \frac{S\mu_s}{f + [f^2 + (S\mu_s)^2]^{1/2}} \quad (47)$$

Hence, in the case of the scattering sample, complete knowledge of the photoacoustic response requires that the product,  $S\mu_s$ , be determined.

Figure 4. Calculated dependence of phase angle on absorbance for increasing values of  $S\mu_s$ .

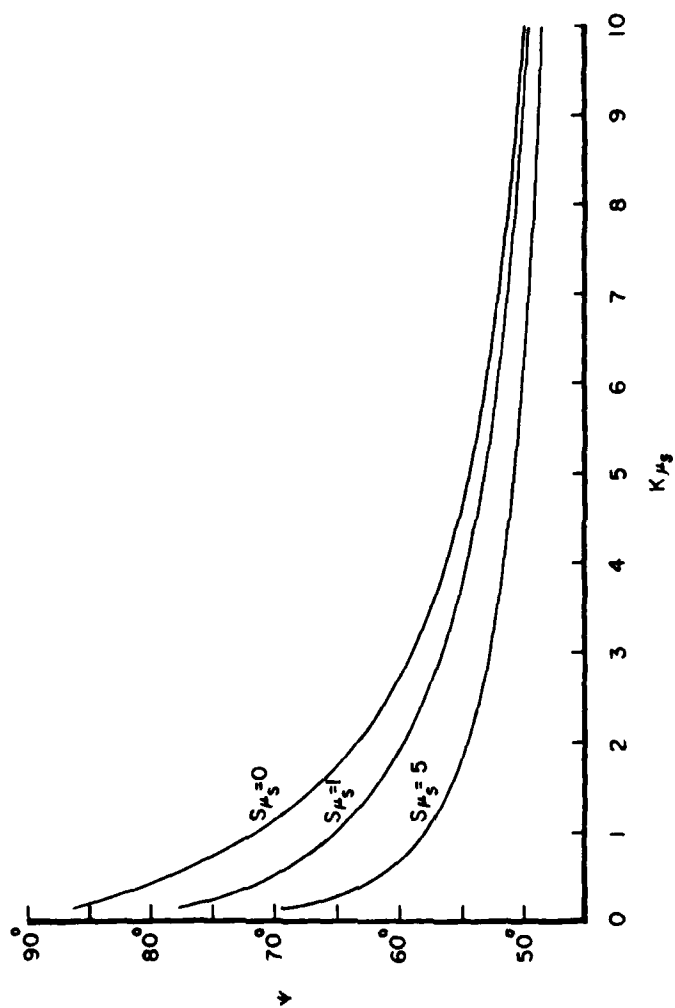
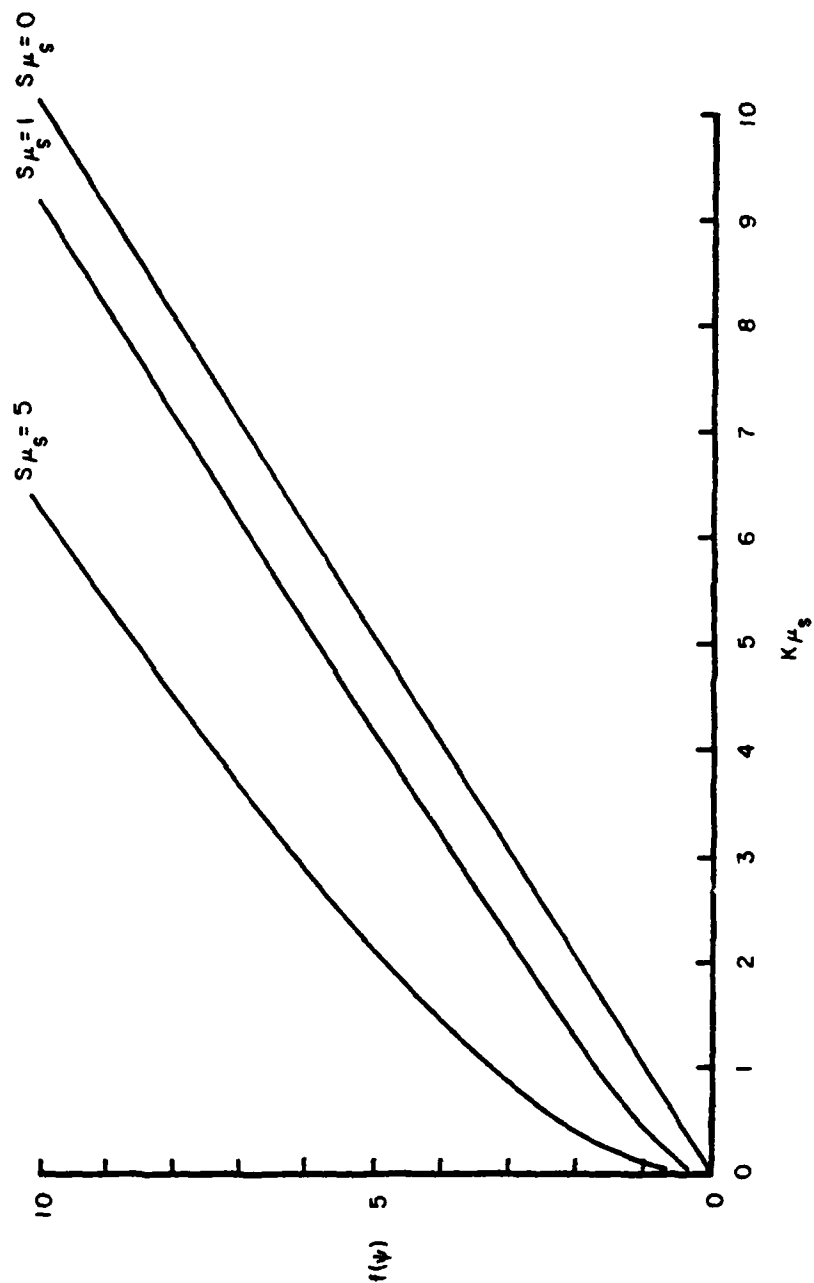




Figure 5. Calculated dependence of phase function on absorbance for increasing values of  $S\mu_s$ .



The scattering coefficient is expected to vary as the reciprocal of the particle diameter,  $d$ , and vary with the wavelength,  $\lambda$ , as:

$$S \propto \lambda^{-\kappa} \quad (48)$$

where  $\kappa \approx 4$  for  $d \ll \lambda$ ,  $\kappa \approx 1$  for  $d \approx \lambda$ , and  $\kappa \approx 0$  for  $d \gg \lambda$ . For particle sizes much larger than the wavelength the product,  $S\mu_s$ , is a constant for a given sample and modulation frequency.<sup>11</sup>

#### Experimental Confirmation

Three substrates,  $\gamma$ -alumina, silica gel, and fumed silica were used in this study because of their usefulness in research on chemically modified surfaces. The  $\gamma$ -alumina (Alfa-Ventron, Danvers, MA; ground and sieved  $\leq 200$  mesh  $\approx 75 \mu\text{m}$ ) was obtained through the courtesy of Dr. D.M. Hercules of the University of Pittsburgh. The silica gel (J.T. Baker Chemical Co., Phillipsburg, New Jersey; 60-200 mesh) was prepared by crushing in a miniature stainless-steel ball mill for one minute. The approximate particle diameter of the resulting powder was  $\geq 1\mu\text{m}$  as determined by optical microscopy. The fumed silica material was scintillation grade Cab-O-Sil (Eastman Kodak Co., Rochester, New York). After wetting, drying, and pulverizing this material, it exists as agglomerates with diameter  $\geq 0.1\mu\text{m}$ .

Samples of these substrates were loaded with  $\text{K}_2\text{CrO}_4$  using the following procedure. Aqueous potassium chromate solutions were prepared from dried reagent grade  $\text{K}_2\text{CrO}_4$  (Mallinckrodt Chemical Co., St. Louis, Missouri) and outgassed deionized water adjusted to pH=8 with KOH. Substrate samples were slurried with weighed amounts of these solutions. The loading of each sample was determined

gravimetrically using tabulated densities of  $K_2CrO_4$  solutions.<sup>12</sup> These slurries were dried at 80°C. The spectrum of aqueous  $K_2CrO_4$  in 0.05 mol/dm<sup>3</sup> KOH was recorded on a Cary 219 absorption spectrometer.

A similar procedure was used to prepare samples of optically opaque reference material. Samples of the prepared substrates were slurried with India ink to deposit finely divided carbon on these surfaces. These samples were dried at 80°C. The carbon reference was charcoal powder (Merck and Co., Rahway, New Jersey).

The importance of correction of spectra for the effects of saturation and scattering is illustrated by considering the uncorrected magnitude spectrum of chromate on alumina measured at several chromate loadings as shown in Figure 6. The qualitative features of the spectra are similar. However, while in the low absorbance region the net magnitudes are nearly in the same ratio as the ratio of chromate loading, in the high absorbance region the magnitude ratios are dramatically reduced. Therefore, in addition to problems with quantification, spectral deconvolution and spectral subtraction at widely different absorption values can result in distortion and false peaks.

The plot of normalized photoacoustic magnitude at 375 nm versus potassium chromate loading shown in Figures 7 and 8 illustrates the characteristic response as the photoacoustic opacity increases. Only at very low chromophore loading is the response linear. The sensitivity decreases with increasing chromophore loading and, ultimately, the photoacoustic magnitude becomes independent of sample absorption in the saturation limit. Figures 9 and 10 are the corresponding plots of the phase function,  $f(\psi)$ , at 375 nm versus loading. In this case the

Figure 6. Photoacoustic spectrum of chromate on alumina substrate for various loadings.

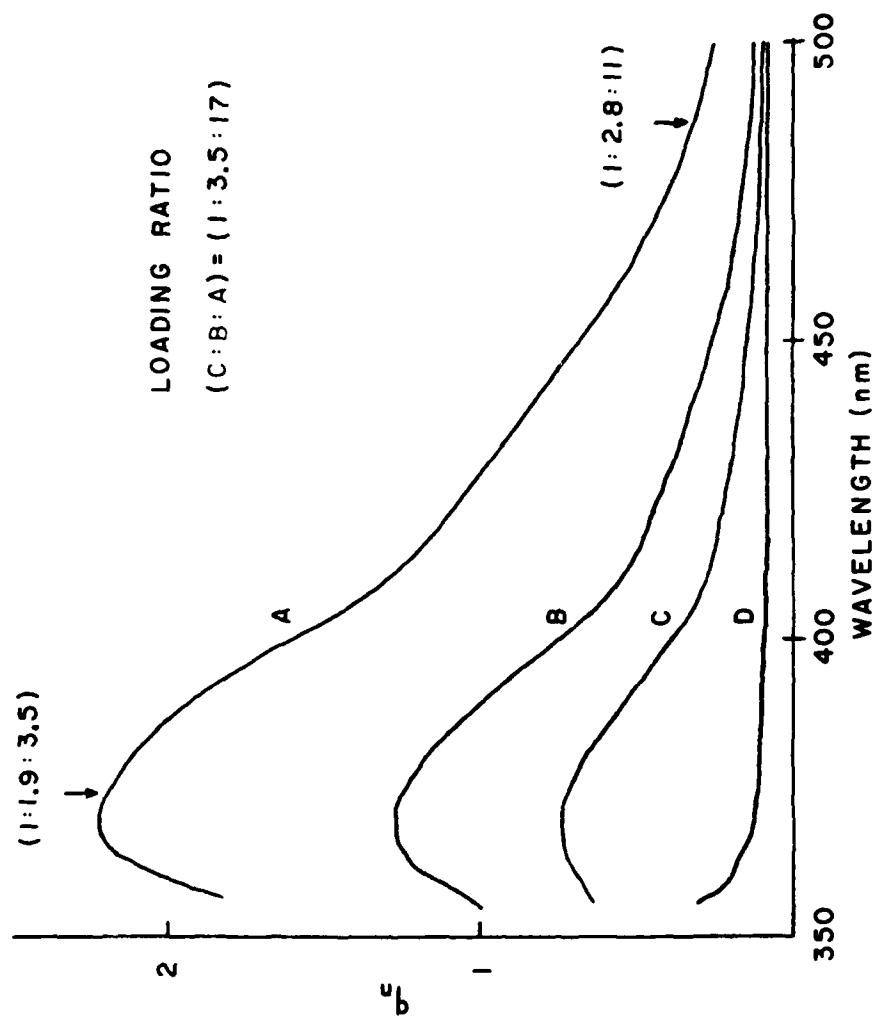


Figure 7. Dependence of photoacoustic magnitude on chromate loading for alumina.

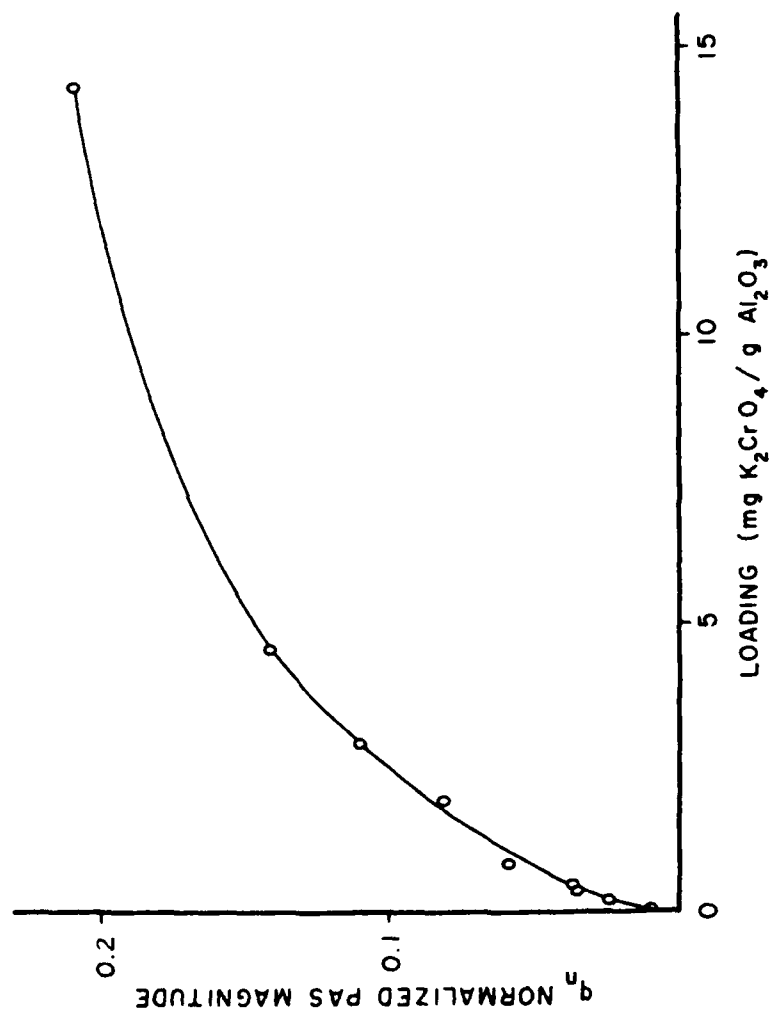




Figure 8. Dependence of photoacoustic magnitude on chromate loading for silica materials.

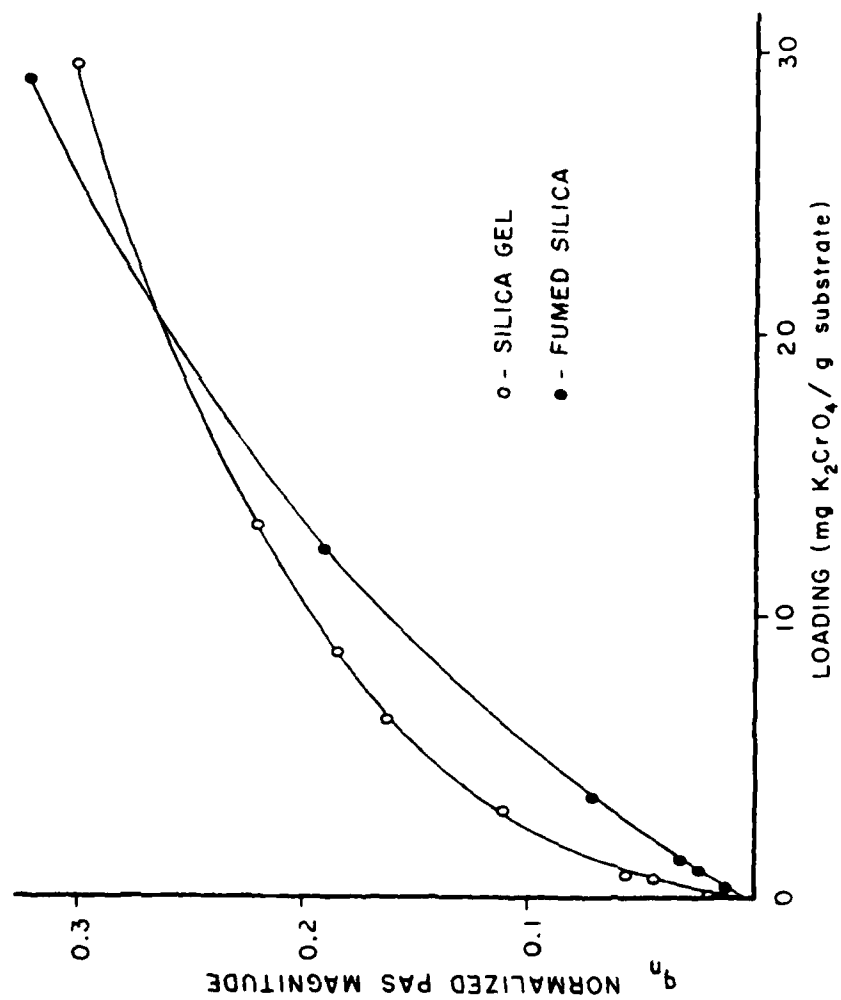


Figure 9. Dependence of phase function on chromate loading for alumina.

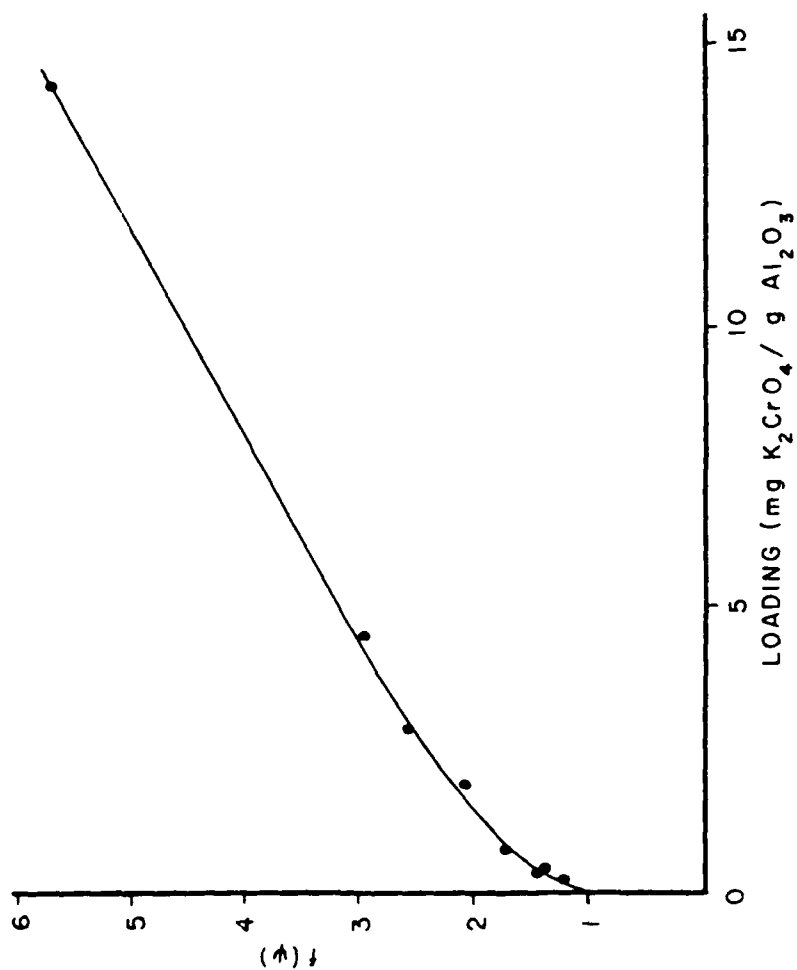
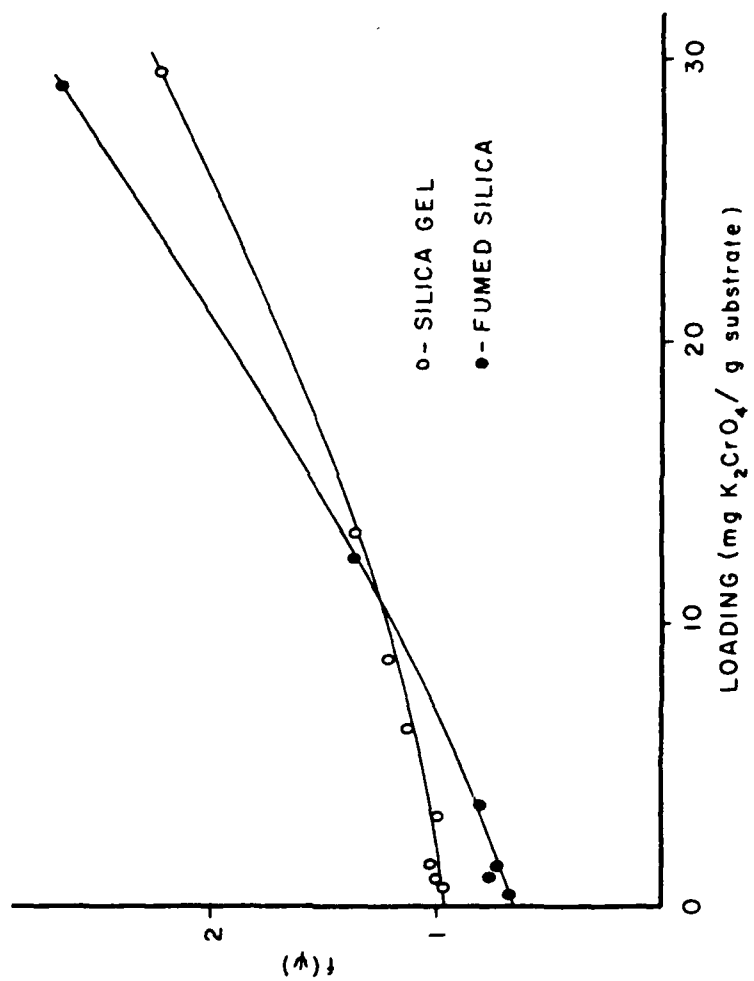


Figure 10. Dependence of phase function on chromate loading for silica materials.



response is nearly linear at very high loading. At low sample absorption the function becomes nonlinear because of the influence of light scattering in the sample. These data have been corrected for the vector contribution of the pure substrate.

The dependence of the phase function on absorptivity for the alumina substrate is very much like the predicted dependence shown in Figure 5. However, the phase function for the silica materials becomes less sensitive to sample absorptivity at low chromophore loading. This effect is more pronounced for silica gel than for fumed silica. The likely reason for this deviation is the failure of the assumption of perfectly diffused light in the first thermal diffusion length. Table 1 compares calculated values of thermal diffusion lengths for these materials.

The magnitude data for silica gel and fumed silica are well fit by a power curve for  $q_n < 0.2$  as shown in Figure 11. For alumina this dependence holds only for  $q_n < 0.035$ . The power curve dependence exists only for the range in which  $f(\psi) \approx 1$ . The reason for this dependence becomes evident when one applies the approximation,  $f + 1 \approx 2\sqrt{F}$ , to the magnitude equations. For silica samples with low absorptivity this relation has proven useful.

The phase measurement was calibrated relative to an opaque reference material. The instrumental phase lag,  $\theta$ , is independent of the sample type. The phase lag due to the production of the acoustic signal,  $\eta$ , derives from the integral of the time-dependent temperature change over the gas boundary layer. This is expected to be relatively insensitive to the type of surface and the surface roughness. Table 2

Table 1  
Thermal diffusion properties of substrate materials.

Substrate Material	Thermal Diffusivity (cm <sup>2</sup> /s)	Thermal <sup>c</sup> Diffusion Length (cm)	Approximate Particle Diameter (cm)
Alumina	0.080 <sup>a</sup>	0.024	5 X 10 <sup>-3</sup>
Silica Gel	0.0018 <sup>a</sup>	0.0036	10 <sup>-3</sup>
Fumed Silica	0.004 <sup>b</sup>	0.005	10 <sup>-4</sup>

<sup>a</sup>Tabulated values from "Thermophysical Properties of Matter: The TPRC Data Series," Y.S. Touloukian (ed.).

<sup>b</sup>Calculated from tabulated values (a) and bulk density.

<sup>c</sup>Calculated from tabulated values (a) for 45 Hz modulation frequency.



Figure 11. Plot of logarithm of photoacoustic magnitude versus logarithm of chromate loading for silica materials.

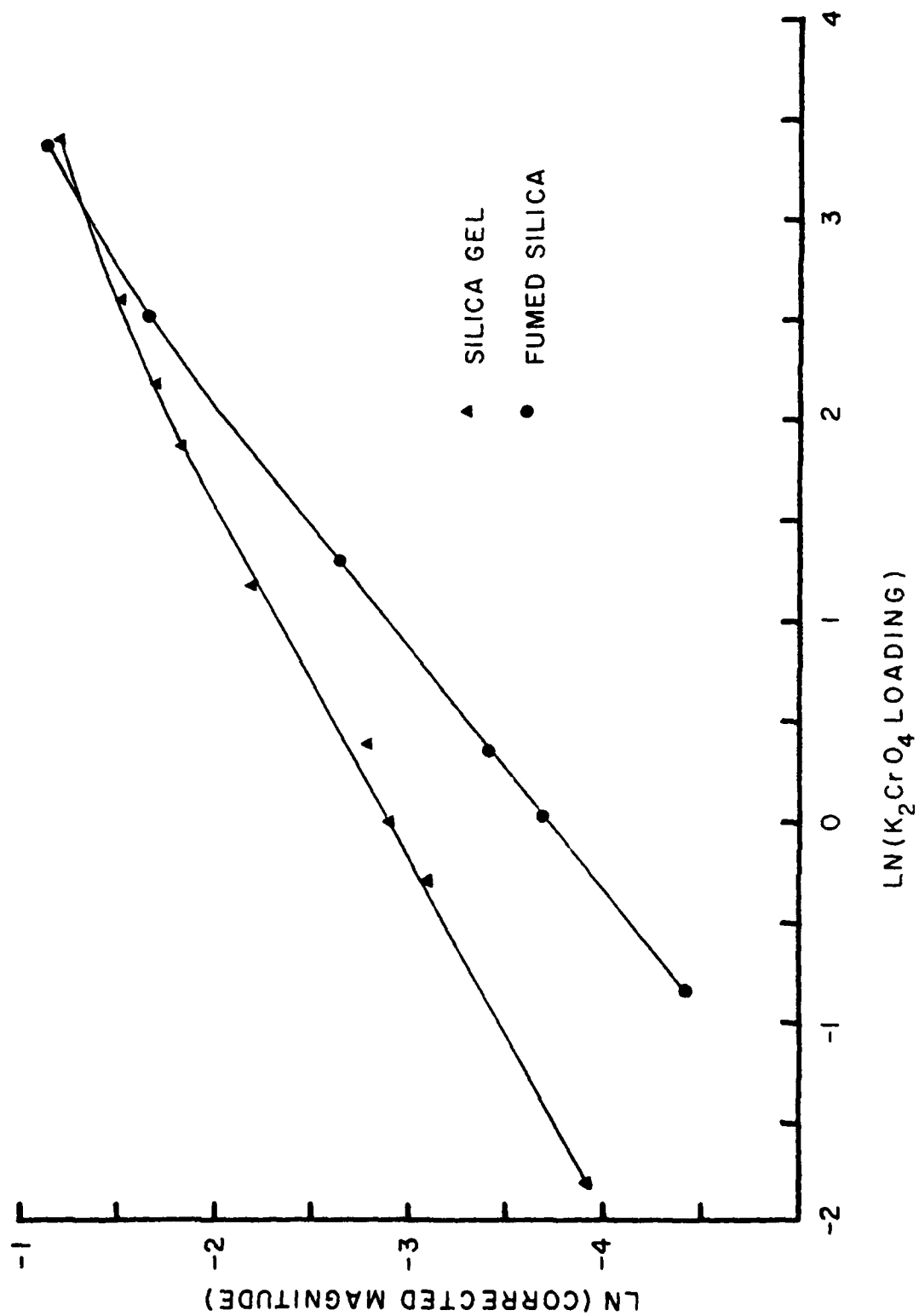


Table 2

Comparison of opaque reference materials  
made by depositing suspended carbon black on substrates.

Sample	$C_r^a$	$\Delta X_r^a$
Fumed Silica	0.51	-1.7 <sup>0</sup>
Silica Gel	0.44	+1.5 <sup>0</sup>
$\gamma$ -alumina	0.26	+1.4 <sup>0</sup>
India Ink	0.060	+0.5 <sup>0</sup>

<sup>a</sup>Relative to carbon powder

summarizes the comparison of opaque reference materials with powdered carbon. The small differences in phase data reflect differences in efficiency of energy transfer to the gas boundary layer.

The comparison of theoretical predictions with the phase data in Figures 9 and 10 is begun by considering the function  $S\mu_s b$ :

$$S\mu_s b = \left[ (K\mu_s)^2 + 2KS\mu_s^2 \right]^{1/2} \quad (47)$$

The loading,  $L$ , is assumed to be proportional to the absorption function,  $K\mu_s$ :

$$K\mu_s = cL \quad (48)$$

Hence, the loading is related to the phase function by the following quadratic equation:

$$(cL)^2 + 2S\mu_s(cL) - f(\psi)^2 = 0 \quad (49)$$

A least-squares fit of the phase data to this function is used to determine the constants  $c$  and  $S\mu_s$  as illustrated in Figure 12. The result is forced into the form of Equation 49 by correcting for a constant residual term,  $\epsilon$ . Table 3 lists the results of this procedure for the three substrates investigated. The direction of change of  $S\mu_s$  suggests that differences in  $\mu_s$  are dominant over particle size differences. For these measurement conditions  $\mu_s$  for alumina is approximately an order of magnitude larger than  $\mu_s$  for silica. The nonzero intercept,  $\epsilon$ , is a measure of the breakdown of the assumption of perfectly diffused light on the scale of the thermal diffusion length. Predominance of forward scattering over reverse scattering

Figure 12. Least-squares fit of quadratic dependence of  $f^2(\psi)$  on chromate loading for alumina substrate.

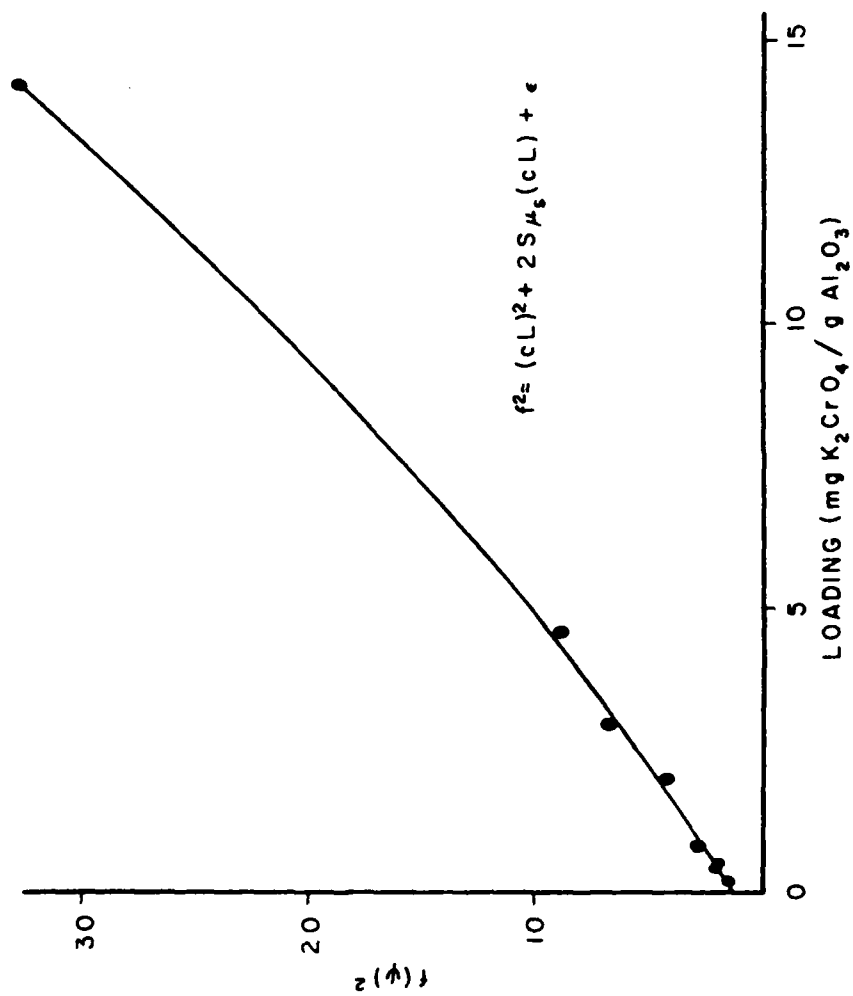


Table 3

Results of least-squares fit of phase data  
for chromate-loaded substrates to Equation 49.

Substrate	$S\mu_s^a$	c	$\epsilon$
$\gamma$ -alumina	3.6	0.217	1.18
Silica Gel	0.2	0.059	0.93
Fumed Silica	0.1	0.085	0.46

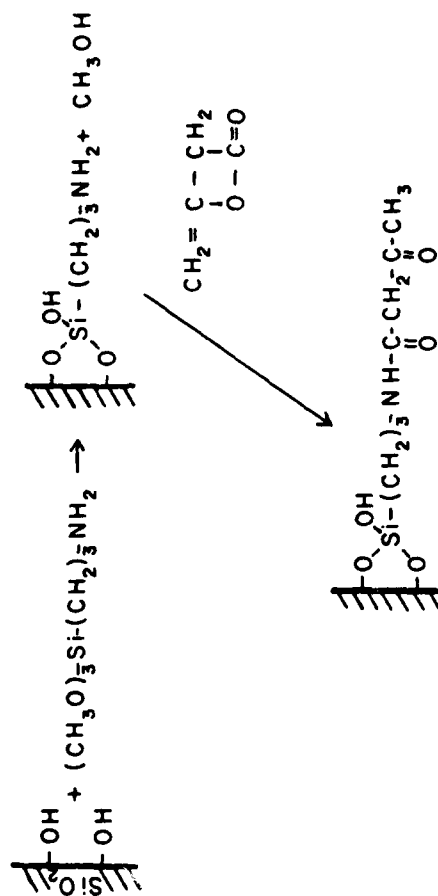
<sup>a</sup>Modulation frequency is 45 Hz.

in the first thermal diffusion length is evidenced by the imperfect reflectance ( $R < 1$ ) of the pure substrate.

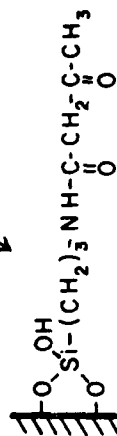
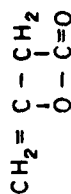
The magnitude and phase measurements are now combined as in Equation 46. The reflectance term, Equation 47, must include the component due to the substrate reflectance, whereas the saturation calculation is corrected for  $\epsilon$ . The resultant response,  $C\beta\mu_s$ , is plotted versus chromate loading of alumina with and without correction for reflectance in Figure 13. It is found that this corrected response function is linear within 8% for more than two orders of magnitude of chromophore loading as shown in Figure 14. The magnitude response for silica gel and fumed silica corrected for saturation and light scattering is plotted versus loading in Figure 15. Since the physical properties of these two silica materials are similar, it is not unexpected that their corrected response functions are similar. Figure 16 shows the chromate spectrum at high loading on fumed silica corrected for saturation effects and light scattering as compared to the solution phase absorption spectrum of chromate in  $0.05 \text{ mol/dm}^3$  KOH demonstrating the success of the method.

Application of this method to a chemically modified substrate is used to demonstrate the potential of PAS in this field. The surface of a sample of the fumed silica material was modified in the manner of Kettrup, et al.<sup>13</sup> as illustrated in Equation 50. The structures shown are not intended to represent details of bonding to the surface. The preparation was carried out by Mr. Fu-Jann Pern.<sup>14</sup> Samples of this product material were well mixed with known quantities of unmodified





(50)



AD-A116 777

AIR FORCE INST OF TECH WRIGHT-PATTERSON AFB OH  
PHOTOACOUSTIC SPECTROSCOPY OF CHEMICALLY MODIFIED SURFACES.(U)  
AUG 81 L W BURGGRAF

F/6 7/4

UNCLASSIFIED

AFIT-81-16D

NL

2 of 3

000000

116...

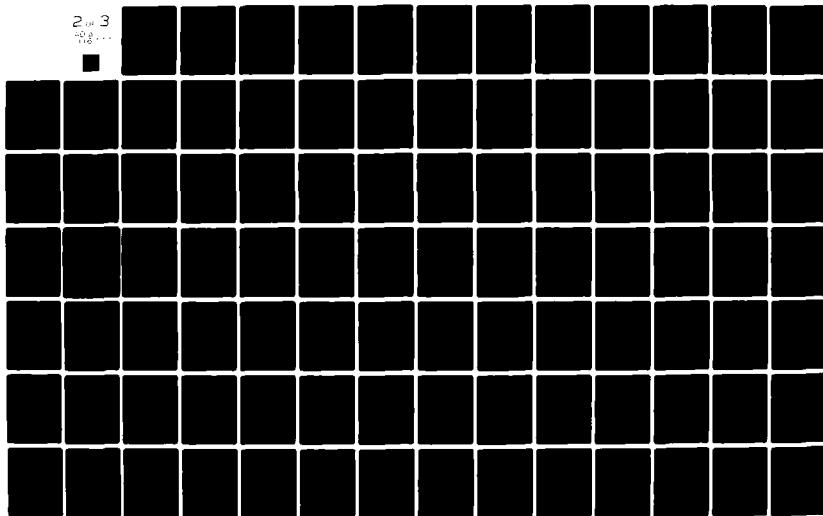


Figure 13. Dependence of corrected response function,  $C\beta\mu_s$ , on chromate loading for alumina substrate with and without reflectance correction.

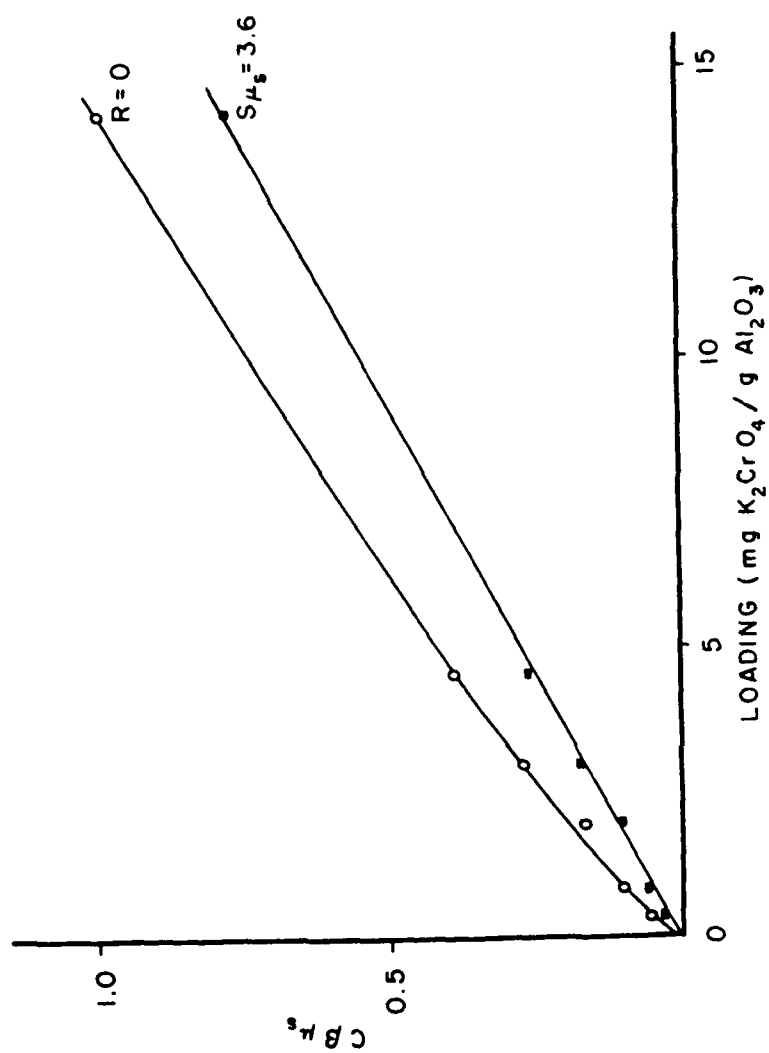


Figure 14. Logarithmic plot of corrected response function versus loading with least-squares linear fit.

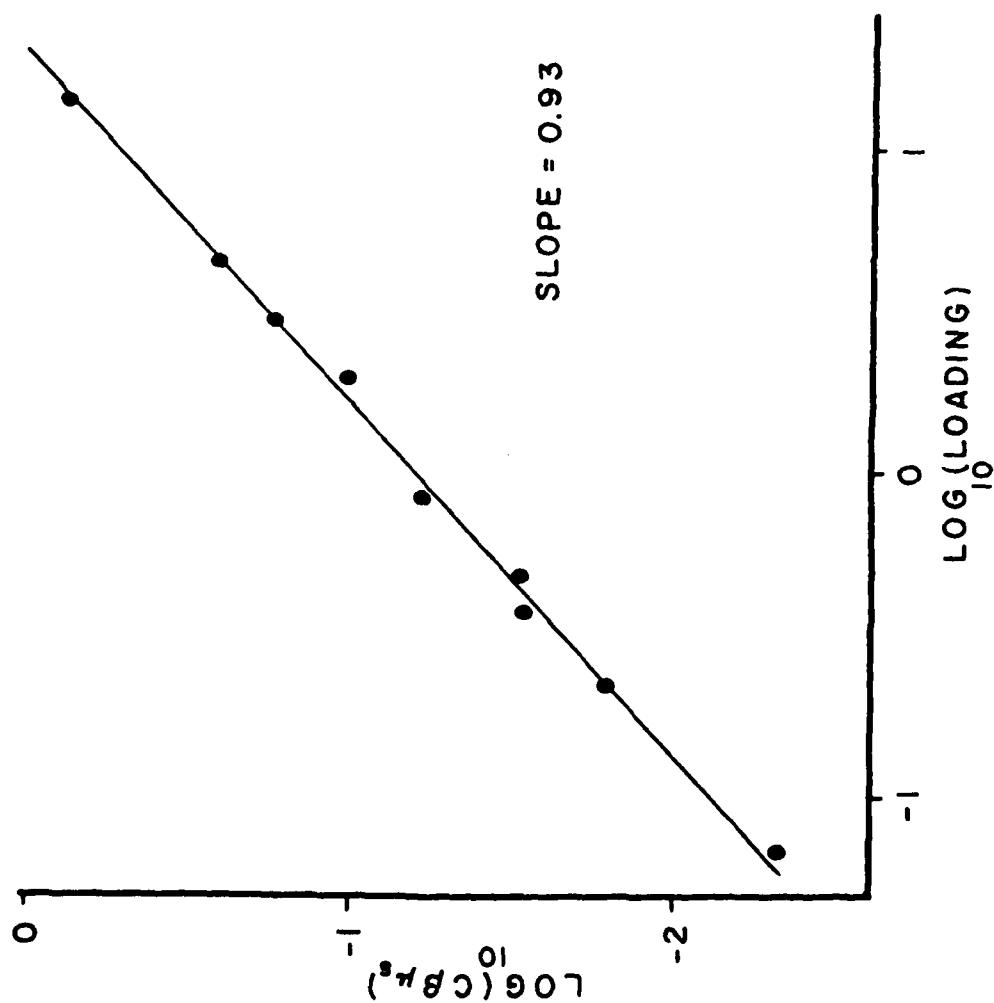


Figure 15. Dependence of corrected response function,  $C\beta\mu_s$ , on chromate loading for silica materials.

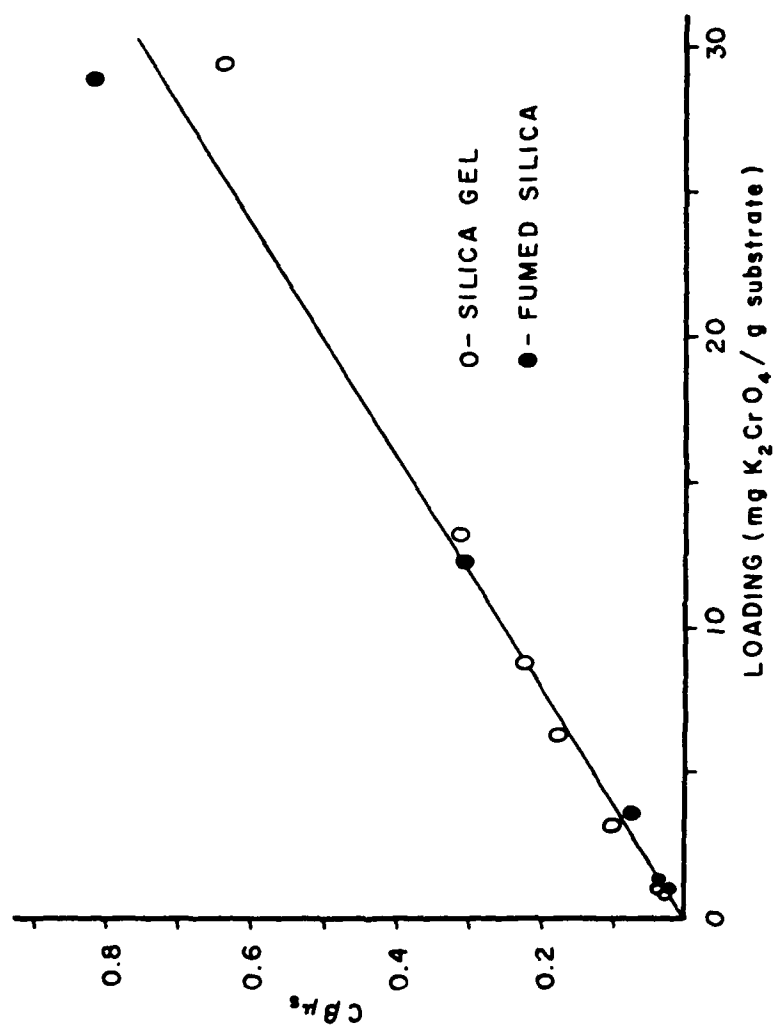
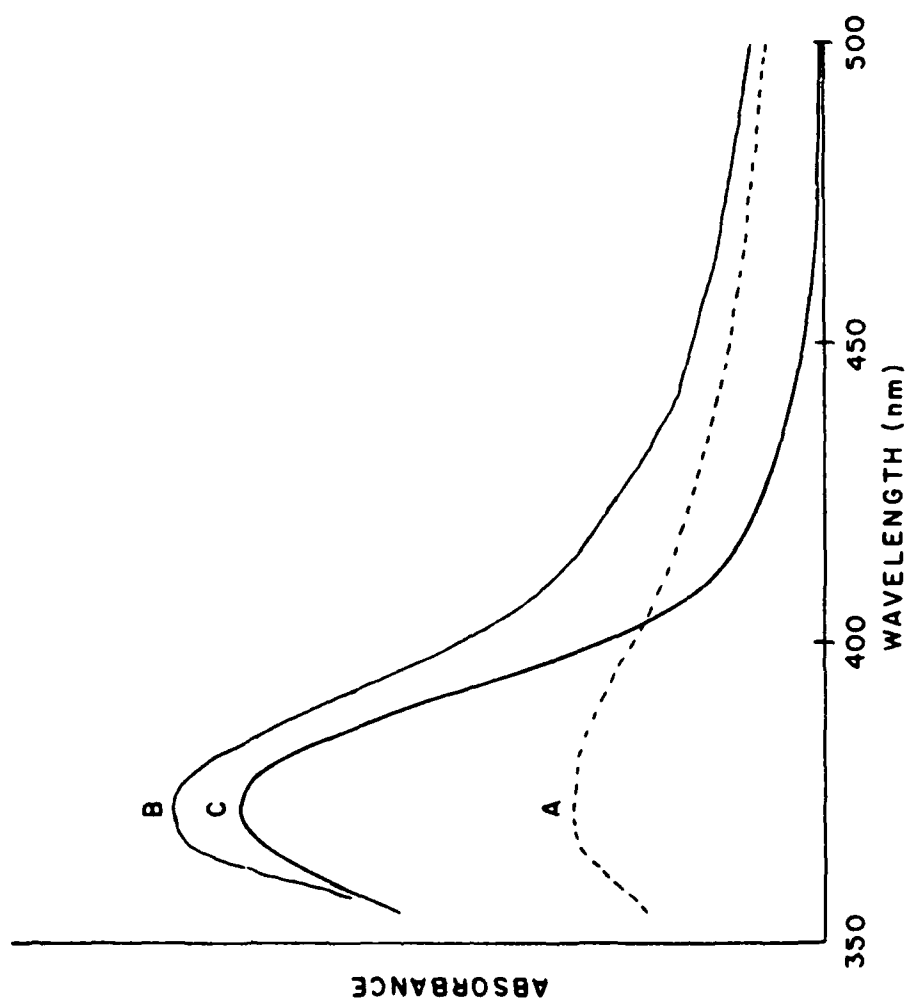




Figure 16. Comparison of photoacoustic magnitude spectrum (A) and corrected photoacoustic spectrum (B) of chromate-loaded fumed silica (29 mg  $K_2CrO_4$ /g substrate) with solution phase chromate spectrum (C).



substrate. The uncorrected photoacoustic magnitude spectrum of chemically modified fumed silica is shown in Figure 17. In Figure 18 the normalized PA magnitude, corrected for the acoustic response of the unmodified substrate, is plotted versus the mass fraction of chemically modified substrate,  $z$ , at two wavelengths near the absorption maximum. Note that qualitative features of the spectrum are evident even though the PA magnitude is relatively insensitive to absorption for a large portion of this spectrum. It is assumed that the thermal and light-scattering properties of the modified substrate are identical to those of the chromate-loaded substrate. Using the values of  $S_{\mu_s}$  and  $\epsilon$  for fumed silica, the phase measurement is used to correct the magnitude for saturation effects and scattering. The corrected response is shown in Figure 19. The corrected response function is linear with mass fraction of the chemically modified substrate.

The Rosencwaig-Gersho theory has been extended for the light-scattering thermally thick case to create a framework for quantitative PAS of particulate solids. In this formulation both phase and magnitude information are combined to account for scattering and saturation effects. Calibration standards are used to determine constants which depend on the optical and thermal properties of the substrate. The absorption spectrum of other chromophores applied to the substrate by absorption or chemical modification can then be measured. Eyring et al.<sup>15</sup> state that a "...damning present criticism of PAS is that it is not yet a reliable quantitative analytical tool." By properly accounting for the effects of acoustic background, light scattering, and saturation effects PAS can be made a reliable quantitative analytical tool.

Figure 17. Photoacoustic magnitude spectrum of undiluted chemically modified fumed silica.

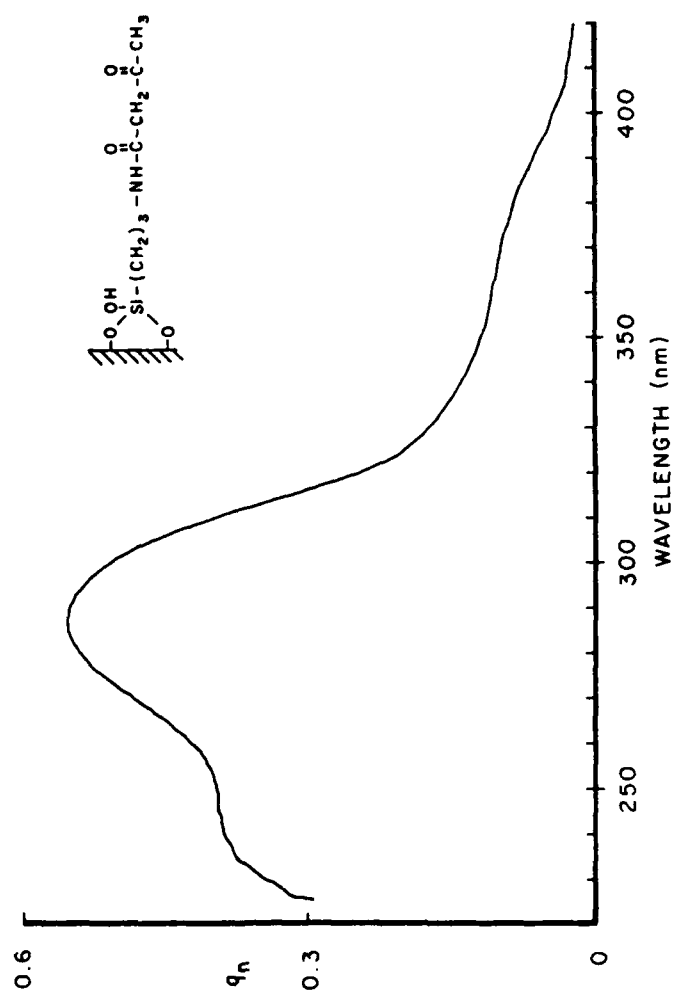


Figure 18. Dependence of photoacoustic magnitude on mass fraction of chemically modified fumed silica,  $z$ .

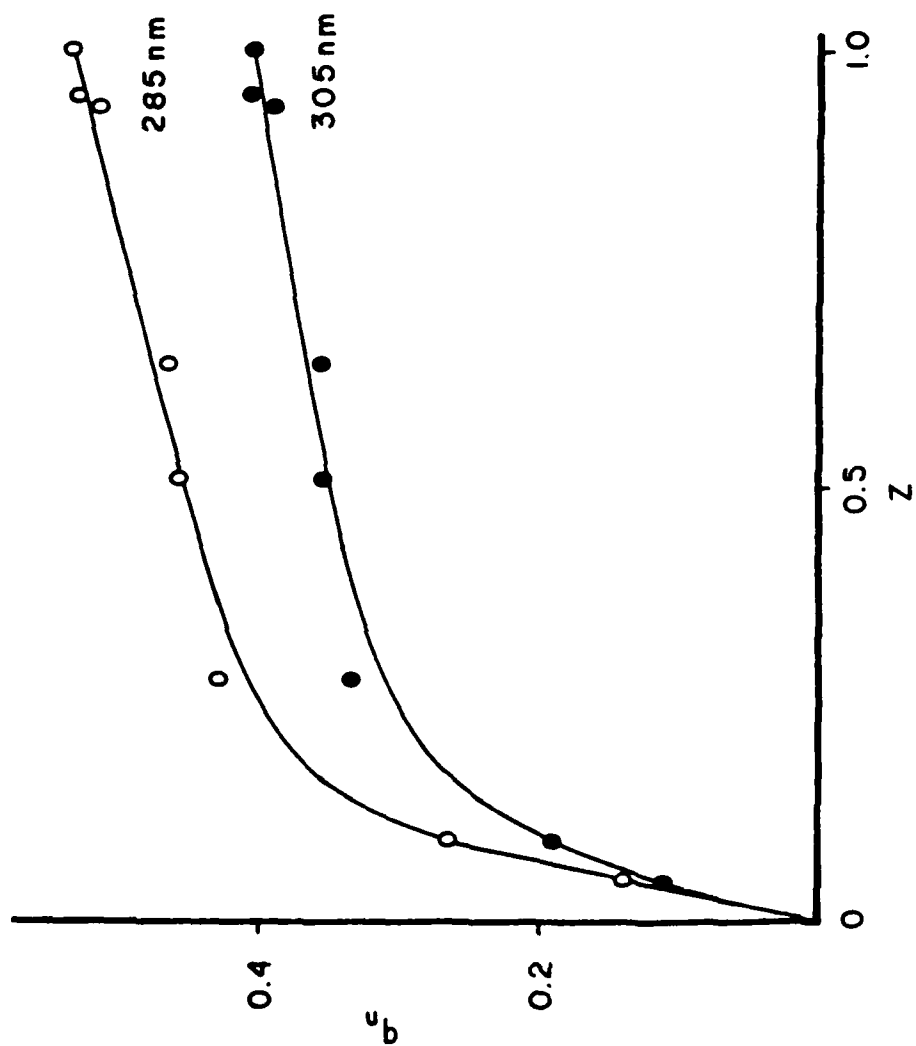
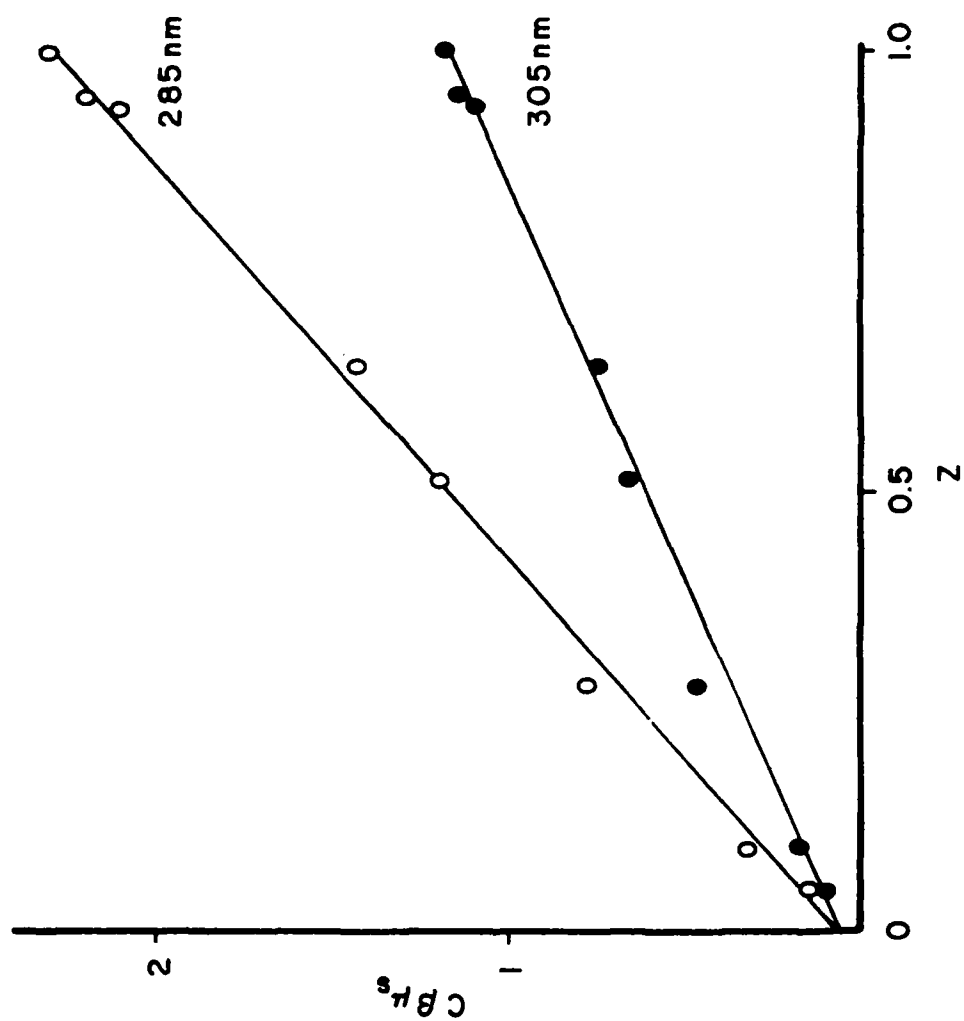


Figure 19. Corrected photoacoustic response versus mass fraction of chemically modified fumed silica,  $z$ .





### Stray Light Correction in Photoacoustic Spectroscopy

The problem of stray light is common to all optical spectroscopies which use broad band sources. The three major sources of stray light are: (1) reflection and scattering of light from walls and optical mountings in the monochromator, (2) reflection and scattering of light at the surfaces of the optics, and (3) scattering of light and fluorescence within the optics.<sup>16</sup> The stray radiant energy (SRE) contribution to the observed signal is the ratio of the signal produced by the detector for light of all wavelengths outside the band width for which the monochromator is set to the total signal.

$$\text{SRE} = \frac{I_s}{I_o + I_s} \quad (51)$$

In Equation 51,  $I_o$  is the signal produced by light at the measurement wavelength,  $\lambda_o$ , and  $I_s$  is the signal produced by stray light. The stray light signal,  $I_s$ , can be divided into three components:

$$I_s = I_{\lambda_i} + I_F - I_{\text{scat}} \quad (52)$$

Where  $I_{\lambda_i}$  is the signal contribution from unwanted wavelengths ( $\lambda_i \neq \lambda_o$ ) transmitted by the monochromator,  $I_F$  is the signal contribution due to fluorescence emission which reaches the detector, and  $I_{\text{scat}}$  is the signal contribution due to net scattering losses in the sample causing light not to reach the detector. The stray light signal,  $I_s$ , is not expected to vary dramatically with monochromator setting. The  $I_{\lambda_i}$  component is expected to have little dependence on the monochromator

setting, while the minor contributors,  $I_F$  and  $I_{\text{scat}}$ , both increase with decreasing wavelength tending to offset each other.

In conventional absorption spectroscopy the absorbance in the absence of stray light is:

$$A = -\log \left( \frac{I}{I_0} \right) \quad (53)$$

where  $I$  is the detector signal for light transmitted through a non-scattering sample. In the presence of stray light the measured absorbance,  $M$ , is:

$$M = -\log \left( \frac{I + I'_S}{I_0 + I_S} \right) \quad (54)$$

where  $I'_S$  is the stray light contribution to the sample signal and  $I_S$  is the stray light contribution to the reference signal. If it is assumed that the sample does not absorb in the wavelength regions from which SRE originates and does not exhibit luminescence or scattering then:

$$I'_S = I_S \quad (55)$$

and the measured absorbance can be written:<sup>17</sup>

$$M = -\log \left[ \frac{I}{I_0} + (\text{SRE}) \left( 1 - \frac{I}{I_0} \right) \right] \quad (56)$$

Comparison of Equations 53 and 56 reveal the way in which increasing SRE causes a smaller measured absorbance producing deviation from Beer's law.

The SRE contribution to the signal can become severe below 250 nm primarily because  $I_0$ , the signal at the measurement wavelength,

decreases. This occurs because of the reduced source intensity below 250 nm, the reduced efficiency of optical elements, and the attenuation of the atmosphere at shorter wavelengths. Each element of the spectrometer has a different influence on the stray light signal. The most important of these are: (1) the source distribution, (2) monochromator/optics design, and (3) detector sensitivity. Slavin<sup>17</sup> summarizes the influence of each of these elements.

For a given spectrometer one can determine the SRE by absorbing all the light within the wavelength limits for which the monochromator is set and report the remaining signal as stray light. While this idealization is never actually accomplished, Cook and Jankow<sup>18</sup> point out that the SRE due to instrumental factors can be estimated by an ASTM method<sup>19</sup> which uses Corning Vycor glass filters. However, this correction does not account for changes in SRE due to sample effects. The case for which the sample does not absorb in regions from which SRE originates and does not exhibit scattering or luminescence is never met in practice. For example, Vandenbelt et al.<sup>20</sup> compared the Beer's law response for three different substances measured at the same wavelength on the same instrument. All three showed different deviations from Beer's law because the three materials absorbed different portions of the instrumental stray light. As a result, absorbance values in the literature are not corrected for SRE. Instead, in ideal cases, techniques are used to minimize stray light.

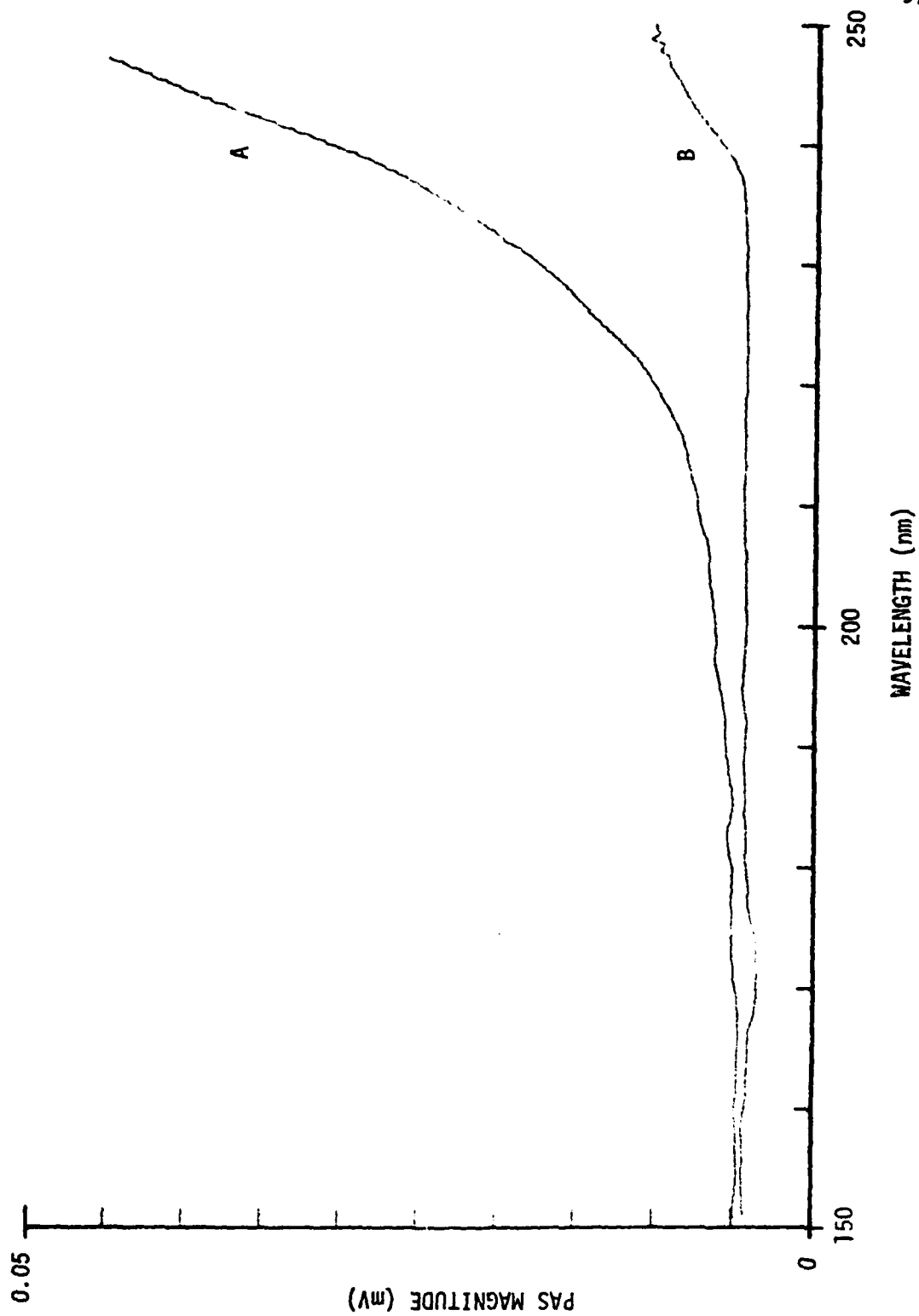
The problem of stray light in conventional absorption spectroscopy is commonly attacked by minimizing the contribution of stray light

to the signal by either employing a detector sensitive to light only in the wavelength region being measured or by minimizing the amount of stray light that reaches the detector. The amount of stray radiation that reaches the detector can be reduced by employing filters or multiple dispersing elements. The latter approach, for example, was employed by this author to minimize the stray light when recording the ultraviolet pentyl radical spectrum<sup>21</sup> in previous work. In these attempts a compromise must be reached between stray light reduction and maintaining adequate signal levels.

In the case of photoacoustic spectroscopy it is possible to make a more acceptable correction for SRE. The key difference between photoacoustic spectroscopy and conventional absorption spectroscopy which permits a better SRE determination is that in photoacoustic spectroscopy the sample itself acts as the radiant energy transducer. Since the detector sensitivity and the sample absorption properties are tied together, the signal due to the fraction of the instrumental stray light absorbed by the sample is more readily measured.

For example, Figure 20 shows the ultraviolet photoacoustic response for carbon powder with air-only absorption ( $\sim 170$  nm absorption cutoff) and with a color glass filter ( $\sim 350$  nm cutoff). This figure illustrates two points. First, the signal below the 170 nm absorption edge is similar for both measurements suggesting that much of the stray light contribution is due to visible and infrared light. Second, the signal due to stray light shows very little wavelength dependence except for the feature at 245 nm due possibly to filter transmission. This

Figure 20. Reference ultraviolet photoacoustic magnitude spectrum with air-only light filter (A) and color glass light filter (B).



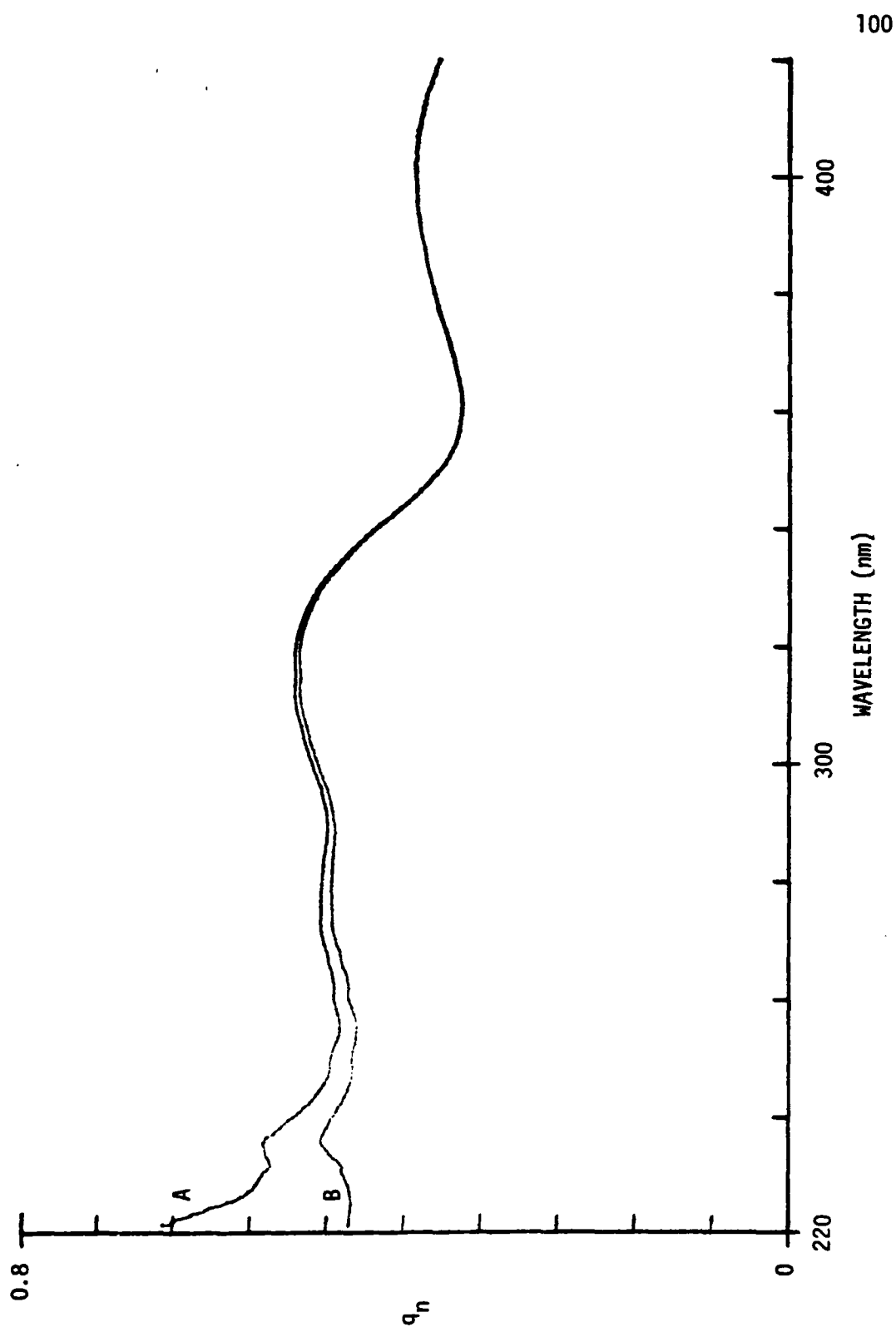
suggests a very simple method for performing the SRE correction for ultraviolet photoacoustic measurements. Measurement of the stray light signal below the atmospheric absorption edge for sample and reference material provide a direct measurement of  $I'_s$  and  $I_s$ . These quantities can then be subtracted from the respective sample and reference signals.

$$q_n = \frac{q_s - I'_s}{q_r - I_s} \quad (57)$$

Figure 21 shows the spectrum of an ultraviolet absorber corrected for stray light in this manner, illustrating the importance of this correction below 250 nm. Without stray light correction the measured absorbance is smaller than the actual absorbance with the result that reported absorption spectra are frequently seen to anomalously decrease at about 220 nm to 230 nm.



Figure 21. Ultraviolet photoacoustic magnitude spectrum of salicylaldehyde derivative of N-2-aminoethyl-3-aminopropyltrimethoxysilane immobilized on silica gel with (A) and without (B) stray light correction.



### References

1. A. Rosencwaig and A. Gersho, J. Appl. Phys. **47**, 64 (1976).
2. S. L. Castleden, E. M. Elliott, G. F. Kirkbright and D. E. M. Spillane, Anal. Chem. **51**, 2152 (1978).
3. D. Hurch and T. Kuwana, Anal. Chem. **52**, 644 (1980).
4. C. H. Lochmuller and D. R. Wilder, Anal. Chim. Acta **118**, 101 (1980).
5. P. Helander, I. Lundstrom and D. Soderberg, "Technical Digest of Topical Meeting on Photoacoustic Spectroscopy," Optical Society of America, Ames, Iowa, 1979, p. WC2-1.
6. P. Helander, I. Lundstrom and D. McQueen, J. Appl. Phys. **51**, 3841 (1980).
7. J. J. Freeman, R. M. Friedman and H. S. Reichard, J. Phys. Chem. **84**, 315 (1980).
8. P. Kubelka, J. Opt. Soc. Am. **38**, 448 (1948).
9. Y. C. Teng and B. S. H. Royce, J. Opt. Soc. Am. **70**, 557 (1980).
10. J. C. Roark, R. A. Palmer and J. S. Hutchison, Chem. Phys. Lett. **60**, 112 (1978).
11. G. Kortum, "Reflectance Spectroscopy," Springer-Verlag, New York, 1969, chapter V.
12. C. D. Hodgman (ed.), "Handbook of Chemistry and Physics," 44th ed., Chemical Rubber Co., Cleveland, 1962, p. 2059.
13. T. Seshadri and A. Kettrup, Fresenius Z. Anal. Chem. **296**, 247 (1979).
14. F.-J. Pern, Masters Thesis, University of Denver, Denver, Colorado, 1980.
15. L. B. Loyd, R. K. Burnham, W. L. Chandler and E. M. Eyring, Anal. Chem. **52**, 1595 (1980).
16. R. A. Sawyer, "Experimental Spectroscopy," 3rd ed., Dover, New York, 1963, p. 121.

17. W. Slavin, Anal. Chem. 35, 561 (1963).
18. R. B. Cook and R. Jankow, J. Chem. Ed. 49, 405 (1972).
19. "Manual on Recommended Practices in Spectroscopy," American Society for Testing and Materials, Philadelphia, 1969, p. 94.
20. J. M. Vandenbelt, J. Forsyth and A. Garrett, Ind. Eng. Chem., Anal. Ed. 17, 235 (1945).
21. L. W. Burggraf and R. F. Firestone, J. Phys. Chem. 78, 508 (1974).

## Chapter 4

### COPPER (II) COMPLEXATION WITH A SURFACE-IMMOBILIZED LIGAND

#### Introduction

Silanes have been widely used to modify surfaces for chemical applications.<sup>1</sup> Two promising applications of chemically modified surfaces to trace metal analysis are the preconcentration of trace metal ions for x-ray fluorescence (XRF) determination and metal-ion chromatography. Choice of a particular immobilized ligand for a specific application is based on the solution-phase equilibrium for the corresponding free ligand. Prediction of the affinity of a particular immobilized ligand for metal ions by extrapolating from analogous solution-phase equilibria ignores the influence of the surface on the heterogeneous equilibria. In particular, the distribution of immobilized ligands on the surface determines the possible metal-ligand stoichiometries. This chapter illustrates a method by which comparisons of solution-phase equilibria with corresponding heterogeneous equilibria may be made.

The complexation of copper (II) by the immobilized ethylenediamine analog was chosen for study for two reasons. First, this immobilized ligand has practical application for preconcentration of trace species. In addition to complexing a variety of transition metal cations,<sup>2</sup>

the immobilized ethylenediamine analog can bind a number of anions.<sup>3</sup> Second, previous experience with this system suggests that the immobilized ligand behaves similarly to its solution-phase counterpart. The uptake of copper (II) by immobilized ethylenediamine as a function of pH has been studied<sup>2</sup> as has the ratio of immobilized material to copper loading.<sup>[4,5]</sup> These studies suggest that the bis chelate is an important species on the surface. Pinnavaia et al.<sup>6</sup> applied electron spin resonance spectroscopy to the study of immobilized ethylenediamine-copper (II) complexes on silica gel with a very low surface density of immobilized ethylenediamine analog,  $0.083 \text{ molecules}/10^2 \text{ \AA}^2$  ( $0.14 \text{ } \mu\text{mol}/\text{m}^2$ ). Both mono and bis complexes were found at all copper-ligand ratios studied with mono complexes predominant at high copper loading (2.3 to 1 maximum mono to bis ratio). The aim of this study was to investigate this heterogeneous equilibrium as a function of copper concentration. Confirmation of the utility of photoacoustic spectroscopy as a tool for monitoring the surface species was of prime interest.

The photoacoustic spectroscopy work was performed in collaboration with Mr. Fu-Jann Pern.<sup>7</sup> The binding study work was a collaborative effort with Dr. Douglas Kendall.

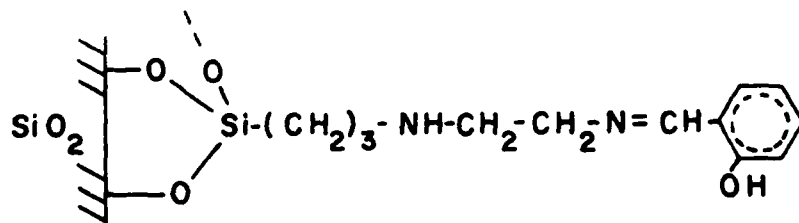
### Experimental

#### Silylation

The silica gel (Baker column chromatography grade, 60-200 mesh) was dried overnight at  $110^\circ\text{C}$  in an evacuated oven. The surface area

of the silica gel was found to be  $300 \text{ m}^2/\text{g}$  as measured by nitrogen adsorption using a Quantachrome Monosorb Surface Area Analyzer. N-(2-aminoethyl)-3-aminopropyltrimethoxysilane (Dow Corning Z-6020), abbreviated AEAPS, was vacuum distilled before use. A 5% solution of AEAPS in dry toluene was prepared. The silica gel was refluxed for two hours in the silane solution (15 mL per gram of silica gel) or, alternatively, the silica gel was stirred with silane solution at room temperature for two hours. No differences were discerned between the products of these methods other than small differences in capacities. After silylation, the silylated silica gel was washed thoroughly with toluene and methanol. The silylated silica gel was cured for several hours at  $80^\circ\text{C}$ . These conditions lead to an approximately monolayer coverage of the surface.<sup>8</sup> From a carbon analysis (Huffmann Laboratory, Wheatridge, Colorado) the average surface coverage was calculated to be 1.4 molecules per  $10^2 \text{ \AA}^2$  ( $2.4 \text{ } \mu\text{mol}/\text{m}^2$ ).

A portion of the silica gel modified with AEAPS by refluxing in toluene solution was further modified to form a Schiff base.<sup>7</sup> A 5% solution of salicylaldehyde in  $\text{CHCl}_3$  was stirred for 30 minutes with the AEAPS-modified silica gel in the proportion of 5 mL of solution per gram of silica gel. The silica gel was recovered by filtration, washed with methanol and air dried. Waddell et al.<sup>9</sup> proposed that the immobilized ligand which is formed under these mild reaction conditions has the structure shown below.



(1)

This material will be designated SAEAPS-modified silica gel. This chemically modified silica gel exhibits a characteristic yellow color which is not removed by washing with alcohol.

#### Photoacoustic Spectroscopy (PAS) Study

Solutions of copper (II) were prepared in the concentration range  $1.0 \times 10^{-1} \text{ mol L}^{-1}$  to  $2.0 \times 10^{-5} \text{ mol L}^{-1}$ . The solutions were made  $0.10 \text{ mol L}^{-1}$  in acetate buffer (pH = 5.0). Other selected copper (II) solutions were adjusted to pH = 5.0 using nitric acid. Portions of silylated silica gel weighing 0.20 gram were equilibrated with 25.0 mL aliquots of the copper (II) solutions. After separation of the silica gel by filtration, the silica gel was air dried. The copper loading was determined using a United Scientific Spectrace 440 energy dispersive x-ray fluorescence spectrometer equipped with a Tracor Northern 880 spectrum analyzer. Dried samples of the copper-loaded silica gel were ground for one minute in a miniature stainless-steel ball mill. Photoacoustic spectra were measured using techniques described in Chapter 3.<sup>10</sup> Visible spectra of copper (II)-AEAPS solutions were recorded on a Cary 219 double-beam spectrophotometer.

#### Binding Studies

Binding studies were conducted both with and without acetate buffer. The most reproducible results were obtained using the buffer. A copper (II) stock solution was standardized using an EDTA titration method. Dilutions of the copper (II) stock solution were made  $0.10 \text{ mol L}^{-1}$  in acetate buffer (pH = 5.0) or, alternatively, were adjusted



to pH = 5.0 with strong acid. Portions of silylated silica gel weighing 0.200 gram were stirred with 50.0 mL of the copper (II) solutions. The contact time was limited to 15 minutes to minimize removal of immobilized AEAPS by hydrolysis. The silica gel and copper solutions were separated by filtration. Bound copper was stripped from the silica gel using a 10% HCl solution. Both the filtrate and the solution containing the stripped copper were diluted and analyzed for copper using a Perkin-Elmer model 2380 atomic absorption spectrophotometer.

### Results and Discussion

#### Solution-Phase Equilibrium

It is expected that the solution-phase equilibrium of copper (II) and AEAPS is similar to that for other substituted ethylenediamines. Large stability constants are observed for mono and bis copper (II) complexes with substituted ethylenediamine compounds, while tris complexes are only weakly formed, if at all.<sup>11</sup> For example, the stability constants for successively formed copper-ethylenediamine complexes are:

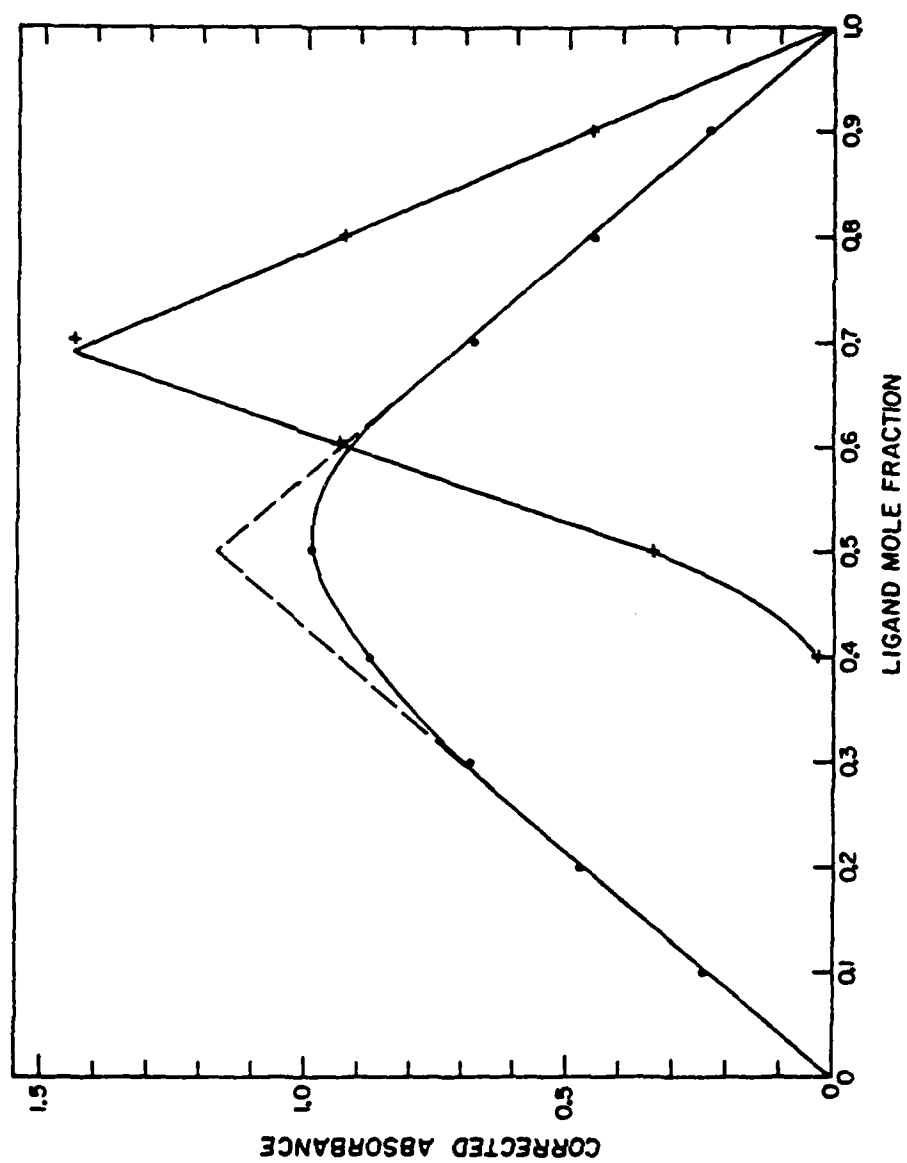
$$\log K_1 = 10.7$$

$$\log K_2 = 9.3$$

$$\log K_3 = -1$$

The result of a classical Job's continuous variation experiment for the aqueous copper (II)-AEAPS system with total concentration equal to  $5.0 \times 10^{-2} \text{ mol L}^{-1}$  is presented in Figure 1. Very stable mono and bis complexes exhibit broad absorption bands with maxima at 658 nm and

Figure 1. Corrected absorbance versus AEAPS mole fraction at 556 nm (+) and 656 nm (●).



556 nm respectively. These spectra are shown in Figure 2. Spectra of solutions with 99 to 1 AEAPS-copper (II) molar ratio were indistinguishable from that of the bis copper (II)-AEAPS complex. Hence, the solution-phase equilibrium for this system is that of a substituted ethylenediamine ligand.

#### Photoacoustic Spectroscopy Results

In Figure 3 the copper loading of AEAPS-modified silica gel, as determined by XRF, and the wavelength of maximum absorption of the surface-bonded species are plotted versus the initial copper concentration in the acetate-buffered solutions. The copper loading curve has the appearance of two consecutive sigmoidal waves. During the second wave the visible absorption band broadens and the wavelength maximum shifts to longer wavelengths. These data are interpreted as representing nearly consecutive formation of predominantly bis then mono copper (II) complexes on the surface. At very low copper concentrations formation of the bis complex is favored because of its greater stability. Throughout the region of high initial copper concentration the mono complex makes an increasing contribution to the absorption spectrum.

The photoacoustic absorption spectrum of the surface species formed at low copper concentration with nitrate counterion is identical to the solution-phase spectrum of the bis copper (II)-AEAPS complex shown in Figure 2. The absorption spectrum of the surface species formed at low copper concentration with acetate counterion is shifted

Figure 2. Visible spectra of bis copper (II)-AEAPS (A) and mono copper (II)-AEAPS (B) with nitrate counterion in aqueous solution.

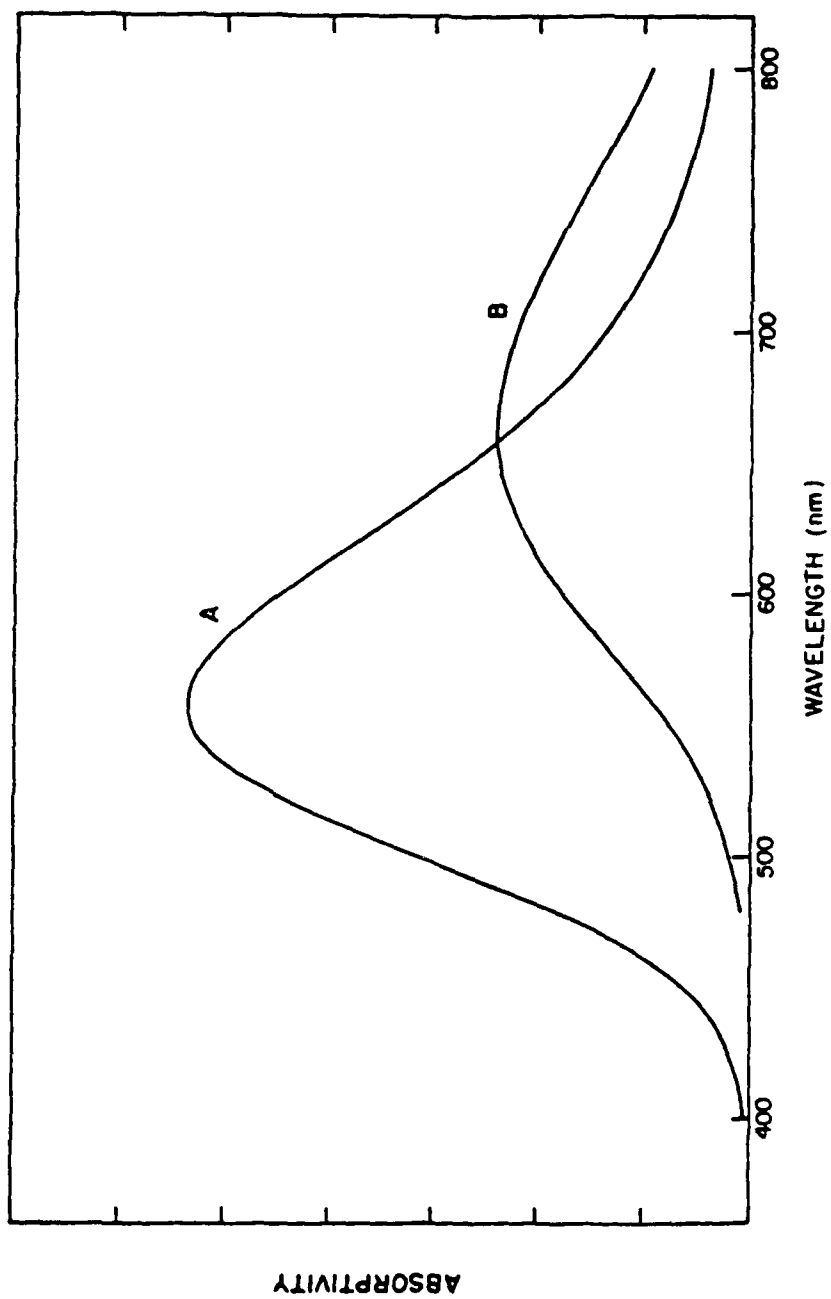
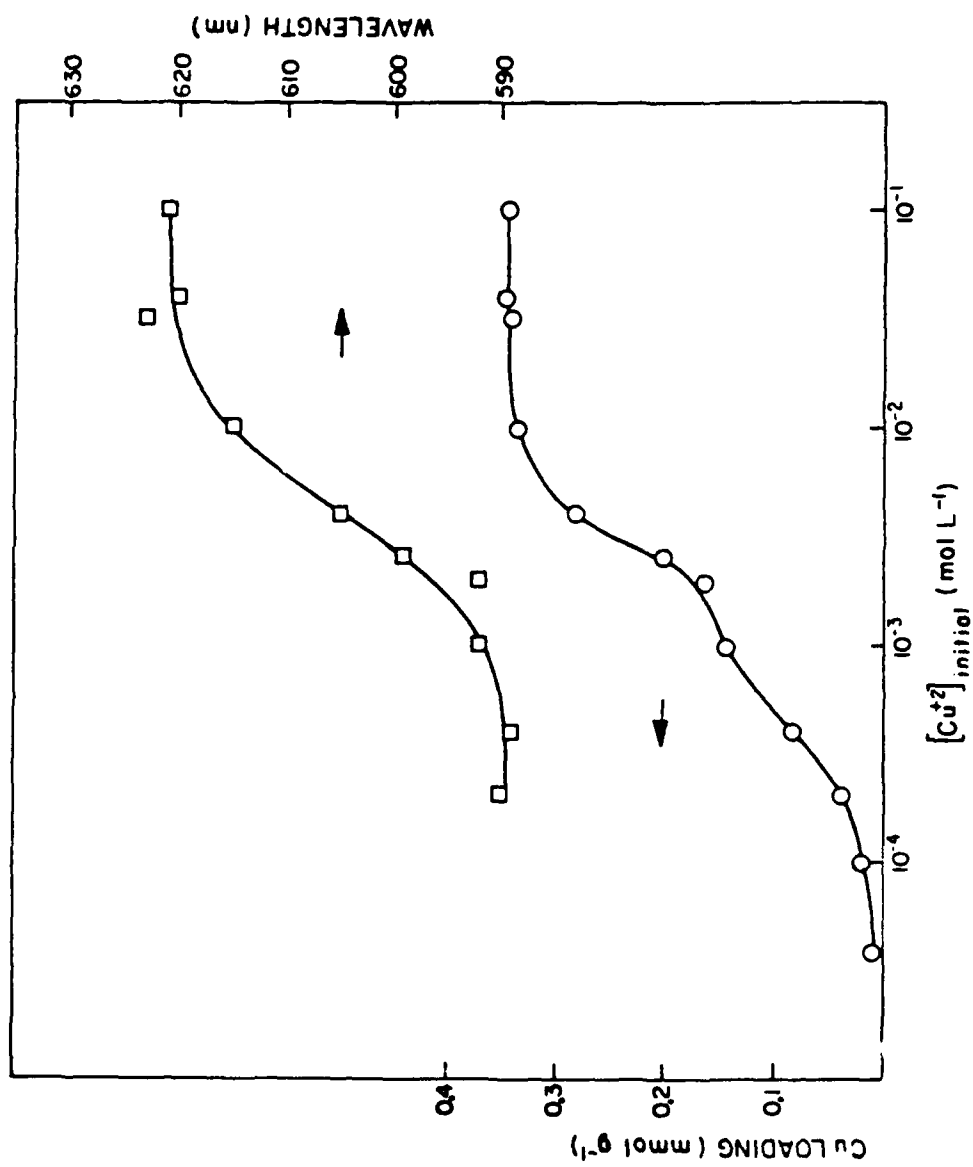


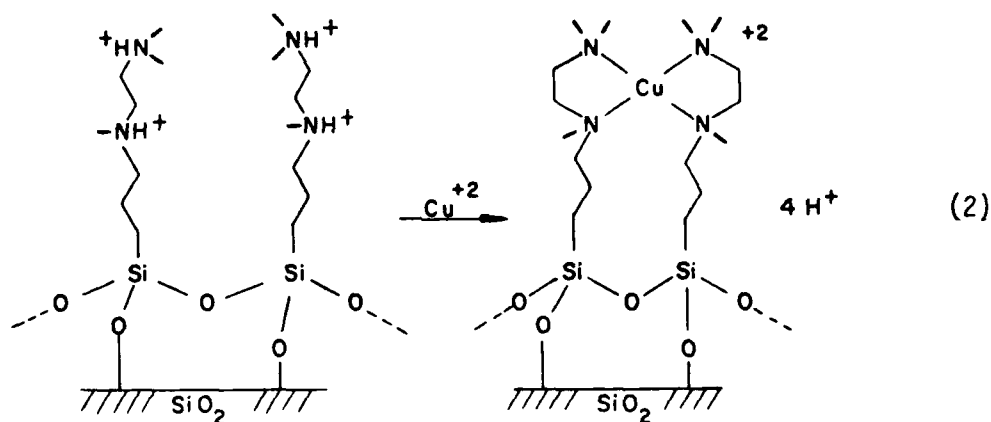
Figure 3. Copper loading and wavelength of absorption maximum for AEAPS-modified silica gel versus initial copper (II) concentration in 0.10 mol L<sup>-1</sup> acetate buffer.





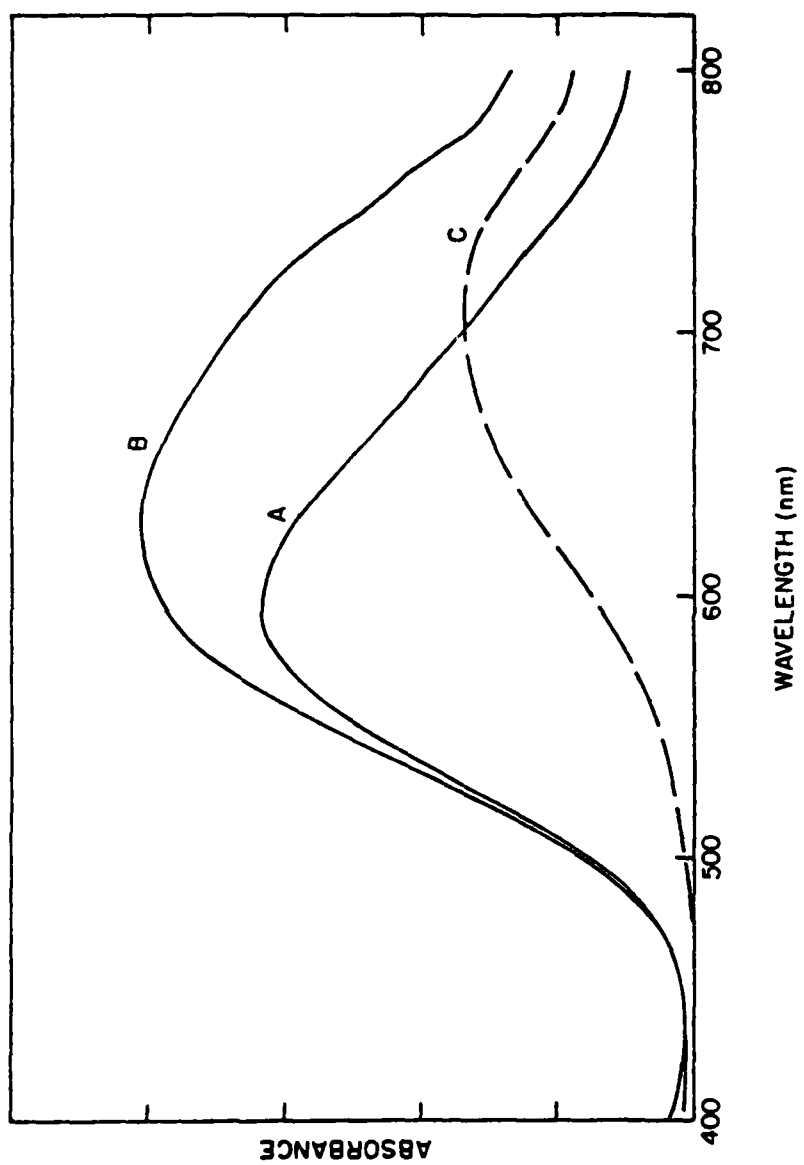
to longer wavelength ( $\sim 590$  nm absorption maximum) while the shape of the absorption spectrum remains unchanged. This shift is a result of the weakened ligand field caused by the association of the acetate ion with the bis copper (II)-AEAPS complex, analogous to the "pentammine effect".<sup>12</sup> The absorption spectra for samples at the beginning and at the end of the high concentration wave in Figure 3 are presented in Figure 4. The spectrum of the mono complex was obtained by stripping out the predominantly bis component from the spectrum obtained at high copper loading. Here also, the association of the acetate ion produces a shift to longer wavelength ( $\sim 710$  nm absorption maximum) relative to the mono spectrum with nitrate counterion.

The immobilized AEAPS is expected to form a bis copper complex at binding sites for which this conformation is possible. For our experimental conditions the following scheme describes this process.



This schematic is not meant to describe the details of bonding to the surface.

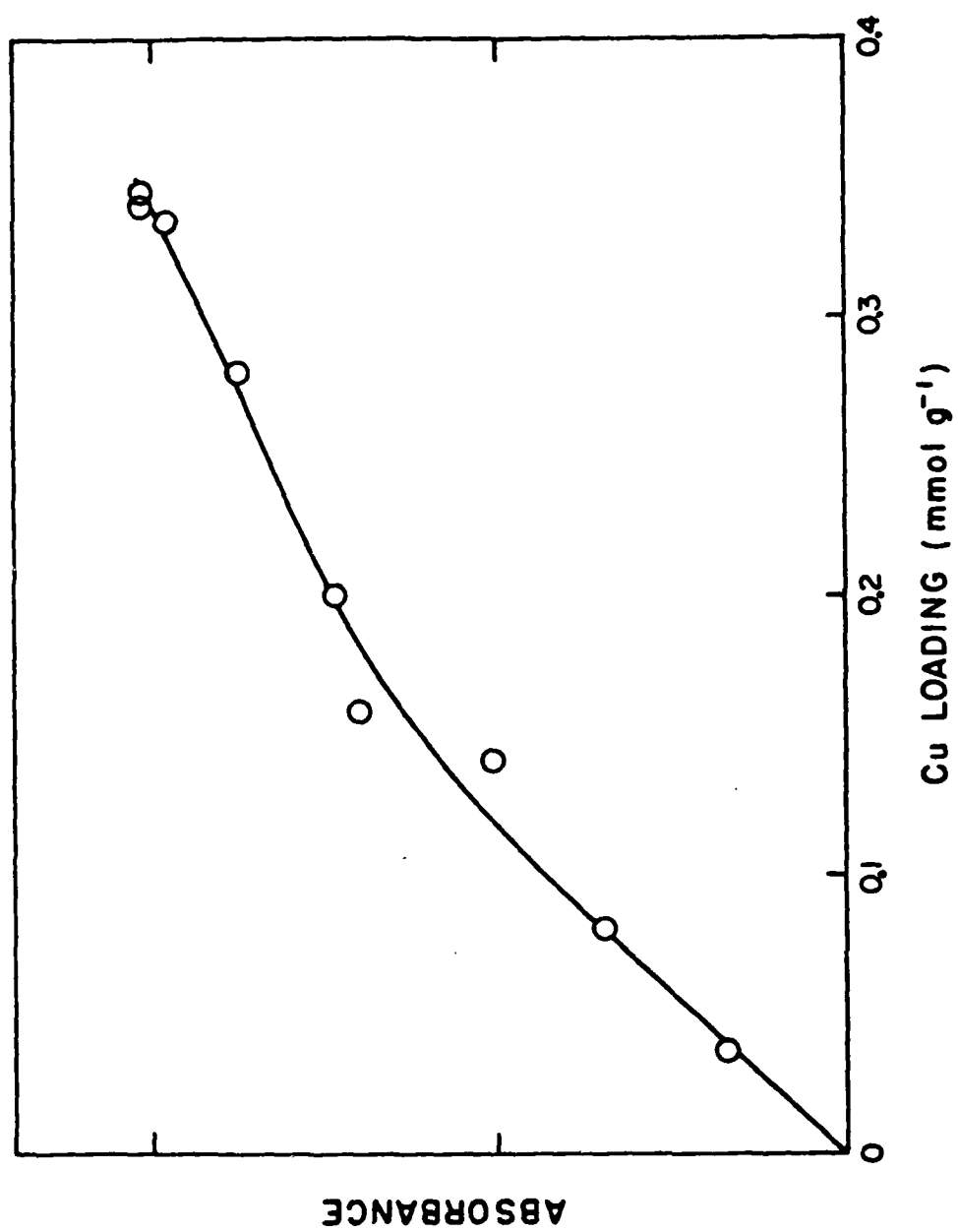
Figure 4. Scaled PAS absorption spectra for AEAPS-modified silica gel loaded with copper (II) at  $1 \times 10^{-3} \text{ mol L}^{-1}$  (A) and  $1 \times 10^{-1} \text{ mol L}^{-1}$  (B) initial copper (II) concentration in  $0.10 \text{ mol L}^{-1}$  acetate buffer. Spectrum of mono species (C) found by difference.



At least two mechanisms can contribute to the formation of mono complexes on the surface at high copper concentrations. First, an immobilized ligand not physically adjacent to another uncomplexed ligand could produce only a mono complex. Isolated ligands might be expected to be dominant for substrates with very low surface coverage as in the work of Pinnavaia et al.<sup>6</sup> Also, the microdistribution of ligands on the surface may limit the possibility of bis copper (II) complex formation. Consider, for example, a trimeric site on the surface. A tris copper (II) complex is unlikely, not only because of the small formation constant, but also because of the conformational constraints introduced by ligand bonding to the surface. So, once two ligands of the trimer are involved in a bis copper (II) complex, the third ligand can only bind in a mono complex. The second mechanism involves the bis copper (II) complex being forced to two mono complexes at high copper concentration by mass action analogous to the solution-phase equilibrium. The very high local "concentration" of surface-bonded ligand and the stability of the bis chelate must be overcome for this process to be important.

The photoacoustic data presented in Figure 5 argue against the second mechanism. The absorbance of the immobilized copper species at 535 nm is plotted versus the copper loading as measured by XRF. At 535 nm the absorptivity of the bis copper (II) complex is approximately ten times greater than the absorptivity of the mono copper (II) complex. If replacement of a bis copper complex by two mono complexes were the dominant factor, the slope of the line would turn negative during the

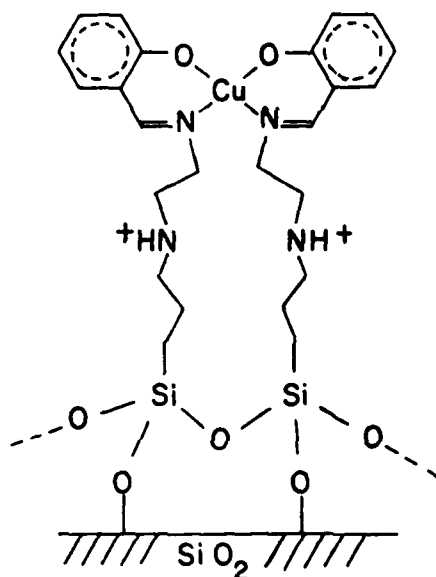
Figure 5. Absorbance of AEAPS-modified silica gel at 535 nm versus total copper loading as determined by XRF measurement.



formation of the mono complex. Instead, the slope becomes less positive as predicted by the hypothesis of independent mono and bis sites. The linearity of the photoacoustic absorbance versus copper loading was confirmed in the region of the isosbestic point ( $\sim 690$  nm). The correlation coefficient for the linear least-squares fit was 0.98.

The Schiff base derivative of the AEAPS-modified silica gel is expected to have the same surface distribution of immobilized silane as the original material since the synthesis procedure is not severe. This contention is supported by the fact that the dependence of copper loading on the initial copper (II) concentration in acetate-buffered solution for SAEAPS-modified silica gel is the same as for AEAPS-modified silica gel (Figure 3) except that the maximum copper loading is larger.<sup>7</sup> Again, the copper loading curve has the appearance of two consecutive sigmoidal waves. In an investigation of a similar system Shields and Boucher<sup>13</sup> found evidence for bis and mono copper (II) species for a salicylaldehyde-imine ligand immobilized on silica gel. It is concluded that in this case, as for AEAPS-modified silica gel, bis-copper (II)-SAEAPS species predominate at low copper (II) concentration. The photoacoustic spectrum of the immobilized copper (II)-SAEAPS formed at low copper (II) concentration shows a broad symmetrical absorption band centered at approximately 610 nm. This is in good agreement with the absorption maximum of 613 nm reported by Maki and McGarvy<sup>14</sup> for the  $d_{xy} \rightarrow d_{x^2-y^2}$  transition in copper (II) bis-salicylaldehyde-imine. The location of this maxima is characteristic of the average in-plane ligand field experienced by the copper (II) ion. The energy is greater the more oxygen ligands are replaced by nitrogen

ligands.<sup>15</sup> The dominant species which suggests itself is a bis chelate with two nitrogen donors and two oxygen donors,  $|N_2O_2|$ .



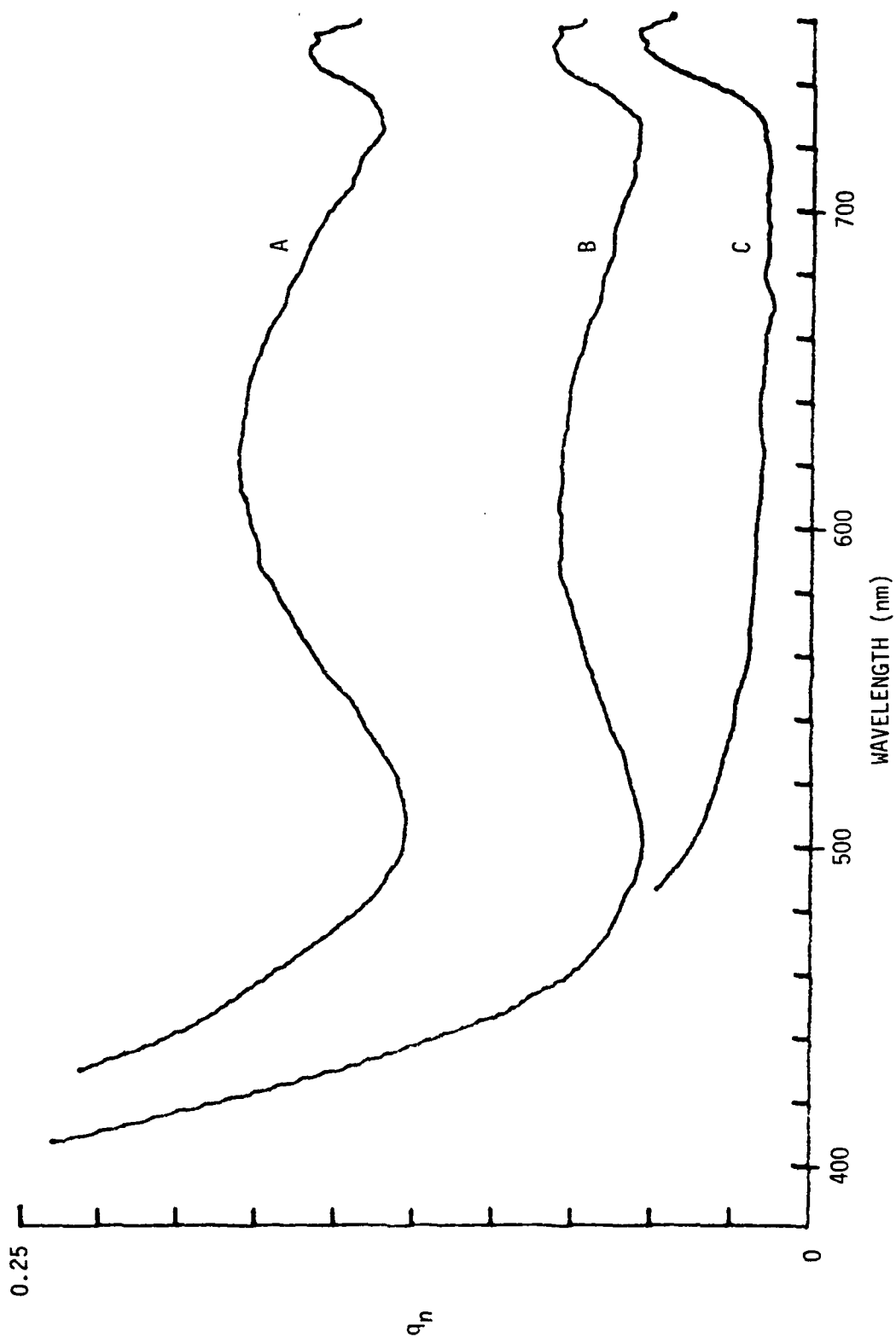
(3)

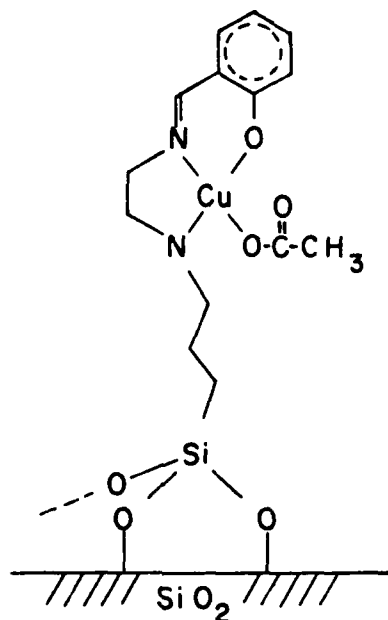
There is no evidence for a  $|N_4|$  chelate species ( $\sim 550$  nm), the formation of which is impeded by steric hindrance between salicylaldehyde groups.

The wavelength maximum of the visible absorption band for the immobilized copper (II)-SAEAPS chelates is essentially independent of copper loading. Photoacoustic spectra of copper (II)-SAEAPS chelates formed on the silica gel surface at low initial copper (II) concentration ( $1.0 \times 10^{-3}$  mol L<sup>-1</sup>) and high initial copper (II) concentration ( $1.0 \times 10^{-1}$  mol L<sup>-1</sup>) are shown in Figure 6. When the sloping background signal is taken into account the maxima are found to be within 10 nm of each other, the maximum at higher copper loading being shifted slightly to longer wavelength. The fact that the mono species also absorbs at the  $|N_2O_2|$  wavelength is not unexpected. The expected mono copper (II)-SAEAPS chelate is illustrated as follows.



Figure 6. Photoacoustic magnitude spectra for copper (II)-SAEAPS chelates on silica gel formed at  $1.0 \times 10^{-1} \text{ mol L}^{-1}$  copper (II) concentration (A), copper (II)-SAEAPS chelates on silica gel formed at  $1.0 \times 10^{-3} \text{ mol L}^{-1}$  copper (II) concentration (B) and unloaded SAEAPS-modified silica gel (C).





(4)

The fact that the sample absorptivity at 620 nm is linear with copper loading, as shown in Figure 7, indicates that the absorptivity of mono and bis species are the same. This also supports the proposed mono and bis structures. For such a chemical system photoacoustic spectroscopy can be used to determine the metal loading.

#### Binding Study Results

It is instructive to consider the type of binding curve expected for metal binding at a single type of site on the surface. The heterogeneous equilibrium can be described by the following equations:

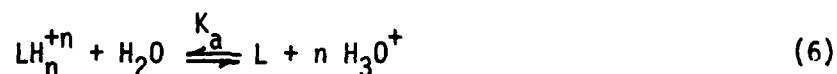
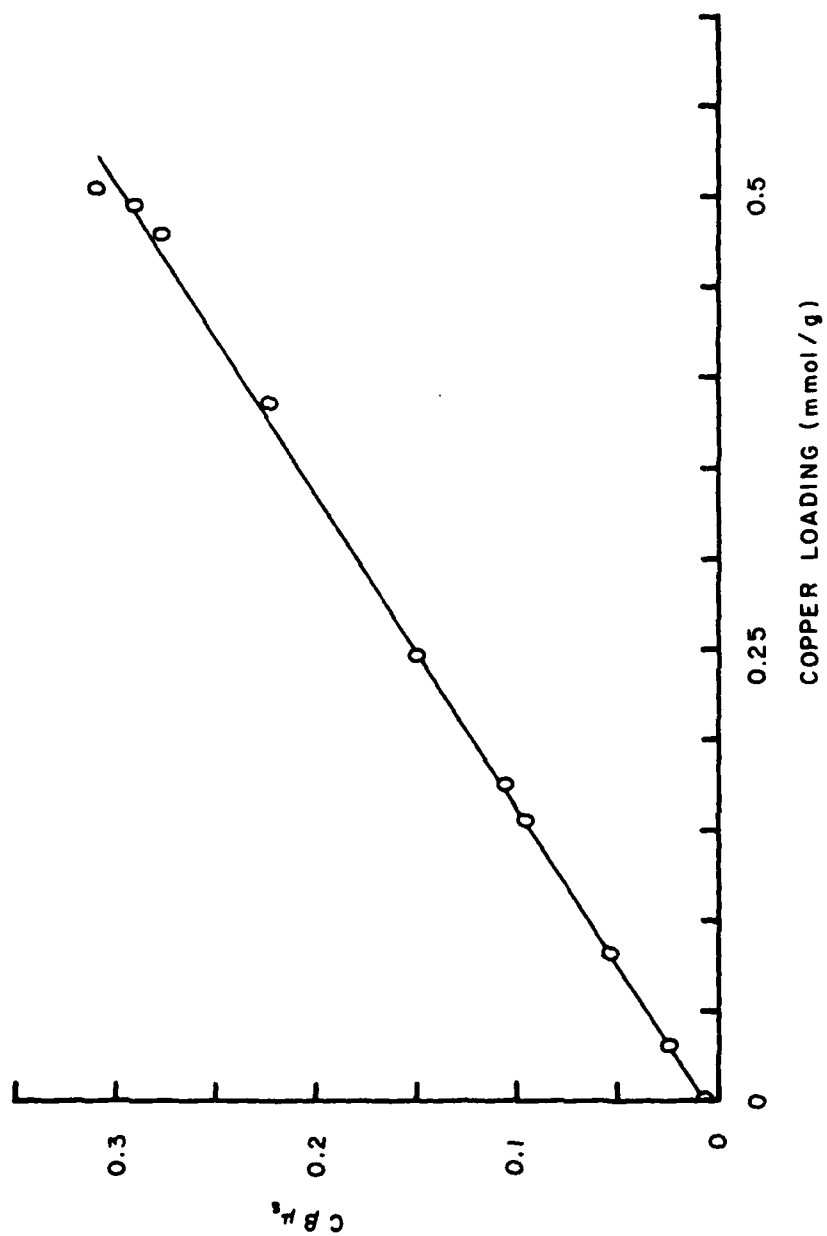


Figure 7. Corrected photoacoustic response function at 620 nm versus copper loading of SAEAPS-modified silica gel as determined by XRF. Statistics at 95 % confidence limit of the least-squares fit are:

Correlation Coefficient	0.9990
Standard Deviation	0.0053
Slope	$2.90 \pm 0.10$
Intercept	$0.0070 \pm 0.0035$
Measured Blank	0.0074



In these equations M is a metal cation, L is an available binding site on the surface, ML is an occupied binding site, and  $K_a$  is the acid dissociation constant for the protonated binding site. The equilibrium between the bound cation and the mobile cation at constant pH can be represented by an operational equilibrium constant:

$$K = \frac{K_L K_a}{[H_3O^+]^n} = \frac{(ML)}{[M] (LH_n^{+n})} \quad (7)$$

where  $(LH_n^{+n}) = \{C - (ML)\}$ . Here, (ML) and  $(LH_n^{+n})$  are measures of the quantity of occupied and unoccupied sites on the surface in units of millimoles per gram of substrate and C represents the maximum capacity of the chemically modified substrate in the same units. Equation 7 can be rearranged to give the linear equation:

$$\frac{1}{(ML)} = \frac{1}{K C} \frac{1}{[M]} + \frac{1}{C} \quad (8)$$

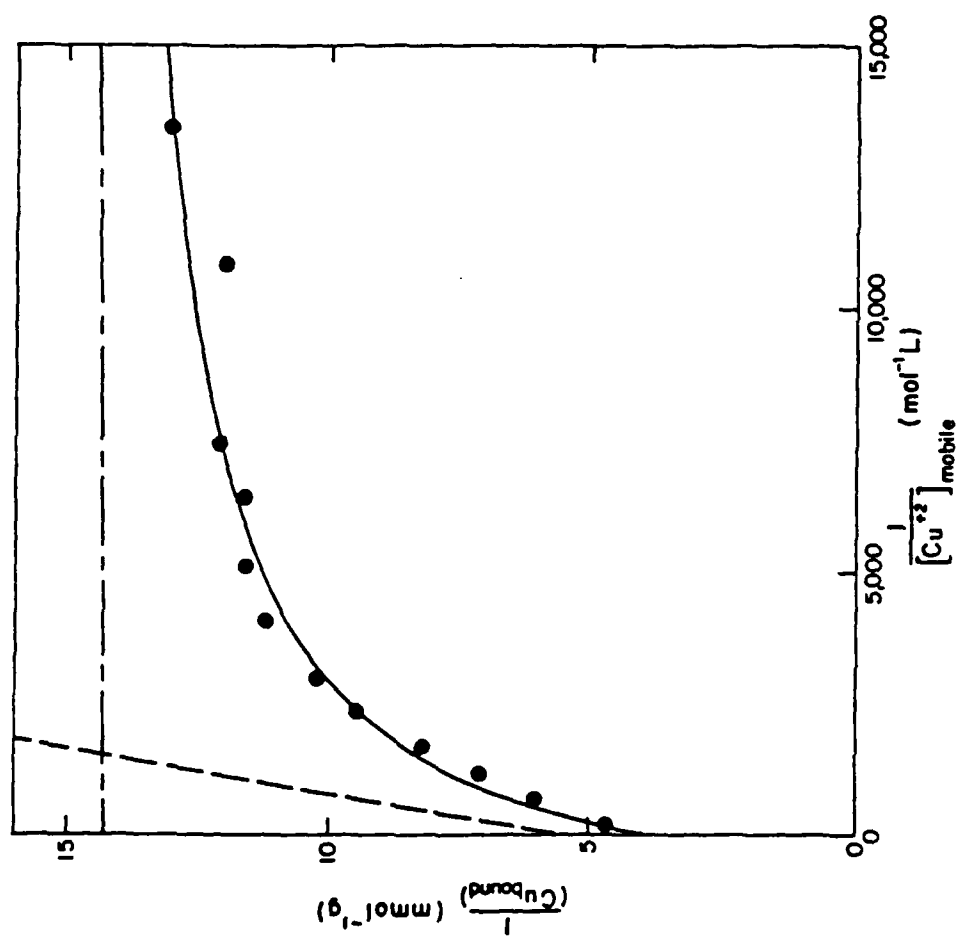
Thus, the reciprocal of the quantity of bound metal is a linear function of the reciprocal of the copper concentration with an intercept equal to the reciprocal of the maximum capacity. This type of analysis has been applied to the evaluation of equilibrium constants by affinity chromatography.<sup>16</sup>

The results of the binding studies were displayed as reciprocal concentration plots which invariably showed two linear regions in the limit of very low and very high copper (II) concentration. For example, the reciprocal concentration plot for the binding of copper (II) to

immobilized AEAPS in acetate buffer is shown in Figure 8. The precision of the data is limited not by the measurement technique error but by the lack of reproducibility of silane hydrolysis from the surface. The presence of the acetate buffer reduces the effective copper concentration causing the reciprocal concentration plots to be compressed while the extrapolated intercepts remain unchanged. The reciprocal concentration plot correlates well with the PAS result. The transition from regions of predominantly bis to predominantly mono binding occurs at the same solution concentration in both studies. The data from the binding study were iteratively fit to a model which assumes two independent types of sites each of which is characterized by an operational equilibrium constant as in Equation 8. This model generates the fit shown in Figure 8, substantiating the two-site model. The value of  $K$  and  $C$  for this system are  $5.8 \times 10^2 \text{ mol}^{-1} \text{ L}$  and  $0.18 \text{ mmol g}^{-1}$ , respectively, for mono binding and  $\approx 10^6 \text{ mol}^{-1} \text{ L}$  and  $0.07 \text{ mmol g}^{-1}$ , respectively for bis binding. The ratio of mono to bis sites on the surface is approximately 2.5 to 1. The agreement of this mono to bis ratio with that found by Pinnavaia et al. (2.3 to 1)<sup>6</sup> is remarkable considering the average surface coverage of silica gel in this study is more than an order of magnitude greater than the surface coverage in their work. This agreement may be explained by the stability of oligomeric silanes bound to the surface as suggested by the work of Waddell et al.<sup>17</sup> The nature of the surface template may promote condensation of especially stable oligomeric binding sites. Condensation of silane triols to oligomeric silanols in aqueous solution is known.<sup>18</sup>

Figure 8. Reciprocal of amount of bound copper versus reciprocal of solution-phase copper (II) concentration (●). Solid curve results from iterative fit of two-site model: bis binding (———) and mono binding (— — — ).





### Conclusions

Evidence for independent mono and bis binding sites for immobilized AEAPS on silica gel was obtained using photoacoustic spectroscopy and heterogeneous distribution measurements. In the concentration range studied, no evidence was found for conversion of bis sites to mono sites with increasing copper (II) concentration. Plots of reciprocal of the amount of immobilized metal versus reciprocal of the mobile metal concentration offer a convenient way of describing the heterogeneous metal distribution as a function of concentration of metal ion. They also provide a basis for comparison with the corresponding solution-phase equilibria. For the ethylenediamine analog immobilized on silica gel the heterogeneous distribution measurements were well fit by a model which assumes two independent types of binding sites.

The Schiff base formed by reacting salicylaldehyde with AEAPS-modified silica gel also binds copper (II) ions. The mono and bis copper (II)-SAEAPS chelates formed on the silica surface are not readily distinguished by photoacoustic spectroscopy because the average ligand field experienced by the copper (II) ion is similar in both mono and bis chelates.

### References

1. D. E. Leyden and W. Collins (eds.), "Silylated Surfaces," Midland Macromolecular Monographs, vol. 7, Gordon and Breach, New York, 1980.
2. D. E. Leyden and G. H. Luttrell, Anal. Chem. **47**, 1612 (1975).
3. D. E. Leyden, G. H. Luttrell, W. K. Nonidez and D. B. Werho, Anal. Chem. **48**, 67 (1976).
4. D. E. Leyden, M. Steel, B. B. Jablonski and R. Somoano, Anal. Chim. Acta **100**, 545 (1978).
5. R. J. Kvitek, P. W. Carr and J. F. Evans, Anal. Chim. Acta **124**, 229 (1981).
6. T. J. Pinnavaia, J. G. Lee and M. Abedeni, in D. E. Leyden and W. Collins (eds.), "Silylated Surfaces," Gordon and Breach, New York, 1980, p. 333.
7. F. -J. Pern, Masters Thesis, University of Denver, 1980.
8. D. F. Untereker, J. C. Lennon, L. M. Wier, P. R. Moses and R. W. Murray, J. Electroanal. Chem. **81**, 309 (1977).
9. T. G. Waddell, D. E. Leyden and D. M. Hercules, in D. E. Leyden and W. Collins (eds.), "Silylated Surfaces," Gordon and Breach, New York, 1980, pp. 55-57.
10. L. W. Burggraf and D. E. Leyden, Anal. Chem. **53**, 759 (1981).
11. M. T. Beck, "Chemistry of Complex Equilibria," Van Nostrand Reinhold, New York, 1970, p. 260.
12. C. K. Jorgensen, "Inorganic Complexes," Academic Press, New York, 1963, pp. 65-66.
13. G. D. Shields and L. J. Boucher, J. Inorg. Nucl. Chem. **40**, 1341 (1977).
14. A. H. Maki and B. R. McGarvey, J. Chem. Phys. **29**, 35 (1958).
15. V. C. Swett and E. P. Dudek, J. Phys. Chem. **72**, 1244 (1968).
16. L. W. Nichol, A. G. Ogston, D. J. Winzor and W. H. Sawyer, Biochem. J. **143**, 435 (1974).

17. T. G. Waddell, D. E. Leyden and M. DeBello, J. Am. Chem. Soc. 103 (1981) to be published.
18. E. P. Plueddemann, in D. E. Leyden and W. Collins (eds.), "Silylated Surfaces," Gordon and Breach, New York, 1980, pp. 37-38.

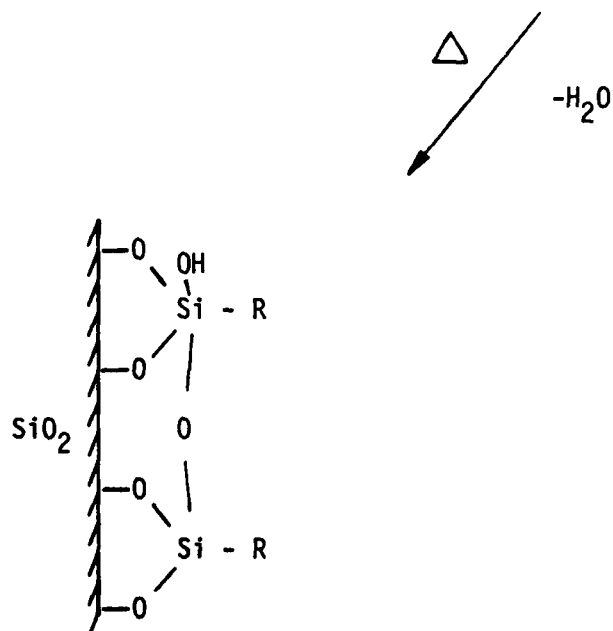
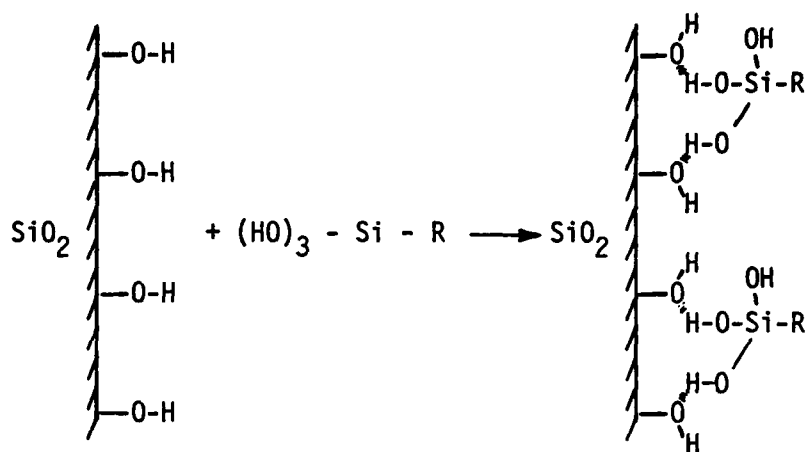
## Chapter 5

### ULTRAVIOLET PHOTOACOUSTIC SPECTROSCOPY OF IMMOBILIZED ORGANIC FUNCTIONAL GROUPS ON SILICA SURFACES

#### Introduction

Applications of surfaces which are chemically modified by silylation are limited only by the imagination of the user and by the availability of the desired organosilanes. Alkoxysilanes and chlorosilanes are commonly used for chemical modification of oxide surfaces. A scheme which describes this process is shown in Figure 1. Practical limitations are imposed on organosilane availability by the labile nature of these materials toward hydrolysis and condensation and by commercial considerations.<sup>1</sup> Thus, it may be necessary to transform the organo-functional group of a readily available organosilane into the desired derivative once the organosilane has been immobilized. Evidence for the success of such a procedure in producing the desired product may be obtained from various chemical and spectroscopic methods. Some novel spectroscopic tools which have been applied to the study of chemically modified surfaces are solid-state nuclear magnetic resonance spectroscopy,<sup>[2,3]</sup> Fourier transform infrared spectroscopy (FTIR)<sup>4</sup> and infrared photoacoustic spectroscopy.<sup>5</sup> This study was performed to determine if ultraviolet photoacoustic spectroscopy might yield useful qualitative information about the structures of organo-functional

Figure 1. Silylation scheme.



$\text{X} = \text{OCH}_3, \text{OCH}_2\text{CH}_3, \text{Cl}$

derivatives immobilized on silica surfaces. No single spectroscopic tool, least of all ultraviolet absorption spectroscopy, can be expected to provide complete structural information for organic materials; rather, a combination of chemical and spectroscopic tools are required. However, this study concentrates on the type of information which ultraviolet photoacoustic spectroscopy may provide.

The capability for making ultraviolet PAS measurements was demonstrated for many different functional groups immobilized on silica gel, fumed silica and controlled pore glass. Table 1 lists several of these. Selected ultraviolet photoacoustic spectra of immobilized functional groups are appended to the end of this chapter. The choice of immobilized organo-functional derivatives for study reflects a bias toward immobilized chelating ligands for metal ion extraction. This chapter presents two short illustrative applications of photoacoustic spectroscopy to the study of immobilized chelating ligands. The applications deal with (1) dithiocarbamate derivatives of immobilized organoamines and (2) an acetylacetone derivative of immobilized benzyl chloride.

### Experimental

This work was done in collaboration with Dr. D. S. Kendall and Mr. Fu-Jann Pern.<sup>6</sup>

### Measurements

Qualitative photoacoustic magnitude spectra were recorded for chemically modified fumed silica and controlled pore glass without



Table 1  
Chelating agents immobilized  
on silica surfaces

Acronym	Proposed Structure	Substrate <sup>a</sup>	Preparation Reference	Preparer <sup>b</sup>	U.V. PAS Spectrum
APS		SG	6	P	—
AEAPS		SG, FS	6	P	Fig. A-1
DTC-APS		FS, CPG	7	P, B	Fig. 2
DTC-AEAPS		FS, CPG	7	P, B	Fig. 2 and Fig. A-2
BCTC-AEAPS		FS, CPG	7	P, B	Fig. 2 and Fig. A-2
DK-APS		SG, FS	6, 8	P	Fig. A-3
DK-AEAPS		SG, FS	6, 8	P	Fig. A-3
AA-AEAPS		SG	9	W	Fig. A-4
HFA-AEAPS		SG	9	W	Fig. A-4
S-AEAPS		SG	6, 9	P	Cha. 3 Fig. 21
BZ		SG	6, 9	P	—
AA-BZ		SG	6, 9	P	Fig. 4

<sup>a</sup> SG = silica gel, FS = fumed silica (cab-o-sil), CPG = controlled pore glass.

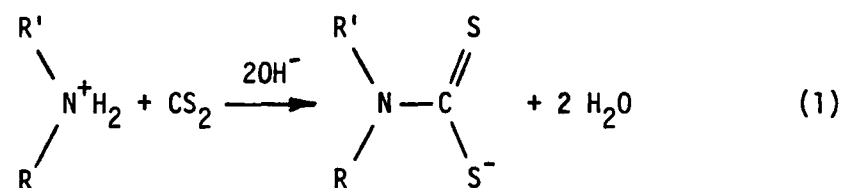
<sup>b</sup> W = T. G. Weddell, P = F. -J. Pern, B = N. Bodnar

special preparation other than drying (80°C). Samples of chemically modified silica gel were ground for one minute in a miniature stainless steel ball mill. Techniques for recording photoacoustic spectra are detailed in Chapter 3. Spectra were corrected for the effects of stray light. Solution-phase ultraviolet absorption spectra were recorded on a Cary 219 double-beam spectrophotometer relative to the pure solvent using 1.0 cm quartz cells. Infrared measurements were made on a Nicolet MX-1 Fourier transform infrared spectrometer.

### Synthesis

Silylation procedures were the same as those described in Chapter 4.

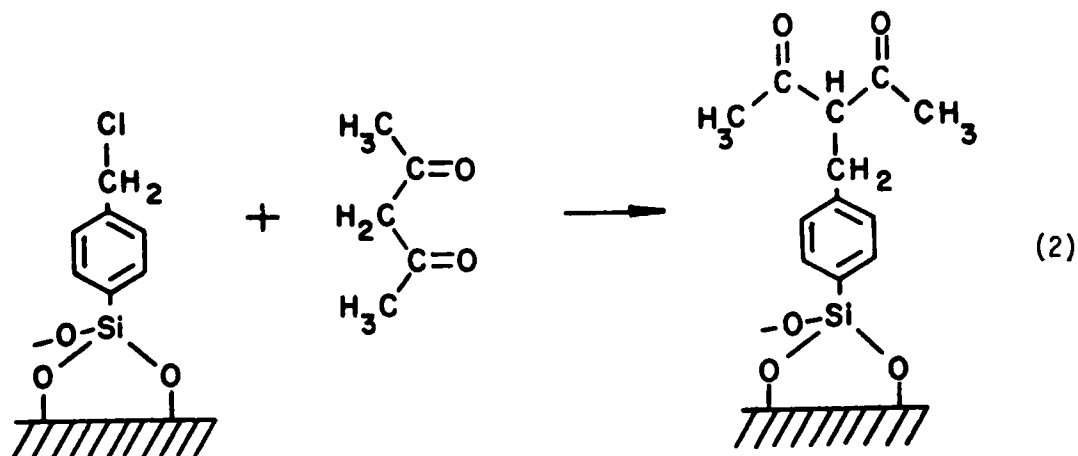
Dithiocarbamate Derivatives. Luttrell<sup>7</sup> has described procedures for synthesis of dithiocarbamate derivatives of immobilized organoamines by reaction with carbon disulfide.



Two procedures were used, one of which produced the mono-dithiocarbamate derivative of immobilized N-(2-aminoethyl)-3-aminopropyltrimethoxysilane (AEAPS) and the second of which produced the bis-dithiocarbamate derivative of immobilized AEAPS. The mono-dithiocarbamate derivative of immobilized AEAPS was prepared from a stirred mixture containing 100 mL of benzene, 20 mL of 2-propanol, 20 mL of carbon disulfide and

5 mL of a 10 percent methanolic solution of tetramethylammonium hydroxide. The reaction time was 15 minutes. The silica material was separated by filtration and washed thoroughly with 2-propanol and water. The bis-dithiocarbamate derivative of immobilized AEAPS was prepared by stirring immobilized AEAPS in a mixture containing 100 mL of water, 25 mL of 2-propanol, 25 mL of  $0.25 \text{ mol L}^{-1}$  NaOH and 20 mL of carbon disulfide. The reaction time was 15 minutes. The silica material was separated by filtration and washed thoroughly with 2-propanol and water. Samples of immobilized N-aminopropyltrimethoxysilane (APS) were also derived by each of these procedures.

Immobilized Benzylacetylacetone Derivative. Waddell et al.<sup>9</sup> offered a procedure for reacting the immobilized benzyl chloride functional group (BZ) with acetylacetone in an alkylation reaction.



The predicted product (AA-BZ) is shown in Equation 2. The synthesis method has been described by Waddell<sup>9</sup> and Pern.<sup>6</sup> Approximately 15 grams of silylated silica gel were added to a flask containing 225 mL of

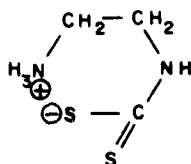
acetone, 5.0 mL acetylacetone and 7.6 grams of dry  $K_2CO_3$ . This mixture was refluxed for 23 hours with stirring using  $CaCl_2$  to maintain a dry atmosphere. The derived substrate was separated by filtration and washed thoroughly with dilute aqueous  $HNO_3$ , water and methanol.

Benzylacetylacetone Model Compounds. To substantiate the structure of the immobilized AA-BZ derivative, model compounds were made using a synthesis analogous to the above procedure. The following materials were combined in a flask: 100 mL of acetone, 11.2 mL of benzylchloride, 10.0 mL of acetylacetone and 6.7 grams of dry  $K_2CO_3$ . The mixture was refluxed for 23 hours with stirring using  $CaCl_2$  to maintain a dry atmosphere. The filtrate was vacuum-distilled. The major product, a yellow liquid ( $\sim 30\%$  yield), was collected at  $145^\circ C - 150^\circ C$ , 2 torr. The vacuum distillation of this product was repeated for purification. The distillate collected at  $175^\circ C - 180^\circ C$  produced a crystalline product ( $\sim 3\%$  yield) upon standing for several days. White crystals were obtained upon recrystallization from a water/ethanol solution. The results of this procedure were similar to those described by Morgan and Taylor.<sup>10</sup> IR and NMR were used to confirm that the major product was 3-benzylacetylacetone (3-phenylmethyl-2,4-pentanedione.) For comparison with the immobilized AA-BZ, portions of purified major and minor products were dissolved in ethanol and adsorbed on samples of powdered silica gel. These samples were dried at  $80^\circ C$ .

## Results and Discussion

### Dithiocarbamate Derivatives of Immobilized Amines

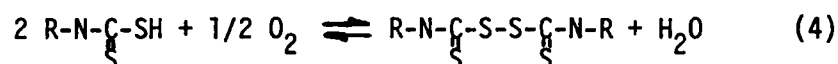
Luttrell<sup>7</sup> suggested that the formation of dithiocarbamates of primary amines occurred under mild reaction conditions and that formation of dithiocarbamates of both primary and secondary amines occurred under more severe reaction conditions. While Luttrell's evidence is convincing for mono- and bis-dithiocarbamates of AEAPS being formed with the two reaction procedures that he describes,<sup>7</sup> the rationale that he offers is at odds with the results of Miller and Latimer.<sup>11</sup> They found that the rate constants for formation of dithiocarbamates from dialkylamines were greater than or equal to those for formation of dithiocarbamates from monoalkylamines. A more likely reason for formation of a mono-dithiocarbamate derivative in benzene is because of a solvent effect. From a study of the decomposition of ethylene bisdithiocarbamate, Miller and Latimer found evidence for formation of a very stable cyclic inner salt for the 2-aminoethyldithiocarbamate compound.<sup>11</sup>



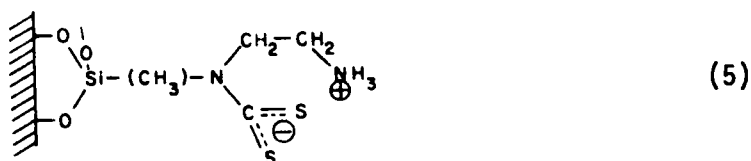
(3)

The protonated amino group exerts an inductive electron shift on the C = S bond causing the C - N bond to be weakened. This cyclic salt is stabilized in a nonpolar solvent. In a polar solvent it is destabilized permitting electrophilic attack on the deprotonated nitrogen.

The ultraviolet spectra of dithiocarbamates exhibit a peak due to  $\text{-N-C-S-}$  and a peak at shorter wavelength due to  $\text{-C-S-}$  at  $\sim 280$  nm and  $\sim 250$  nm for the n-methyldithiocarbamate ion. The protonated form also shows two peaks, both shifted to shorter wavelengths ( $\sim 265$  nm and  $\sim 235$  nm). In the presence of oxygen the spectrum of the acid form slowly changes to one having a peak at  $\sim 240$  nm and a shoulder at  $\sim 275$  nm, which reverts to that of the ion form on neutralization.<sup>11</sup> This is likely due to the reversible dimerization in Equation 4.<sup>12</sup>



The ultraviolet photoacoustic spectra for dithiocarbamate derivatives of immobilized AEAPS using the mono and bis synthesis procedures are shown in Figure 2. Spectral features of the mono preparation are nearly identical to those of a solution-phase analog, 1-piperazinecarbodithioic ion (269 nm shoulder, 283 nm and 350 nm).<sup>13</sup> The broad spectral feature at long wavelength is probably a charge transfer band. Based on the work of Miller and Latimer, the spectrum of the immobilized mono preparation is attributed to a cyclic inner salt.



In comparison, the spectrum of the immobilized bis preparation is shifted to shorter wavelength, the charge transfer band disappears and the absorptivity of the band at  $\sim 280$  nm is diminished. This is consistent with formation of a disulfide bond.

Figure 2. Ultraviolet photoacoustic magnitude spectra of dithiocarbamate derivatives of AEAPS immobilized on fumed silica using mono (A) and bis (B) synthesis procedures and dithiocarbamate derivatives of APS immobilized on fumed silica using mono (C) and bis (D) synthesis procedures.

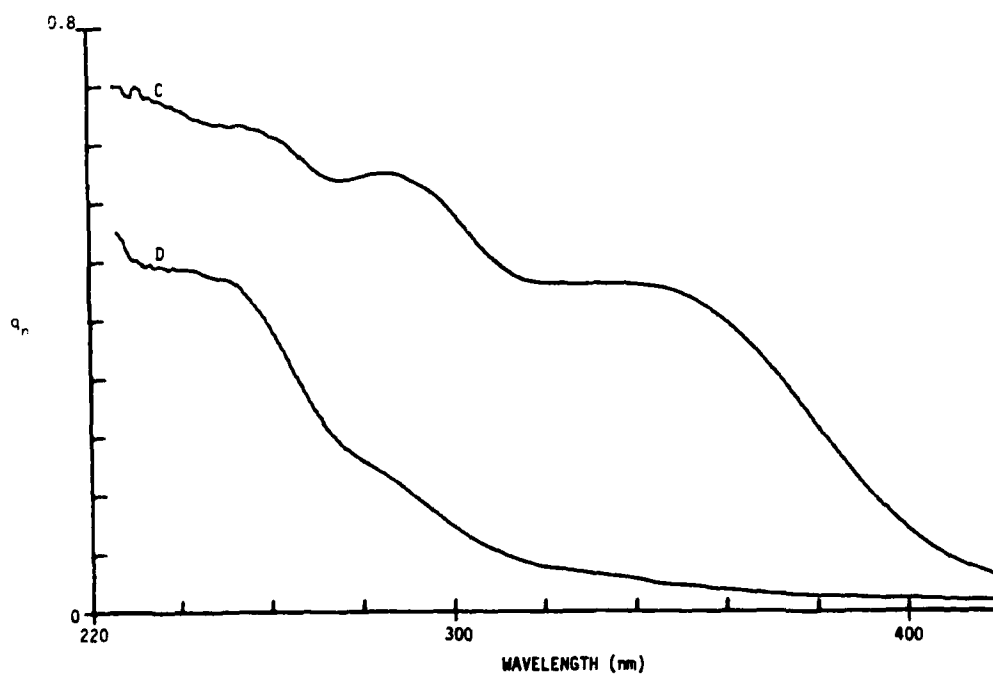
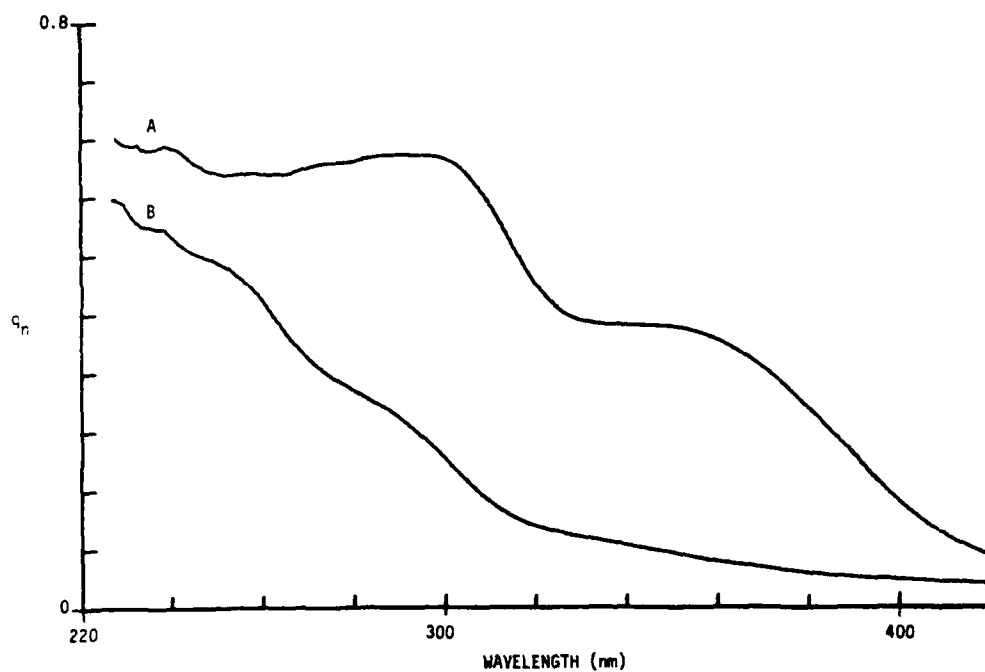
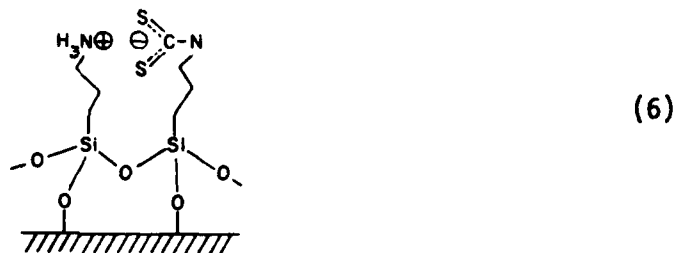




Figure 2 shows the ultraviolet photoacoustic spectra for dithiocarbamate derivatives of immobilized APS using the mono and bis synthesis procedures. The product of the mono procedure shows a spectrum similar to that of the AEAPS mono-dithiocarbamate material. The photoacoustic spectrum of the mono preparation exhibits spectral features nearly identical to those of a solution-phase analog, 1-piperidinecarbodithioic ion (261 nm, 280 nm and 346 nm).<sup>13</sup> This spectrum is assigned to an intermolecular salt formed between adjacent immobilized APS molecules. In this case also, the quarternary ammonium ion would be stabilized relative to electrophilic attack on the deprotonated nitrogen. The spectrum of the bis preparation using immobilized APS is similar to that for the bis preparation using immobilized AEAPS.



For this system, ultraviolet photoacoustic spectroscopy has the potential for providing useful structural information. Additionally, PAS could be used to monitor the rate of decomposition of immobilized dithiocarbamate derivatives.

#### Immobilized 3-Benzylacetylacetone Derivative

Waddell et al.<sup>9</sup> presented evidence for formation of an immobilized 3-benzylacetylacetone analog (Equation 2). An equivalent model reaction was conducted for comparison to confirm this structure. The major

product of the model reaction was identified as 3-benzylacetylacetone (BZAC). The minor crystalline product was identified as the disubstituted alkylation product, 3,3-dibenzylacetylacetone. The ultraviolet spectra of these materials, shown in Figure 3, agree with these assignments. The spectrum of 3-benzylacetylacetone has a maximum at 287 nm in cyclohexane ( $\epsilon \approx 2100 \text{ L mol}^{-1} \text{ cm}^{-1}$ ) which shows a small bathochromic (red) shift in ethanol ( $\lambda_{\text{max}} = 290 \text{ nm}$ ). This is characteristic of the  $\pi \rightarrow \pi^*$  band of the enol form. In dilute nonpolar solution this compound exists predominantly in the enol form (68% enol).<sup>14</sup> The keto band occurs at approximately the same wavelength with an absorptivity an order of magnitude less.<sup>15</sup> The 3,3-dibenzylacetylacetone product is incapable of enolization. The keto band ( $n \rightarrow \pi^*$ ) at 296 nm ( $\epsilon \approx 130 \text{ L mol}^{-1} \text{ cm}^{-1}$ ) in cyclohexane shows a characteristic hypsochromic shift to 293 nm in ethanol.

The formation of the disubstituted product on the surface is much less likely than for the reaction in solution because of steric constraints imposed by bonding the benzyl chloride group to the surface. Thus, only the monosubstituted product is expected. The infrared spectra of the immobilized AA-BZ and BZAC adsorbed on silica gel are similar in the carbonyl region supporting this conclusion. The infrared spectrum shows that the keto form is dominant on the surface; little enol is present. Thus, the expected ultraviolet spectrum is that of keto and enol forms ( $\lambda_{\text{max}} \approx 290 \text{ nm}$ ). However, the photoacoustic spectra of the immobilized AA-BZ and BZAC adsorbed on the silica gel (Figure 4) show a large absorbance which masks the small keto/enol band.

Figure 3. Ultraviolet spectra of (I) 3-benzylacetylacelone in cyclohexane ( $0.038 \text{ mg mL}^{-1}$  (A) and  $0.0076 \text{ mg mL}^{-1}$  (B)) and (II) 3,3-dibenzylacetylacetone in cyclohexane ( $0.29 \text{ mg mL}^{-1}$ ).

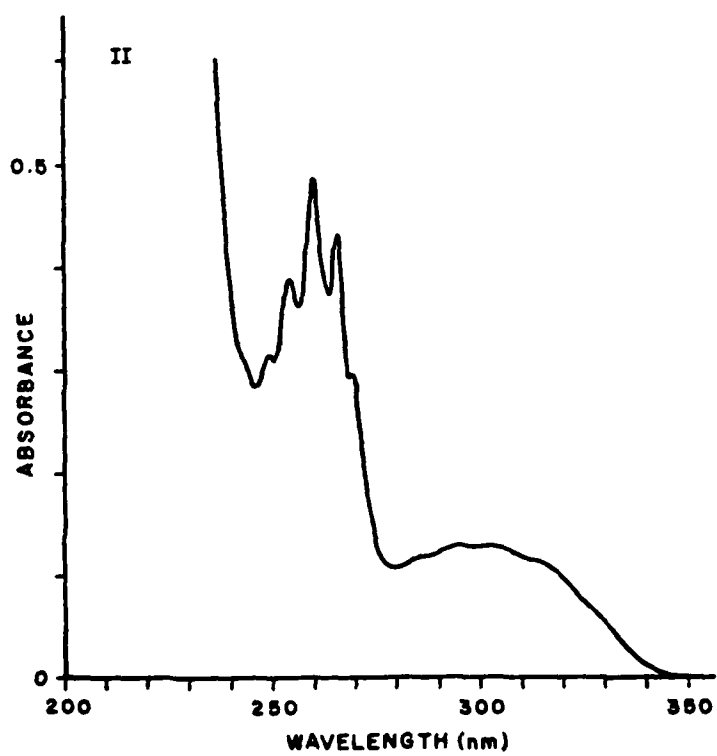
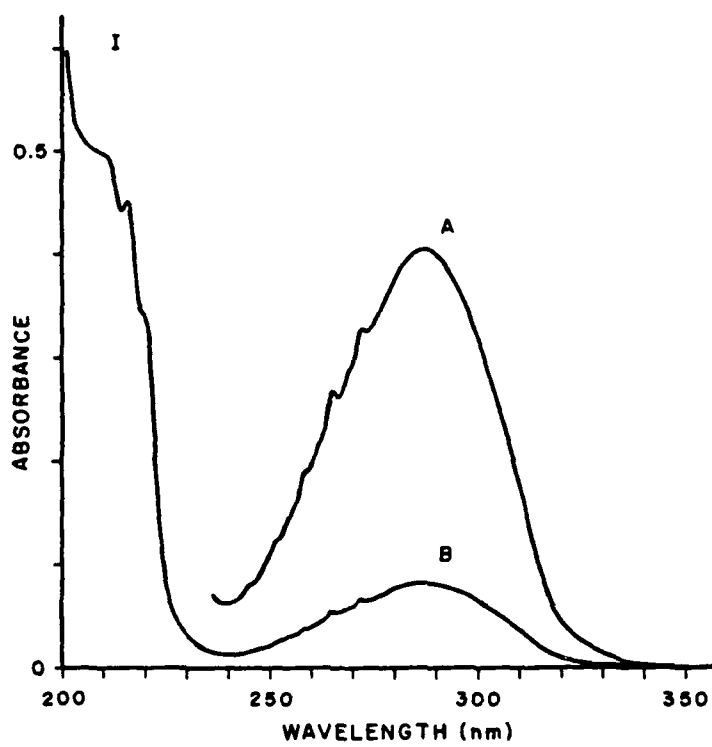
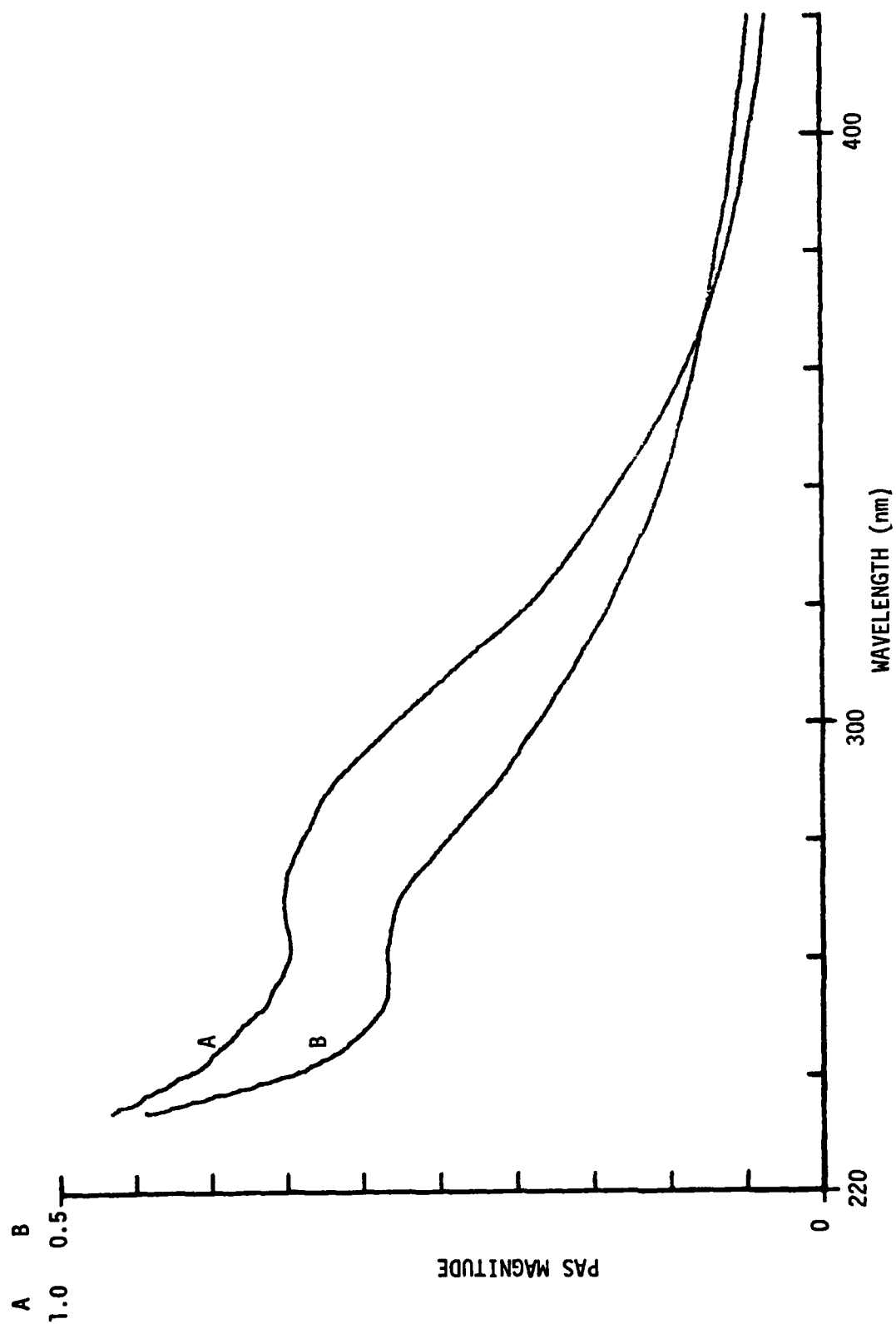


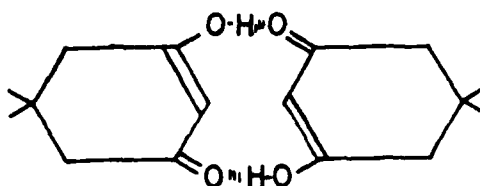
Figure 4. Ultraviolet photoacoustic magnitude spectra of 3-benzylacetylacetone analog immobilized on silica gel (A) and 3-benzylacetylacetone adsorbed on silica gel (B).



The absorption maximum for immobilized AA-BZ and adsorbed BZAC are at 270 nm and 265 nm, respectively. The fact that these spectra are so similar also supports the proposed structure. The new absorption is apparently a result of interaction of the acetylacetone functional group with the surface of the silica gel.

Based on the photoacoustic spectrum, a strongly hydrogen-bonded enol surface species is postulated for which intramolecular hydrogen bonding is destroyed. If the near-planar enol structure were destroyed due to interaction with the surface, the  $\pi \rightarrow \pi^*$  transition would be expected to shift to higher energy as is observed. In such a system a case can be made for a 20 nm shift of the  $\pi \rightarrow \pi^*$  transition toward shorter wavelength. For example, the  $\pi \rightarrow \pi^*$  band for the enol form of 2,4-pentanedione, which is intramolecularly hydrogen-bonded, is centered at 273 nm. For 1,3-cyclohexanedione, which exists in an s-trans configuration that is incapable of intramolecular hydrogen-bonding, the  $\pi \rightarrow \pi^*$  transition is centered at 253 nm.<sup>16</sup> Thus, if such a trans configuration were to exist for BZAC on the surface, the  $\pi \rightarrow \pi^*$  transition would be expected at  $\sim 270$  nm. This is in good agreement with the experimental absorption maxima.

Confirmation for this postulate was sought from infrared spectroscopy. An analogous solution phase system has been studied by Bellamy, Beecher and others. (See reference 17.) Formation of the intermolecularly hydrogen-bonded enol form of 5,5-dimethylcyclohexane-1,3-dione is inhibited. In solution, dimers are formed with structures analogous to the postulated structure, namely:



(7)

The infrared spectrum of concentrated 5,5-dimethylcyclohexane-1,3-dione shows a normal carbonyl absorption at  $1700\text{ cm}^{-1}$  and a conjugated chelate band at  $1605\text{ cm}^{-1}$  produced by strong hydrogen bonding in the dimer. The FTIR spectrum of the immobilized BZ-AA showed a normal ketone carbonyl absorption at  $1700\text{ cm}^{-1}$  and a small absorption at  $1606\text{ cm}^{-1}$ , lending support for the postulated surface species.

#### Conclusion

Ultraviolet photoacoustic spectroscopy has been demonstrated to be a useful tool, in conjunction with other tools, for studying immobilized functional groups and their derivatives.



References

1. E. P. Plueddemann, in D. E. Leyden and W. Collins (eds.) "Silylated Surfaces," Gordon and Breach, New York, 1980, pp. 31-53.
2. D. E. Leyden, D. S. Kendall and T. G. Waddell, Anal. Chim. Acta. **126**, 207 (1981).
3. D. W. Sindorf and G. E. Maciel, to be published.
4. H. Chiang, H. Ishida and J. L. Koenig, J. Colloid Interface Sci. **75**, 396 (1980).
5. M. J. D. Low and G. A. Parodi, Spectrosc. Lett. **11**, 581 (1978).
6. F. -J. Pern, Masters Thesis, University of Denver, 1980.
7. G. H. Luttrell, Doctoral Dissertation, University of Georgia, 1975; D. E. Leyden and G. H. Luttrell, Anal. Chem. **47**, 1612 (1975).
8. T. Seshadri and A. Kettrup, Fresenius Z. Anal. Chem. **296**, 247 (1979).
9. T. G. Waddell, D. E. Leyden and D. M. Hercules, in D. E. Leyden and W. Collins (eds.) "Silylated Surfaces," 1980, pp. 55-72.
10. G. T. Morgan and C. J. A. Taylor, J. Chem. Soc. **127**, 797 (1925).
11. D. M. Miller and R. A. Latimer, Canad. J. Chem. **40**, 246 (1962).
12. J. March, "Advanced Organic Chemistry: Reactions Mechanisms, and Structure," McGraw-Hill, New York, 1968, pp. 888-889, 903.
13. J. P. Phillips, D. Bates, H. Fever and B. S. Thyagarajan (eds.), "Organic Electronic Spectral Data," vol. XV, John Wiley and Sons, New York, 1973, pp. 2, 29, 52.
14. A. G. Gordon and R. A. Ford, "The Chemist's Companion," John Wiley and Sons, New York, 1972, p. 50.
15. C. N. R. Rao, "Ultra-violet and Visible Spectroscopy," 3rd ed., Butterworths, London, 1975, pp. 102-103.
16. R. M. Silverstein and G. C. Bassler, "Spectrometric Identification of Organic Compounds," 2nd ed., John Wiley and Sons, New York, 1967, pp. 159-160.
17. L. J. Bellamy, "Infra-red Spectra of Complex Molecules," 3rd ed., Chapman and Hall, London, 1975, p. 161.

Appendix

Figure A-1. Ultraviolet photoacoustic spectrum of AEAPS immobilized on silica gel.

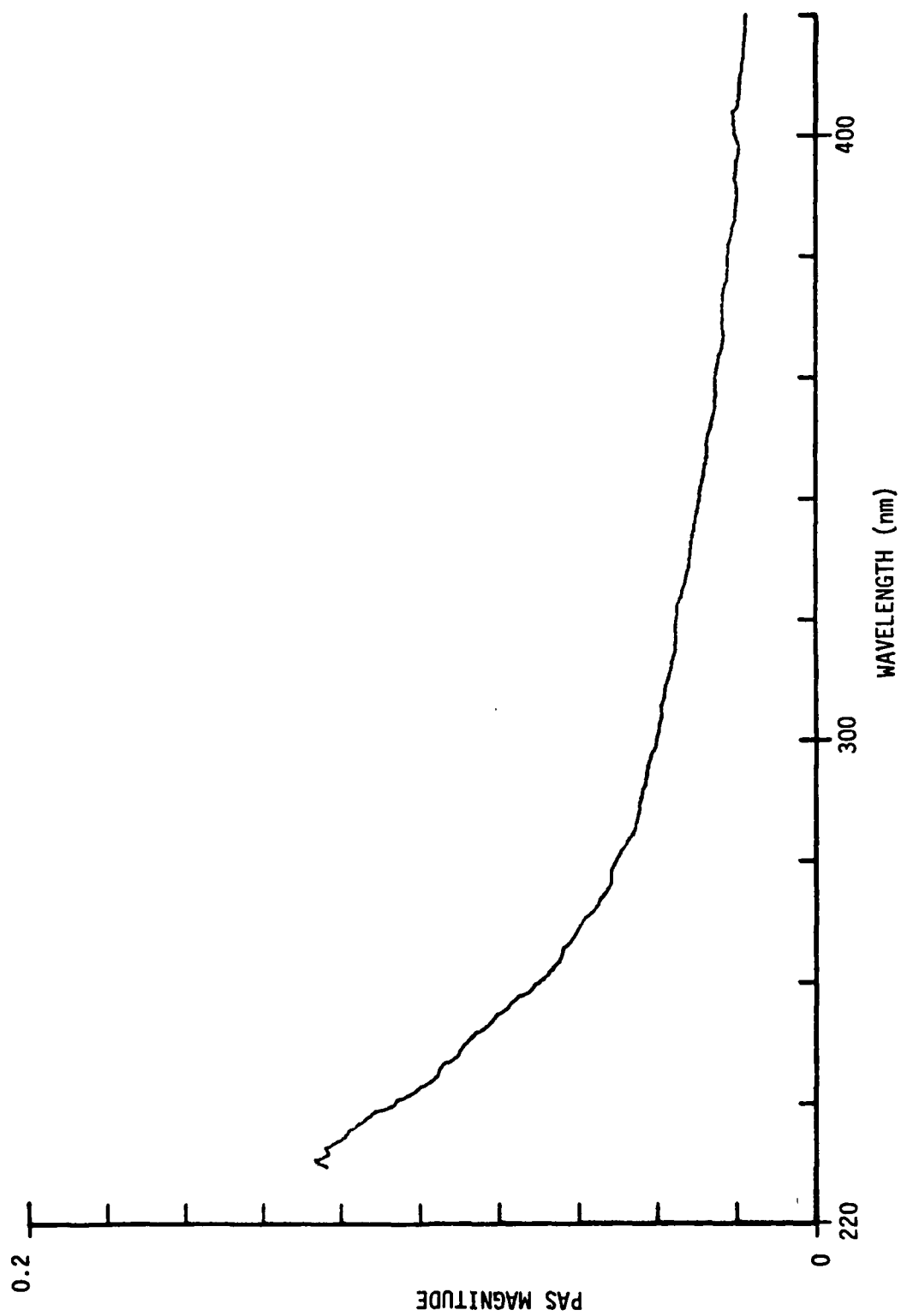


Figure A-2. Ultraviolet photoacoustic spectra of DTC-AEAPS immobilized on controlled pore glass.

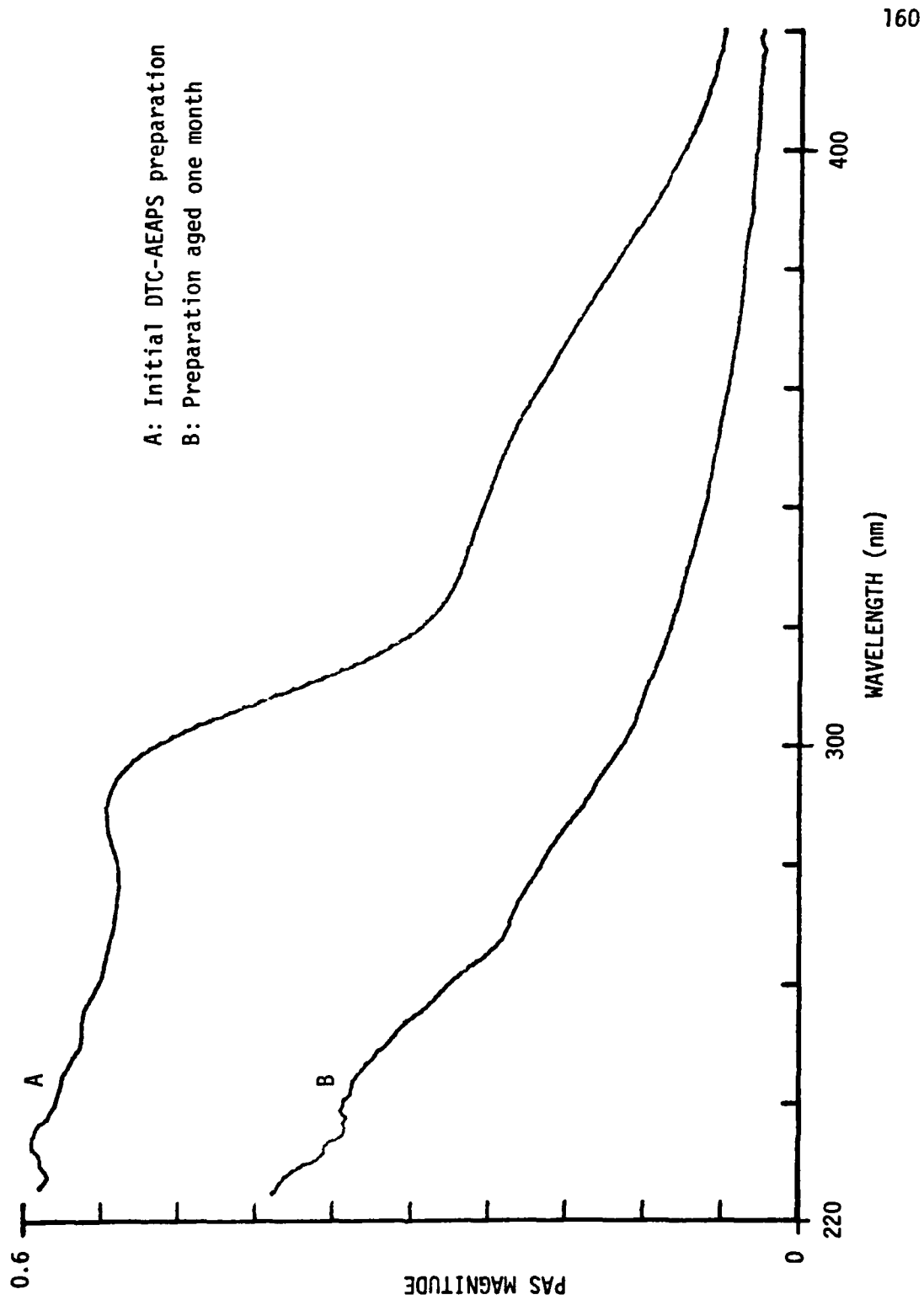


Figure A-3. Ultraviolet photoacoustic spectra of DK-APS (A) and DK-AEAPS (B) immobilized on fumed silica.

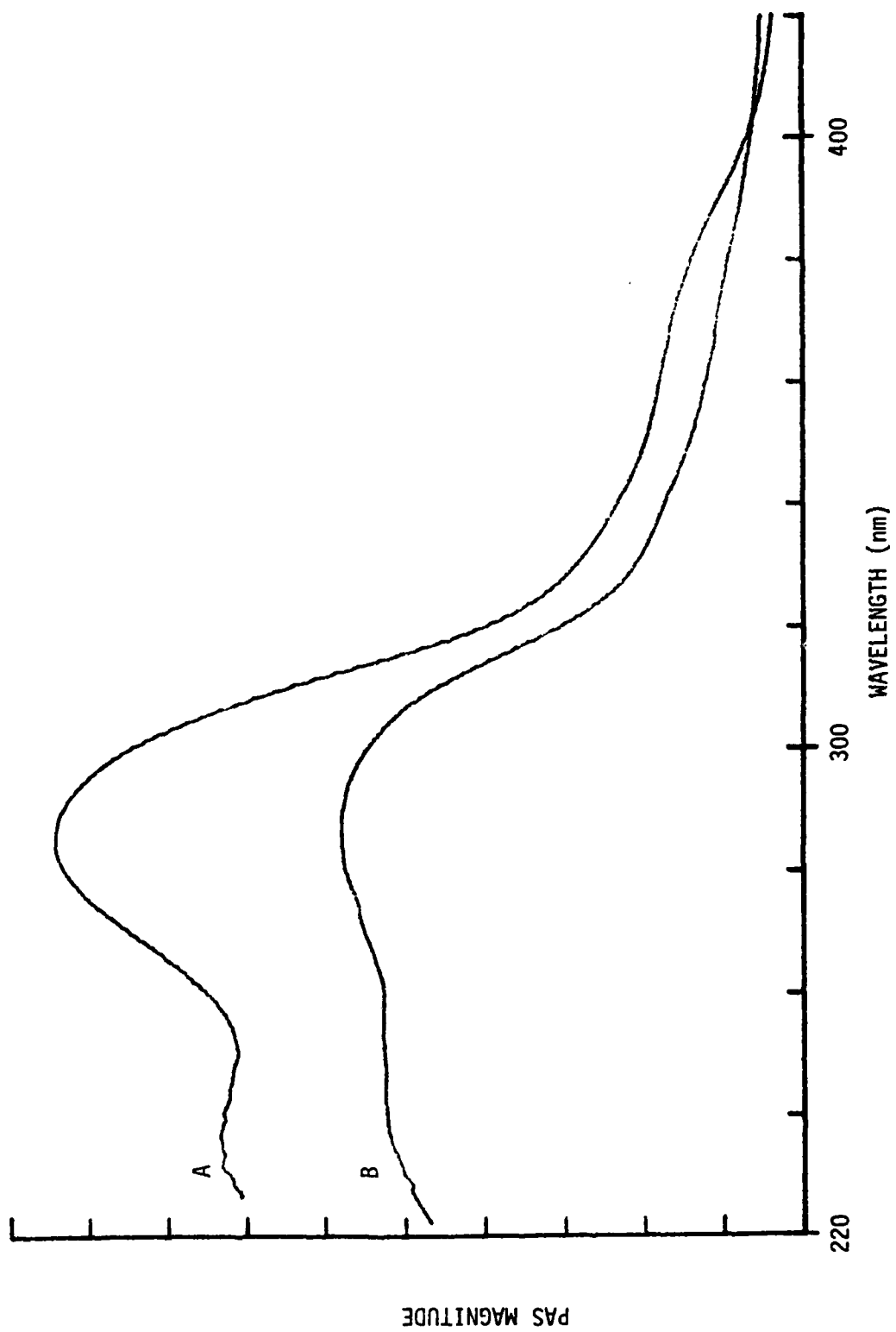
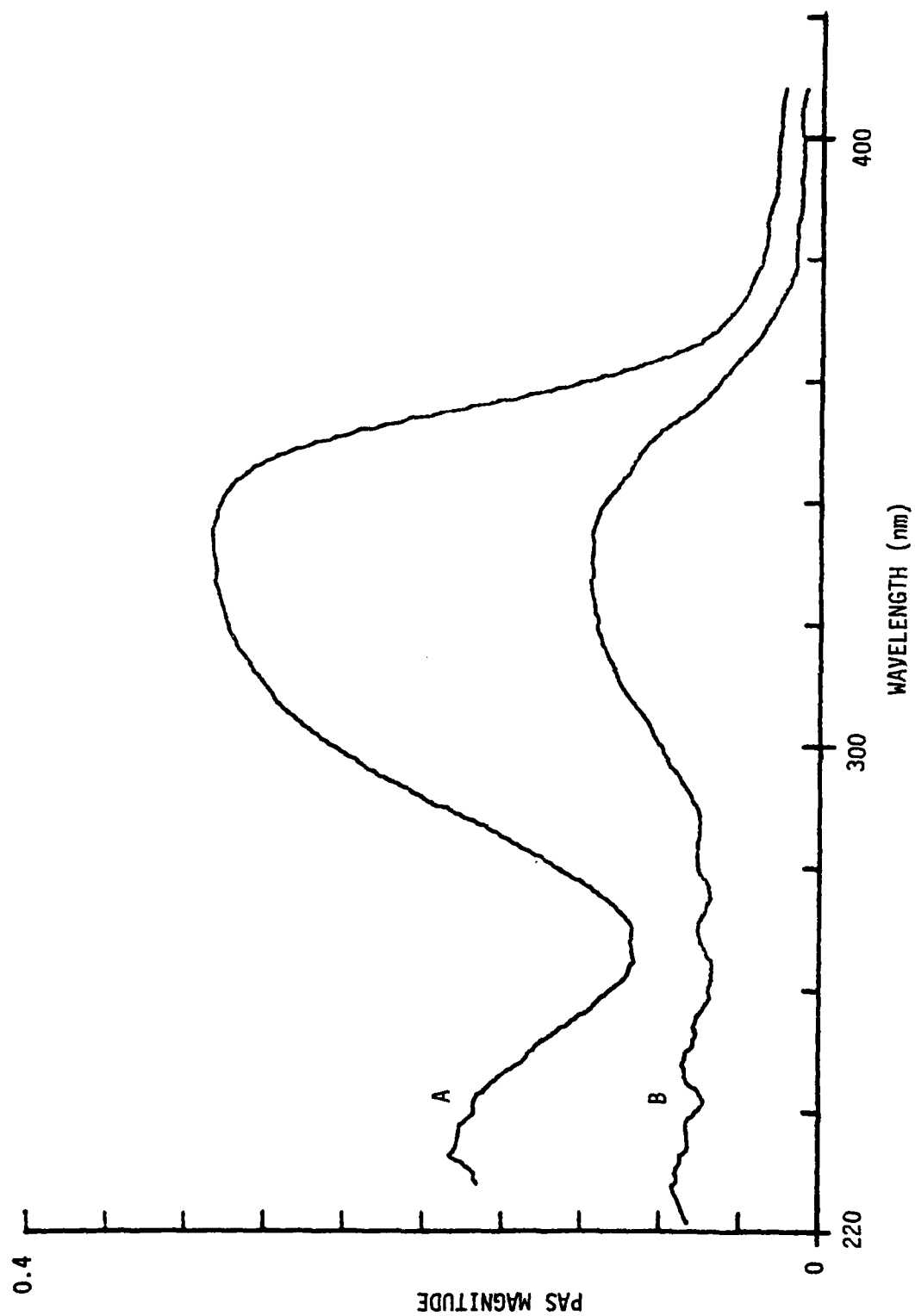




Figure A-4. Ultraviolet photoacoustic spectra of AA-AEAPS (A) and HFA-AEAPS (B) immobilized on silica gel.



## Chapter 6

### PHOTOACOUSTIC SPECTROSCOPY OF $\gamma$ -ALUMINA SUPPORTED METAL OXIDE CATALYSTS

#### Introduction

Catalysis by metals and metal oxides is an old and much-studied field of chemistry. Because of the industrial importance of these materials, a large body of empirical knowledge about catalytic phenomena has been accumulated over more than 100 years.<sup>1</sup> The chemical industry, especially the petroleum industry, employs a variety of supported metal catalysts and supported metal oxide catalysts. However, the empirical practice of heterogeneous catalysis has preceded understanding of the nature of catalyst surfaces. Surface spectroscopy techniques have recently made important contributions to the understanding of the influence of preparation parameters on the catalyst surface. This study adds photoacoustic spectroscopy to the list of spectroscopic techniques which have been applied to the investigation of supported metal oxide catalysts. In this work the value of photoacoustic spectroscopy for qualitative and quantitative study of catalyst surface is demonstrated.

Alumina supported nickel and cobalt catalysts have been widely studied because of their catalytic activity in industrially important reactions, especially hydrocracking, hydrogenation and methanation. Moreover, knowledge of alumina supported cobalt catalysts may

ultimately be extended to provide a better insight into the nature of alumina supported cobalt-molybdenum catalysts which are particularly important in catalytic hydrodesulphurisation of crude petroleum. The University of Pittsburgh research group under the direction of Dr. D. M. Hercules has employed a variety of surface spectroscopy techniques to study metal-support interactions in  $\text{Ni}/\gamma\text{-Al}_2\text{O}_3$  and  $\text{Co}/\gamma\text{-Al}_2\text{O}_3$  catalysts.<sup>[2,3,4,5]</sup> X-ray photoelectron spectroscopy (ESCA), ion scattering spectroscopy (ISS) and extended x-ray absorption fine structure spectroscopy (EXAFS) were employed to investigate the change in surface species as a function of metal loading and calcination temperature. In the case of the  $\text{Co}/\gamma\text{-Al}_2\text{O}_3$  system, secondary ion mass spectrometry (SIMS) was also used to help characterize surface species.<sup>5</sup> Recent popularization of photoacoustic spectroscopy (PAS) prompted its application to the study of these catalyst systems. The primary objective of this study was to use PAS to confirm and, if possible, to extend the results of surface spectroscopic investigations of  $\gamma$ -alumina supported metal oxide catalysts. This chapter reports the results of a quantitative PAS study of  $\text{Ni}/\gamma\text{-Al}_2\text{O}_3$  and  $\text{Co}/\gamma\text{-Al}_2\text{O}_3$  oxide catalysts using the same samples which were characterized by surface spectroscopy techniques.<sup>[2,3,4,5]</sup> A preliminary, qualitative investigation of the  $\text{Co-Mo}/\gamma\text{-Al}_2\text{O}_3$  catalyst system using PAS is also reported.

#### Experimental Section

Catalyst samples were prepared by members of the Pittsburgh research group. Details of catalyst preparation and characterization

of  $\text{Co}/\gamma\text{-Al}_2\text{O}_3$  and  $\text{Ni}/\gamma\text{-Al}_2\text{O}_3$  catalysts have been reported previously.<sup>[2,3,5]</sup> The  $\gamma$ -alumina (Alpha-Ventron,  $90 \text{ m}^2/\text{g}$ ) used as a support for catalysts was prepared by grinding until the powder passed through a 200 mesh sieve. The nickel and cobalt catalysts were made by impregnation of the powdered  $\gamma$ -alumina with aqueous solutions of reagent grade  $\text{Ni}(\text{NO}_3)_2$  or  $\text{Co}(\text{NO}_3)_2$ , drying at  $110^\circ\text{C}$  and calcining in air for 5 hours. These catalyst samples were prepared with various bulk metal loadings using calcination temperatures in the range  $400^\circ\text{C}$  to  $600^\circ\text{C}$ . The  $\text{Co-Mo}/\gamma\text{-Al}_2\text{O}_3$  catalyst samples were prepared by sequential impregnation of  $\gamma\text{-Al}_2\text{O}_3$  with molybdenum and cobalt. The  $\gamma\text{-Al}_2\text{O}_3$  (Harshaw,  $190 \text{ m}^2/\text{g}$ ) was prepared by grinding it and then sieving the powder through a 100 mesh sieve. The resulting material was dried overnight at  $110^\circ\text{C}$ . An aqueous solution of  $(\text{NH}_4)_6\text{Mo}_7\text{O}_{24}\cdot 9\text{H}_2\text{O}$  (Fisher) was mixed with the prepared  $\gamma$ -alumina. This mixture was dried at  $110^\circ\text{C}$  overnight. Molybdenum impregnated  $\gamma$ -alumina was calcined at  $550^\circ\text{C}$  in air for 16 hours. Samples of the molybdenum-loaded alumina were mixed with aqueous solutions of  $\text{Co}(\text{NO}_3)_2$  (Fisher). Then the drying and calcination steps were repeated. The amount of molybdenum loaded on the support was found to be within  $\pm 1\%$  Mo of the calculated value; the amount of cobalt loaded on the support was found to be within  $\pm 0.3\%$  Co of the calculated value.

Samples of pure materials were obtained for comparison with catalyst samples. When necessary these materials were physically diluted with the  $\gamma$ -alumina used in catalyst preparation. Before use the  $\gamma$ -alumina was dried at  $80^\circ\text{C}$  in a vacuum oven. When mixing with

$\gamma$ -alumina was inadequate to yield a uniform sample, the mixture was ground for a short time in a miniature stainless-steel ball mill. Samples of  $\text{Ni}(\text{NO}_3)_2 \cdot 6\text{H}_2\text{O}$  (Baker),  $\text{Co}(\text{NO}_3)_2 \cdot 6\text{H}_2\text{O}$  (Mallinckrodt),  $\text{CoAl}_2\text{O}_4$  (CERAC),  $\text{Co}_3\text{O}_4$  (Pfaltz and Bauer) and  $\text{Co}(\text{CH}_3\text{COCHCOCH}_3)_3$  were prepared by grinding with  $\gamma$ -alumina for 3 minutes. The  $\text{Co(III)}$  acetylacetonate sample was a student preparation made according to a modified procedure of Bryant and Fernelius.<sup>6</sup> This material was supplied by Dr. G. Eaton. The  $\text{NiAl}_2\text{O}_4$  samples were made by heating a mixture of  $\text{Ni}(\text{NO}_3)_2$  and  $\gamma$ -alumina at  $1300^\circ\text{C}$ . The  $\text{NiAl}_2\text{O}_4$  materials were not so optically absorbant as to require dilution.  $\text{NiO}$  (Baker, gray-black) was powdered by calcining at  $600^\circ\text{C}$  for 5 hours. Quantitative dilutions of this material were made by mixing with  $\gamma$ -alumina. The octahedral component of a cobalt oxide sample was enhanced by heating powdered  $\text{Co}_3\text{O}_4$  at  $1100^\circ\text{C} \pm 15^\circ\text{C}$  for 11 hours and then cooling the material in a vacuum. This procedure makes use of the phase transition, described in Equation 1, which occurs at about  $900^\circ\text{C}$ .



Although the stoichiometry of the resulting material is uncertain, the octahedral  $\text{Co(II)}$  component is enhanced. The resulting material was ground for 3 minutes with  $\gamma$ -alumina. A sample of  $\text{CoMoO}_4$  (Pfaltz and Bauer) was prepared by dilution with  $\gamma$ -alumina for comparison with  $\text{Co-Mo}/\gamma\text{-Al}_2\text{O}_3$  samples.

## Results and Discussion

### Considerations for Quantitative PAS

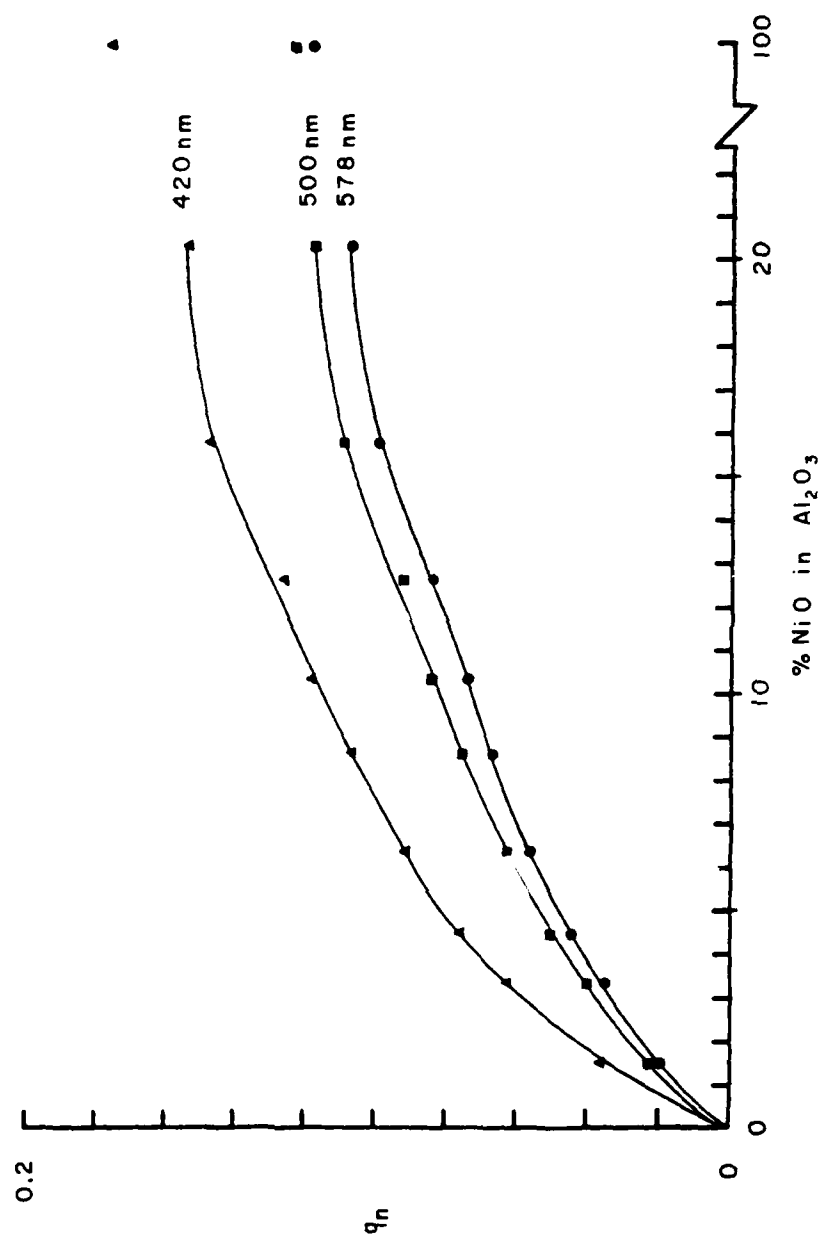
The PAS data analysis method and calibration procedure<sup>7</sup> were described in Chapter 3. In this formalism, photoacoustic phase and magnitude information are combined in a response function which is proportional to the bulk absorption coefficient multiplied by the thermal diffusion length for the sample,  $\beta\mu_s$ . This analysis assumes that the thermal and light-scattering properties of the sample are identical to those of the calibration standards which were prepared by loading the  $\gamma$ -alumina surface with small amounts of  $K_2CrO_4$ . In the case of the supported metal oxide catalyst samples, the metal is not a minor constituent. The catalyst samples used in this study contain 0.5% to 24% of metal by mass. In order to determine the limits for which the PAS response function is linear with respect to sample absorptivity, the PAS response function was evaluated for dilutions of NiO. Nickel oxide was chosen instead of cobalt oxide because the absorptivities of the nickel materials are less than those of the corresponding cobalt materials; hence, larger fractions of nickel catalyst in diluted samples are required to achieve the same signal level as obtained for diluted cobalt catalyst samples. The thermal diffusion length for NiO is smaller than that for alumina by a factor of 18. If change in the thermal properties of the samples is the dominant factor, then the magnitude and the phase function,  $f(\psi)$ , are expected to show a negative deviation with increasing NiO percentage producing a negative deviation

from linearity for the PAS response function. The scattering coefficient for the finely powdered NiO is expected to be larger than that for the  $\gamma$ -alumina substrate. If this factor is dominant, the PAS magnitude and phase function,  $f(\psi)$ , are expected to show a positive deviation with increasing NiO percentage, producing a positive deviation from linearity for the PAS response function.

The normalized photoacoustic magnitude versus percentage of NiO in  $\gamma$ -Al<sub>2</sub>O<sub>3</sub> is shown for selected wavelengths in Figure 1. From 0% to 10% of NiO the curves have the appearance of a typical magnitude response curve as the saturation limit is approached. However, from 11% to 20% of NiO the curves appear to seek a higher saturation limit. Similarly, the photoacoustic phase function at selected wavelengths versus percentage of NiO in  $\gamma$ -Al<sub>2</sub>O<sub>3</sub>, shown in Figure 2, exhibits typical curve shapes up to about 11% of NiO. Beyond this point the phase function deviates from linearity in a positive direction. These data are combined in the PAS response function in Figure 3. The PAS response function is linear with percent of NiO in  $\gamma$ -Al<sub>2</sub>O<sub>3</sub> up to 11% NiO with zero intercept as substantiated by the statistics for the least-squares fits shown in Table 1. It is concluded that the deviation from linearity beyond 11% NiO is predominantly due to increased light-scattering in the sample. The implications of this information for quantitative PAS of catalysts is merely that the catalyst samples require sufficient dilution to limit the maximum NiO content of the samples to no more than 10%. It was found to be satisfactory to dilute the Ni catalysts samples having high metal loading to 10% Ni by mass



Figure 1. Photoacoustic magnitude,  $q_{\eta}$ , versus percent NiO in  $\gamma\text{-Al}_2\text{O}_3$  for wavelengths 420 nm, 500 nm and 578 nm.



AIR FORCE INST OF TECH WRIGHT-PATTERSON AFB OH F/  
PHOTOACOUSTIC SPECTROSCOPY OF CHEMICALLY MODIFIED SURFACES. (U)  
AUG 81 L W BURGGRAF  
AFIT-81-160 NI

NL

3.3

END  
DATE  
FILMED  
8-82  
DTIC

Figure 2. Photoacoustic phase function,  $f(\psi)$ , versus percent NiO in  $\gamma\text{-Al}_2\text{O}_3$  for wavelengths 420 nm, 500 nm and 578 nm.

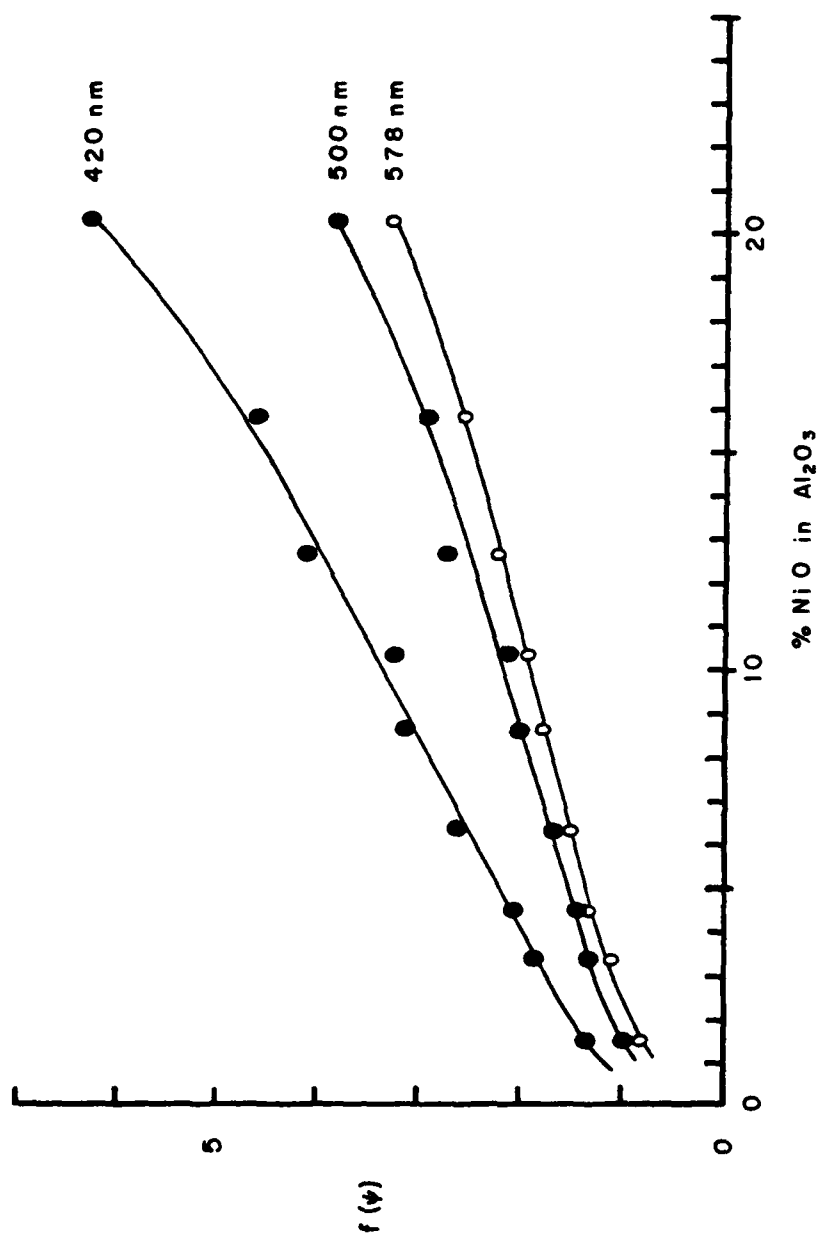


Figure 3. Photoacoustic response function,  $C\beta\mu_s$  versus percent NiO in  $\gamma\text{-Al}_2\text{O}_3$  for wavelengths 420 nm, 500 nm and 578 nm.

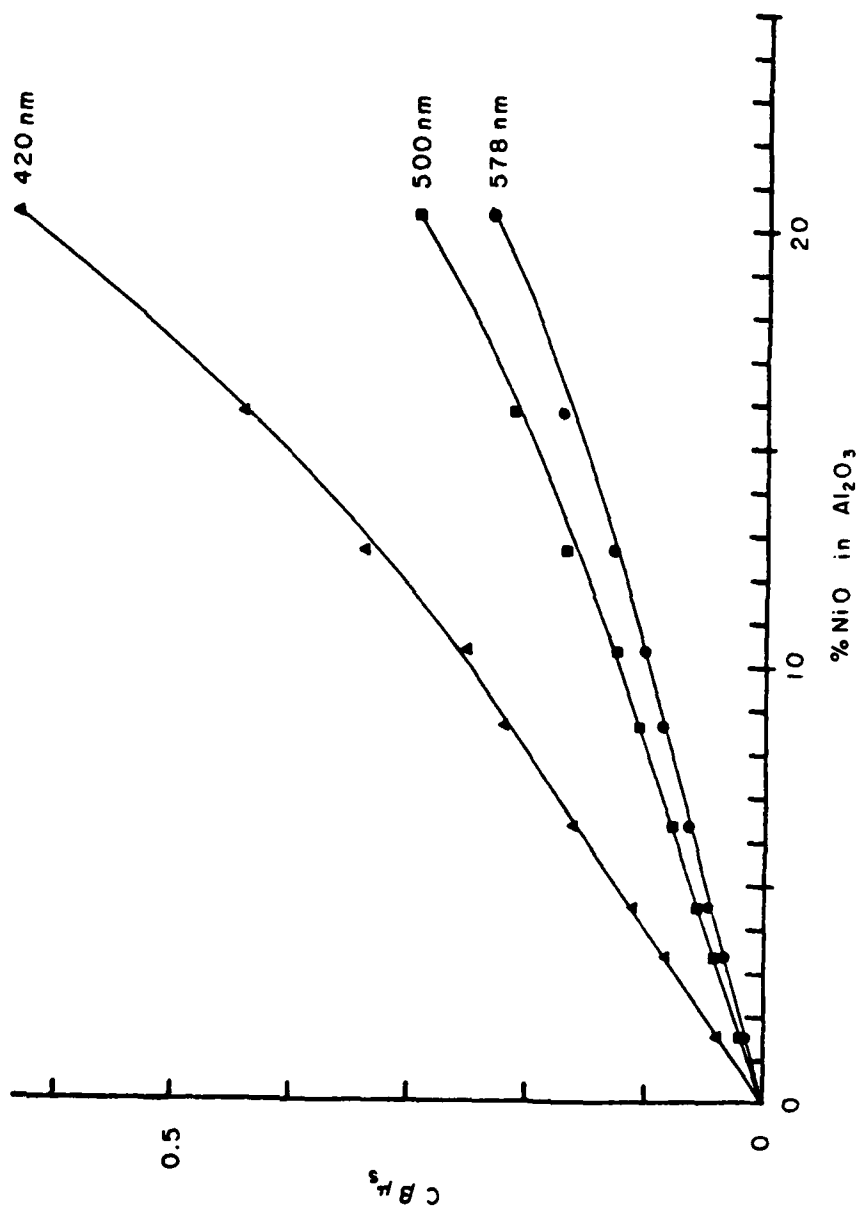


Table 1

Statistics, at 95% confidence limit,  
for least-squares fit of  $C\beta_{\mu_s}$  versus  
percent of NiO in  $\gamma\text{-Al}_2\text{O}_3$  up to 11% NiO

Measurement Wavelength	Slope	Y-Intercept	Standard Deviation	Correlation Coefficient
420 nm	$0.0248 \pm 6.6\%$	$0.0014 \pm .009$	0.0047	0.9987
500 nm	$0.0120 \pm 3.4\%$	$0.0025 \pm .0023$	0.0012	0.9997
578 nm	$0.0098 \pm 4.3\%$	$0.0018 \pm .0024$	0.0012	0.9994



for quantitative work. Cobalt catalyst samples were diluted to 0.5% Co by mass for quantitative work.

#### Nickel/ $\gamma$ -Alumina Catalysts

Metal-support interactions are known to influence the surface properties and, hence, the catalytic activity of alumina supported metal catalysts. During calcination the metal ion diffuses into the first few atomic layers of the alumina lattice (0.1 - 0.4 nm) where they may occupy sites of tetrahedral or octahedral symmetry.<sup>8</sup> At high metal loading a metal oxide species forms on the support surface. The octahedrally coordinated metal ions and the metal oxide species are readily reducible to the metal, while the tetrahedrally coordinated metal ions are not readily reduced and are catalytically inactive. The relative abundance and the distribution of these species depends on the metal loading and the calcination temperature.

Surface spectroscopy techniques showed that nickel strongly interacts with the  $\gamma$ -alumina support at low nickel loading.<sup>[2,3]</sup> The ESCA peak width for the Ni 2p<sub>3/2</sub> line was correlated with the presence of two surface species: (1) nickel ions in surface sites of octahedral symmetry, Ni(O), and (2) nickel ions in surface sites of tetrahedral symmetry, Ni(T). As expected, increased calcination temperature was found to favor formation of the Ni(T) species because of enhanced diffusion into the  $\gamma$ -alumina lattice. Increased nickel loading favored formation of the Ni(O) species. The EXAFS results supported this interpretation.<sup>4</sup> The average coordination number was found to increase

from 4.8 to 5.3 as nickel loading increased from 2% to 15% in  $\text{Ni}/\gamma\text{-Al}_2\text{O}_3$  catalysts calcined at  $400^\circ\text{C}$ . In the ESCA study of the  $\text{Ni}/\gamma\text{-Al}_2\text{O}_3$  catalysts,<sup>3</sup> the Ni/Al intensity ratio increased linearly with bulk nickel loading up to 17% nickel content. Beyond 17% nickel loading there was an enhancement of the Ni/Al ratio. This result was interpreted to mean that a separate phase ( $\text{NiO}$ ) exists at the surface for nickel loading greater than 17%. After nickel saturates the surface sites, additional nickel contributes to an oxide phase on top of the substrate surface. The ISS Ni/Al intensity ratio showed a large increase beyond 20% nickel loading, consistent with the ESCA results. However, the intensity ratio exhibited a pronounced plateau between 10% and 17% nickel loading especially at high calcination temperature ( $600^\circ\text{C}$ ). This effect was attributed to the greater sensitivity of ISS to the depth distribution of  $\text{Ni}(\text{T})$  and  $\text{Ni}(\text{O})$  species. The ISS sampling depth is approximately 0.3 nm as compared to approximately 2 nm for ESCA. It has been proposed that nickel cations in tetrahedral surface sites tend to move below the surface where they are more shielded from the ion beam.<sup>9</sup> The photoacoustic spectroscopy results are interpreted in terms of these ideas.

When  $\text{Ni}(\text{II})$  is heated with  $\gamma\text{-Al}_2\text{O}_3$  at very high temperatures  $\text{NiAl}_2\text{O}_4$  is formed by inclusion of  $\text{Ni}(\text{II})$  ions into the tetrahedral sites of the  $\gamma$ -alumina "defect" spinel structure.<sup>10</sup> For a stoichiometric material at equilibrium, a disordered spinel structure is formed with about 22% of the  $\text{Ni}(\text{II})$  ions in tetrahedral sites and the remainder in octahedral sites.<sup>8</sup> Inversion occurs for the  $\text{NiAl}_2\text{O}_4$  system because the

energy preference for octahedral sites over tetrahedral sites is not substantially different for Ni(II) and Al(III).<sup>11</sup> In Figure 4 the visible photoacoustic spectra of a largely tetrahedral bulk  $\text{NiAl}_2\text{O}_4$  spinel and a disordered bulk  $\text{NiAl}_2\text{O}_4$  spinel structure are shown. The enhanced spectral features at 410 nm - 455 nm ( ${}^3\text{A}_{2g} \rightarrow {}^3\text{T}_{1g}(\text{P})$ ) and 640 nm - 715 nm ( ${}^3\text{A}_{2g} \rightarrow {}^3\text{T}_{1g}(\text{F})$ ) are due to octahedrally coordinated Ni(II) and the intense feature centered at about 610 nm ( ${}^3\text{T}_1(\text{F}) \rightarrow {}^3\text{T}_1(\text{P})$ ) is due to tetrahedrally coordinated Ni(II).<sup>12</sup> The photoacoustic spectrum of octahedrally coordinated Ni(II) in  $\text{Ni}(\text{NO}_3)_2 \cdot 6\text{H}_2\text{O}$  is shown in Figure 5 for comparison. The photoacoustic spectrum of NiO, an octahedral oxide (NaCl structure) made by decomposing  $\text{Ni}(\text{NO}_3)_2 \cdot 6\text{H}_2\text{O}$ , is shown in Figure 6. This spectrum exhibits the same characteristic octahedral absorption bands as the hexahydrate nickel and, additionally, a broad absorption in the region 500 nm to 600 nm which has been attributed to a Ni(III) charge transfer band.<sup>13</sup>

#### Qualitative PAS Results

Selected photoacoustic spectra of nickel catalysts which were calcined at  $600^\circ\text{C}$  are shown in Figure 7. For nickel loading less than 7% the spectrum is dominated by the Ni(T) surface species absorption. The expanded spectrum for the catalyst loaded with 2.5% nickel, presented in Figure 8, shows little evidence for octahedral nickel species. The  ${}^3\text{T}_1(\text{F}) \rightarrow {}^3\text{T}_1(\text{P})$  transition is shifted to shorter wavelength by approximately 6 nm as compared to the bulk Ni(T) spectrum shown in Figure 4. The tetrahedral field is apparently slightly increased for

Figure 4. Photoacoustic spectrum of largely normal  $\text{NiAl}_2\text{O}_4$  spinel (A) and a disordered  $\text{NiAl}_2\text{O}_4$  spinel (B).

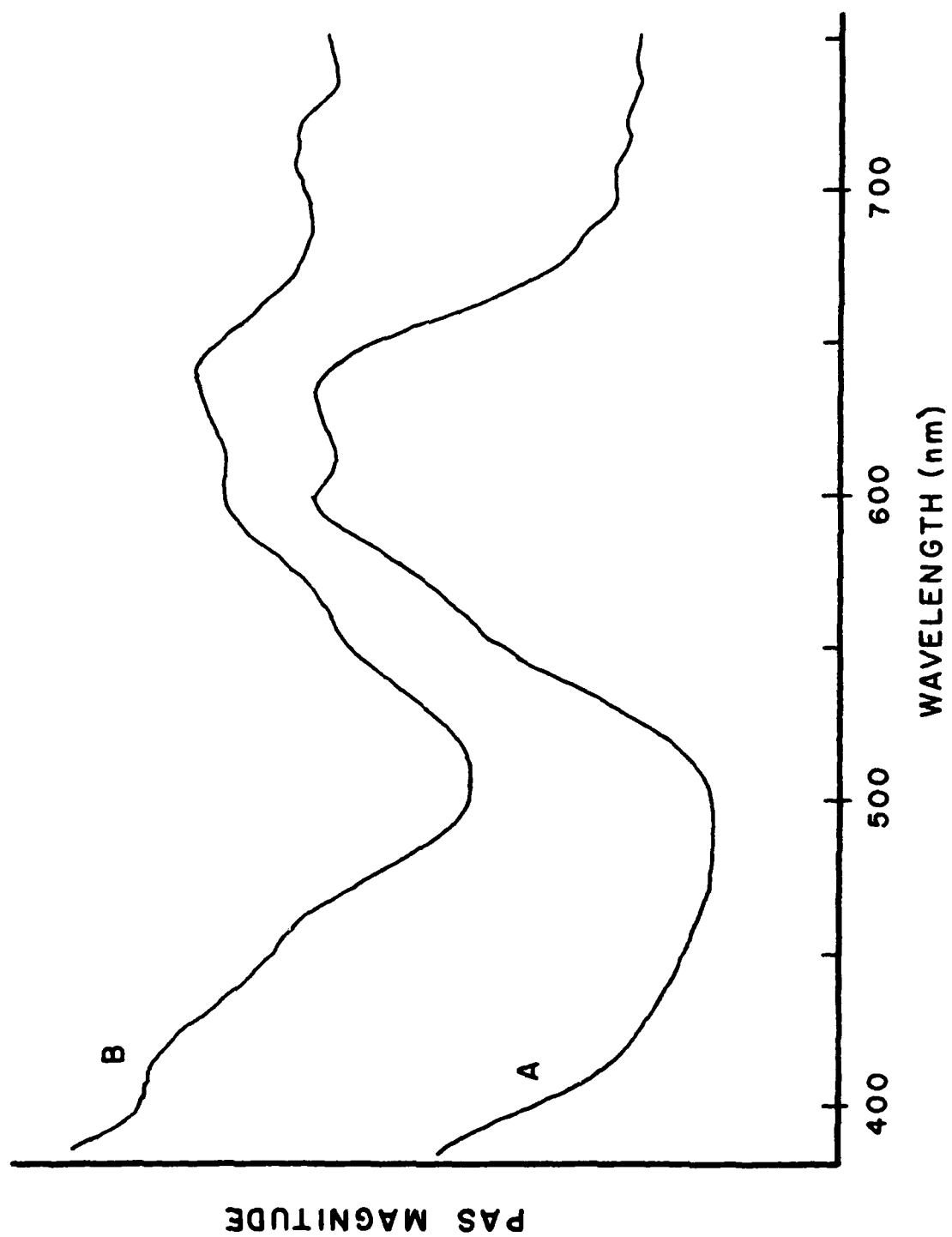


Figure 5. Photoacoustic spectrum of 20%  $\text{Ni}(\text{NO}_3)_2 \cdot 6\text{H}_2\text{O}$  ground in  $\gamma\text{-Al}_2\text{O}_3$ .

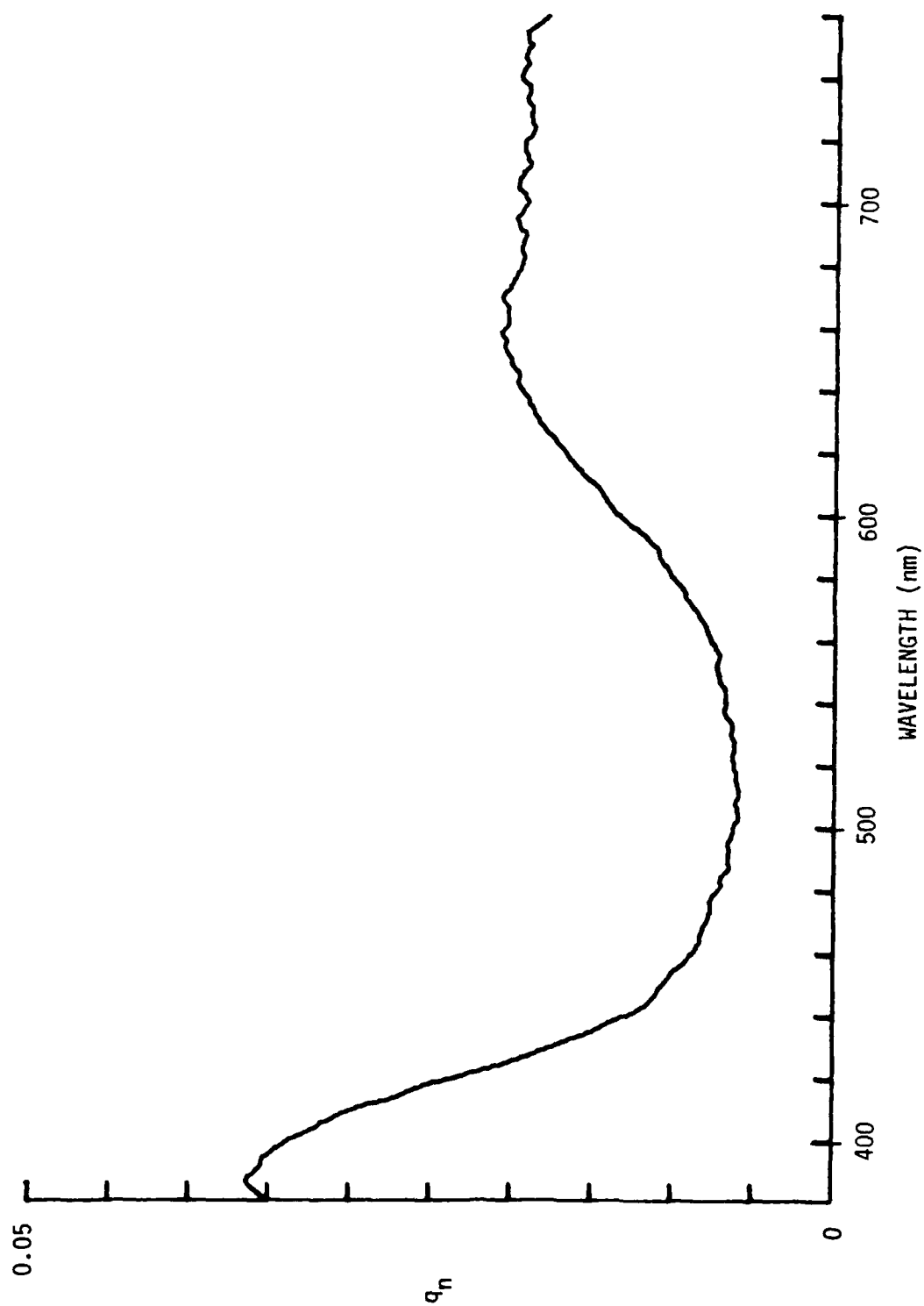


Figure 6. Photoacoustic spectrum of NiO.



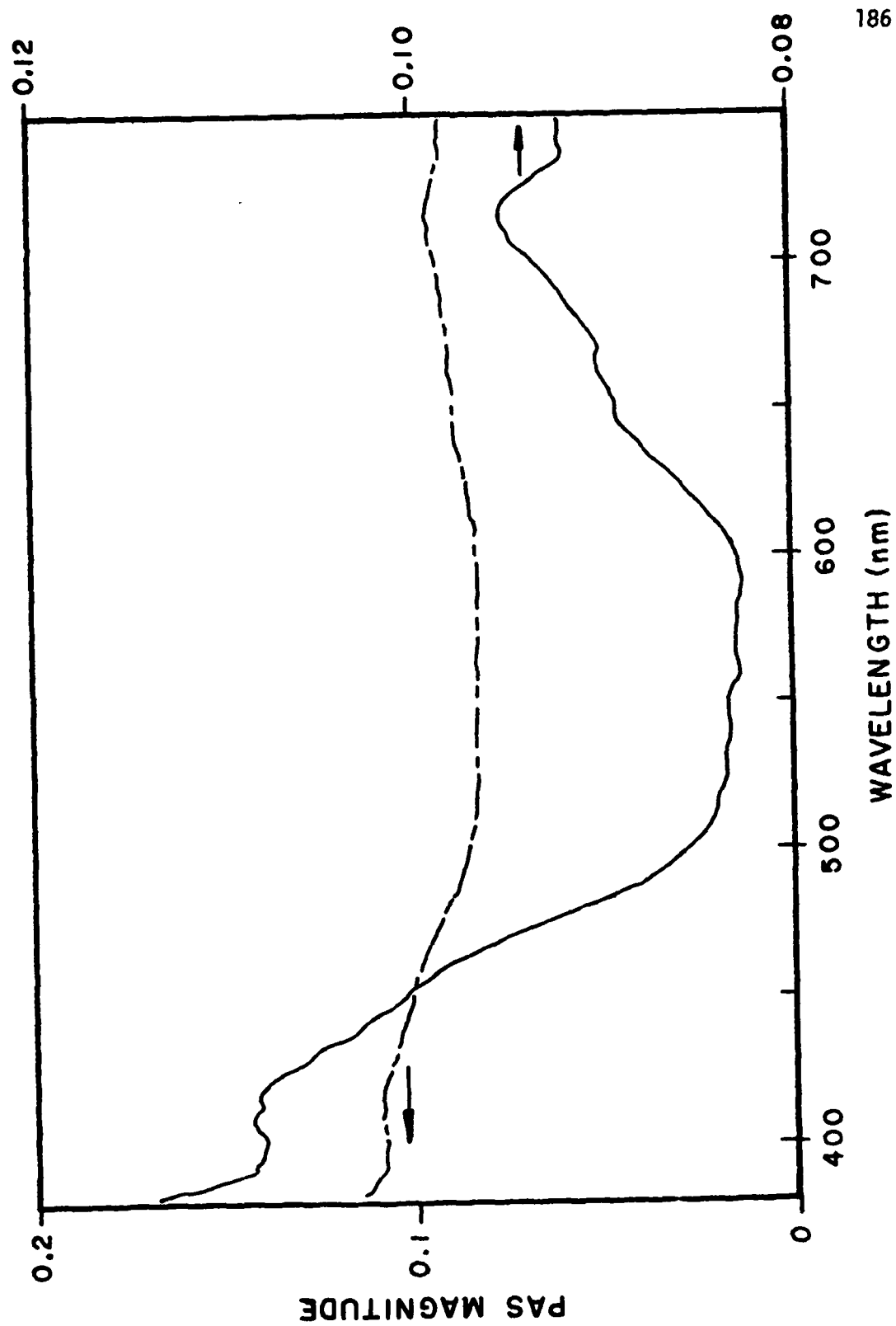


Figure 7. Photoacoustic spectra of  $\text{Ni}/\gamma\text{-Al}_2\text{O}_3$  catalysts calcined at  $600^\circ\text{C}$ .

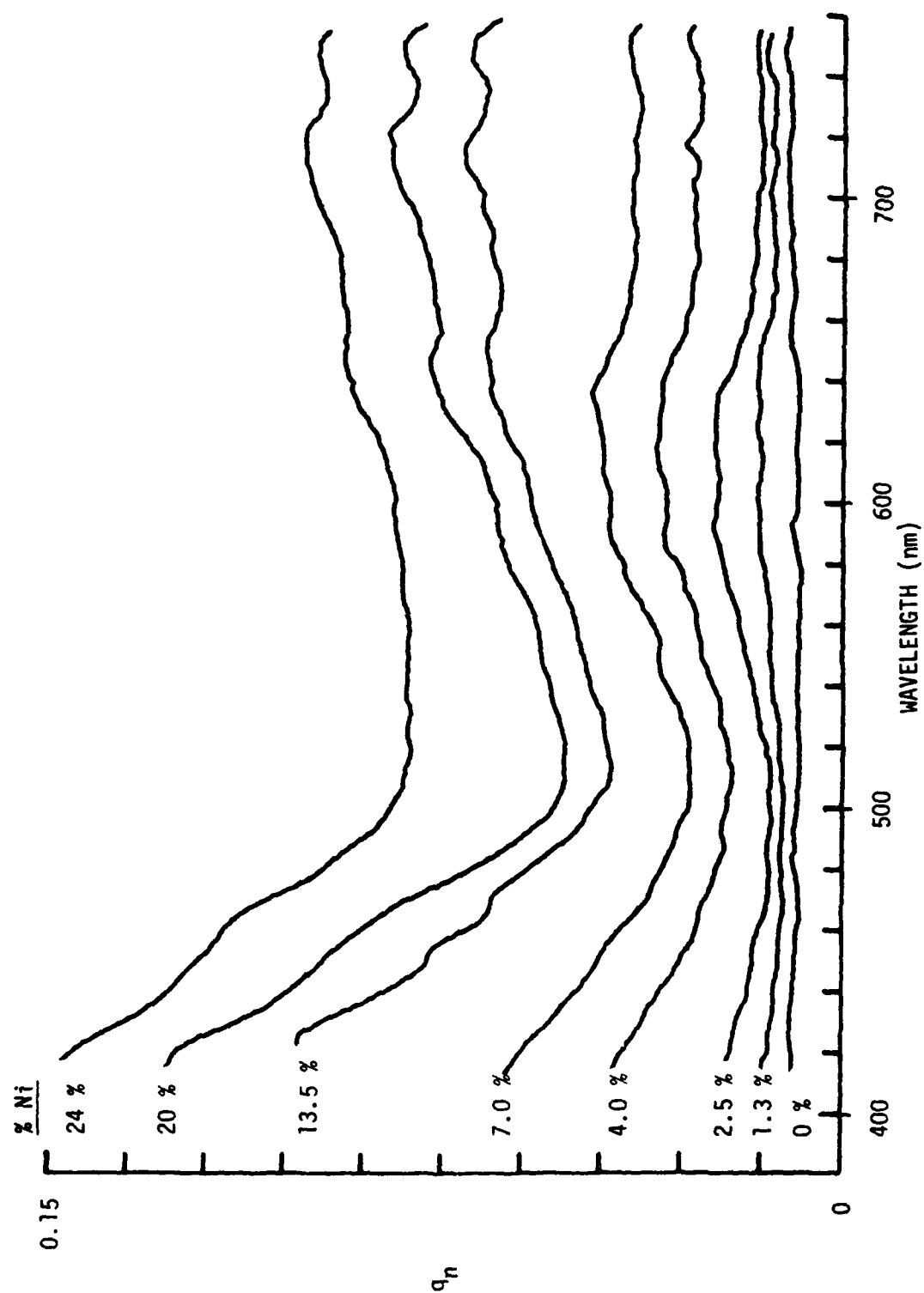
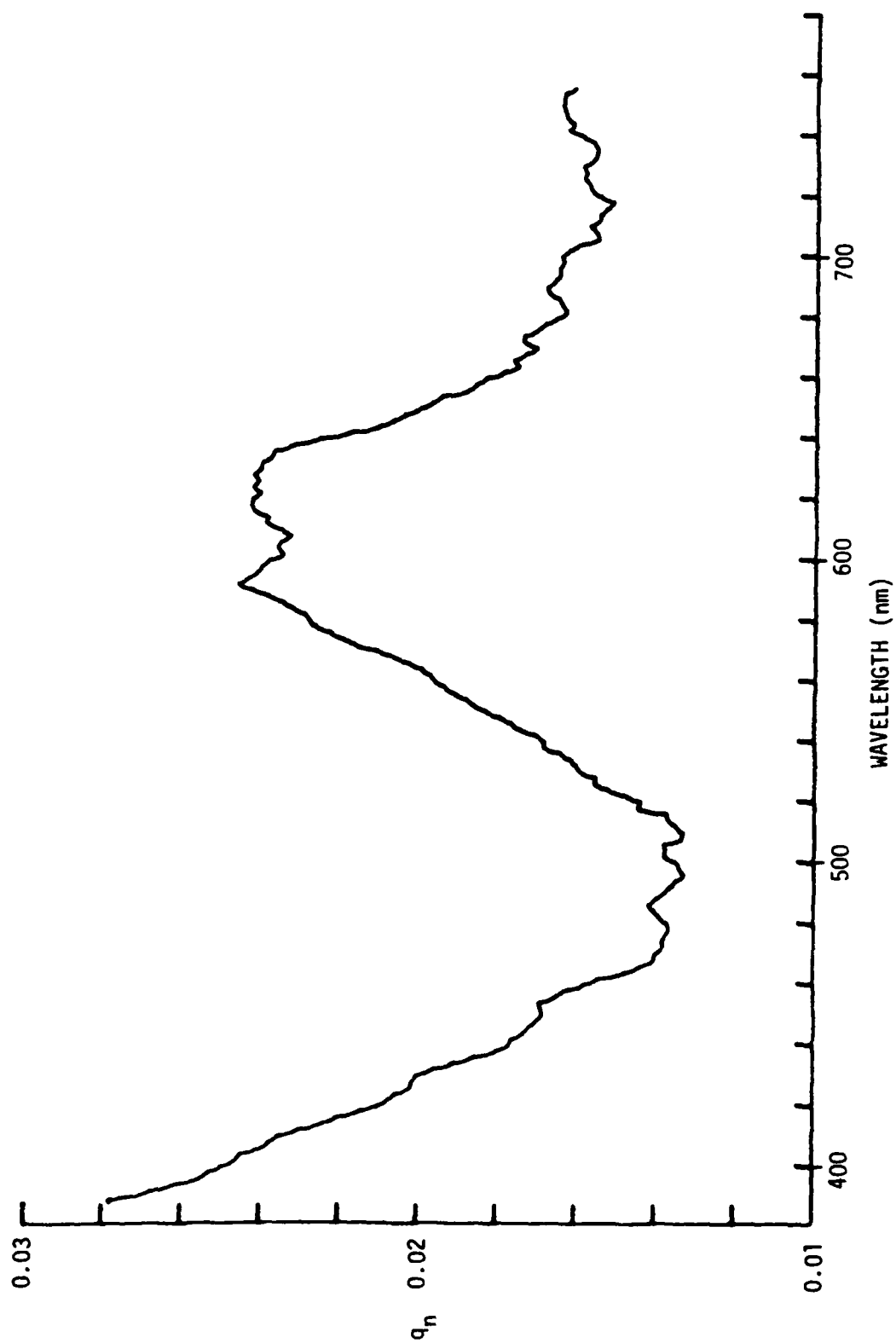


Figure 8. Photoacoustic spectrum of  $\text{Ni}/\gamma\text{-Al}_2\text{O}_3$  catalyst loaded with 2.5% Ni calcined at  $600^\circ\text{C}$ .



sites near the surface. For nickel loading between 7% and 20%, the absorption of the Ni(O) species makes an increasing contribution to the catalyst spectrum. Beyond 20% nickel loading, NiO is the dominant species adding to the absorption spectrum as evidenced by the increased absorption in the 500 nm to 600 nm region. At 24% nickel loading the Ni(T) spectrum is masked by NiO.

Photoacoustic spectra for selected Ni catalysts calcined at 500°C are shown in Figure 9. In this case the octahedral nickel species make a substantial contribution even at 1.25% nickel loading. At 4% nickel loading the spectrum is dominated by absorption of octahedral species. These data are in agreement with the conclusion of Wu and Hercules<sup>3</sup> from ESCA studies that the ratio of Ni(T) to Ni(O) decreases with decreasing calcination temperature. At the lowest calcination temperature used, 400°C, the simple spectral assignments which were applied to the other nickel catalysts are no longer applicable. Figure 10 shows photoacoustic spectra of Ni/ $\gamma$ -Al<sub>2</sub>O<sub>3</sub> catalysts calcined at 400°C. Spectral features centered at about 620 nm in the spectrum of the 1.25% nickel catalyst can be identified with Ni(T). However, the spectra for catalysts with less than 20% nickel are dominated by a broad visible absorption band which cannot be identified with the octahedral species, Ni(O) or NiO, or the tetrahedral species, Ni(T). Catalysts calcined at 400°C exhibit a broad absorption in the visible region with a structureless enhanced absorption at ~400 nm. This material is kinetically stable relative to NiO and Ni(O) as evidenced by the fact that heating the material in air at 600°C produces no appreciable change in the

Figure 9. Photoacoustic spectra of Ni/ $\gamma$ -Al<sub>2</sub>O<sub>3</sub> catalysts calcined at 500°C.

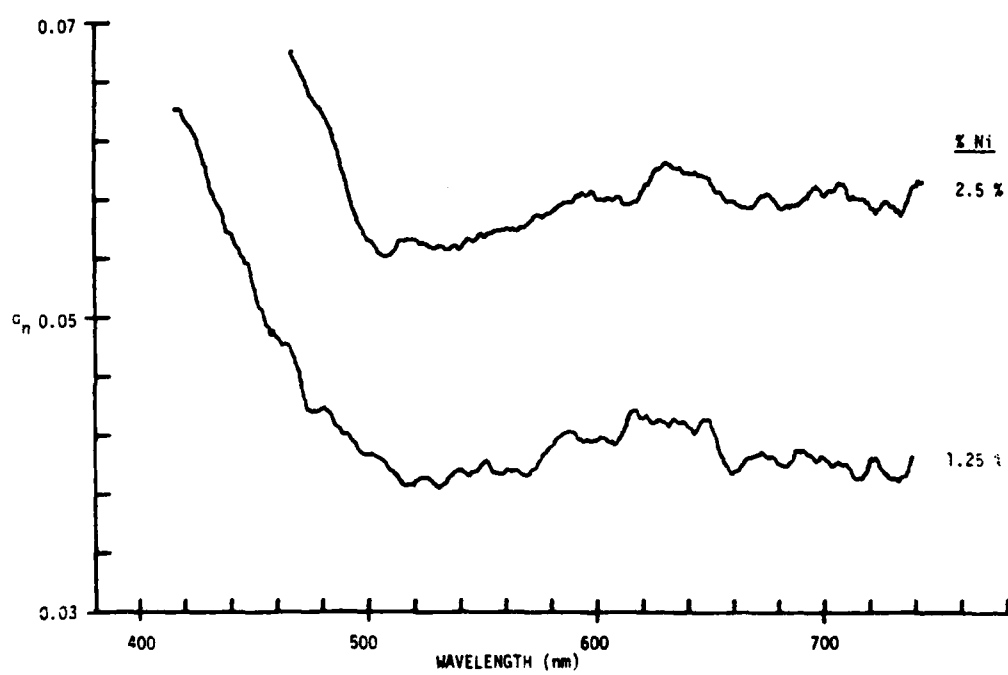
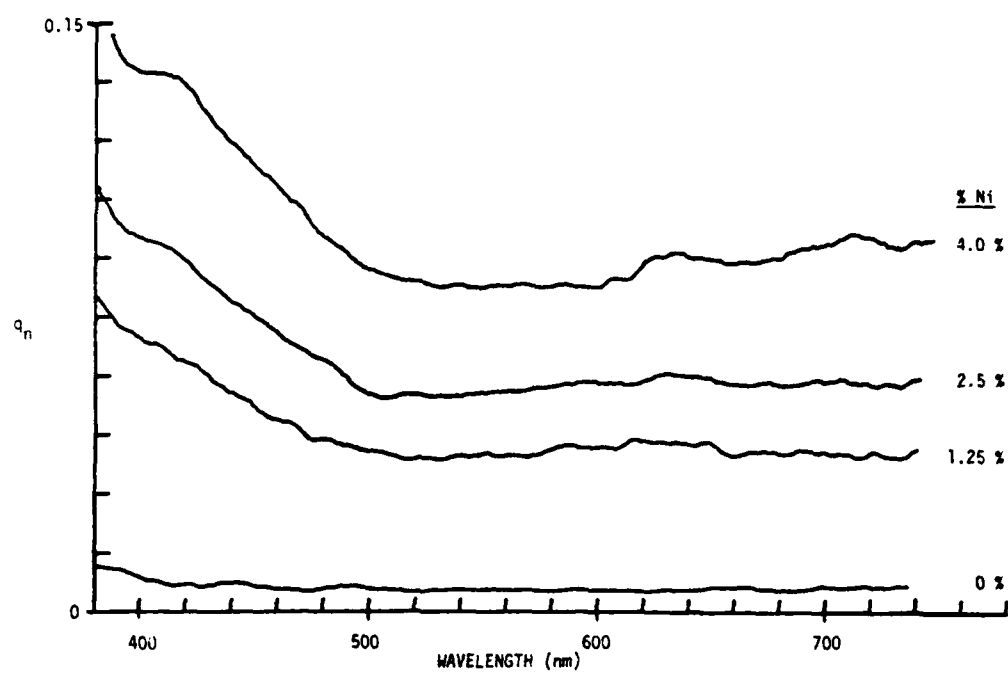
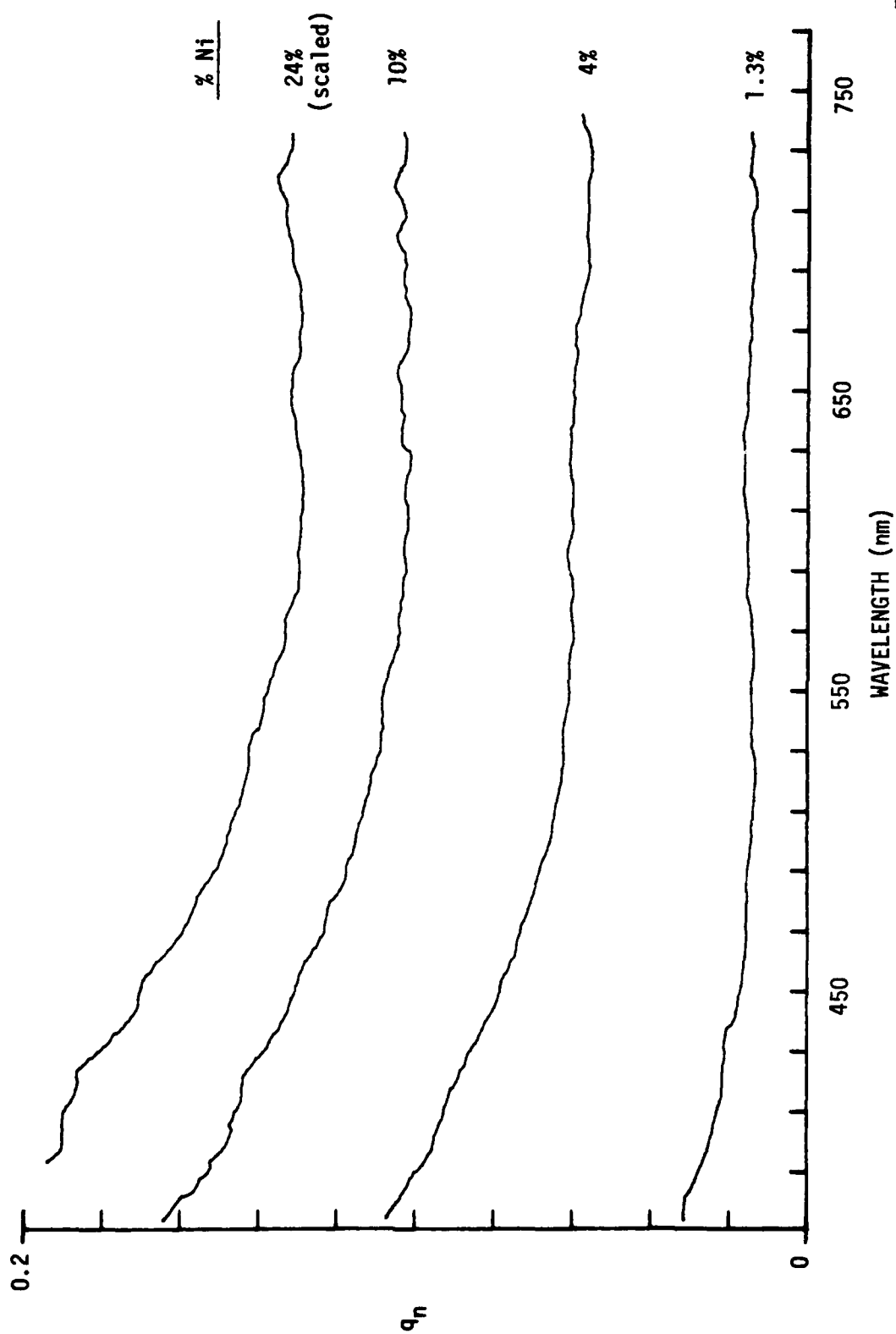




Figure 10. Photoacoustic spectra of selected  $\text{Ni}/\gamma\text{-Al}_2\text{O}_3$  catalysts calcined at  $400^\circ\text{C}$ .



visible absorption spectrum. Figure 11 compares photoacoustic spectra of a  $\text{Ni}/\gamma\text{-Al}_2\text{O}_3$  catalyst (7%,  $400^\circ\text{C}$ ) which were recorded before and after calcining the catalyst at  $600^\circ\text{C}$  for 5 hours. It is tempting to invoke the  $\text{Ni(III)}$  oxidation state to account for these spectra. The hypothesis of nickel species with oxidation state greater than +2 on alumina surfaces was first proposed by Hill and Selwood<sup>14</sup> to account for average nickel valences between 2 and 3 found in reduction studies. This unusual stoichiometry is dominant only for nickel loading less than 5% and for low calcination temperatures.<sup>[14,15]</sup> Stable gray-black nickel (III) hydroxides are known, whereas stable anhydrous nickel (III) oxides are not found.<sup>16</sup> Nickel (III) hydroxides have broad absorption bands and large absorptivities in the visible region, supporting this hypothesis. It is known that the presence of water influences the speciation in these materials.<sup>8</sup> It is possible that the greater surface hydroxyl coverage in a humid, low-temperature preparation enhances the formation and stability of  $\text{Ni(III)}$  species. For high nickel loading of catalysts calcined at  $400^\circ\text{C}$ , spectral features appear which can be identified with octahedral nickel species.

Quantitative PAS Results. As was pointed out earlier,  $\text{NiO}$  can be distinguished from the  $\text{Ni(O)}$  species by the broad absorption in the region 500 nm to 600 nm. At about 500 nm the absorption of the  $\text{Ni(T)}$  species exhibits a minimum; hence, the absorbance at 504 nm was selected to attempt to monitor  $\text{NiO}$  buildup. In Figure 12 the photoacoustic response function at 504 nm divided by the percent of nickel is plotted versus the bulk percent of nickel for catalysts calcined at  $600^\circ\text{C}$  and

Figure 11. Photoacoustic spectrum of Ni/ $\gamma$ -Al<sub>2</sub>O<sub>3</sub> catalyst loaded with 7% nickel prepared by calcining at 400°C. Spectra were recorded before (I) and after (II) calcining at 600°C for 5 hours.

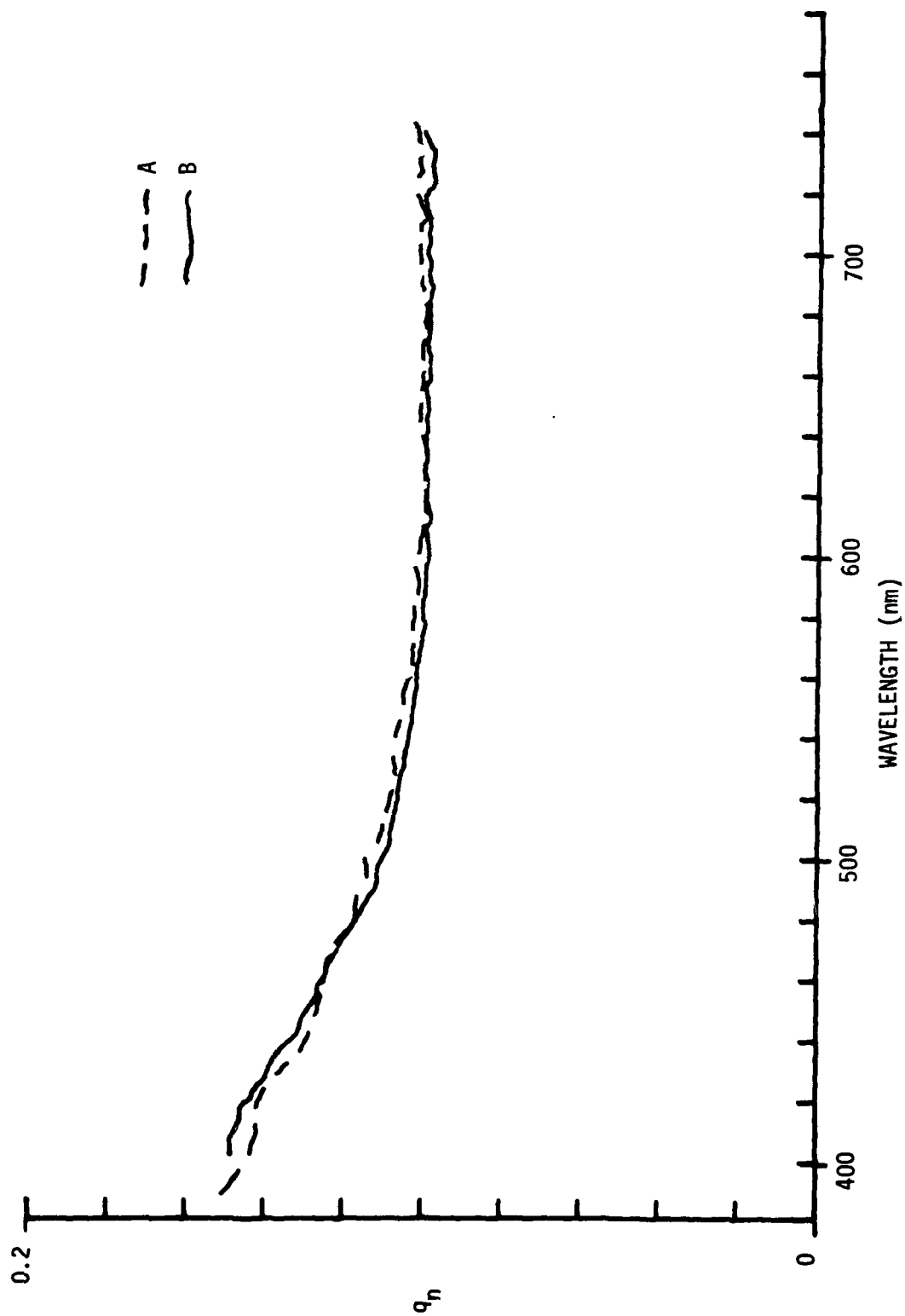
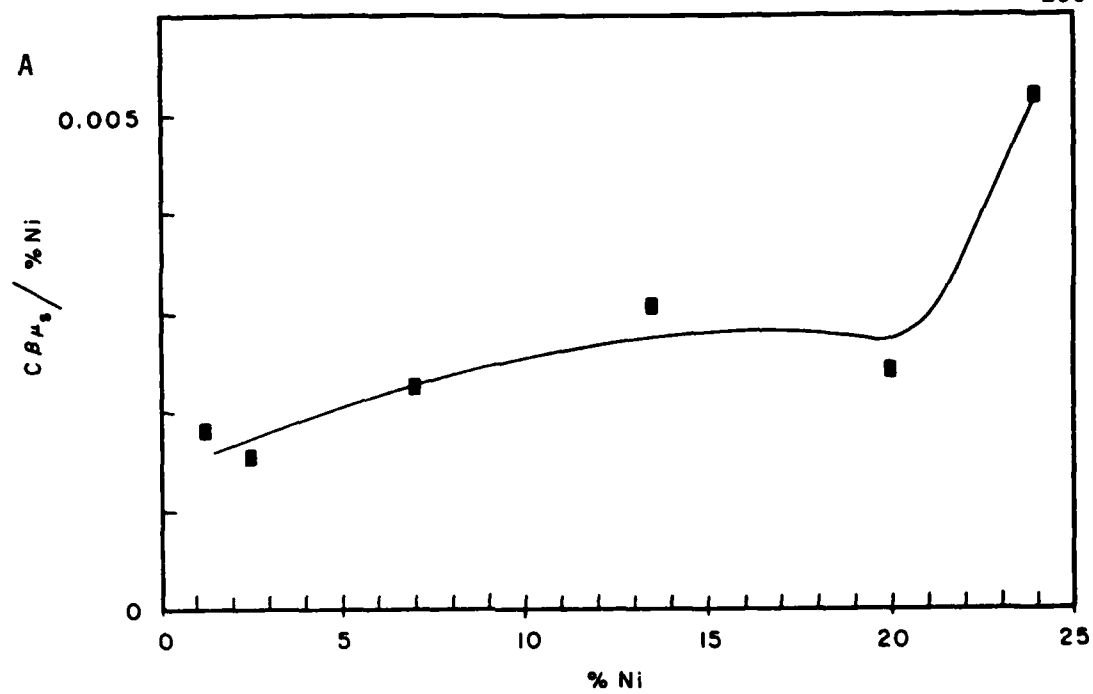


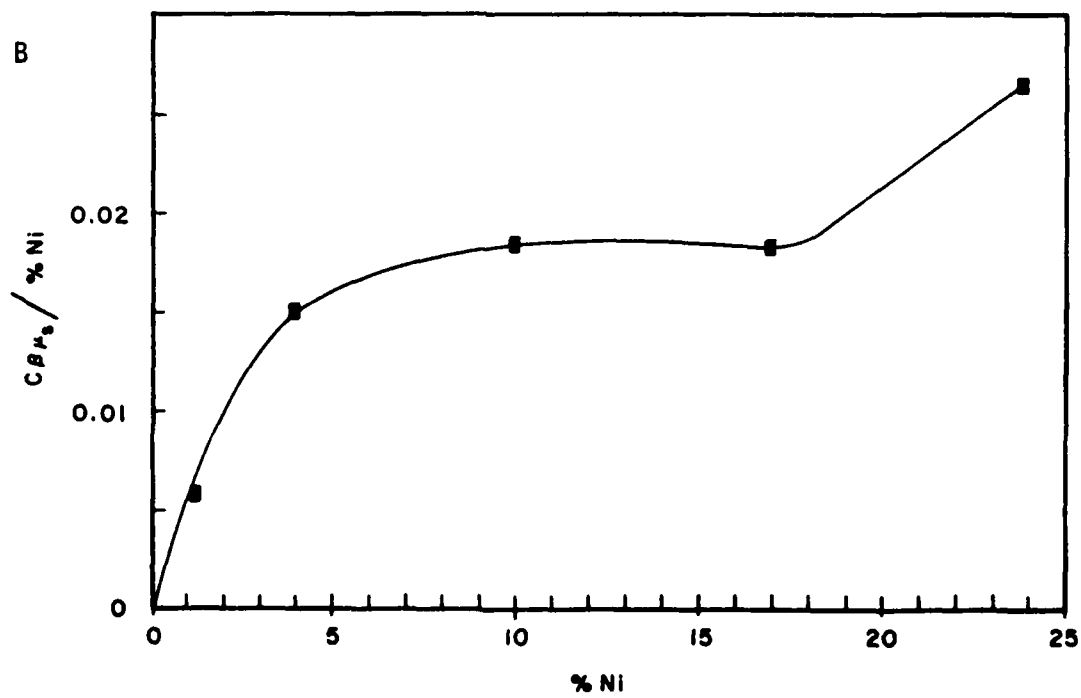
Figure 12. Photoacoustic response function,  $C\beta\mu_s$ , at 504 nm divided by the percent of nickel in the catalyst plotted versus the percent of nickel for catalysts calcined at 600°C (A) and 400°C (B).

200

A



B



at 400°C. This type of plot represents the absorbance per unit percentage of metal on the surface. For both calcination temperatures a plateau is reached at about 10% nickel. The absorbance at the plateau is much higher for the 400°C calcination temperature due predominantly to the low-temperature absorber hypothesized to be a Ni(III) species. In both cases, a large absorption enhancement occurs at about 20% nickel content. This is in good agreement with the Ni/Al intensity ratio results of ESCA and ISS which show enhancement beyond 17% nickel and 20% nickel, respectively. In the case of the photoacoustic results also, this discontinuity can be associated with the segregation of a NiO phase on the alumina surface.

Measures of the absorbance due to Ni(T) and Ni(O) species on the surface which account for NiO contribution to the absorption were created. The estimated enhanced absorption of the tetrahedral nickel species above the absorption of octahedral species is designated  $A_{590}$ ,

$$A_{590} = C\beta_{\mu_s}(590) - \left[ \frac{C\beta_{\mu_s}(\text{NiO}, 590)}{C\beta_{\mu_s}(\text{NiO}, 504)} \right] C\beta_{\mu_s}(504) \quad (2)$$

where  $C\beta_{\mu_s}(590)$  and  $C\beta_{\mu_s}(504)$  are photoacoustic response functions for catalysts at 590 nm and 504 nm, respectively.  $C\beta_{\mu_s}(\text{NiO}, 590)$  and  $C\beta_{\mu_s}(\text{NiO}, 504)$  are photoacoustic response functions for NiO in  $\gamma$ -alumina at 590 nm and 504 nm, respectively, each determined by a linear least-squares fit as illustrated in the section of this chapter dealing with considerations for quantitative PAS. In a similar way, the enhanced absorbance at 450 nm,  $A_{450}$ , is a measure of the Ni(O) absorbance.



$$A_{450} = C\beta_{\mu_s}(450) - \left[ \frac{C\beta_{\mu_s}(\text{NiO}, 450)}{C\beta_{\mu_s}(\text{NiO}, 504)} \right] C\beta_{\mu_s}(504) \quad (3)$$

The terms used are defined in an analogous way to those used in Equation 2.

In Figure 13,  $A_{590}$  and  $A_{590}/\% \text{ Ni}$  are plotted versus the percent of nickel in catalysts calcined at  $600^\circ\text{C}$ . As expected, the fraction of nickel existing as  $\text{Ni(T)}$  is greatest at low nickel loading. This fraction diminishes smoothly to 20% nickel loading. At about 20% nickel content  $A_{590}$  shows a negative-going discontinuity. It is reasonable to suggest that the  $\text{NiO}$  phase which segregates at about 20% nickel loading optically masks the  $\text{Ni(T)}$  species thereby reducing the  $\text{Ni(T)}$  signal. This interpretation agrees well with a catalyst model for which a  $\text{NiO}$  phase is stabilized and supported on top of  $\text{NiAl}_2\text{O}_4$  spinel material.

In Figure 14,  $A_{450}$  and  $A_{450}/\% \text{ Ni}$  are plotted versus percent of nickel in catalysts calcined at  $600^\circ\text{C}$ .  $\text{Ni(O)}$  is seen to make little contribution for nickel loading less than 5%, where the dominant species is  $\text{Ni(T)}$ . The fraction of nickel existing as  $\text{Ni(O)}$  increases rapidly above 5% nickel loading.  $A_{450}$  does not show the discontinuity at 20% nickel content that  $A_{590}$  does.

The qualitative interpretation of photoacoustic spectra for catalysts calcined at  $600^\circ\text{C}$  required reference only to  $\text{Ni(T)}$  and  $\text{Ni(O)}$  contributions for nickel loading up to 20%. Based on the assumption that  $\text{Ni(O)}$  and  $\text{Ni(T)}$  are the only species which make significant contribution to the absorbance, Equation 4 was solved for  $a_T$  and  $a_O$  using

Figure 13. Net photoacoustic response function at 590 nm,  $A_{590}$ , and  $A_{590}/\% \text{ Ni}$  plotted versus percent of nickel in catalysts calcined at 600°C.

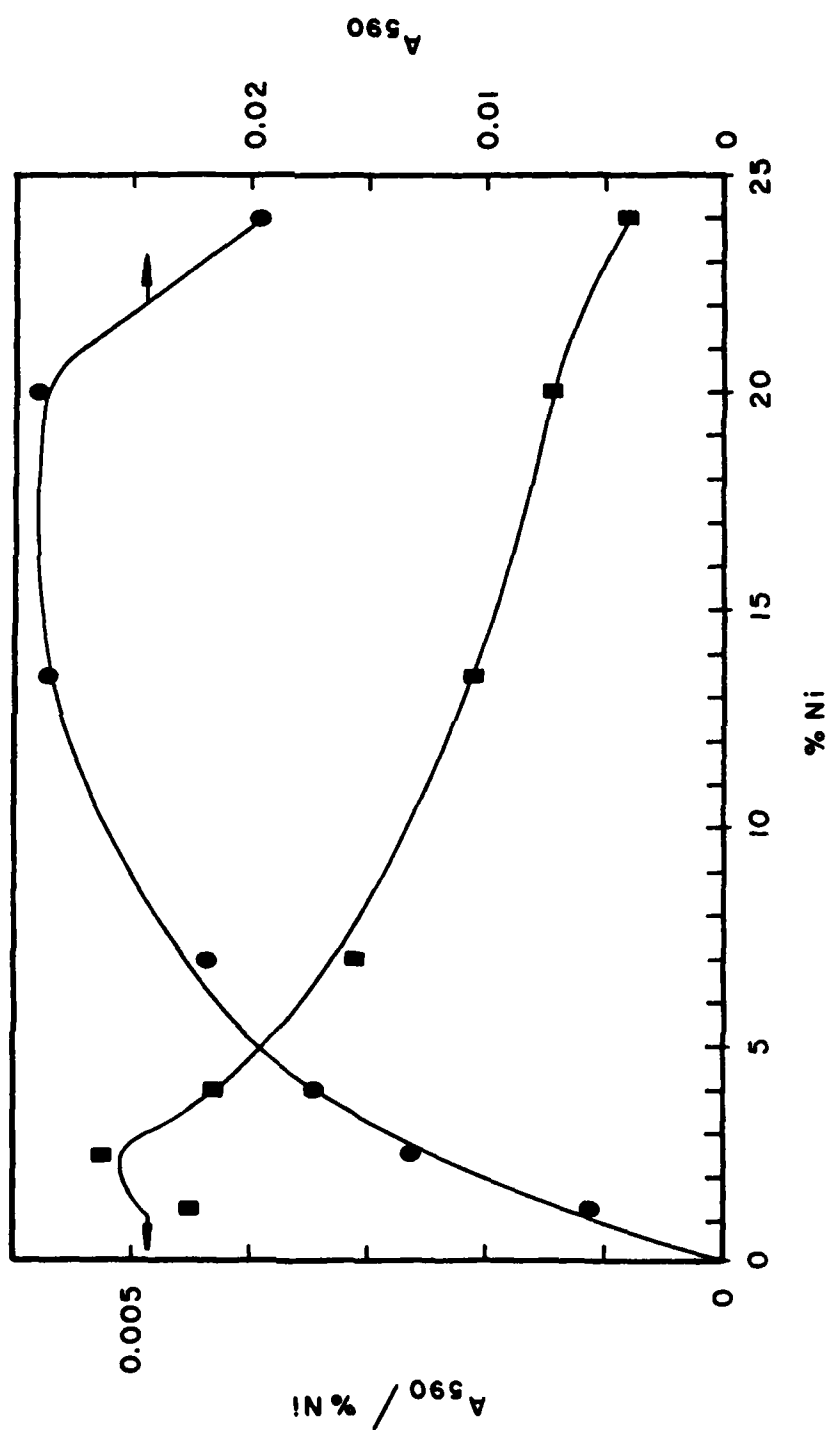
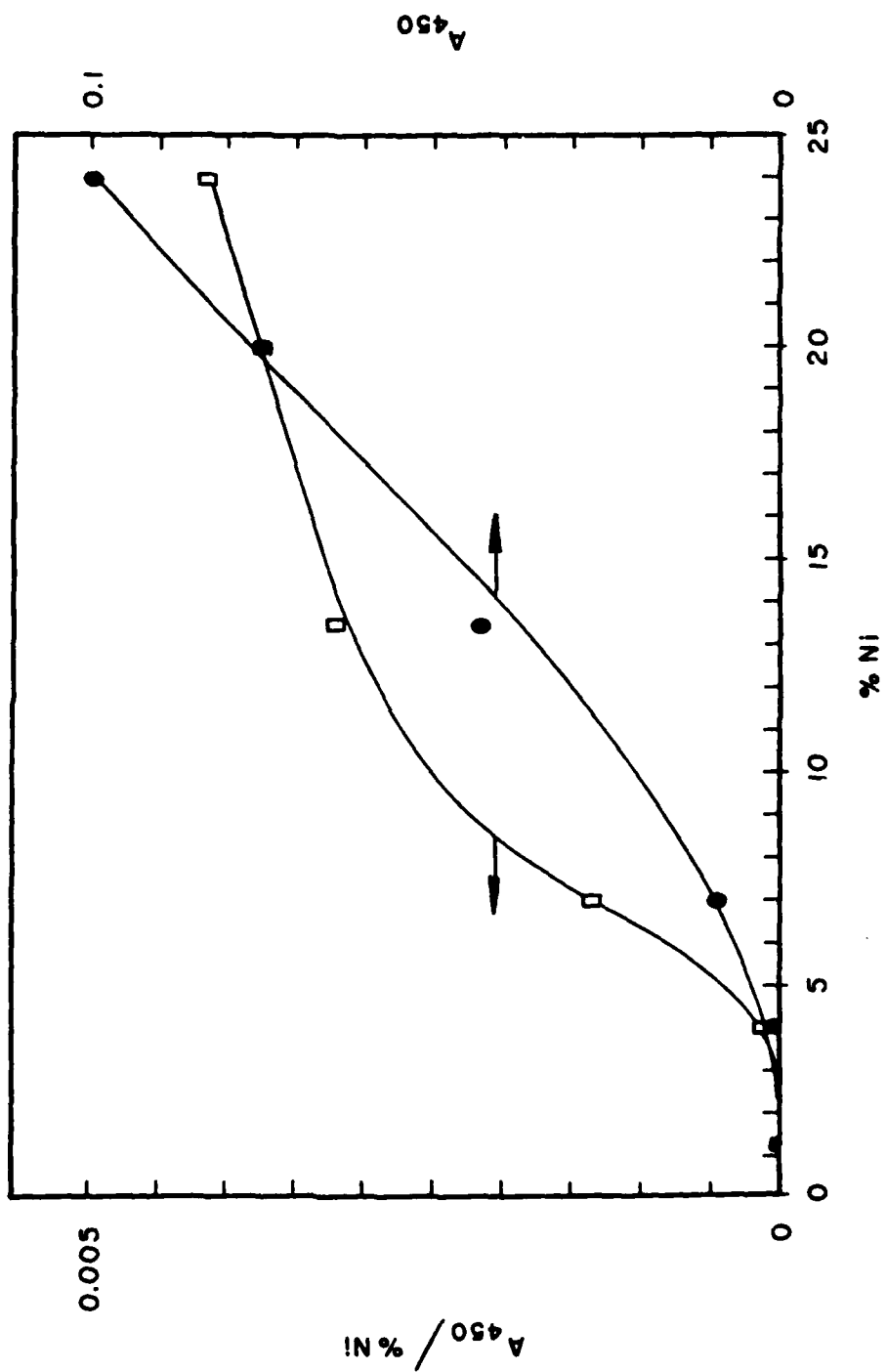


Figure 14. Net photoacoustic response function at 450 nm,  $A_{450}$ , and  $A_{450}/\% \text{ Ni}$  plotted versus percent of nickel in catalysts calcined at 600°C.



values of  $A_{590}$  and  $A_{450}$  at low nickel loading (<3%) where Ni(T) dominates and high nickel loading (20%) where Ni(O) dominates.

$$\frac{\left[ \frac{A_{590}}{a_T} + \frac{A_{450}}{a_0} \right]}{\% \text{ Ni}} = 1 \quad (4)$$

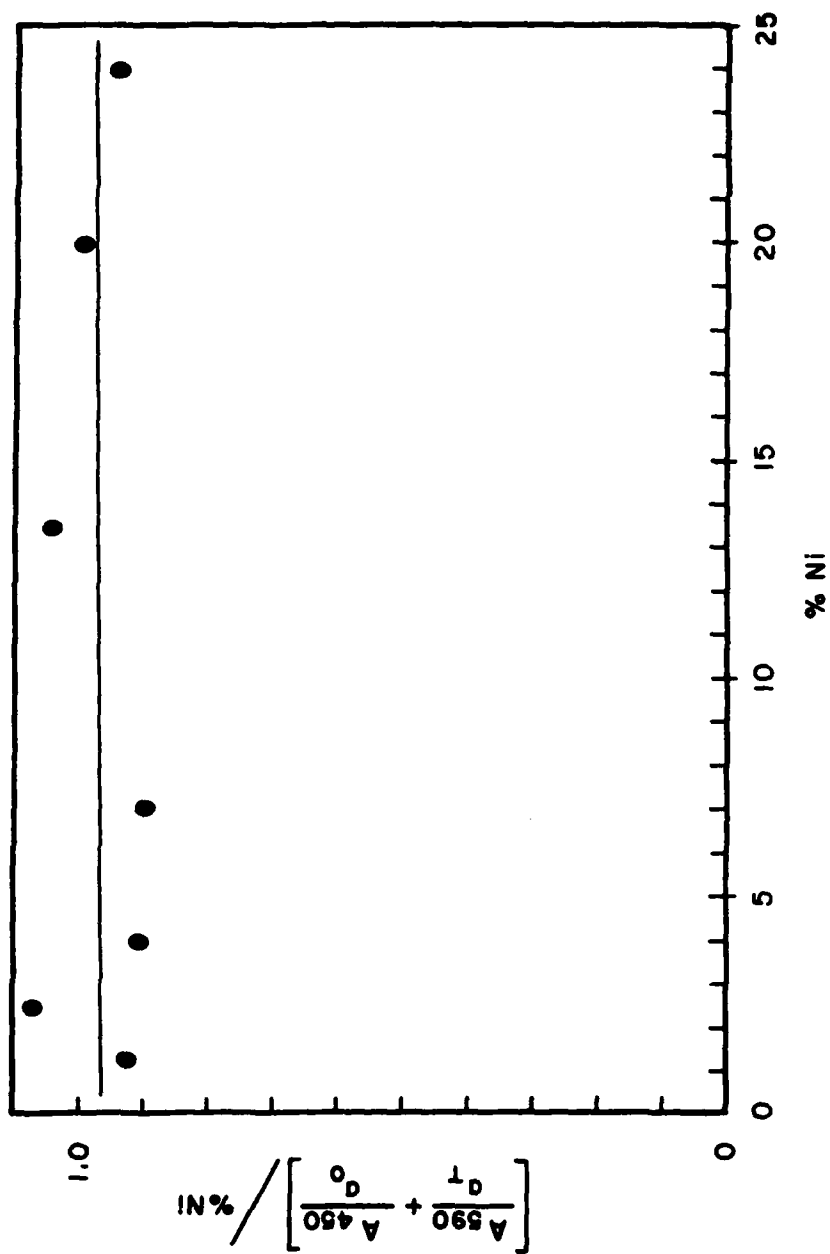
The values of the constants were found to be:  $a_T = 0.0049$  and  $a_0 = 0.0053$ . These values of  $a_T$  and  $a_0$  were used to compute the function used in Equation 4 for all the catalyst samples calcined at 600°C. This function is plotted versus percent nickel loading in Figure 15. The least-squares fit yields a standard deviation of 0.08, a slope of 0.007 and an intercept of 0.96. This result is consistent with the conclusion that Ni(O) and Ni(T) are the dominant species on the surface of these catalyst samples. Under this assumption the distribution ratio of Ni(T) to Ni(O) is found to vary from 1 : 0 for nickel loading less than 3% to 0.3 : 0.7 at 20% nickel loading. The latter value is close to the bulk ratio for the inverted bulk  $\text{NiAl}_2\text{O}_4$  spinel, 0.22 : 0.78.<sup>8</sup>

Conclusions. Several conclusions can be drawn from the photo-acoustic spectroscopy study of impregnated Ni/ $\gamma\text{-Al}_2\text{O}_3$  oxide catalysts correlated with surface spectroscopy results.

(1) For 600°C calcination temperature the distribution ratio of Ni(T) to Ni(O) varies from 1 : 0 for nickel loading less than 3% to 0.3 : 0.7 at 20% nickel loading.

(2) The amount of nickel existing as Ni(T) decreases with decreasing calcination temperature.

Figure 15. Sum of weighted photoacoustic response functions for Ni(T) and Ni(O) divided by percent of nickel plotted versus percent of nickel in catalysts calcined at 600°C.





(3) Nickel material exists on the surface having a spectrum not identified with Ni(T), Ni(O) or NiO for 400°C calcination temperature. This material was tentatively associated with the Ni(III) specie postulated by Hill and Selwood.<sup>14</sup>

(4) NiO segregates on the surface above 20% nickel loading for catalysts calcined at 400°C and 600°C. The Ni(T) signal is obscured by NiO formation.

#### Cobalt/ $\gamma$ -Alumina Catalysts

Surface spectroscopy investigations of the Co/ $\gamma$ -Al<sub>2</sub>O<sub>3</sub> catalyst system have offered evidence for significant metal-support interaction. In ESCA spectra of these catalysts,<sup>5</sup> the Co 2p<sub>3/2</sub> line became less symmetrical and shifted to lower binding energy with increasing cobalt loading. At low cobalt content the peak shape and binding energy resembled the tetrahedral CoAl<sub>2</sub>O<sub>4</sub> spinel; whereas, at high cobalt loading the peak shape and binding energy resembled Co<sub>3</sub>O<sub>4</sub>. The cobalt oxide, Co<sub>3</sub>O<sub>4</sub> is a normal spinel oxide having Co(II) ions in tetrahedral interstices and an equal number of Co(III) ions in octahedral interstices.<sup>17</sup> The ESCA Co 2p line of Co<sub>3</sub>O<sub>4</sub> corresponds to an unresolved cobaltous-cobaltic doublet. As the cobalt loading on  $\gamma$ -alumina was increased the cobaltic line was enhanced. Higher calcination temperature favored formation of the tetrahedral cobaltous specie, Co(T). Indirect evidence for octahedral cobalt on the catalyst surfaces was obtained from EXAFS.<sup>4</sup> The average coordination number increased from 4.2 at 2% cobalt content to 5.2 at 16% cobalt content. (The average coordination number in Co<sub>3</sub>O<sub>4</sub>

is 5.3.) The ESCA Co/Al intensity ratio increased gradually with metal loading up to 10% cobalt content. Above 10% cobalt loading the Co/Al intensity ratio was abruptly enhanced suggesting that a cobalt rich layer is formed at the surface. The ISS Co/Al intensity ratio shows a similar discontinuity at about 12% cobalt content.<sup>4</sup> The reduction studies showed a corresponding effect. The percent reducibility of cobalt steadily increased with cobalt loading up to 12% cobalt loading, above which the increase was much less pronounced.<sup>4</sup> A picture of cobalt speciation emerges in which Co(II) ions predominantly diffuse into tetrahedral  $\gamma$ -alumina surface sites at low cobalt loading. As the cobalt concentration on the surface increases, Co(III) occupies octahedral surface lattice sites; and above 12% cobalt content  $\text{Co}_3\text{O}_4$  segregates on the  $\gamma$ -alumina surface. Again, the photoacoustic spectroscopy results are interpreted in terms of these ideas.

Qualitative PAS Results. Photoacoustic spectra of reference materials were recorded for comparison with catalyst spectra. In Figure 16 the photoacoustic spectrum of  $\text{CoAl}_2\text{O}_4$  physically diluted to 1% with  $\gamma$ -alumina is presented. The broad absorption band centered at 590 nm is due to the  $^4\text{A}_2 \rightarrow ^4\text{T}_1(\text{P})$  transition for the tetrahedrally coordinated Co(II).<sup>18</sup> The visible photoacoustic spectrum of  $\text{Co}_3\text{O}_4$  physically diluted to 0.5% with  $\gamma$ -alumina is shown in Figure 17. The two broad bands centered at approximately 420 nm and 680 nm are due to  $^1\text{A}_{1\text{g}} \rightarrow ^1\text{T}_{1\text{g}}$  and  $^1\text{A}_{1\text{g}} \rightarrow ^1\text{T}_{2\text{g}}$  transitions, respectively, for octahedrally coordinated Co(III).<sup>19</sup> In CoO (NaCl structure) the Co(II) is octahedrally coordinated. The spectrum of CoO enhanced cobalt oxide is also shown in

Figure 16. Photoacoustic spectrum of 1%  $\text{CoAl}_2\text{O}_4$  ground in  $\gamma\text{-Al}_2\text{O}_3$ .

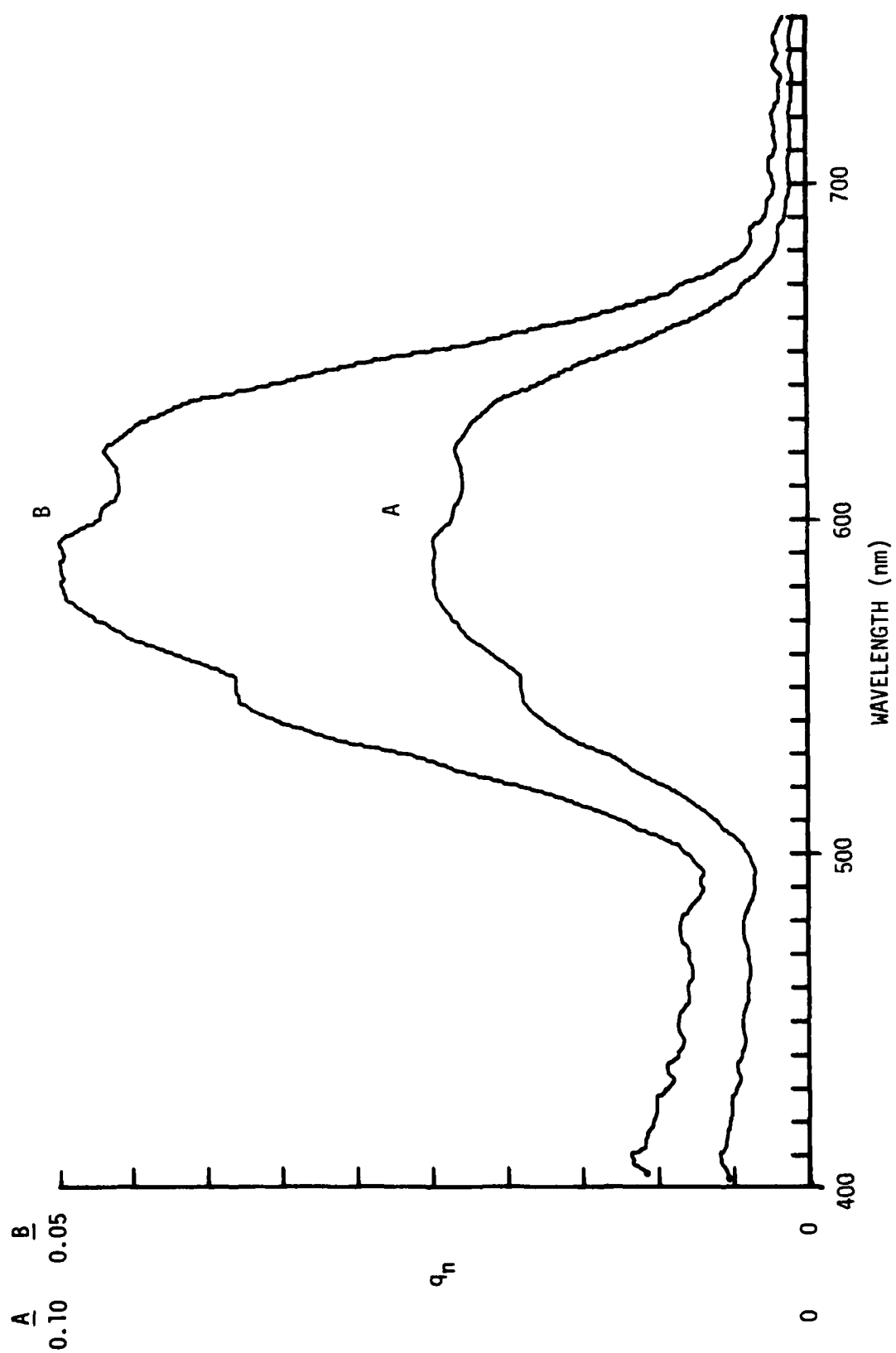


Figure 17. Photoacoustic spectrum of (I)  $\text{Co}_3\text{O}_4$  ground with  $\gamma$ -alumina and (II) CoO-enhanced cobalt oxide ground with  $\gamma$ -alumina.

I

215

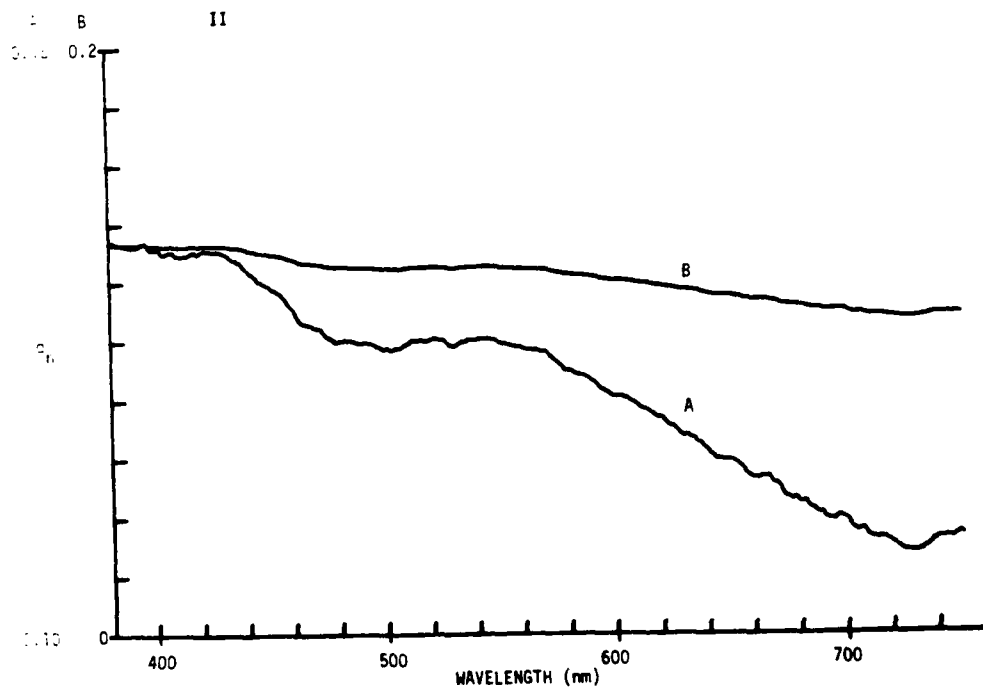
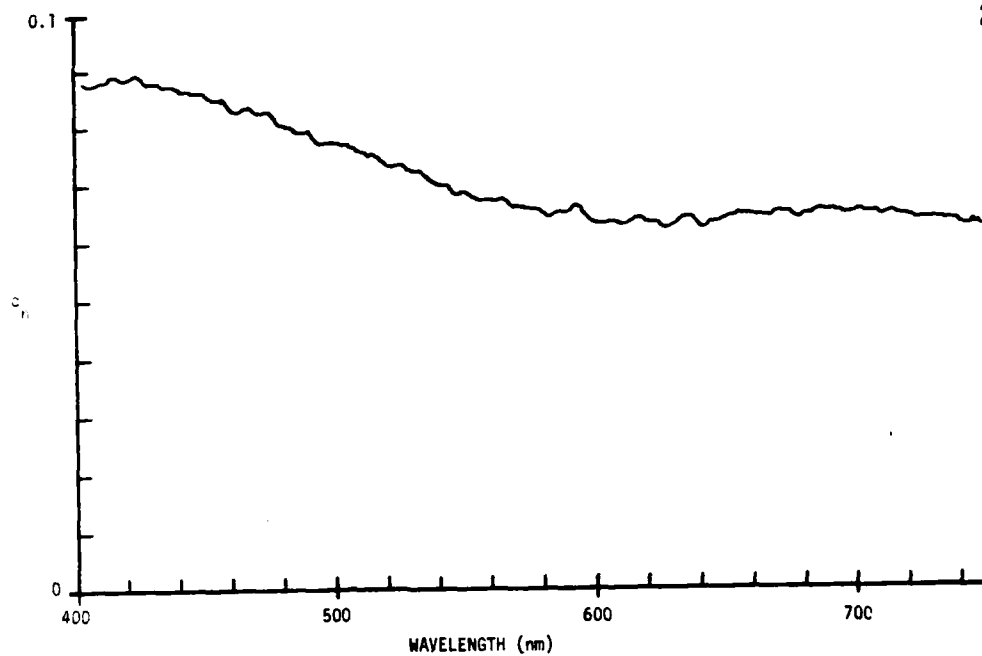


Figure 17. The new band at about 530 nm arises from the  ${}^4T_{1g}(F) \rightarrow {}^4T_{1g}(P)$  transition of octahedrally coordinated Co(II).<sup>18</sup> For comparison, spectra of  $\text{Co}(\text{NO}_3)_2 \cdot 6\text{H}_2\text{O}$  and  $\text{Co}(\text{CH}_3\text{COCHCOCH}_3)_3$  diluted in  $\gamma$ -alumina are given in Figures 18 and 19 as examples of octahedrally coordinated Co(II) and Co(III), respectively.

In Figure 20 selected spectra of  $\text{Co}/\gamma\text{-Al}_2\text{O}_3$  catalysts calcined at  $600^\circ\text{C}$  are shown. At 0.5% cobalt loading the spectrum is very similar to that of  $\text{CoAl}_2\text{O}_4$  except that the Co(T) spectrum is shifted to lower wavelengths by approximately 6 nm as compared to that of bulk  $\text{CoAl}_2\text{O}_4$ , just as in the case of the  $\text{Ni}/\gamma\text{-Al}_2\text{O}_3$  system. Again, it is concluded that the surface tetrahedral sites experience a slightly larger ligand field at surface of the  $\gamma$ -alumina than in the bulk material. For cobalt loadings larger than 1%, the catalyst spectrum is dominated by a spectrum similar to  $\text{Co}_3\text{O}_4$ . Above 12% cobalt content the visible catalyst spectrum is indistinguishable from that of  $\text{Co}_3\text{O}_4$ .

In Figure 21 selected spectra of  $\text{Co}/\gamma\text{-Al}_2\text{O}_3$  catalysts calcined at  $400^\circ\text{C}$  are shown. Unlike the  $\text{Ni}/\gamma\text{-Al}_2\text{O}_3$  system, the spectral differences with calcination temperature are only differences of relative magnitude, not differences of kind. In the catalysts calcined at  $400^\circ\text{C}$  the Co(T) component is smaller than in catalysts calcined at  $600^\circ\text{C}$ . A difference spectrum accentuates the effect of calcination temperature on catalyst spectra. In Figure 22 a difference spectrum is shown for two catalysts loaded with 0.5% cobalt in which the spectrum of the catalyst calcined at  $400^\circ\text{C}$  is subtracted from the spectrum of the catalyst calcined at  $600^\circ\text{C}$ . The spectral feature labeled Co(O) is consistent with an

Figure 18. Photoacoustic spectrum of 20%  $\text{Co}(\text{NO}_3)_2 \cdot 6 \text{H}_2\text{O}$  ground with  $\gamma$ -alumina with background subtracted.



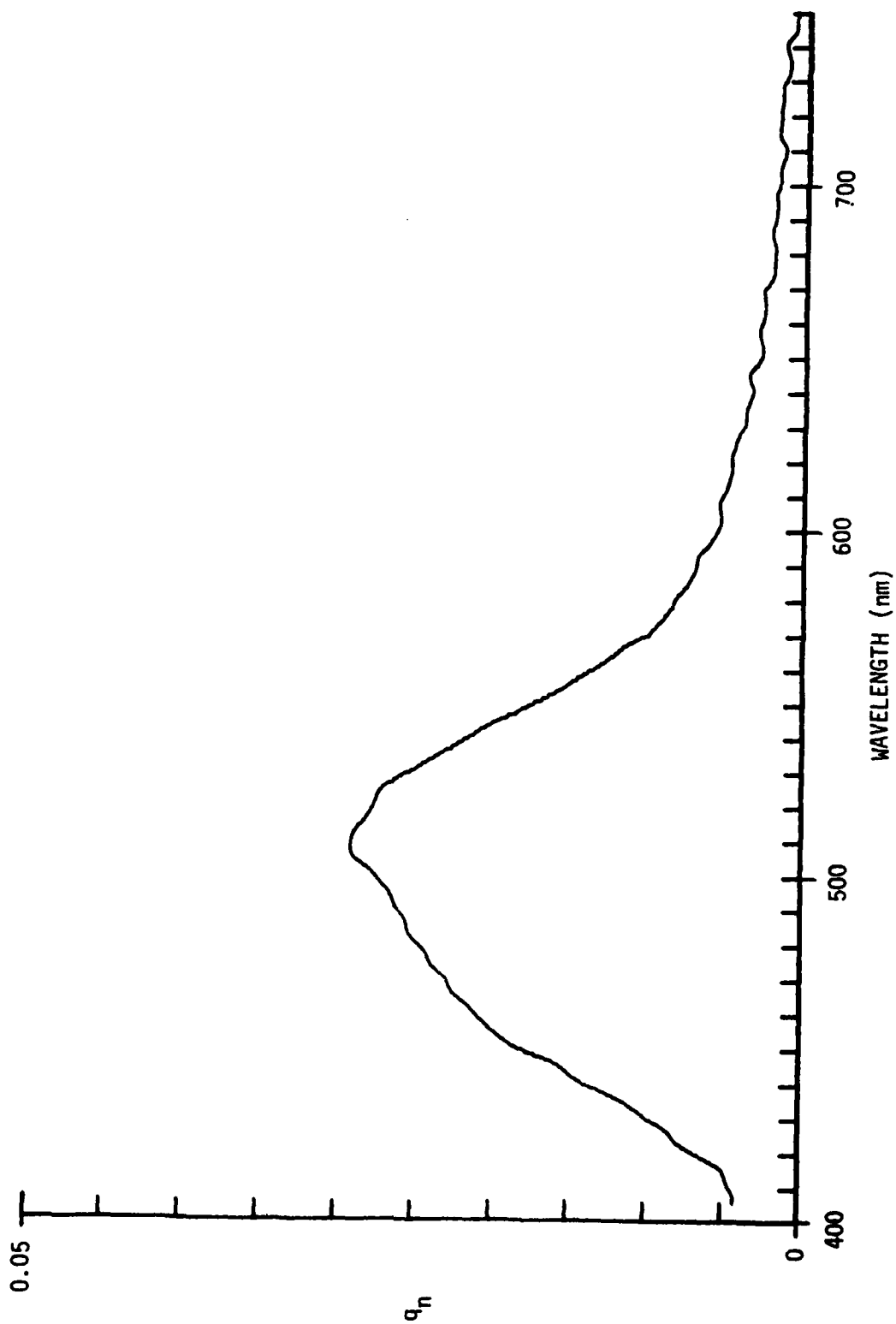


Figure 19. Photoacoustic spectrum of 5%  $\text{Co}(\text{CH}_3\text{COCHCOCH}_3)_3$  ground with  $\gamma$ -alumina.

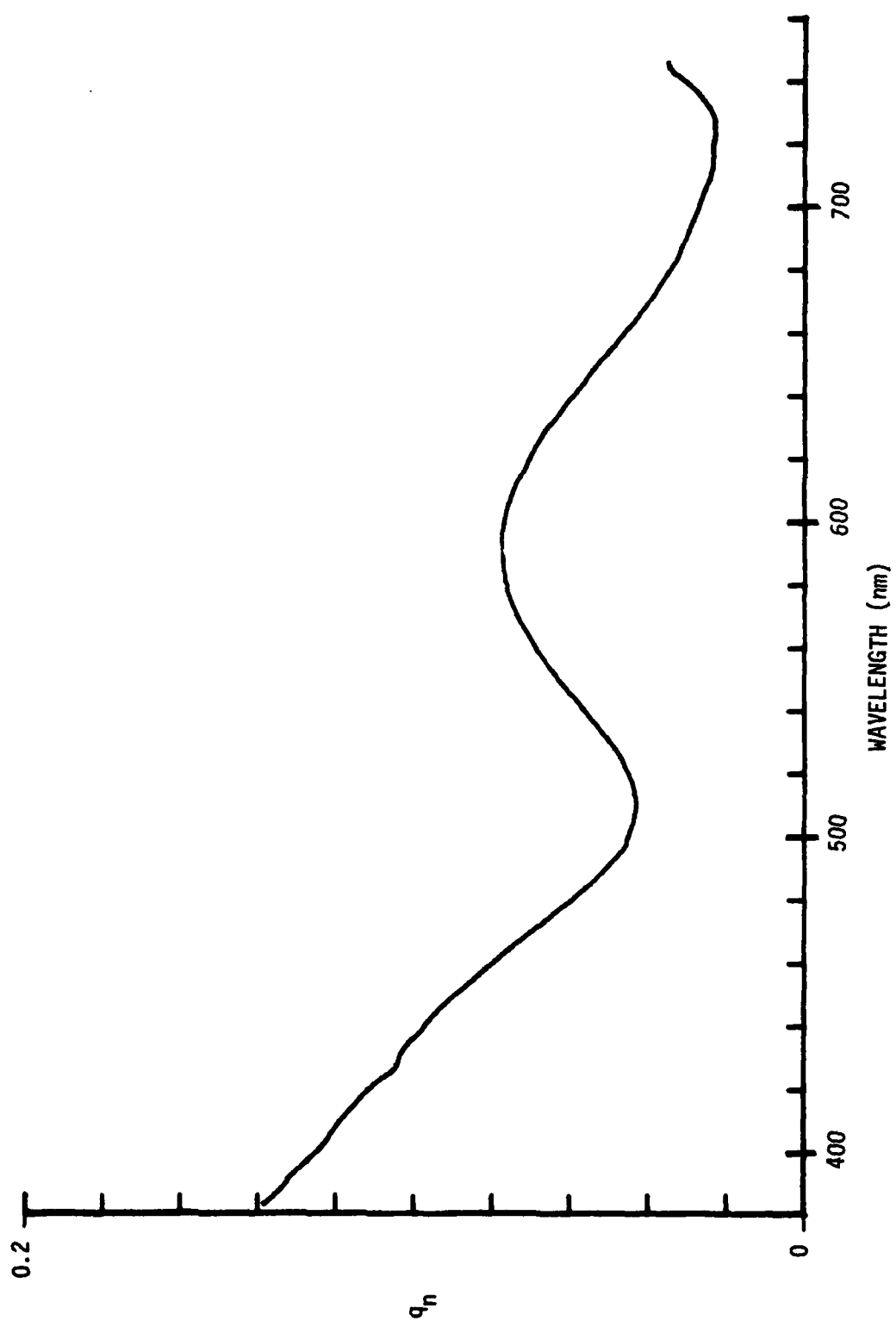


Figure 20. Photoacoustic spectra of  $\text{Co}/\gamma\text{-Al}_2\text{O}_3$  catalysts calcined at  $600^\circ\text{C}$ .

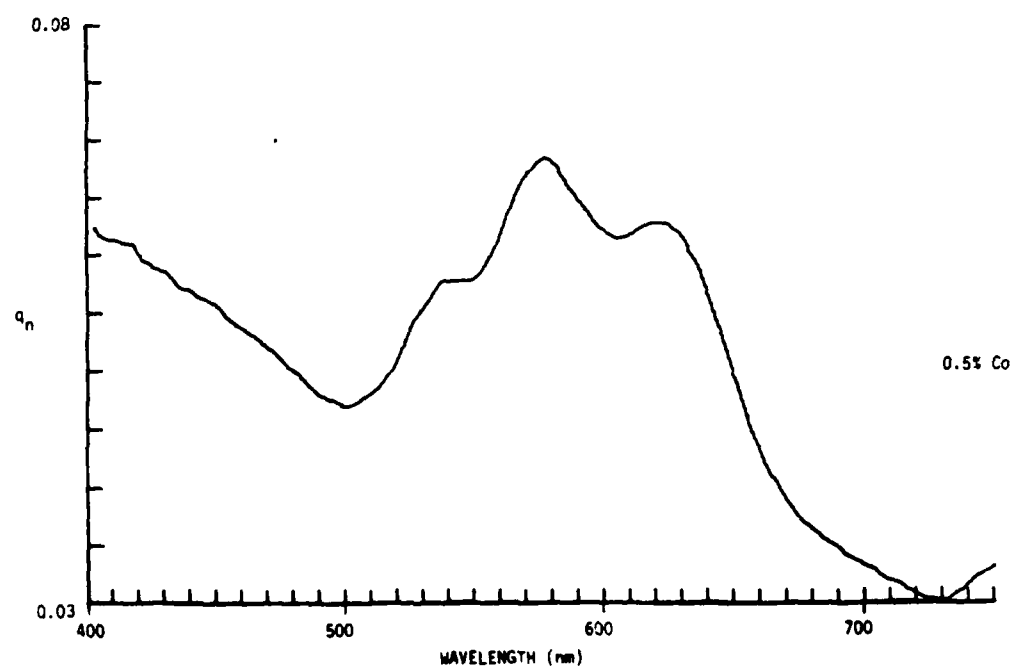
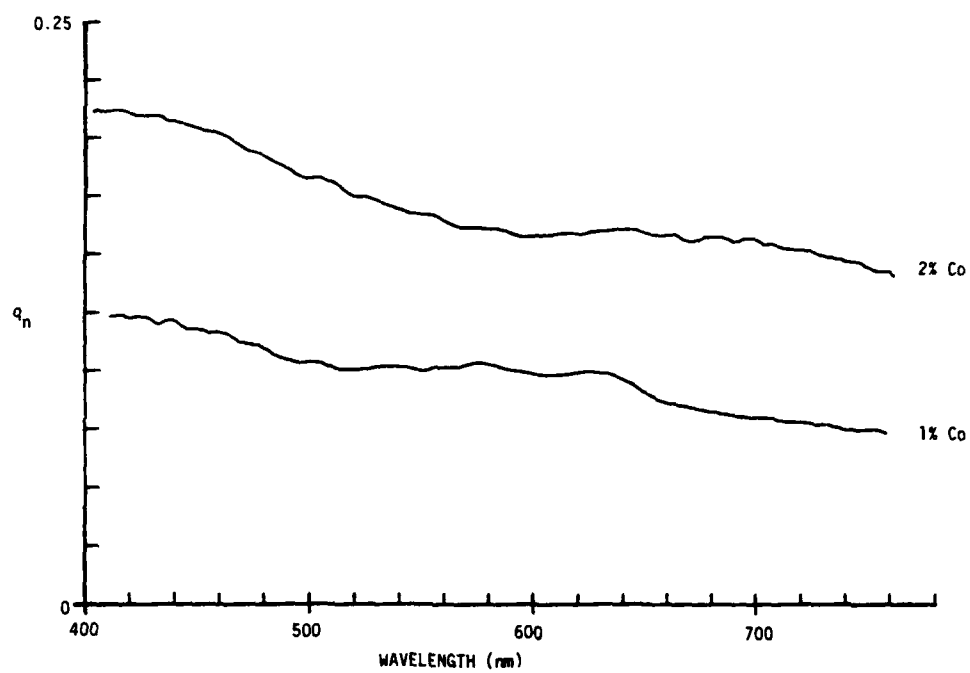


Figure 21. Photoacoustic spectra of  $\text{Co}/\gamma\text{-Al}_2\text{O}_3$  catalysts calcined at  $400^\circ\text{C}$ .

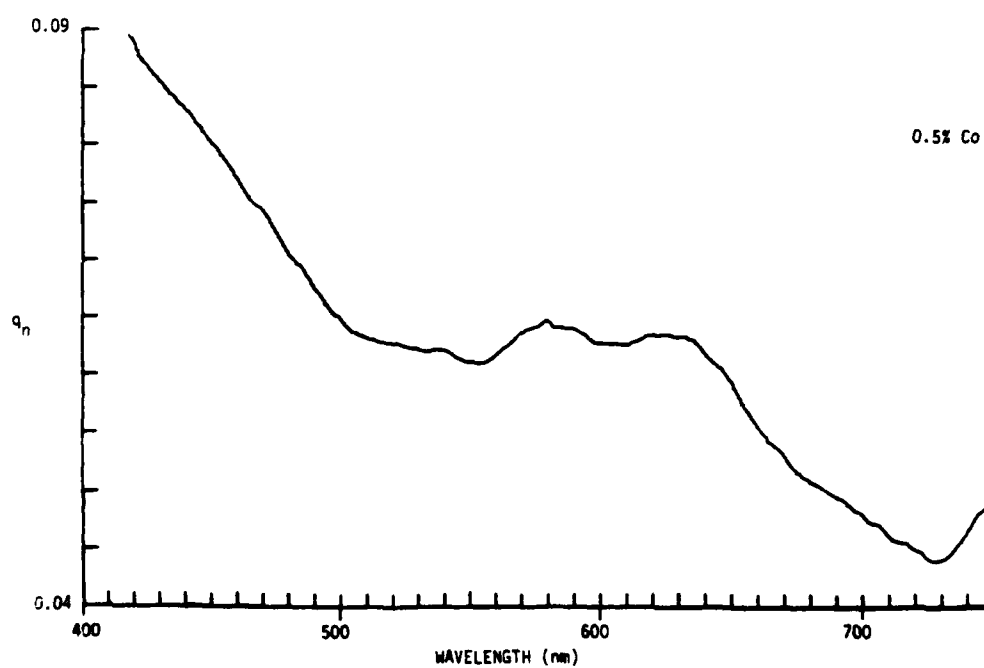
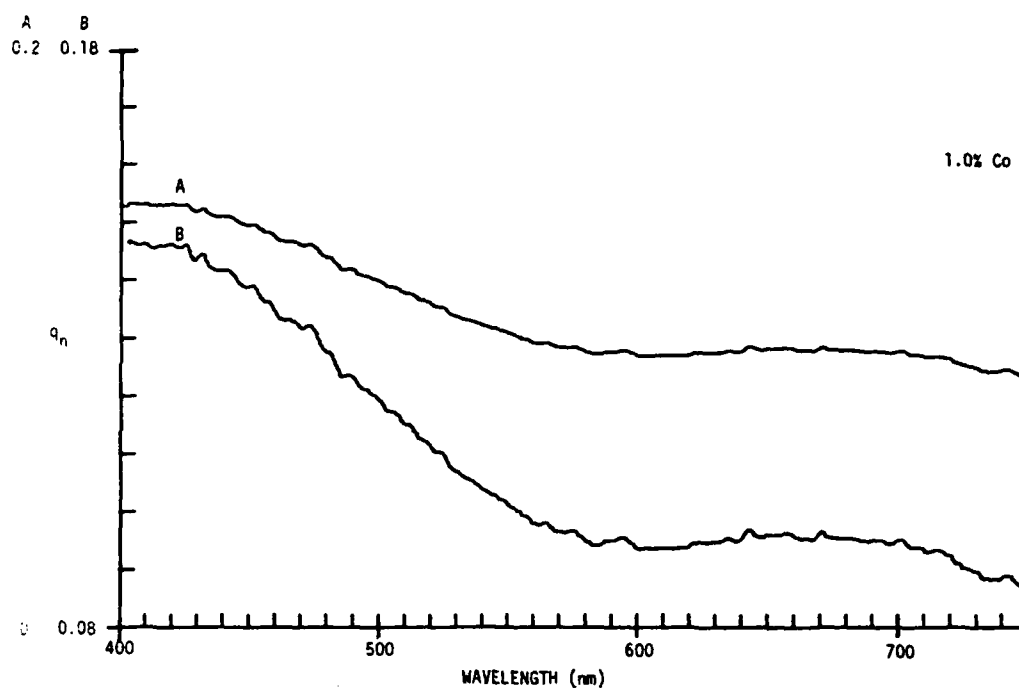
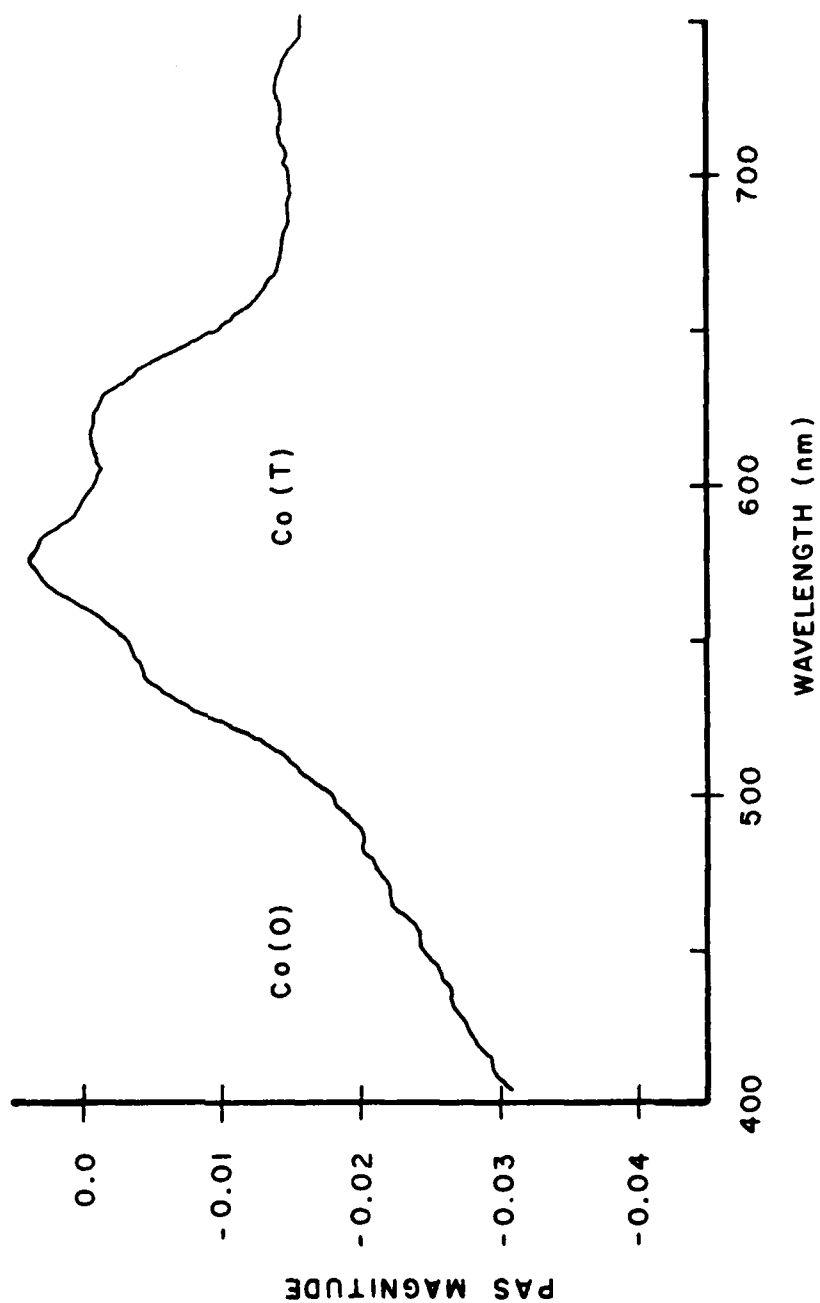


Figure 22. Difference spectrum for 0.50% Co/ $\gamma$ -Al<sub>2</sub>O<sub>3</sub> catalysts in which the spectrum of the catalyst calcined at 400°C is subtracted from that of the catalyst calcined at 600°C.





assignment of the  ${}^1A_{1g} \rightarrow {}^1T_{2g}$  transition of octahedrally coordinated Co(III). There is no evidence for octahedral Co(II). The assignments for Co(T) and Co(O) are in agreement with those made by Asmolov and Krylov in the diffuse reflectance spectroscopy study of the Co/ $\gamma$ -Al $_2$ O $_3$  system.<sup>20</sup>

Quantitative PAS Results. In this case there are no visible spectral features which can be used to differentiate between Co(O) and Co $_3$ O $_4$ . However, the Co(O) feature is especially enhanced compared to the Co $_3$ O $_4$  spectrum. As in the case of the Ni/ $\gamma$ -Al $_2$ O $_3$  system, measures of the absorbance due to Co(T) and Co(O) species are determined. The enhanced absorbance of Co(T) above the estimated absorbance of octahedral species is designated  $A_{578}$ ,

$$A_{578} = C\beta_{\mu_s}(578) - \left[ \frac{C\beta_{\mu_s}(\text{Co}_3\text{O}_4, 578)}{C\beta_{\mu_s}(\text{Co}_3\text{O}_4, 722)} \right] C\beta_{\mu_s}(722) \quad (5)$$

where  $C\beta_{\mu_s}(578)$  and  $C\beta_{\mu_s}(722)$  are photoacoustic response functions for catalysts at 578 nm and 722 nm, respectively.  $C\beta_{\mu_s}(\text{Co}_3\text{O}_4, 578)$  and  $C\beta_{\mu_s}(\text{Co}_3\text{O}_4, 722)$  are photoacoustic response functions for Co $_3$ O $_4$  in  $\gamma$ -alumina at 578 nm and 722 nm, respectively. In a similar way the enhanced absorbance at 420 nm,  $A_{420}$ , associated with the Co(O) specie is calculated:

$$A_{420} = C\beta_{\mu_s}(420) - \left[ \frac{C\beta_{\mu_s}(\text{Co}_3\text{O}_4, 420)}{C\beta_{\mu_s}(\text{Co}_3\text{O}_4, 722)} \right] C\beta_{\mu_s}(722) \quad (6)$$

The terms used in Equation 6 are defined in an analogous way to those in Equation 5.

In Figure 23,  $A_{578}$  and  $A_{578}/\% \text{ Co}$  are plotted versus percent of cobalt in catalysts calcined at  $400^{\circ}\text{C}$  and  $600^{\circ}\text{C}$ . The amount of  $\text{Co(T)}$  climbs to a plateau at about 2% cobalt content. The fraction of cobalt existing as  $\text{Co(T)}$  is greatest below 2% cobalt content. As expected, higher calcination temperature enhances  $\text{Co(T)}$  formation. The average ratio of  $\text{Co(T)}$  formed at  $600^{\circ}\text{C}$  compared to  $400^{\circ}\text{C}$  is 0.70. From this ratio an approximate activation energy for  $\text{Co(T)}$  formation relative to the formation of  $\text{Co(O)}$  is calculated to be 2.1 kcal/mol. For catalysts calcined both at  $400^{\circ}\text{C}$  and  $600^{\circ}\text{C}$  the  $\text{Co(T)}$  signal,  $A_{578}$ , decreases at 12% cobalt content. This suggests that the tetrahedral component is optically masked by the oxide phase at 12% cobalt content, analogous to the  $\text{Ni}/\gamma\text{-Al}_2\text{O}_3$  system. This is in complete agreement with the interpretation of ESCA, ISS and reduction study results.<sup>5</sup>

In Figure 24,  $A_{420}$  and  $A_{420}/\% \text{ Co}$  are plotted versus the percent of cobalt in catalysts calcined at  $400^{\circ}\text{C}$  and  $600^{\circ}\text{C}$ . There is little  $\text{Co(O)}$  formed for cobalt content less than 2% where  $\text{Co(T)}$  is greatest. The fraction of cobalt existing as  $\text{Co(O)}$  increases steadily up to approximately 2% cobalt content beyond which the fraction is insensitive to cobalt loading. At both calcination temperatures the quantity of  $\text{Co(O)}$  increases in a nearly linear way for cobalt loading greater than 2%. This is in good agreement with the reduction study.<sup>5</sup> The average ratio of  $\text{Co(O)}$  formed at  $400^{\circ}\text{C}$  compared to  $600^{\circ}\text{C}$  is 0.65. From this ratio an approximate activation energy for  $\text{Co(O)}$  formation relative to  $\text{Co(T)}$

Figure 23. Net photoacoustic response function at 578 nm,  $A_{578}$ , and  $A_{578}/\% \text{ Co}$  plotted versus percent of cobalt in catalysts calcined at 400°C (■) and 600°C (●).

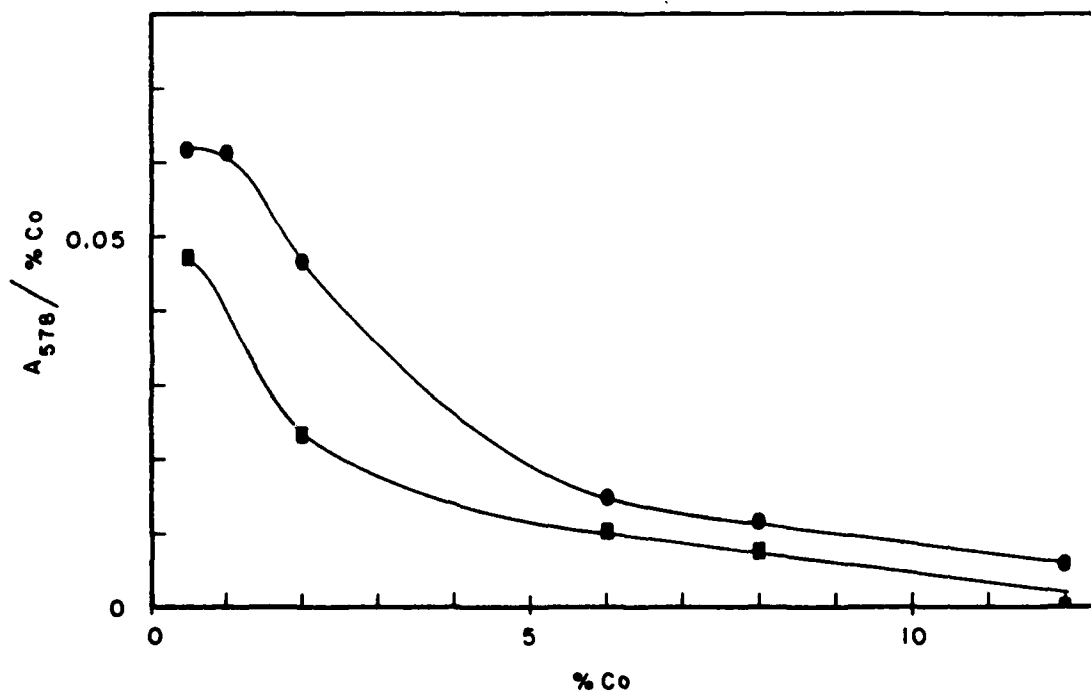
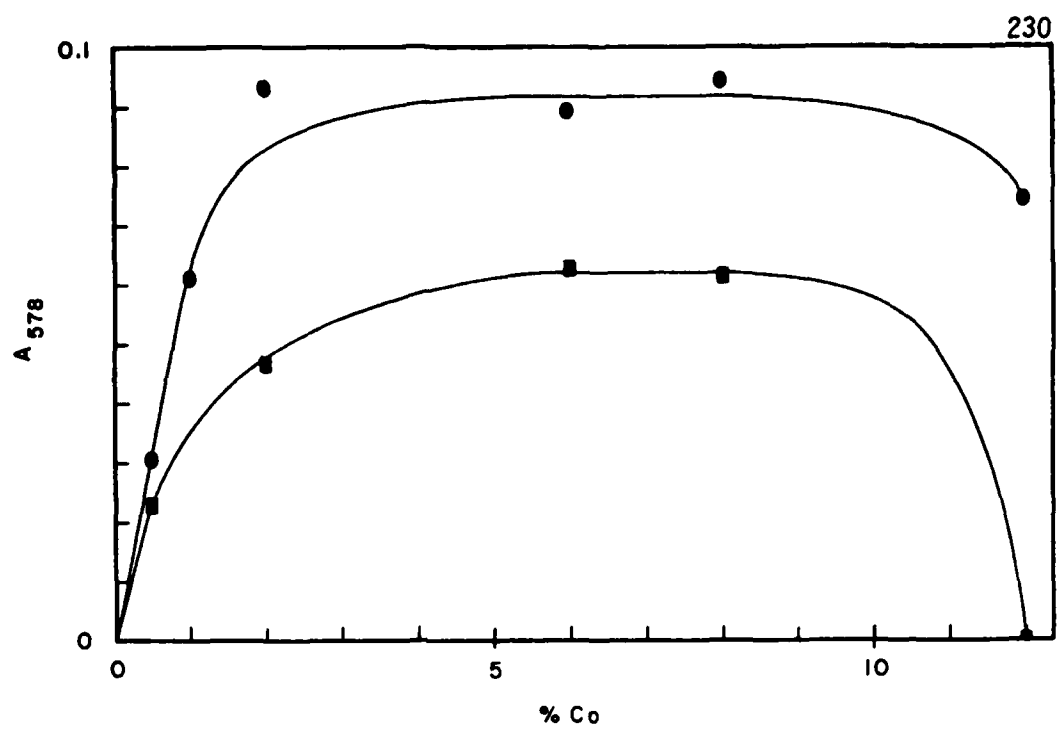
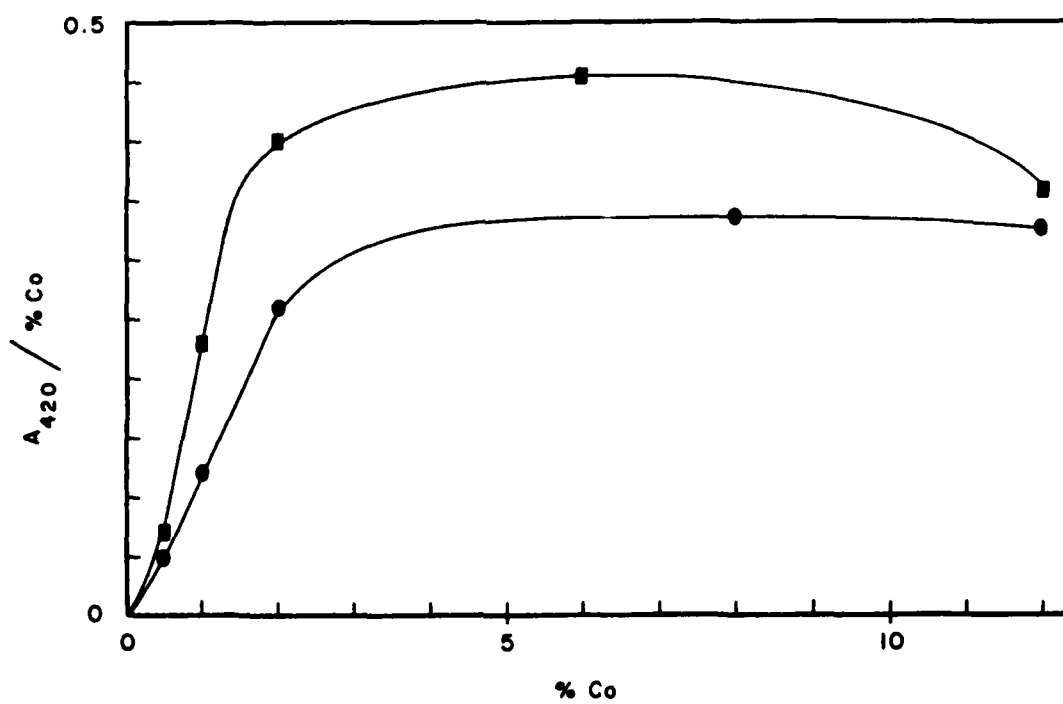
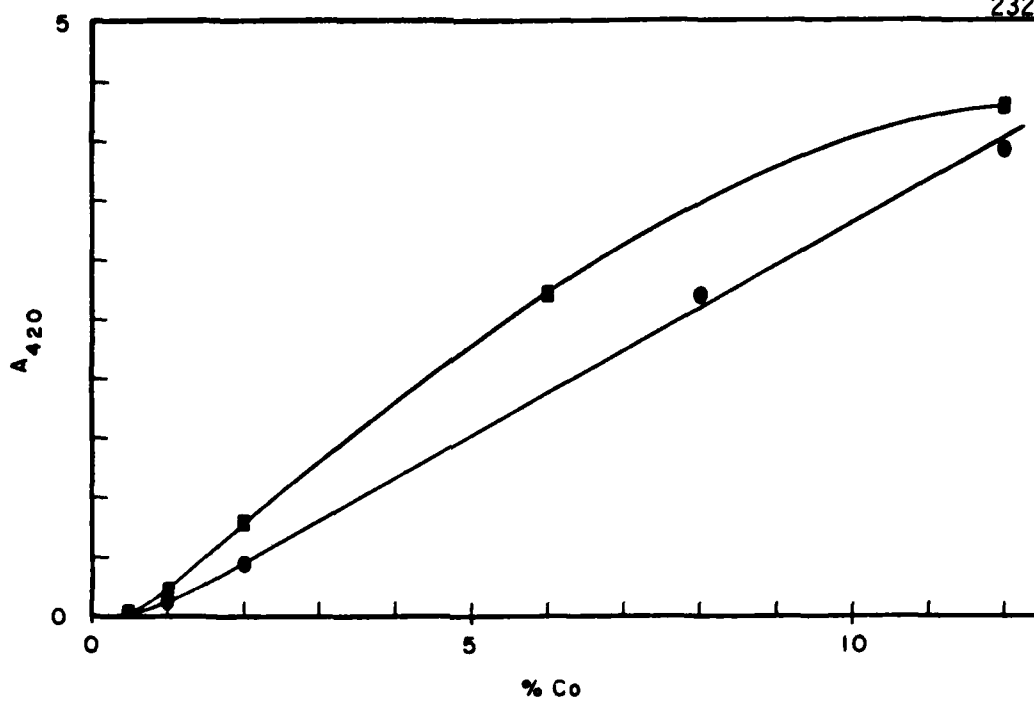


Figure 24. Net photoacoustic response function at 420 nm,  $A_{420}$ , and  $A_{420}/\%$  Co plotted versus percent of cobalt in catalysts calcined at 400°C (■) and 600°C (●).



formation is calculated to be -2.5 kcal/mol. This is in excellent agreement with the relative activation energy calculated from the Co(T) data.

By assuming that only Co(O) and Co(T) are the only species which make significant contribution to the visible absorption, Equation 7 was solved for  $a_T$  and  $a_O$  using values of  $A_{578}$  and  $A_{420}$  at low cobalt loading ( $\leq 1\%$  Co) and high cobalt loading (8% Co). The values of  $a_T$  and  $a_O$  were calculated to be 0.069 and 0.43, respectively.

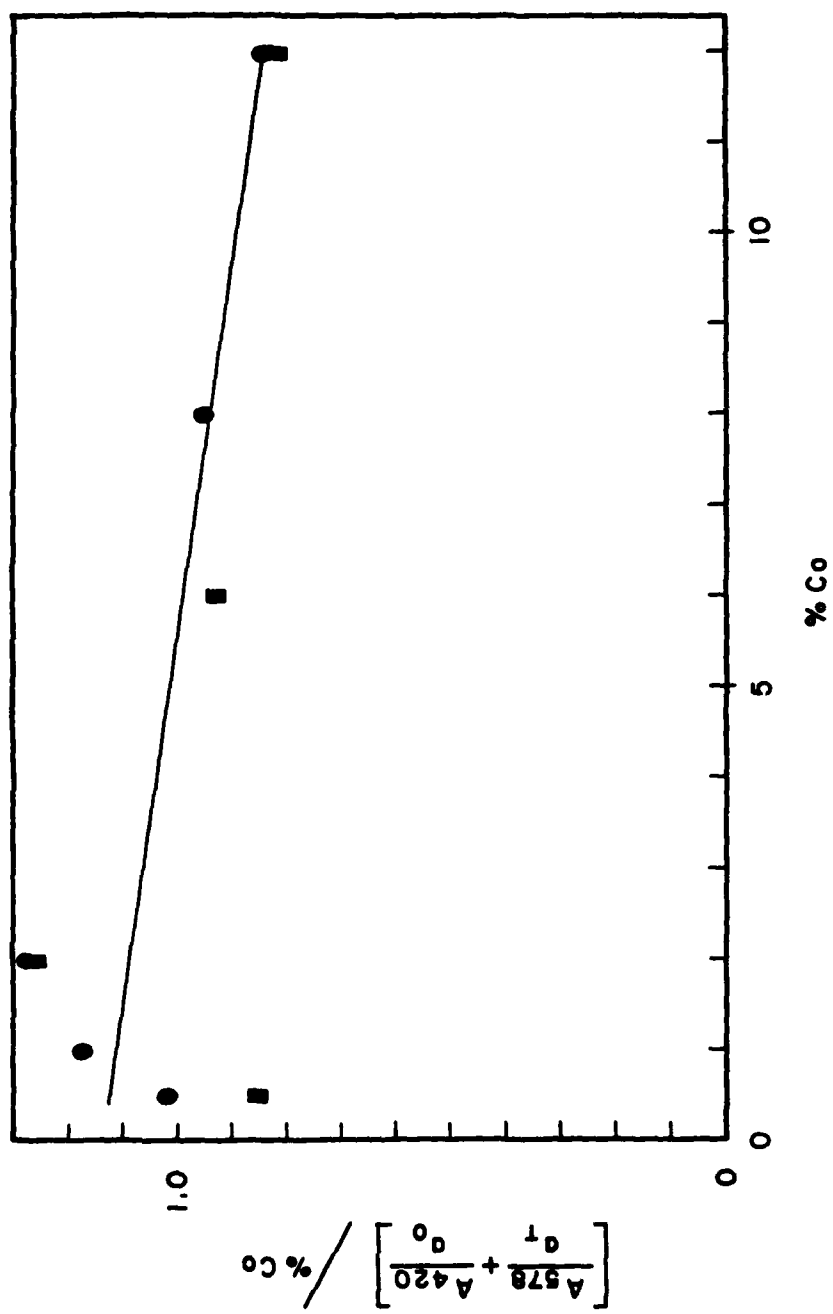
$$\left[ \frac{A_{578}}{a_T} + \frac{A_{420}}{a_O} \right] \frac{1}{\% \text{ Co}} = 1 \quad (7)$$

The function in Equation 7 is plotted versus the percent of cobalt in Figure 25. The significance of the negative slope is uncertain. However, based on a report of  $\text{Co}_3\text{O}_4$  detected by x-ray diffraction on Co/ $\gamma$ - $\text{Al}_2\text{O}_3$  catalysts with cobalt content as low as 2%,<sup>21</sup> the negative slope may reflect the unaccounted contribution of oxide material. Using the calculated values of  $a_T$  and  $a_O$ , the distribution ratio of Co(T) to Co(O) was found to vary from 0.9 : 0.1 for 0.5% cobalt content to 0.2 : 0.8 for 8.0% cobalt content at 600°C calcination temperature. For catalysts calcined at 400°C, the ratio of Co(T) to Co(O) was found to vary from approximately 0.8 : 0.2 for 0.5% cobalt content to 0.1 : 0.9 for 8.0% content.

**Conclusions:** A summary of the conclusions for the photoacoustic spectroscopy study of impregnated Co/ $\gamma$ - $\text{Al}_2\text{O}_3$  oxide catalysts, correlated



Figure 25. Sum of weighted photoacoustic response functions for Co(T) and Co(O) divided by percent of cobalt plotted versus percent of cobalt in catalysts calcined at 400°C (■) and 600°C (●).



with surface spectroscopy results, are listed below.

(1) Spectral features in the visible photoacoustic spectra were identified with tetrahedral Co(II), designated Co(T), and octahedral Co(III), designated Co(O).

(2) The Co(T) to Co(O) ratio in Co/ $\gamma$ -Al<sub>2</sub>O<sub>3</sub> catalysts is consistently larger for catalysts calcined at 600°C as compared to those calcined at 400°C. An apparent activation energy for Co(T) formation relative to Co(O) formation was found to be approximately  $2.3 \pm 0.5$  kcal/mol.

(3) The ratio of Co(T) to Co(O) diminished steadily with increasing cobalt loading. For 600°C calcination temperature, the Co(T) to Co(O) ratio varied from 0.9 : 0.1 at 0.5% cobalt content to 0.2 : 0.8 at 8.0% cobalt content.

(4) Masking of the Co(T) signal at 12% cobalt content was associated with Co<sub>3</sub>O<sub>4</sub> segregation on the catalyst surface.

#### Cobalt-Molybdenum/ $\gamma$ -Alumina Catalysts

The role of cobalt in Co-Mo/ $\gamma$ -Al<sub>2</sub>O<sub>3</sub> hydrodesulphurisation catalysts is not known with certainty. It is known that various molybdenum compounds are catalytically active in the desulphurisation process while cobalt compounds which contain no molybdenum are not catalytically active. However, the presence of cobalt enhances the catalytic activity. For example, cobalt molybdate is superior in activity to CoO and MoO<sub>3</sub> alone or as a mixture. The most active catalysts are those prepared by impregnation of alumina with solutions of ammonium

molybdate and a cobalt salt, followed by drying and calcining. Thus, the activity of the catalyst is associated with the presence of both molybdenum and cobalt.<sup>22</sup> Many theories, some conflicting, have been proposed to explain the role of cobalt as a catalysis promotor. Massoth has reviewed some of these.<sup>21</sup> He concludes that none are entirely satisfactory. In the words of P. C. H. Mitchell,<sup>22</sup> "A problem of fundamental importance is whether the arrangement of cobalt and molybdenum atoms on the surface of the catalyst is determined by the structure of the alumina surface or by the possibility of forming cobalt-molybdenum oxides during calcining. Since the method of preparing the catalysts has an important effect on its activity a study of the interaction of alumina with cobalt and molybdenum compounds would be worthwhile." This short study does not propose to solve this long-standing problem; rather, a qualitative study of a series of Co-Mo/ $\gamma$ -Al<sub>2</sub>O<sub>3</sub> catalysts was performed to determine if photoacoustic spectroscopy might provide useful information about the nature of precursors of the catalytically active surface species.

For the purpose of studying cobalt interaction with the alumina support and molybdenum, a series of Co-Mo/ $\gamma$ -Al<sub>2</sub>O<sub>3</sub> catalysts were prepared by sequential impregnation of  $\gamma$ -Al<sub>2</sub>O<sub>3</sub> with molybdenum and cobalt. All the catalysts in this series were first loaded with molybdenum, 15% molybdenum as MoO<sub>3</sub>. (The final molybdenum loading on the catalysts was found to be 14.2% molybdenum as MoO<sub>3</sub>.) Calcining this material produces what is believed to be a monolayer of MoO<sub>3</sub> on the alumina surface.<sup>21</sup> Samples of molybdenum-loaded alumina were impregnated with

various amounts of cobalt nitrate and calcined. The competition between the cobalt interaction with the  $\text{MoO}_3$  layer and the  $\gamma\text{-Al}_2\text{O}_3$  support was of interest. It is known that for silica supports, for which cobalt-support interaction is small,  $\text{CoMoO}_4$  is formed on the catalyst surface. For alumina-supported cobalt catalysts the cobalt-alumina interaction is large.<sup>23</sup> The presence of  $\text{CoMoO}_4$  has been proposed, but it has not been convincingly demonstrated.

Qualitative PAS Results. The visible photoacoustic spectrum of 6%  $\text{CoMoO}_4$  in  $\gamma$ -alumina is shown in Figure 26. The spectrum is characterized by an absorption maximum centered at about 570 nm, with spin-orbit splitting features at 528 nm, 560 nm and 584 nm. These spectral features are sufficiently well separated from the spin-orbit triplet of  $\text{Co(T)}$  to permit a qualitative statement about the cobalt species which is dominant in the visible spectrum. Figure 27 compares the photoacoustic spectra of  $\text{Co-Mo}/\gamma\text{-Al}_2\text{O}_3$  catalysts. It is apparent that at 9% cobalt (as  $\text{CoO}$ ) the spectrum becomes dominated by the broad-band absorbance of  $\text{Co}_3\text{O}_4$  just as for large cobalt loading of  $\gamma\text{-Al}_2\text{O}_3$  alone. For cobalt loadings less than 9% the spectrum resembles that of the  $\text{Co(T)}$  spinel. There is no evidence for  $\text{Co(O)}$  buildup. For 1% cobalt the spectrum appears to be intermediate between that of a surface spinel and a bulk spinel as suggested in Table 2. Although this evidence is not conclusive, it would not be unexpected for the  $\text{Co(T)}$  to be buried beneath the  $\text{MoO}_3$  phase. This would also reduce formation of  $\text{Co(O)}$  at the surface. At 7% cobalt loading minor spectral features are

Figure 26. Photoacoustic spectrum of 6%  $\text{CoMoO}_4$  in  $\gamma\text{-Al}_2\text{O}_3$ .

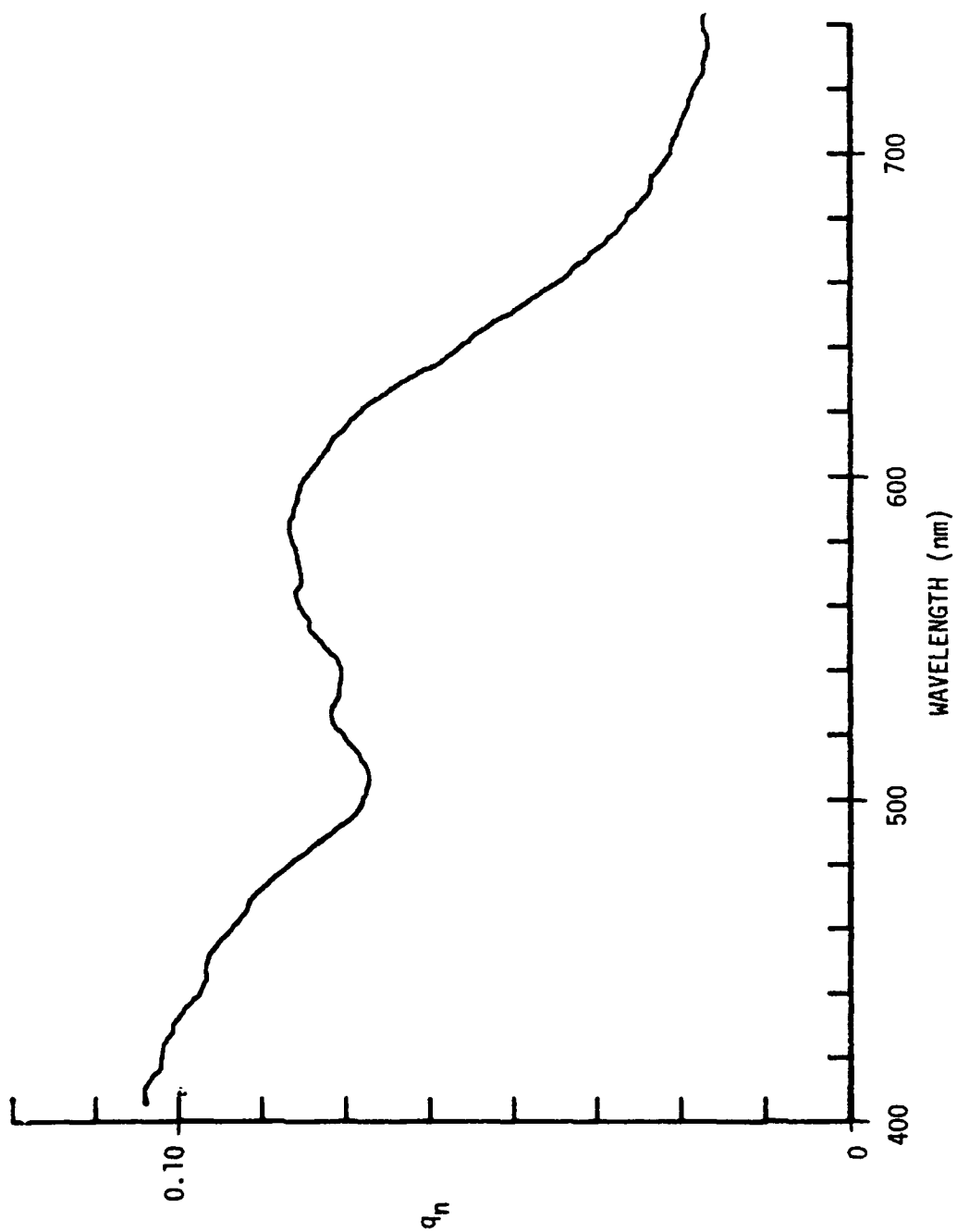


Figure 27. Photoacoustic spectra of Co-Mo/ $\gamma$ -Al<sub>2</sub>O<sub>3</sub> catalysts calcined at 550°C.



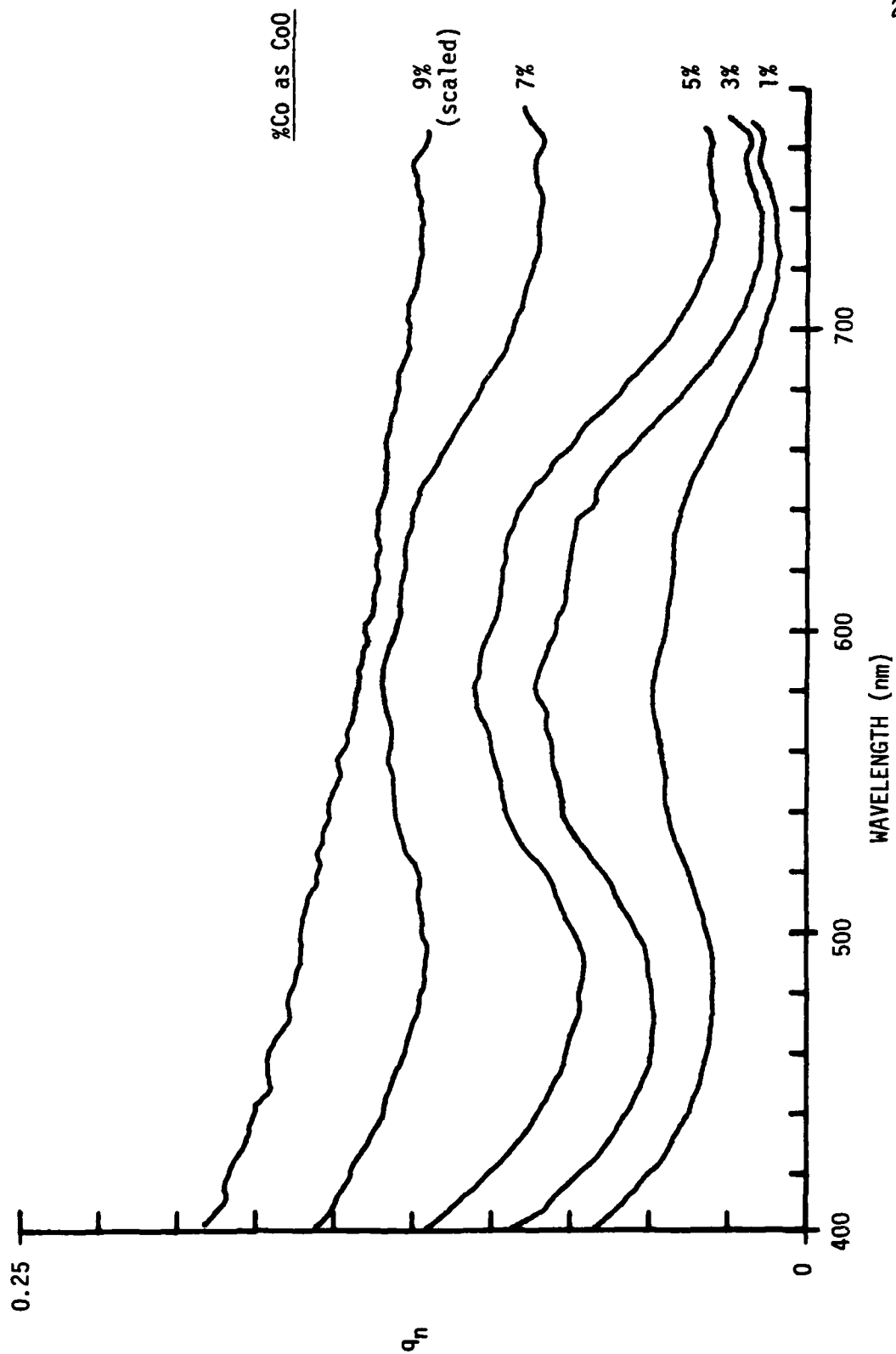


Table 2  
Approximate wavelengths of  
spin-orbit maxima

Material	Wavelengths (nm) <sup>a</sup>		
CoMoO <sub>4</sub>	528	560	584
CoAl <sub>2</sub> O <sub>4</sub> Bulk Spinel	548	~585 (broad)	624
Co/γ-Al <sub>2</sub> O <sub>3</sub> Surface Spinel	539	578	~619 (broad)
Co-Mo/γ-Al <sub>2</sub> O <sub>3</sub> (1% CoO)	545	~580	625

<sup>a</sup>Estimated error is ±3nm.

observed which are associated with  $\text{CoMoO}_4$ , as illustrated in Figure 28. The Co-Mo oxide is, however, not a major constituent.

Conclusions. Several conclusions may be drawn based on comparison of the Co-Mo/ $\gamma\text{-Al}_2\text{O}_3$  system with the Co/ $\gamma\text{-Al}_2\text{O}_3$  system.

(1) The dominant form of cobalt at low cobalt loading is Co(T) in both systems. In the case of Co-Mo/ $\gamma\text{-Al}_2\text{O}_3$  there is evidence that the Co(T) specie is not formed as close to the support surface as in Co/ $\gamma\text{-Al}_2\text{O}_3$ .

(2) At very high Co loading an oxide phase is formed which masks other spectral features.

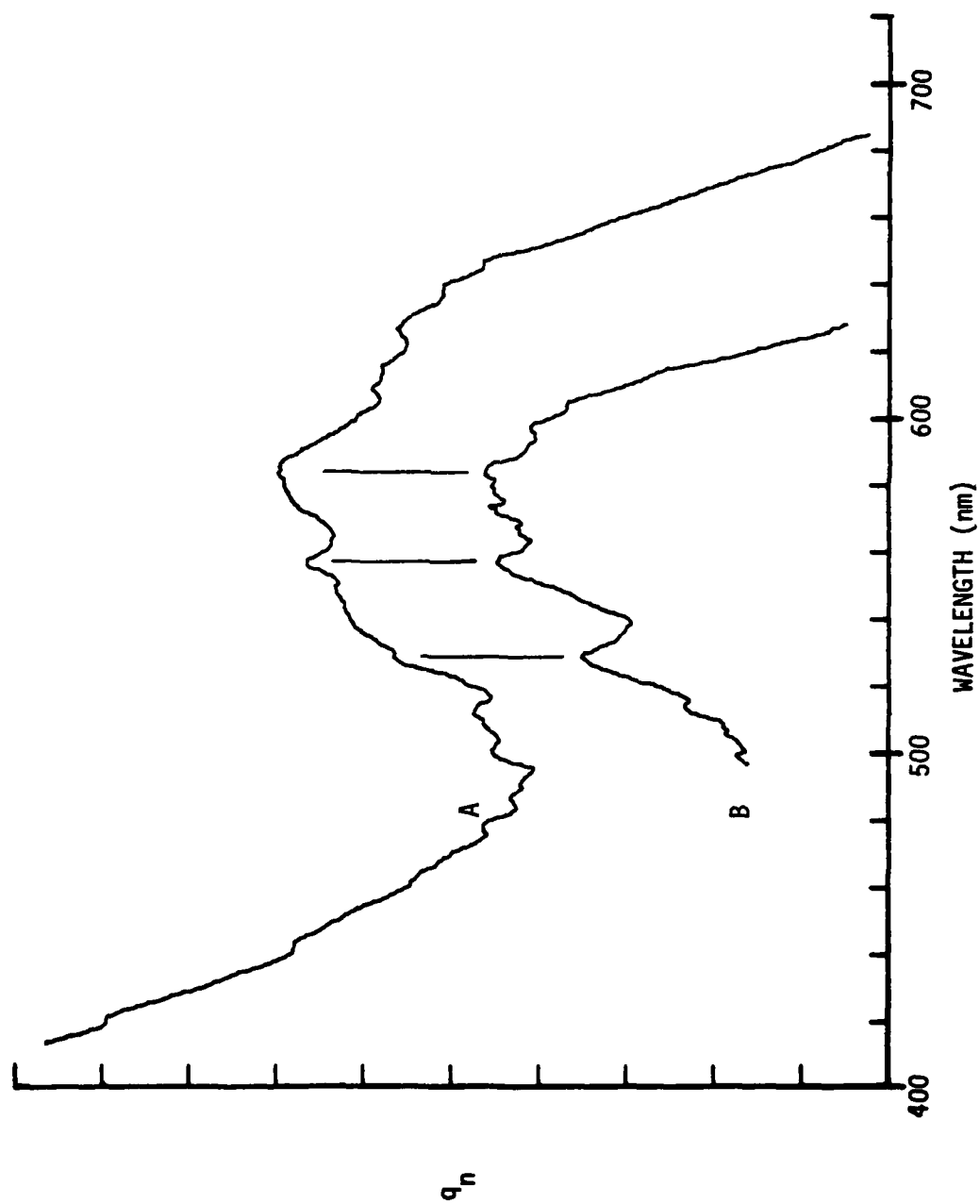
(3) The presence of Mo inhibits the formation of Co(O); instead, a small amount of a cobalt-molybdenum oxide is formed.

#### Model for Metal-Support Interactions

The phenomenon of metal-support interactions as a function of metal loading and calcination temperature for Ni/ $\gamma\text{-Al}_2\text{O}_3$  and Co/ $\gamma\text{-Al}_2\text{O}_3$  catalysts has been described. A simple model is advanced here to account for the qualitative dependence of surface speciation on metal loading and calcination temperature.

Mixed metal oxides,  $\text{M}^{\text{II}}\text{M}_2^{\text{III}}\text{O}_4$ , often have a spinel structure based on a cubic close packing array of oxide ions in which one-eighth of the tetrahedral holes (2 per anion) are occupied by  $\text{M}^{\text{II}}$  ions and one-half of the octahedral holes (1 per anion) are occupied by  $\text{M}^{\text{III}}$  ions. This arrangement is designated  $\text{M}^{\text{II}}[\text{M}_2^{\text{III}}]\text{O}_4$  where the square brackets enclose the ions which occupy octahedral interstices. Other mixed metal oxides

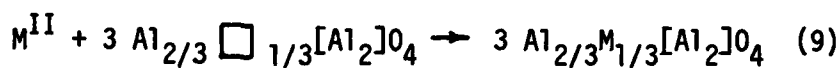
Figure 28. Comparison of photoacoustic spectra of Co-Mo/ $\gamma$ -Al<sub>2</sub>O<sub>3</sub> catalyst loaded with 7% Co (A) with CoMoO<sub>4</sub> spectrum (B).



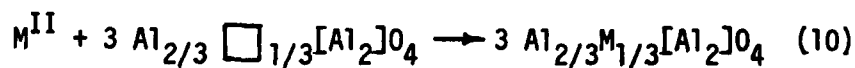
take on an inverse spinel structure,  $M^{III}[M^{II}M^{III}]O_4$ , in which the  $M^{II}$  ions occupy octahedral interstices instead of tetrahedral interstices. In disordered spinels, i.e. partially inverted spinels, a fraction of  $M^{II}$  ions occupy tetrahedral interstices and a corresponding fraction occupy octahedral interstices.<sup>24</sup> The degree of inversion,  $x$ , in the hypothetical reaction shown in Equation 8 has been related to a site preference energy for various transition metal ions relative to  $Al^{3+}$  in  $Al_2O_3$ .<sup>11</sup> The values of  $x$  and the interchange enthalpy for  $NiAl_2O_4$  are 0.78 and -2 kcal, respectively; the corresponding values for  $CoAl_2O_4$  are 0.05 and +13 kcal.



The catalyst support,  $\gamma-Al_2O_3$ , has a defect spinel structure which can be represented  $Al_{2/3} \square_{1/3}[Al_2]O_4$ . This is a spinel structure with a deficit of cations, represented by  $\square$ . The formation of  $M(T)$  can, therefore, be represented by diffusion of  $M^{II}$  into these lattice vacancies.



The formation of  $M(O)$  can similarly be described as follows.





For M(O) formation there is a net exchange of an  $\text{Al}^{3+}$  from an octahedral position to a tetrahedral position. The activation energy for this process is expected to be higher than that for M(T) formation. Narrotsky and Kleppa<sup>11</sup> report the octahedral site preference energy for  $\text{Al}^{3+}$ , described by Equation 12, to be 10.6 kcal/mole.



The Boltzman factor for this process is 0.002 for 600°C compared to 0.03 for 1200°C at which temperature interchange occurs rapidly in aluminates. The Tammann temperature for bulk lattice mobility in alumina (melting point = 2015°C) is approximately 870°C.<sup>25</sup> Hence, it is surmised that the inversion process is slow at the calcination temperatures used in this study. This conjecture is supported by experiment. After calcining a Ni/ $\gamma\text{-Al}_2\text{O}_3$  sample (4% Ni, 600°C) for an additional time of 54 hours at 600°C, no detectable change in the M(T)/M(O) ratio was observed. However, this is not expected to be the case for the inversion process at the surface where the activation energy will be less. Surface diffusion is often important at a much lower temperature than bulk diffusion solids.<sup>26</sup> The Tammann temperature for surface mobility in alumina is approximately 410°C. This phenomenon is very dependent on the surface history. A model for speciation in these catalysts is developed based on an inversion process important only at the surface of the  $\gamma\text{-Al}_2\text{O}_3$  support.

A hypothetical model for speciation at the  $\gamma\text{-Al}_2\text{O}_3$  surface is given in Equation 13.



Within seconds of beginning calcination of a  $\gamma\text{-Al}_2\text{O}_3$  sample impregnated with a small amount of  $\text{Ni}(\text{NO}_3)_2$  or  $\text{Co}(\text{NO}_3)_2$ , the sample takes on a gray color as the nitrate is decomposed. The gray color slowly gives way to the blue color of  $M(T)$ . The gray material,  $M_s$ , which is initially formed may be an amorphous metal oxide bound on the surface. The first step involves incorporation of metal ions into available tetrahedral defect sites on the surface.  $M_s(T)$  is removed from the surface by inversion to  $M(O)$ , with rate  $k_i(M_s(T))$ , or by diffusion into the bulk  $\gamma\text{-Al}_2\text{O}_3$  lattice which is characterized by the diffusion coefficient  $D$ . It is assumed that inversion does not occur in the bulk alumina at the calcination temperatures used. There are three basic mechanisms for diffusion in ionic solids: (1) ions exchange positions with vacant lattice sites, (2) migration through interstitial sites, (3) exchange of lattice sites by rotation of ions about a midpoint.<sup>27</sup> The rate of diffusion of  $M(O)$  into the bulk is expected to be much smaller than for  $M(T)$ . If a vacancy diffusion model is involved then  $M(O)$  diffuses via thermally created lattice vacancies as opposed to defect lattice



vacancies. Interstitial and exchange diffusion mechanisms are expected to have higher activation energies than does a vacancy diffusion mechanism.<sup>28</sup> When the lattice near the surface becomes saturated with  $M(O)$  and  $M(T)$  both diffusion and inversion processes slow and growth of microcrystals of metal oxide accounts for the remaining metal. The arguments used to justify this model are made referring only to an inversion reaction at the surface, the dominant surface reaction for the  $Ni/\gamma-Al_2O_3$  system. In Table 3 surface reaction assignments are proposed for the three catalyst systems studied.

A simple competition between inversion of the spinel forming  $M_s(O)$  at the surface and diffusion of  $M(T)$  into the bulk of the  $\gamma-Al_2O_3$  spinel is envisaged. If a steady state concentration,  $C_T$ , of  $M_s(T)$  is assumed then the rate of removal of  $M_s(T)$  from the surface by diffusion is<sup>29</sup>

$$\text{diffusion rate} = C_T \sqrt{\frac{DA}{\pi t}} \quad (14)$$

where  $A$  is the area of the surface and  $t$  is the time. The rate of removal of  $M_s(T)$  from the surface by inversion is

$$\text{inversion rate} = k_i C_T \quad (15)$$

The approximate time required to incorporate the metal into the lattice is related to the metal loading by

$$(M)_{\text{total}} \approx \left( 2 \sqrt{\frac{DA}{\pi}} t + k_i t \right) C_T \quad (16)$$

Table 3  
Assignments for application of interaction  
model to catalyst systems

System	$M_S(T)$ : Surface Tetrahedral Sites	$M_B(T)$ : Bulk Tetrahedral Interstices	$M(O)$	$M_S(T) \xrightarrow{k} M(O)$
Ni/ $\gamma$ -Al <sub>2</sub> O <sub>3</sub>	Ni <sup>2+</sup>	Ni <sup>2+</sup>	Ni <sup>2+</sup> (O)	Ni <sub>S</sub> <sup>2+</sup> (T) $\rightarrow$ Ni <sub>S</sub> <sup>2+</sup> (O)
Co/ $\gamma$ -Al <sub>2</sub> O <sub>3</sub>	Co <sup>2+</sup>	Co <sup>2+</sup>	Co <sup>3+</sup> (O)	Co <sub>S</sub> <sup>2+</sup> (T) $\rightarrow$ Co <sub>S</sub> <sup>3+</sup> (O)
Co-Mo/ $\gamma$ -Al <sub>2</sub> O <sub>3</sub>	Co <sup>2+</sup>	Co <sup>2+</sup>	Co-Mo oxide (CoMoO <sub>4</sub> )	Co <sub>S</sub> <sup>2+</sup> (T) $\rightarrow$ CoMoO <sub>4</sub>

The relative amounts of metal incorporated into tetrahedral interstices is given by

$$\frac{(M_B(T))}{(M)} = \frac{2\sqrt{\frac{DA}{\pi}}}{2\sqrt{\frac{DA}{\pi}} + k_i\sqrt{t}} \quad (17)$$

and the relative amount of metal incorporated into octahedral interstices is given by

$$\frac{(M_B(0))}{(M)} = \frac{k_i\sqrt{t}}{2\sqrt{\frac{DA}{\pi}} + k_i\sqrt{t}} \quad (18)$$

The time can be eliminated in these expressions by solving Equation 16 for time,  $t$ , and substituting the result into Equations 17 and 18 with the following results.

$$\frac{(M_B(T))}{(M)} = \frac{2}{1 + \sqrt{1 + m \frac{k_i\pi}{DA}}} \quad (19)$$

$$\frac{(M_B(0))}{(M)} = \frac{\sqrt{1 + m \frac{k_i\pi}{DA}} - 1}{1 + \sqrt{1 + m \frac{k_i\pi}{DA}}} \quad (20)$$

In these relationships  $m$  is given by

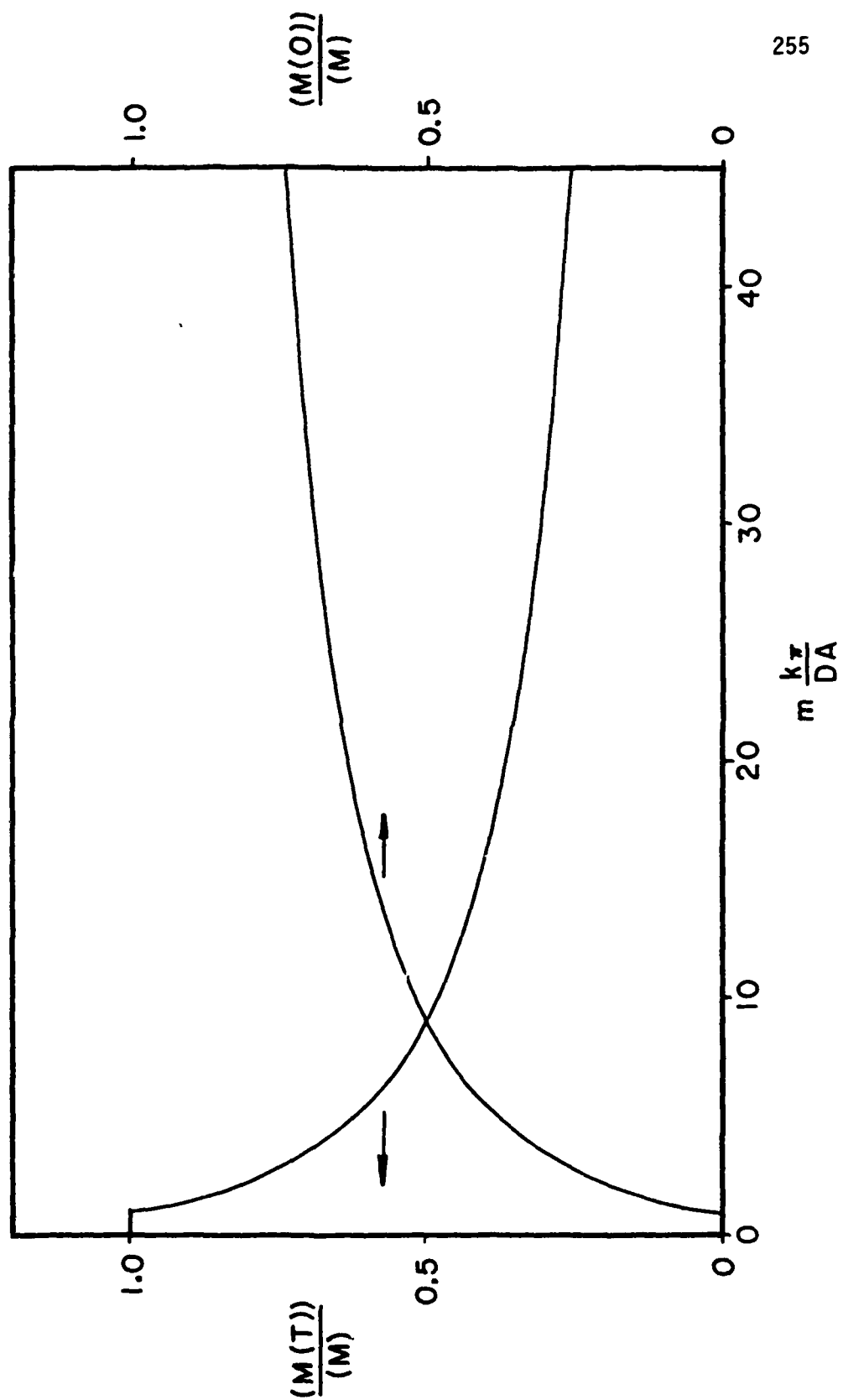
$$m = \frac{(M)}{C_T} \quad (21)$$

The relative amounts of  $M(T)$  and  $M(0)$  are plotted versus the metal loading as represented by  $mk_i\pi/DA$  in Figure 29. An induction period corresponding to  $k_i\pi/DA$  is included for achieving steady state. Formation of  $M(T)$  dominates at low metal loading and  $M(0)$  formation dominates at high metal loading. Even for this crude model, the predicted dependence of the formation of tetrahedral and octahedral species on metal loading is very similar to the corresponding experimental curves for  $Ni/\gamma-Al_2O_3$  and  $Co/\gamma-Al_2O_3$  in Figures 13 - 14 and Figures 23 - 24, respectively. This model predicts that the relative amount of  $M(T)$  compared to  $M(0)$  varies with temperature as

$$\frac{e^{-E_d/RT}}{e^{-E_i/RT}} = e^{(E_i - E_d)/RT} \quad (22)$$

where  $E_i$  is the activation energy for inversion at the surface and  $E_d$  is the activation energy for diffusion of  $M(T)$  into bulk alumina. It has been shown that  $M(T)$  increases at the expense of  $M(0)$  with increasing temperature. Based on the model, it is expected that the relative quantity of  $M(T)$  to  $M(0)$  increases with temperature if  $E_d > E_i$ . It has already been argued that  $E_i > E_d$  for inversion in the bulk lattice. This is another reason to believe that only inversion at the substrate surface is significant.

Figure 29. Prediction by model of relative amounts of  $M(T)$  and  $M(0)$  versus metal loading, represented by  $mk_1\pi/DA$ .



The mechanism advanced satisfactorily accounts for the dependence of the  $M(T)/M(0)$  ratio on metal loading and calcination temperature in these catalyst systems.

### References

1. S. Beckman, J. C. Morrell and G. Egloff, "Catalysis," Reinhold, New York, 1940.
2. M. Wu, R. L. Chin and D. M. Hercules, Spectro. Lett. **11**, 615 (1978).
3. M. Wu and D. M. Hercules, J. Phys. Chem. **83**, 2003 (1979).
4. R. B. Gregor, F. W. Lytle, R. L. Chin and D. M. Hercules, to be published.
5. R. R. Chin and D. M. Hercules, J. Phys. Chem., to be published.
6. Procedure of B. E. Bryant and W. C. Fernelius, Inorg. Syn. **5**, 188 (1957) as adapted in H. B. Gray, J. G. Swanson and T. H. Crawford, "Project ACAC," Bogden and Quigley, New York, 1972, pp. 102-103.
7. L. W. Burggraf and D. E. Leyden, Anal. Chem. **53**, 759 (1981).
8. M. L. Jacono, M. Schiavello and A. Cimino, J. Phys. Chem. **75**, 1044 (1971).
9. M. Shelef, M. A. Z. Wheeler and H. C. Yao, Surface Science **47**, 697 (1975).
10. J. T. Richardson and W. O. Milligan, J. Phys. Chem. **60**, 1223 (1956).
11. A. Navrotsky and O. J. Kleppa, J. Inorg. Nucl. Chem. **29**, 2701 (1967).
12. F. A. Cotton and G. Wilkinson, "Advanced Inorganic Chemistry," 2nd ed., Interscience, New York, 1967, pp. 881-885.
13. K. Klier, Catalysis Reviews **1**, (2) 207 (1967).
14. F. N. Hill and P. W. Selwood, J. Am. Chem. Soc. **71**, 2522 (1949).
15. V. C. F. Holm and A. Clark, J. Catalysis **11**, 317 (1968).
16. F. A. Cotton and G. Wilkinson, op. cit., p. 891.
17. F. A. Cotton and G. Wilkinson, op. cit., p. 864.



18. F. A. Cotton and G. Wilkinson, op. cit., pp. 871-872.
19. F. A. Cotton and G. Wilkinson, op. cit., pp. 874-876.
20. G. N. Asmolov and O. V. Krylov, Kinet. Catal. **12**, 403 (1971).
21. F. E. Massoth, Adv. Catal. **27**, 265 (1978).
22. P. C. H. Mitchell, "The Chemistry of Some Hydrosulphurisation Catalysts Containing Molybdenum," Climax Molybdenum Co., London, 1967.
23. P. Grange, Catal. Rev. Sci. Eng. **21**, (1) 135 (1980).
24. F. A. Cotton and G. Wilkinson, op. cit., p. 51.
25. W. E. Garner, "Chemistry of the Solid State," Butterworths, London, 1955, p. 307.
26. A. W. Adamson, "Physical Chemistry of Surfaces," 2nd ed., Interscience, New York, 1967, p. 265.
27. C. Kittel, "Introduction to Solid State Physics," 3rd ed., John Wiley and Sons, New York, 1967, pp. 564-567.
28. J. R. Manning, "Diffusion Kinetics for Atoms in Crystals," D. Van Nostrand, Princeton, N. J., 1968, cha. 1.
29. D. A. Frank-Kamenetskii, "Diffusion and Heat Transfer in Chemical Kinetics," Plenum, New York, 1969, pp. 142-143.

DATA  
FILM  
8